Tobias Burnus

Study of Charge, Spin, and Orbital States in Novel Transition-Metal Oxides Using X-Ray Absorption Spectroscopy

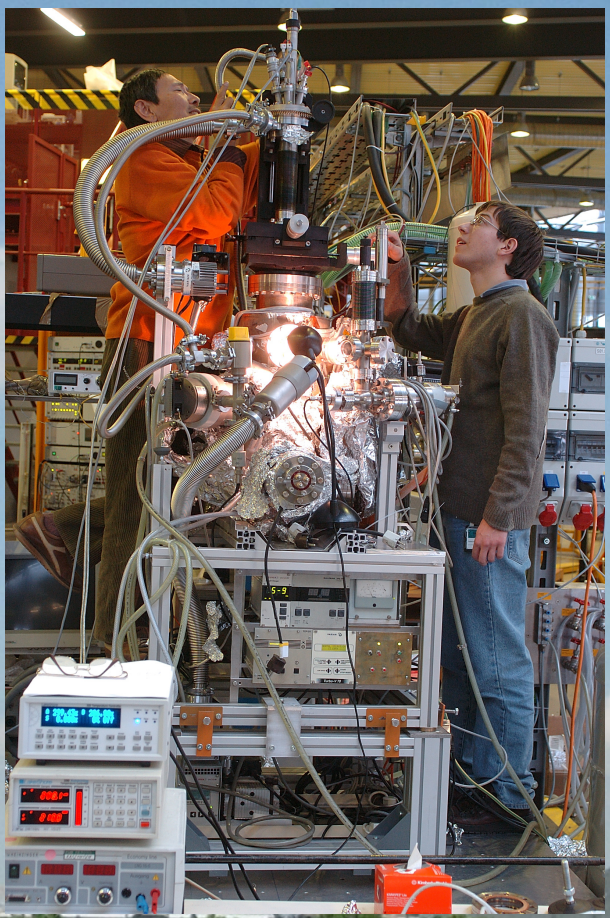

Study of Charge, Spin and Orbital States in Novel Transition-Metal Oxides Using X-Ray Absorption Spectroscopy

View of Cologne in the Sixteenth Century. – From a copper plate in the "Theatrum Geographicum" of Petrus Bertius (1565–1629).

Study of Charge, Spin and Orbital States in Novel Transition-Metal Oxides Using X-Ray Absorption Spectroscopy

Inaugural-Dissertation zur Erlangung des Doktorgrades
der Mathematisch-Naturwissenschaftlichen Fakultät
der Universität zu Köln

vorgelegt von

Tobias Burnus

aus Freiburg im Breisgau

TB Tobias Burnus

Berichterstatter:
Prof. Dr. L. Hao Tjeng
Prof. Dr. Stefan Blügel

Tag der mündlichen Prüfung: 25. Juni 2008

Reprinted as electronic version with minor corrections: May 2010.

Elektronische Hochschulschrift der Universität zu Köln,
http://kups.ub.uni-koeln.de/

The electronic version is also available for free from the Deutsche Nationalbibliothek, http://www.d-nb.de.

The Deutsche Nationalbibliothek lists this publication in the Deutsche Nationalbibliografie; detailed bibliographic data are available in the Internet at http://dnb.d-nb.de. A catalogue record for the printed edition of this book is available from the British Library.

Cover image: Zhiwei Hu (left) and Tobias Burnus at BESSY while measuring Ca_2RuO_4 (24 January 2006). (Photo: Hans Wiedl.) In the background a view from Cologne-Deutz across the river Rhine to the centre of Cologne with the Cathedral *Dom* on the right. (Photo: Tobias Burnus.)

Frontispiece: View of Cologne – the three large stars represent supposedly the Trinity and the several small ones the Electors of the Empire. Taken from www.gutenberg.net (EBook #10940).

Typeset in Latin Modern 10pt with ConTEXt.

Transition-metal compounds show a wealth of intriguing properties such as superconductivity, piezoelectricity, giant magnetoresistance, spin and metal-insulator transitions, which are governed by the interplay of charge, spin, and orbital degrees of freedom. The knowledge of their electronic structure is crucial for understanding and predicting the fascinating properties of these often strongly correlated materials. In this thesis x-ray absorption spectroscopy including x-ray magnetic circular dichroism is combined with theoretical calculations to investigate the orbital occupation and orbital ordering of $La_4Ru_2O_{10}$, which shows a 4*d* orbital-ordering transition with spin-gap opening due to spin-singlet formation, and of Ca_2RuO_4 for which the orbital occupation across phase transitions have been studied. The valence state, spin state and orbital moment has been studied for $Ca_3Co_2O_6$, which have peculiar step-wise jumps in the magnetization, and in Ca_3CoRhO_6 and Ca_3FeRhO_6. For $LaMn_{0.5}Co_{0.5}O_3$ the valence, spin state, magnetic alignment, and magnetocrystalline anisotropy was investigated.

Die Ladungs-, Spin- und orbitalen Freiheitsgrade sind verantwortlich für den vielfältigen Eigenschaften von Übermetallverbindungen; dazu zählen Supraleitung, Ferroelektrizität, Riesenmagnetwiderstand, Spin- und Metall-Isolator-Übergänge. Die Kenntnis der elektronischen Struktur ist essentiell für das Verständnis und die Vorhersage der faszinierenden Eigenschaften, die diese hochkorrelierten Materialien zeigen. In dieser Arbeit wurde die Röntgenabsorptionsspektrosopie einschließlich magnetischem Röntgenzirklardichroismus mit numerischen Rechnungen kombiniert, um die orbitale Besetzung und orbitale Ordnung zu untersuchen in $La_4Ru_2O_{10}$, das einen 4d-Orbitalübergang mit Öffnung einer Spinlücke durch Bildung eines Spin-Singulets zeigt, und in Ca_2RuO_4, bei dem die Änderung der orbitalen Besetzung bei Phasenübergängen studiert wurde. Die Valenz- und Spinzustände und die orbitalen Besetzungen von $Ca_3Co_2O_6$, das ungewöhnliche Sprünge in der Magnetisierung zeigt, und von Ca_3CoRhO_6 und Ca_3FeRhO_6 wurden untersucht. Bei $LaMn_{0.5}Co_{0.5}O_3$ wurde die Valenz, Spinzustand, magnetische Kopplung zwischen Mn und Co und die magnetokristalline Anisotropie erforscht.

This above all: to thine own self be true,
And it must follow, as the night the day,
Thou canst not then be false to any man.
— William Shakespeare, 1564–1616

Preface

TRANSITION-METAL compounds show legions of stunning properties – both macroscopically and microscopically – such as giant magnetorestance, superconductivity, charge- and spin-density waves, metal-insulator transitions, spin-state transitions. But, unfortunately, correlated systems are difficult to describe; neither a purly local nor a simple band picture work. However, a detailed knowledge about the electronic structure is needed to understand and possibly also predict material properties. In this thesis we concentrate on a group of transition-metal oxides, showing a variety of interesting properties and focus especially on the valence state, spin and orbital physics as well as on spin-orbit coupling. These have been studied using x-ray absorption spectroscopy and using numerical calculations. X-ray absorption spectroscopy (XAS) in conjunction with configuration-interaction cluster calculation and density-functional theory calculation provides a means to access information about the properties coming from the interplay of charge, orbital, and spin states in transition-metal compounds.

More about the exciting properties exhibited transition-metal compounds and a primer into ab initio techniques and especially about density-functional theory is given in Chapter 1. In the succeeding Chapter 2, the generation of x-rays in synchrotrons and the basis of x-ray absorption spectroscopy are covered, including the useful sum rules which allow the extraction of quantitative data from spectra without needing complicated calculations. In order to understand the orbital occupation depending on the crystal symmetry and the ions surrounding the atom of interest, the ligand-field theory plays a major role. It is also the basis for the configuration-interation (CI) cluster calculation, which has been used to calculate the absorption spectra. Both ligand-field theory and CI cluster calculations are covered in Chapter 3. Hereafter, the result of our studies is presented.

Using XAS combined with calculations, the valence, spin and orbital state of the quasi one-dimensional cobaltates $Ca_3Co_2O_6$ (Chapter 4) have been ascertained and the unusually large orbital moment and magnetocrystalline anisotropy explained. For $LaMn_{0.5}Co_{0.5}O_3$ (Chapter 5) the magnetic alignment, valence and spin state, and a large orbital could be determined; model calculations point to the presence of a large magnetocrystalline anisotropy and nontrivial temperature dependence of the susceptibility. For the one-dimensional Ca_3CoRhO_6 and of Ca_3FeRhO_6 (Chapter 6) the valence and spin states, and a large orbital moment could be determined; the active role of the spin-orbit coupling explains the strong magnetocrystalline anisotropy and Ising-like magnetism of Ca_3CoRhO_6. The quasi two-dimensional $La_4Ru_2O_{10}$ (Chapter 7) shows a rare $4d$ orbital-ordering transition with spin-gap formation for which no spin-state transition is present but an orbital-induced spin-singlet formation. In Chapter 8 the orbital occupation of Ca_2RuO_4 was studied in the antiferromagnetic, the paramagnetic insulating, and the paramagnetic metallic phase.

A summary in English is given in Chapter 9 and in German in Chapter 10. More about spherical harmonics can be found in Appendix A and details of the transition-metal–ligand hybridization in Appendix B.

Acknowledgement

While it has become a custom to write an acknowledgment and it is often only a mere item on the list of the things which are part of a thesis, for me it has not lost its original meaning since I know that I would not have reached this point and finished the thesis without the help and support of various people. I would like to thank especially the following people who have helped me with all the research projects which lead to this thesis.

I am deeply indebted to my adviser Professor L. Hao Tjeng. He came up with several exciting projects and his deep understanding of and his excitement for physics – both in terms of experiments and of theory – rubbed off on the whole group. I am grateful for all the physics he taught me, be it during his lectures, the experiments or while scrutinizing the draft articles. I thank him also for making me aware about the failures of simple pictures and approximations, which

often work that well and are that simple that one overlooks cases where they are not slightly wrong but give qualitatively the wrong physics.

Secondly, I would like to thank Zhiwei Hu (胡志伟), with whom I did the experiments and the analysis. I learnt a lot from him both in terms of performing the experiments but even more importantly about the configuration-cluster calculation; we discussed all the results in this thesis and especially every result from the cluster calculations. Additionally, his knowledge about x-ray absorption spectra is really amazing, he has virtually measured all transition-metal compounds and can immediately tell the valence state or whether a spectrum is correct or not. Going to the different synchrotrons was always fun as was exploring Taiwan and especially the restaurants in Hsinchu.

Hua Wu (吴骅) I would like to thank for augmenting my knowledge of LDA+U and of band-structure theory; it was also nice to have someone to talk with, who has also a background in density-functional theory. Additionally, his results and the discussion with him about our results were crucial for every paper we published. (And his wife makes really tasty dumplings!)

I would like to thank Maurits W. Haverkort for introducing me into the configuration-interaction cluster calculation program XTLS of Tanaka. He was always open for questions and with his deep knowledge of physics and especially of configuration-interaction cluster calculation, discussing results was always productive.

Furthermore, I would like to thank my office mate Chun-Fu "Roger" Chang (張春富), with whom I had a lot of fun at the office, when exploring the Cologne area or at synchrotrons (including the surroundings of ESRF). But I also liked our discussion about physics, where we successfully tried together to really understand some equations and the physics behind them. Roger, you are a true friend!

But also several others contributed in one way or the other to the thesis. Professor Daniel I. Khomskii had always time to discuss physics; he is a treasure trove regarding new materials and for non-numerical theoretical physics. I would like to thank also Christian Schüßler-Langeheine for helping with countless things, be it the construction of parts, introduction into resonant scattering, helping with the setup of chambers at BESSY, having an ear for physics and non-physics problems. Thanks also to Lucie Hamdan for ensuring (from Cologne) that pumps, chambers etc. working in Taiwan, and for ensuring flawless

that shipping parts and samples from and to Taiwan. I also want to thank the everyone in the group; they helped me in one or the other way – and be it only by providing a nice atmosphere (in alphabetical order, partially moved to other places by now or having been a guest only): Simone Altendorf, Sven Binder, Marcel Buchholz, Beatrice Coloru, Hidenori Fujiwara, Jan Gegner, Rainald Gierth, Philipp Hansmann, Stefan Heise, Andreas Hendricks, Nils Hollmann, Stefan Klein, Peter Körner, Thomas Koethe, Dilek Madenci, Igor Mazin, Marco Moretti, Maxim Mostovoy, Holger Ott, David Regesch, Bruno Roden, Holger Roth, Justina Schlappa, Sergey Streltsov, Ronny Sutarto, Jonas Weinen, Thomas Willers, Hsueh-Hung Wu, Michael Zell.

For the experiments there is another group of people, whose importance is often forgotten: the sample makers (cf. Physics Today, August 2007, pp. 26ff.). I want to thank especially Seiji Niitaka, Hidenori Takagi, V. L. Joseph Joly, P. A. Joy, Delphine Flahaut, Vincent Hardy, Antoine Maignan, Peter G. Khalifah, David G. Mandrus, Robert J. Cava, Satoru Nakatsuji, and Yoshiteru Maeno. We had also inhouse samples and support for aligning the samples, measuring susceptibility, checking samples etc. My thanks also go to all of the II. Physikalisches Institut, especially for providing the support and samples, organizing the Ph.D. seminar, and providing a nice atmosphere. I especially would like to thank: Helena Hartmann, Marco Reuther, C. Zobel, Thomas Lorenz, Paul Steffens, Olaf Schumann, Matthias Cwik, Wolf-Dieter Stein, Markus Braden, Inge Simons. I also would like to thank the mechanical and electronics workshop; especially W. Külzer and P. Hansmann.

I would furthermore thank Arata Tanaka (田中新) for his great and fast configuration-interaction cluster-calculation program XTLS. Thanks go also to the staff at the National Synchrotron Radiation Research Center (NSSRC) in Hsinchu, Taiwan, at the European Synchrotron Radiation Facility (ESRF) in Grenoble, France, and at the Berliner Elektrontronenspeichering Gesellschaft für Synchrotronstrahlung (BESSY) in Berlin, Germany. In particular, I would like to thank Júlio C. Cezar and Nicholas B. Brookes at ESRF; Hong-Ji Lin (林宏基), Ling-Yun Jang (張凌雲), Chien-Te Chen (陳建德), and Keng S. Liang (梁耕三) at NSRRC and Hui-Huang Hsieh (謝輝煌; Chung Cheng Institute of Technology, National Defense University); and Frank Schäfers and Marcel Mertin at BESSY.

I also want to thank Prof. Stefan Blügel of the Forschungszentrum Jülich for reviewing this thesis and for (co)organizing many spring and winter schools in Jülich, in particular for the NIC Winter School 2006 "Computational Nanoscience: Do It Yourself!".

Last but not least I want to thank my parents, Christiane and Thomas†, who encouraged and supported me, and where there when I needed them. And, I would like to thank my aunt Iris Mücke, who accommodated me until I found my own flat and did several tours with me to the various attractions in and around Cologne.

Let all things be done decently and in order.

— I Corinthians

Contents

Images
split the truth
in fractions. — Denise Levertov, 1923–

List of Figures

Believe nothing of what you hear, and only half of what you see. — Proverb

List of Tables

Dictum sapienti sat est. A sentence is enough for a sensible man. — Plautus, *c.* 250-184 BC

Abbreviations

Commonly used appreviations only. See also list of used symbols in the following section.

AF	Antiferromagnet, antiferromagnetic
BESSY	Berliner Elektronenspeicherring-Gesellschaft für Synchrotronstrahlung (synchrotron facility in Berlin, Germany)
CFS	Crystal-field splitting
CI	Configuration interaction
DFT	Density-functional theory
DFG	Deutsche Forschungsgemeinschaft (German funding agency)
DOS	Density of states
ESRF	European Synchrotron Radiation Facility (in Grenoble, France)
FM	Ferromagnet, ferromagnetic
HS	High-spin state
IS	Intermediate-spin state
LDA	Local-density approximation, sometimes also Local spin-density approximation
LDA+U	Local-density approximation with a Hubbard U term
LS	Low-spin state
LSDA	Local spin-density approximation
MIT	Metal-insulator transition
NM	Nonmagnetic
NSRRC	National Synchrotron Radiation Research Center (in Hsinchu, Taiwan)
TM	Transition metal (ion)
SFB	Sonderforschungsbereich ("Collaborative Research Centres", funded by DFG)
XAS	X-ray absorption spectorscopy
XMCD	X-ray magnetic circular dichroism
XTLS	Name of a CI code by A. Tanaka, pronounce "crystals"

I know of only one rule: style cannot be too clear, too simple. — Stendhal, 1783–1842

Used symbols

Symbols of common physical constants can be found in Appendix E

$\partial_x^n = \frac{\partial^n}{\partial x^n}$	n-th partial derivation in x
$\frac{\mathrm{d}^n}{\mathrm{d}x^n}$	n-th total derivation in x
$\frac{\delta^n}{\delta x^n}$	n-th functional derivation in x
$\underline{x}$	denotes a hole (missing electron), e.g. $\underline{n}$ number of holes or $\underline{L}$ a hole in the ligand
$10Dq, \Delta_{\mathrm{CF}}$	crystal-field splitting between t_{2g} and e_g in O_h symmetry
Δ	Charge-transfer energy; as prefix: difference
D_{3d}, D_{3h}	trigonal point symmetry with *h*orizonal or *d*iagonal reflection plane
D_{4h}	tetragonal point symmetry
$d_1, d_{xy}, \ldots$	denotes the symmetry of a d orbital (see Appendix A)
e_g	Mulliken symbol denoting a doubly degenerated state
$\hbar$	Planck constant h over 2π
H_{ex}	(super-)exchange field
i	imaginary unit, $\mathrm{i}^2 = -1$
J	total moment $J = S + L$, denotes either the operator $\hat{J}^2$ or its eigenvalue $\hbar^2 J(J+1)$
$\tilde{J}$	effective moment, often the moment restricted to the t_{2g} subshell
J_{ex}	exchange constant, either per bond or per cluster
J_z	moment J projected to a quantization axis (here: z axis); the eigenvalue of the operator $\hat{J}_z$ is denoted as $\hbar J_z$ or $\hbar m_{J_z}$; denotes also the exchange constant J_{ex} in a certain direction
$L, \tilde{L}, L_z$	orbital moment (cf. J)
O_h	octahedral point symmetry (cubic)
μ_B	Bohr magneton
M	Magnetization, usually in units of μ_B
Ψ	an N-particle wave function
ψ, ϕ	a single-particle wave function

ψ_i, ϕ_i	the i-th single-particle wave function, the i-th orbital
$p_x, \ldots$	denotes the symmetry of a p orbital (see Appendix A)
σ	the spin, here restricted to $\sigma \in \{-\frac{1}{2}, \frac{1}{2}\}$ and often denoted as $\downarrow$ and $\uparrow$
$S, \tilde{S}, S_z$	orbital moment (cf. J)
t_{2g}	Mulliken symbol denoting a triply degenerated state
T_c	critical temperature; here, mostly Curie temperature (T_C), but also Néel temperature (T_N) or "jump" temperature of a superconducture
U_{dd}	Coulomb repulsion between two same-site d electrons, usually denotes the screened (or effective) U
Y_l^m	spherical harmonics

There is something fascinating about science. One gets such wholesome returns of conjectures out of such trifling investment of fact. — Mark Twain, 1835–1910

1 Introduction

TRANSITION-METAL compounds play a major role in the material-science industry, only rivaled by the semiconductor industry. For the industry the magnetic properties are of most interest – be it in form magnetic layers for hard discs, reading heads for hard discs (using the giant magnetoresistance) or nonvolatile magnetic storage (MRAM). Other uses include the superconductivity for powerlines or for magnets used to inductively heat pipes for power stations such that they can be bend. Also for the basic research, transition-metal compounds play a major role: they account for a large part of the solid-state physics but also beyond; in molecular nanotechnology they are represented by single-magnetic molecules [1] and they are also essential for several organic molecules such as the iron ion in haemoglobin. The ubiquitous availability of some of the transition metals (such as iron) combined with their peculiar electronic properties make transition metals that interesting. Their often unpaired spin together with electrons which are on the verge between tightly bound and freely roaming, and the possibility of numerous valence states allows for the large charge, spin, and orbital degrees of freedom. These in turn are the reason for

the multifarious properties. While the transition-metal alloys and intermetallic compounds have various important properties, the most fascinating properties are shown by the oxides. Similarly to carbon-based organic materials, the number of transition-metal compounds and especially of oxides is virtually unlimited.

In the remaining of this chapter, we first take a short tour through the properties shown by transition-metal oxides. This is followed by an introduction into density-functional theory, the Hubbard model, and LDA+U.

1.1 The rich physical properties of transition-metal oxides

The transition-metal oxides exhibit legions of stunning features, some of which are barely understood. They have conductivities ranging from good metals to strong insulators (of Mott–Hubbard, charge-transfer or band type) and often show metal–insulator transitions; they can be ferro-, ferri-, antiferro-, para-, or diamagnetic. The magnetic as well as the spin and orbital states can change upon temperature, pressure, field, or doping. They show effects such as giant magnetoresistance (GMR), (high-temperature) superconductivity, multiferroicity (ferroelectricity, ferroelasticity, piecoelectricity), spin and charge density waves. Some of these effects only occur at interfaces or surfaces or are modified by those. In the following, we highlight some materials and their properties, which show how vibrant the research of transition-metal oxides.

Last year's Nobel Prize in Physics [2], awarded to Albert Fert [3]and Peter Grünberg [4], honours the discovery of the GMR effect just twenty years after its discovery and after already several years of wide-spread use in devices. Hereby magnetic multilayers, where ferromagnetic and nonmagnetic metals are stacked on each other, show a drastic change of electric resistivity upon applying a magnetic field. The layers (initially of iron–chromium–iron) are grown such that the ferromagnetic layers are antiferromagneticly coupled; thus up-spin and down-spin electrons scatter at the interfaces. However, in a magnetic field all ferromagnetic layers are aligned and thus the scattering for one spin channel is reduced as is the resistivity.

Superconductivity (SC), i.e. the drop of the electric resistivity to zero and formation of a perfect diamagnet (Meißner–Ochsenfeld effect,

found 1933), is known since the beginning of last century. However, only with the discovery of the so-called high-temperature superconductors in 1986 in $Ba_xLa_{5-x}Cu_5O_{5(3-y)}$ [5], the route to superconductors with critical temperatures reachable by cheap liquid nitrogen (boiling point 77.36 K) was opened. High-temperature superconductors, which are typically cuprates, are so far not fully understood theoretically. Sr_2RuO_4 is one of the few no copper containing, transition-metal-oxide superconductors and this year even an iron-based SC (fluorine-doped LaOFeAs) was found [6]. Additionally, in superconducting cuprates, the existence of a real-space stripe structure is debated; they were reported in neutron-scattering studies and predicted theoretically, however, both results have not been universally accepted. Furthermore, doped nickel oxides and Nd-doped $La_{2-x}Sr_xCuO_4$ are believed to have stripes. (See Ref. 7, references there in and Refs. 8 and 9.)

A prime example for different spin-states and transitions between those are cobaltates. Cobalt is typically either divalent (2+, $3d^7$) or trivalent (3+, $3d^6$). For trivalent Co there are three spin states possible: a high-spin state following Hund's rules with $S = 2$ (5 up, 1 down spin), a low-spin state with $S = 0$ with all electrons paired which happens if the octahedral-splitting between the three lower-lying t_{2g} and the two higher e_g orbitals is large, and even an intermediate spin case with $S = 1$. An example for spin-state transitions is $LaCoO_3$, which has a nonmagnetic low-temperature ground state and becomes gradually paramagnetic with increasing temperature (and over 500 K it becomes metallic); in the 1960s this was interpreted as gradual population of a high-spin excited state starting from a low-spin ground state. Starting from 1996 [10] studies suggested that the excited state is a intermediate-spin state instead, which was ten years later rebutted and the initial picture was re-established based on an x-ray absorption study (see Ref. [11] and citations therein). However, as one might have expected, this result has not settled spin-state issue until today (see e.g. Ref. 12 of 2008, which again suggests an intermediate state). The following materials have been studied in this thesis.

The Ising-like one-dimensional cobaltate $Ca_3Co_2O_6$ shows step-like jumps in the magnetization, whereas the iso-structural Ca_3CoRhO_6 has a single jump at high field and Ca_3FeRhO_6 is a three-dimensional antiferromagnet; using XAS plus calculations, the valence and spin states were determined and the explain the large orbital moment explained

(see Chapters 4 and 6). Upon manganese doping the above mentioned $LaCoO_3$ becomes ferromagnetic with a Curie temperature of about 240 K for $LaMn_{0.5}Co_{0.5}O_3$; our study (see Chapter 5) not only reveals their charge and spin state, but also the sizable orbital moment which together with model calculations suggests a strong magnetocrystalline anisotropy and a nontrivial temperature dependence of the magnetic susceptibility.

The series $Ca_{2-x}Sr_xRuO_4$ shows a rich phase diagram, ranging from the superconducting metallic Sr_2RuO_4 via metamagnetic compounds to antiferromagnetic paramagnets for $x < 0.2$; Ca_2RuO_4 itself becomes first paramagnetic and then metallic, which is accompanied by strong orbital occupation changes (see Chapter 8). The importance of orbital physics can also be seen for $La_4Ru_2O_{10}$, which exhibits a rare $4d$ orbital ordering transition and spin-gap formation; the orbital physics drives the formation of spin-singlet dimers in this $S = 1$ system (see Chapter 7).

1.1.1 Theoretical methods

The electronic structure of transition-metal oxides is, maybe not surprisingly, complex and thus it is challenging to calculate and understand the properties . In theoretical physics, the problem has been attacked from two sides: On one hand using ab initio calculations which are based on (effectively) single-particle approximations such as Hartree–Fock or density-functional theory (DFT) and on the other hand using models which contain only very few particles and interactions, but which describe the important physics of interest such as the Hubbard or Anderson impurity model [13–15]. Both approaches have made tremendous progress in the last decades (cf. Table 1.1). (The much increased computational power also helped a lot, though the progress in understanding and the invention of clever approximations was more important.[1]) Besides the intrinsic improvements of the theories – such as using improved functionals in density-functional theory (from LDA to GGA to meta-GGA to hybrid-functionals and

[1] "If given the choice between the computers of today together with the physical concepts of the 1970s *or* the computers of the 1970s along with current concepts, I'd choose the latter." (Quip by James R. Chelikowsky in 2000 and often cited by Marvin L. Cohen.)

optimal effective potentials, from collinear to noncollinear magnetism, from DFT to density-matrix functional theory, etc.) – one finds more and more combinations with either many-body perturbation theory or model-Hamilton approaches, yielding methods such as LDA+U, DFT-based *GW* and Bethe–Salpeter calculations but also the dynamical-mean-field theory (DMFT) which is often based on DFT calculations (LDA+DMFT).

With regards to experiments, the model descriptions help with understanding and qualitatively predicting results whereas the ab-initio based calculations allow a quantitative comparison, but give sometimes less insight. The band structure stemming from calculations is widely used and provides useful information, which can be compared with experiment, especially with photoemission spectroscopy (PES) in terms of band gap, density of states (DOS) and (via angle-resolved photoemission) with the band structure itself. However, there are plenty of issues with this approach. By construction one cannot expect that the DFT band structure has anything to do with the real system, although it often gives a good description. Additionally, many transition-metal oxides are insulating but in DFT calculations they are metallic (this can be cured using LDA+U or LDA+DMFT). Furthermore and fundamentally, in experiment one removes a fully interacting electron from the system, which is influenced by the remaining system while being emitted; in the calculation one assumes that its energy matches the ground-state DOS/band structure. The *GW* method describes PES spectra in principle correctly, however, most calculations miss terms needed to describe multiplet states. Fortunately, a comparison of DFT, DFT+U or DMFT calculated DOS with PES is often meaningful, though one has to be careful with the interpretation.

For x-ray absorption spectroscopy (XAS) one excites a core electron into the valence band, which matches in an independent particle picture of a simple transition into the unoccupied DOS. However, contrary to PES where one can use the sudden approximation, the created hole and the excited electron strongly interact with another. Therefore, a spectrum calculated by shifting the unoccupied DOS by the core-hole energy is often qualitatively wrong. The spectrum can be properly calculated ab initio using time-dependent density function theory and Bethe–Salpeter equation (see e.g. Ref. 16–17), however, this is computationally expensive and does not completely reproduce the fine structure (which

is of more interest than the absolute energy position). Therefore, we use the computationally much simpler configuration-interaction cluster calculation, which includes the full multiplet structure and reproduces the spectra well. While this technique is not fully ab initio (though most parameters come from ab-initio calculations, though some fitting to the experiment is done), it contains the essential and for the experiment relvant physics; more about this technique can be found in Chapter 3.

Table 1.1 A short history about progress in solid-state calculations, compiled by M. Cohen [18].

1920s	Quantum Mechanics Atomic Spectra Sharp; Solid State Spectra Broad
1930s	Fermi's Atomic Pseudopotentials; Thomas-Fermi Model; Dirac's DFT; Hartree, Hartree-Fock
1940s	'Dilemma' of Band Structure Calculations (localized core states and itinerant valence states); Orthogonalized Plane Wave (OPW) of Herring; Augmented Plane Waves (APW) by Slater
1950s	Applications of OPW and APW; Results Were Marginal; OPW $\rightarrow$ Pseudopotentials (computers improve)
1960s	Empirical Pseudopotential Method (EPM); Planewaves and Optical Data; Strong Experimental-Theoretical Collaborations; Importance of Critical Points, Photoemission; Spectroscopy, and Transferability Realized; Electronic/Optical Problem Basically Solved!
1970s	EPM Applications to Many Crystals; Electronic Charge Densities; Bonding and Self-Consistency; Supercells; Surfaces, Interfaces and Localized Configurations; Semiempirical '$X\alpha$'-Type Methods; $\varepsilon(q,\omega)$; (large mainframe computers)
1980s	Total Energy Approach [Structural, Mechanical, Vibrational, Superconducting, High Pressure, other Ground State Properties]; Ab Initio Pseudopotentials plus DFT
1980s and 1990s	Excited States, 'GW' Method, Quantum Monte Carlo, Real Space Methods, Excitonic Effects, Car-Parrinello Molecular Dynamics
1990–present	The Standard Model Emerges with Applications to Complex Materials, Nanocrystals and Nanostructures, Molecules, Superconductors, Optical and Photoemission Experiments (parallel machines, powerful workstations and 'canned' programs)

1.1.2 Experimental progress

But also on the experimental side, there was a tremendous progress over the decades. This begins with the sample quality, which has continuously improved over the years; this includes the invention of mirror

furnaces which help to obtain single crystals but also the advances in growing epitaxial thin films. For magnetization measurements invention of the SQUID (invented 1964), which contains superconducting loops [transition-metal compound!] with Josephson junctions, helped as much as the other advances in resistivity, optical or neutron measurements. For the soft x-ray spectroscopic methods, the progress in the generation of x-rays and in particular the development of synchrotrons (see next chapter) boosted the brilliance and made polarization-dependent measurements more feasible. Using valence-band and core-level (x-ray) photoemission (PES, XPS) the electronic structure of material can be studied and directly compared with *GW* calculations and with the density of states (DOS) or with the band structures (using angular-resolved PES, ARPES) from DMFT, DFT, or even tight-binding calculation. Using spin-polarized PES one can also obtain information about spin-orbit coupling. Of prime interest for this thesis is the x-ray absorption spectroscopy, which is contrary to PES a charge-neutral excitation. Here, a core electron is excited into the valence band; typically one measures in transition-metal (TM) compounds $2p \rightarrow 3d$ (or $4d$) excitations for the TM ion (TM-$L_{2,3}$ edge) and $1s \rightarrow 2p$ for oxygen (O-K edge). Due to the created core hole the excitation is excitonic (thus local) and, as the energy difference for $2p \rightarrow 3d$ is highly element specific, the edges of different TM ions can be measured separately. The excitation is dipole allowed and sensitive to the detailed electronic structure of valence shell, which allows to obtain the valence, spin and orbital information. More about this in the next chapter. Note that due to averaging over all sites (consisting of the same element) x-ray absorption spectroscopy is unable to measure certain kinds of orbital ordering, in this case techniques such as x-ray resonant diffraction should be used.

An interesting development is optical lattices, which are a result of the research on Bose–Einstein condensates and have a potential application in quantum computing. In optical lattices, counterpropagating laser beams create a periodic potential in which neutral atoms can be trapped via the Stark shift; these grids of atoms can be one, two, or three dimensional. Optical lattices are also an ideal test bed to study model solids: The atoms for a perfect crystal without defects and by tuning the laser one can tune between more atomistic atoms having little overlap with other atoms and strongly overlapping wavefunctions.

This allows to study the intermediate range systems which are neither fully localized nor metallic and match thus strongly correlated "normal" solids, in which this parameter tuning can only be done via doping or pressure.

1.1.3 Further reading

An introduction into the world of strongly correlated materials and their calculation can be found in several articles such as the review article by Imada, Fujimori and Tokura [19], but also in articles by Tokura and Nagaosa [20] and Khomskii and Sawatzky [21]; in the book by Fulde [22], in the book by Fazekas [23], in the review articles by Pavarini, Yamasaki, Nuss, and Andersen [24], and by Katsnelson *et al.* (more about half metals, but good overview about techniques) [25], and legions of other books and articles. Some more general introduction about magnetism and the experimental and theoretical techniques can be found in the books of the IFF Spring Schools [26–27]; for ab-initio calculations beyond LDA see Refs. 28 and 29.

We now continue with a primer into density-functional theory, followed by the Hubbard model and LDA+U. More about configuration interaction can be found in the ligand-field theory chapter (Chapter 3).

1.2 Density-functional theory (DFT)

1.2.1 Schrödinger equation

In order to describe the transition-metal compounds – or any kind of other molecule or solid – one "merely" needs to solve the Schrödinger equation; the stationary Schrödinger equation of a system with N electrons and N_n nuclei is given by

$$H\Psi(\boldsymbol{r}) = [T + V(\boldsymbol{R}, \boldsymbol{r})]\Psi(\boldsymbol{r}) = E\Psi(\boldsymbol{r}), \tag{1.1}$$

where r denotes the electron and R the nuclear coordinates. Assuming that the mass of the nuclei M is infinite, the kinetic energy operator of the electrons is given by

$$T = -\frac{\hbar^2}{2m_e} \sum_{i=1}^{N} \nabla_i^2 \tag{1.2}$$

and the potential, consisting of electron–nuclei and electron–electron interaction, is given by

$$V = -\sum_{i=1}^{N} \sum_{j=1}^{N_n} \frac{1}{4\pi\varepsilon_0} \frac{Z_j e^2}{|\boldsymbol{r}_i - \boldsymbol{R}_j|} + \frac{1}{2} \sum_{j=1, i\neq j}^{N} \frac{1}{4\pi\varepsilon_0} \frac{e^2}{|\boldsymbol{r}_i - \boldsymbol{r}_j|}. \tag{1.3}$$

Ignoring relativistic effects to which also the important spin–orbit coupling counts, solving this is enough to describe the system. However, the following quote of Paul Dirac, who shared the Nobel Prize in physics for 1933 with Erwin Schrödinger, still holds. In 1929 he wrote the following in an article titled "Quantum Mechanics of Many-Electron Systems" [30], which is frequently quoted.

> The general theory of quantum mechanics is now almost complete, the imperfections that still remain being in connection with the exact fitting of the theory with relativity ideas. These give rise to difficulties only when high-speed particles are involved, and are therefore of no importance in consideration of atomic and molecular structure and ordinary chemical reactions, in which it is, indeed, usually sufficiently accurate if one neglects relativity variations of mass with velocity and assumes only Coulomb forces between the various electrons and atomic nuclei. The underlying physical laws necessary for the mathematical theory of a large part of physics and the whole of chemistry are thus completely known, and the difficulty is only that the exact application of these laws leads to equations too complicated to be soluble. It therefore becomes desirable that approximate practical methods of applying quantum mechanics should be developed, which can lead to an explanation of the mean features of complex atomic systems without too much computation.

This is unfortunately still true; essentially, the only calculable systems are single particles in a potential, be it that potential is an external field, a nucleus or the effective field created by other electrons. This technique is used for Hartree–Fock calculations (cf. Section 3.5), but also in density functional theory, on which we concentrate now.

1.2.2 Hohenberg–Kohn theorem

Density functional theory is based on two clever ideas. It is known that, knowing the Hamilton operator, we can in principle calculate the wavefunction which gives us access to all expectation values and, by integrating the square modulus of the wavefunction over all coordinates but one, we can easily obtain the electron density. Hohenberg and Kohn [31] have now shown that one can take the reverse route and reconstruct in principle the potential (up to a constant) from the ground-state density alone; this means that the density $n(\boldsymbol{r})$ contains the same information as the wavefunction $\Psi(\boldsymbol{r}_1, \ldots, \boldsymbol{r}_N)$, which depends on the coordinates of all N electrons. For wavefunctions, we know that the Rayleigh–Ritz principle applies: Be Ψ the ground-state wavefunction to a Hamiltonian H and be $\tilde{\Psi}$ any other normalized wavefunction; we then know that

$$E_0 = \langle \Psi | H | \Psi \rangle \leq \langle \tilde{\Psi} | H | \tilde{\Psi} \rangle. \tag{1.4}$$

Thus one can obtain the ground-state wavefunction in principle by plugging in all possible trial wavefunctions and looking for the minimal energy. (In practice one starts with some guess and calculates the trial wavefunctions iteratively [self-consistent field (SCF) method].) This technique is used in Hartree–Fock. Using the density, the energy can be written as (unknown) functional of the density as follows

$$E[n] = F_{\mathrm{HK}}[n] + \int V(\boldsymbol{r}) n(\boldsymbol{r}) \, \mathrm{d}^3 r, \tag{1.5}$$

where V is the so-called external potential of the system (potential nuclei, external fields). It is important to note that F is a functional which is universal, i.e. it is system independent and only depends on the kind of interaction (here, the Coulomb interaction), and all system dependence is in the second term. If one now minimizes the above energy functional, one obtains the ground-state energy and density.

1.2.3 Kohn–Sham formalism

The next step was the Kohn–Sham formalism [32], which shows a practical route. First, Kohn and Sham showed that one can construct a Hamiltonian describing a noninteracting system such that it has the

same density as the original interacting system. Then they derived an approximation for the energy functional which allows to use this scheme: the local-density approximation, which became hugely important in solid-state physics, and via improved functionals (GGAs [generalized-gradient approximation] and beyond) also in chemistry. The Kohn–Sham Schrödinger equation of the auxiliary system is given by

$$\left(-\frac{\hbar^2}{2m}\nabla^2 + v_{\mathrm{KS}}(\boldsymbol{r})\right)\phi_i(\boldsymbol{r}) = \varepsilon_i\phi_i(\boldsymbol{r}), \tag{1.6}$$

where summing the square moduli of the lowest N eigenstates yields the density of the fully interacting system and summing the eigenenergies of ϕ_i yields the energy of the noninteracting system; the energy of the interacting system is given by

$$\begin{aligned} E[n] &= T[n] + W[n] + \int n(\boldsymbol{r})V(\boldsymbol{r})\,\mathrm{d}^3r \\ &= T_{\mathrm{KS}}[n] + \frac{1}{4\pi\varepsilon_0}\frac{e^2}{2}\int\int \frac{n(\boldsymbol{r})n(\boldsymbol{r}')}{|r-r'|}\,\mathrm{d}^3r\,\mathrm{d}^3r' \\ &\quad + \int n(\boldsymbol{r})V(\boldsymbol{r})\,\mathrm{d}^3r + E_{\mathrm{xc}}[n]. \end{aligned} \tag{1.7}$$

Here, the second term is the direct, or Hartree, term and the last term is the so-called exchange-correlation (xc) energy functional, defined as

$$E_{\mathrm{xc}}[n] = F_{\mathrm{HK}}[n] - \frac{1}{4\pi\varepsilon_0}\frac{e^2}{2}\int\int \frac{n(\boldsymbol{r})n(\boldsymbol{r}')}{|r-r'|}\,\mathrm{d}^3r\,\mathrm{d}^3r' - T_{\mathrm{KS}}[n]. \tag{1.8}$$

The exchange-correlation potential is then given by

$$v_{\mathrm{xc}}[n](\boldsymbol{r}) := \frac{\delta E_{\mathrm{xc}}[n]}{\delta n(\boldsymbol{r})}. \tag{1.9}$$

and the potential in the Kohn–Sham equation is finally

$$V_{\mathrm{KS}}(\boldsymbol{r}) = V(\boldsymbol{r}) + \frac{1}{4\pi\varepsilon_0}e^2\int \frac{n(\boldsymbol{r}')}{|r-r'|}\,\mathrm{d}^3r' + v_{\mathrm{xc}}(\boldsymbol{r}). \tag{1.10}$$

Before we can use this in practice, one needs still to find an approximation for $E_{\mathrm{xc}}[n]$; the first and still one of the most important approximations is the local density approximation (LDA) published in the same article of Kohn and Sham:

$$E_{\mathrm{xc}}^{\mathrm{LDA}}[n] := \int n(\boldsymbol{r})\varepsilon_{\mathrm{uni}}(n(\boldsymbol{r}))\,\mathrm{d}^3 r, \tag{1.11}$$

where $\varepsilon_{\mathrm{uni}}$ denotes the exchange-correlation energy per particle of a uniform electron gas with the density n; there exists several essentially identical versions of $\varepsilon_{\mathrm{uni}}$, coming from parameterizations of quantum Monte Carlo calculations or from simple estimates by Wigner.

In principle the electron density itself is enough to treat magnetism; however, lacking a suitable functional, one treats the spin-up and spin-down density separately. The density n and the magnetization density m are then given by

$$\begin{aligned} n(\boldsymbol{r}) &= n_{\uparrow}(\boldsymbol{r}) + n_{\downarrow}(\boldsymbol{r}) \\ m(\boldsymbol{r}) &= n_{\uparrow}(\boldsymbol{r}) - n_{\downarrow}(\boldsymbol{r}). \end{aligned} \tag{1.12}$$

In the local-density approximation, the functional for these calculations is called local spin-density approximation (LSDA) but sometimes "LDA" is used as umbrella name for both spin polarized and unpolarized calculations. An overview about spin-polarized DFT calculations can be found for instance in Ref. 33; more about noncollinear magnetism can be found, e.g., in Refs. 34 and 35.

1.2.4 LDA and beyond

The density-functional theory gives in principle the exact result (if we knew the true exchange-correlation functional). And for the homogeneous electron gas LDA is exact – including all electron–electron interactions present there. Another advantage of DFT using LDA or GGA functional is the relatively cheap computational effort, which is cheaper than for instance Hartree–Fock. Compared with the latter, the DFT functionals contain an approximation for the electron correlation (which Hartree–Fock lacks) but not the exact exchange term (which Hartree–Fock has). (One can use the exact exchange term in DFT but the results do not improve consistently as the correlation term is not known exactly enough and non-exact-exchange functionals rely on the cancellation of errors.) The result is the band gaps in Hartree–Fock are overestimated while in density functional theory the gap is often too small (insulating materials have no calculated band gap and are

thus metallic); an empirical solution is to mix both potentials, yielding so-called hybrid functionals. Another related problem of many DFT functionals is that an electron can interact with itself (self-interaction error) – contrary to Hartree–Fock; this causes especially problems for localized electrons in strongly correlated materials (valence d electrons in transition-metals). This can be fixed using a self-interaction correction (SIC) [36](which is unfortunately basis dependent and scales one over the system size; one thus needs to use a local [Wannier] basis). For strongly correlated systems one often also goes beyond normal DFT by including a Hubbard-like U term (for certain Kohn–Sham orbitals only, e.g. the valence d electrons) in the potential and by approximately substracting the Coulomb interaction, which is already present in the functional (typically LDA or GGA); another way is to use the DFT result as starting point for the dynamic mean-field theory.

Note that essentially only the density of the noninteracting system matches the interacting one; the energies and energy differences of the Kohn–Sham system have no meaning according to the theory. One can still use the band structure and calculated density of states to compare with experiment (PES, ARPES; optical or photoemission band gap); while this often works it also fails frequently especially for Mott insulators but also for other materials where correlation plays a role. For the optical band gap and other charge-neutral excitations, one has to go beyond the ground-state DFT: The time-dependent density functional theory (TDDFT) [37]describes these in principle exact, in practise the exact functional (the exchange-correlation kernel) is also not known. (An alternative to TDDFT in terms of the many-body perturbation theory is the Bethe–Salpeter equation.) For non-charge-neutral excitations one should use Green function based methods such as GW (G stands for the Green function and W for the screened Coulomb interaction). (Also the CI cluster program used for calculating the XAS spectra in this thesis is able to calculate XPS spectra using Green functions.)

A short and simple but more rigorous introduction about DFT and TDDFT can be found in my diploma thesis [38]and more extensively in Kohn's Nobel lecture [39], the lecture notes by Perdew and Kurth [40], Burke's *ABC of DFT* [41], or in the book of Richard Martin [42]. For TDDFT, see the textbook by Marques *al* [43]. For many-body techniques see the book by Mahan [44]or by Fetter and Walecka [45].

An overview about TDDFT, *GW* and Bethe–Salpeter can be found in the review article by Onida, Reining and Rubio [46]. For *GW*, LDA+U, DFT+SIC and OEP (optimal-effective potential) methods for strongly correlated materials see Ref. 28, and for LDA+U see also the following section.

1.2.5 The Hubbard model and LDA+U

As written above, the (known) density functionals show deficits for strongly correlated materials; these usually contain transition-metal (or rare-earth) ions with partially filled d (or f) shells. For an orbital-independent potential – such as generated by LDA – one then obtains partially filled d bands, metallic electronic structure and itinerant d electrons, whereas d electrons are usually well-localized. In (Mott–Hubbard) insulators the localized d electrons are separated into two subbands, called lower and upper Hubbard band. One solution is the self-interaction correction (SIC), which reproduces the localized nature of the d electrons but whose one-electron energies are usually in strong disagreement with spectroscopic data [28, 47]. In Hartree–Fock [48]the self-interaction term cancels exactly and thus Mott insulators are properly described. However, the Coulomb interaction is unscreened in Hartree–Fock – the "bare" Coulomb interaction parameter U is thus rather large (15–20 eV) while in a solid it is only about 8 or less [49–50]. Consequently, also the Hartree–Fock gap is usually more than 2–3 times too large [48]. The screening problem is addressed rigorously by going to the *GW* approximation [51–52], however, while the method has been applied successfully to real systems, more complex systems have not been feasible due to their high computational demands. Additionally, the response function used in pratical applications [53] is calculated from DFT energy bands and wavefunctions, which is an insufficient starting point for strongly correlated materials.

In the following LDA+U [28, 54–57] is described where the non-local and energy-dependent self-energy is approximated by a frequency independent but non-local screened Coulomb potential. A similar approximation has been successfully used in a model Hamiltonian approach [58–59](see also Chapter 3).

1.2.6 The Hubbard Model

The Hubbard model was introduced essentially simultaneously by Gutzwiller [60], Hubbard [61–64], and Kanamori [65] and is a simple model which describes two competing tendencies: The kinetic energy (electron hopping) wants to delocalize the electrons into itinerant (Bloch) states, leading to a metal. The electron-electron interaction (approximately on-site Coulomb interaction) wants to localize the electrons on site, driving the system into a Mott insulator. (See Fazekas [23] for a more detailed description and a historic account.) The one-band Hubbard model Hamiltonian is given by

$$H = -t \sum_{\langle ij \rangle} \sum_{\sigma} (c^{\dagger}_{i\sigma} c_{j\sigma} + c^{\dagger}_{j\sigma} c_{i\sigma}) + U \sum_{i} n_{i\uparrow} n_{i\downarrow}, \tag{1.13}$$

where i and j are lattice site indices and $c^{\dagger}_{i\sigma}$ creates an electron in the Wannier state $\phi(\boldsymbol{r} - \boldsymbol{R}_i)$ with spin σ. The first term describes the kinetic energy (the hopping from site to site) while the second term describes the Coulomb repulsion between electrons sharing the same orbital; the Hubbard U is defined as

$$U = \int \mathrm{d}^3 r_1 \int \mathrm{d}^3 r_2 \, |\phi(\boldsymbol{r}_1 - \boldsymbol{R}_j)|^2 \frac{1}{4\pi\varepsilon_0} \frac{e^2}{|\boldsymbol{r}_1 - \boldsymbol{r}_2|} |\phi(\boldsymbol{r}_2 - \boldsymbol{R}_j)|^2. \tag{1.14}$$

Note that contrary to this Hubbard on-site interaction, the real Coulomb interaction is long ranged and contains lots of intersite terms.

There are two limiting cases: $U = 0$ with noninteracting band electrons and $t = 0$ where the system decomposes into a set of insulated atoms, which is equivalent to $U/t = \infty$. In a band picture, the t is equivalent to the band width W. The effects of different U/W values is shown in FIG. 1.1; the quasiparticle peak shown there is important for Kondo physics and can be reproduced numerically using DMFT. In the following we are not interested in the quasiparticle peak. For $U \gg t$ the band splits in a lower and an upper Hubbard band (LHB, UHB); note that contrary to valence and conduction band of a semiconductor, the very existing of the UHB depends on the occupation of the LHB. If U/t changes with temperature, pressure, doping, or applied field, the system may change from a insulating Mott–Hubbard insulator into a metal (or vice versa).

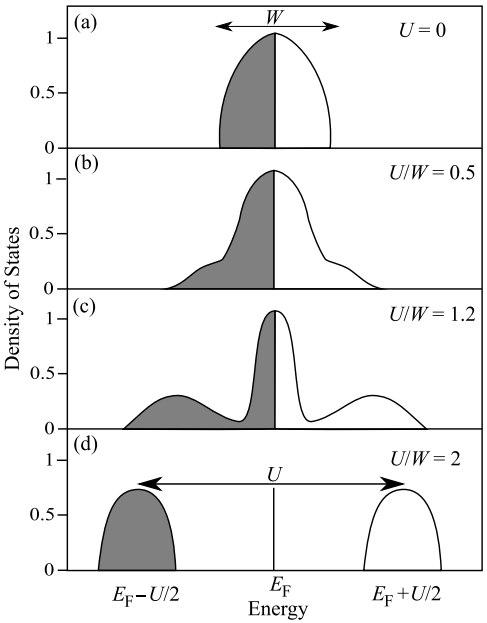

Fig. 1.1 Density of states of electrons in a solid as function of the local Coulomb interaction, where U is the interaction energy and W the bandwidth of the noninteracting electrons. (a) For independent electrons, one obtains a half ellipse, filled up to the Fermi energy E_F. (b) For weakly correlated systems the DOS still resembles the free electrons. (c) In strongly correlated materials one finds a characteristic three-peak structure: the two Hubbard bands and a quasiparticle peak near the Fermi level. (d) The Mott–Hubbard insulating state where the electron interaction are strong enough to suppress the quasiparticle peak, whose weight is transferred to the Hubbard bands. (Figure after Ref. 66.)

At exactly half filling, the large-U effective Hamiltonian is the well-known antiferromagnetic Heisenberg model

$$H = -\frac{1}{2}\sum_{i,j} J_{ij}\boldsymbol{S}_i \cdot S_j. \tag{1.15}$$

A note of warning: Different publications use different conventions with regards to the sum (e.g. by leaving the $\frac{1}{2}$ out) and to the sign of J.

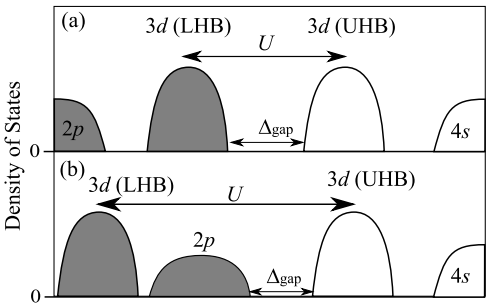

Fig. 1.2 (a) Mott–Hubbard insulator the gap (activation enery) Δ_{gap} is approximately $U - W$. (b) If there are ligand $2p$ bands between the lower and upper Hubbard band, the gap is smaller than $U - W$ and one has a charge-transfer insulator.

In the Heisenberg model we have $J = 4t^2/U$ which is the $n = 1$ case of the $t - J$ model. (If one wants to go beyond the uniaxial anisotropy of the Heisenberg model, one can also include the Dzyaloshinskii–Moriya interaction, $-\frac{1}{2}\sum_{i,j} \boldsymbol{D}_{ij} \cdot (\boldsymbol{S}_i \times \boldsymbol{S}_j)$, which we will ignore in this thesis.)

In case of the transition-metal (TM) compounds the direct exchange between d orbitals of different TM ions is often unlikely; in this case the hopping can happen via the anions in the crystals such as the oxygen ions. This concept goes back to Anderson [67] and is called superexchange. Hereby an electron hops from the oxygen to one transition-metal ion, leaving a hole which can be filled by an electron from another transtion-metal ion. Depending on the details and especially on the TM–O–TM binding angle this interaction can be ferro- or antiferromagnetic [68].

In the Mott–Hubbard insulators the gap is given by the splitting of the transition-metal valence band into two bands (such as in V_2O_3 or $LaTiO_3$). However, in other materials such as La_2CuO_4 the gap is determined by excitations of transitions from the oxygen $2p$ band into upper Hubbard band, as here the filled oxygen $2p$ band lies energy wise between the LHB and UHB (see FIG. 1.2). Such a system is then called a charge-transfer insulator [69–70].

1.2.7 LDA+U

In the LDA+U method, there are two kinds of electrons: for the valence d electrons, for which the Coulomb interaction should be taken into account, a Hubbard-like $\frac{1}{2}\sum_{i\neq j} n_i n_j$ term (with the d orbital occupation n_i) as in Hartree–Fock (mean-field) approximation is used, while for the other electrons are treated in normal LDA. In order to prevent double counting, $UN(N-1)/2$ is substracted. The LDA+U energy functional is then given by

$$E = E_{\mathrm{LDA}} - UN(N-1)/2 + \frac{1}{2}U\sum_{i\neq j} n_i n_j, \tag{1.16}$$

where exchange and the asphericity have been ignored. For the Kohn–Sham eigenenergies this gives

$$\varepsilon_i = \frac{\partial E}{\partial n} = \varepsilon_{\mathrm{LDA}} + U(\frac{1}{2} - n_i), \tag{1.17}$$

i.e. for filled orbitals the energy is $U/2$ lower and for unoccupied orbitals $U/2$ higher, which reproduces qualitatively the lower and upper Hubbard band (LHB, UHB) and thus explains the physics of Mott–Hubbard insulators. In order to do a proper definition, one needs to define a more general orbital basis set, include the direct and exchange Coulomb interactions, and identify the region in space where the atomic characteristics of an atom have mostly survived. One obtains then the following single-particle Hamiltonian

$$H = H_{\mathrm{LSDA}} + \sum_{m,m'} |inlm\sigma\rangle V^{\sigma}_{mm'} \langle inlm'\sigma| \tag{1.18}$$

where i is the site index, nlm the atomic like quantum numbers and σ the spin quantum number. V_{ee} is the screened Coulomb interaction between nl electrons and is given by

$$\begin{aligned} V^{\sigma}_{mm'} = \sum_{\{m\}} \big[& \langle m, m''|V_{ee}|m', m'''\rangle n^{-\sigma}_{n''m'''} \\ & + (\langle m, m''|V_{ee}|m', m'''\rangle - \langle m, m''|V_{ee}|m''', m'\rangle) n^{\sigma}_{m''m'''} \big] \\ & - U\left(N - \frac{1}{2}\right) + J\left(N^{\sigma} - \frac{1}{2}\right). \end{aligned} \tag{1.19}$$

The matrix elements can be expressed in spherical harmonics and effective Slater integrals F^k [71] as

$$\langle m, m''|V_{ee}|m', m'''\rangle = \sum_{k=0}^{2l} a_k(m, m', m'', m''')F^k, \tag{1.20}$$

with

$$a_k(m, m', m'', m''') = \frac{4\pi}{2k+1} \sum_{q=-k}^{k} \langle lm|Y_k^q|lm'\rangle\langle lm''|Y_k^{q*}|lm'''\rangle. \tag{1.21}$$

For d electrons one needs F^0, F^2 and F^4 (which can also be expressed in Racah parameters, cf. Eq. (3.34)). These can also be expressed in Coulomb U and Stoner J parameters as $U = F^0$ and $J = (F^2+F^4)/14$ where F^2/F^4 is approximately 0.625 for $3d$ elements [72–73]. The values for U can be regarded as parameter taken from either core-level PES measurements or be fitted to the band gap, but one can also calculate its value in DFT. In many cases the exact value of parameters (beyond a certain threshold) has only marginal influence on the result (except for the band gap). By presetting the density matrix $n^{\sigma}_{mm'}$ one can explore metastable solutions for orbital occupation and orbital ordering, and by comparing the differences in such obtained total energies, one can extract crystal-field parameters from the calculation.

Besides using the LDA (or LDSA) functional as starting point for the U correction, one can also use other functionals such as a GGA functional; however, estimating the double-counting term is then more difficult.

1.3 References

[1] L. Bogani and W. Wernsdorfer, *Molecular spintronics using single-molecule magnets*, Nature Materials **7**, 179 (2008). DOI: 10.1038/nmat2133.

[2] See http://nobelprize.org/nobel_prizes/physics/laureates/2007 /index.htm% l, where also the Nobel Lectures can be found.

[3] M. N. Baibich, J. M. Broto, A. Fert, F. N. Van Dau, F. Petroff, P. Eitenne, G. Creuzet, A. Friederich, and J. Chazelas, *Giant magnetoresistance of (001)fe/(001)cr magnetic superlattices*, Physical Review Letters **61**, 2472 (1988). DOI: 10.1103/PhysRevLett.61.2472.

[4] G. Binasch, P. Grünberg, F. Saurenbach, and W. Zinn, *Enhanced magnetoresistance in layered magnetic structures with antiferromagnetic interlayer exchange*, Physical Review B **39**, 4828 (1989). DOI: 10.1103/PhysRevB.39.4828.

[5] J. G. Bednorz and K. A. Müller, *Possible high T_c superconductivity in the Ba–La–Cu–O system*, Zeitschrift für Physik B **64**, 189 (1986). DOI: 10.1007/BF01303701.

[6] Y. Kamihara, T. Watanabe, M. Hirano, and H. Hosono, *Iron-based layered superconductor $La(O_{1-x}F_x)FeAs$ (x = 0.05–0.12) with t_c = 26 K*, Journal of the American Chemical Society **130**, 3296 (2008). DOI: 10.1021/ja800073m.

[7] E. Dagotto, *Complexity in strongly correlated electronic systems*, Science **309**, 257 (2005). DOI: 10.1126/science.1107559.

[8] A. Bianconi and N. L. Saini, editors, *Stripes and Related Phenomena* (Springer, Berlin, 2001). ISBN: 9780306464195. doi:10.1007/b119246.

[9] V. J. Emery, S. A. Kivelson, and J. M. Tranquada, *Stripe phases in high-temperature superconductors*, Proceedings of the National Academy of Science of the United States of America **96**, 8814 (1999). DOI: 10.1073/pnas.96.16.8814.

[10] M. A. Korotin, S. Y. Ezhov, I. V. Solovyev, V. I. Anisimov, D. I. Khomskii, and G. A. Sawatzky, *Intermediate-spin state and properties of lacoo*3, Physical Review B **54**, 5309 (1996). DOI: 10.1103/PhysRevB.54.5309.

[11] M. W. Haverkort, Z. Hu, J. C. Cezar, T. Burnus, H. Hartmann, M. Reuther, C. Zobel, T. Lorenz, A. Tanaka, N. B. Brookes, H.-H. Hsieh, H.-J. Lin, C.-T. Chen, and L. H. Tjeng, *Spin State Transition in $LaCoO_3$ Studied Using Soft X-ray Absorption Spectroscopy and Magnetic Circular Dichroism*, Physical Review Letters **97**, 176405 (2006). DOI: 10.1103/PhysRevLett.97.176405.

[12] S. K. Pandey, A. Kumar, S. Patil, V. R. R. Medicherla, R. S. Singh, K. Maiti, D. Prabhakaran, A. T. Boothroyd, and A. V. Pimpale, *Investigation of the spin state of Co in $LaCoO_3$ at room temperature: Ab initio calculations and high-resolution photoemission spectroscopy of single crystals*, Physical Review B **77**, 045123 (2008). DOI: 10.1103/PhysRevB.77.045123.

[13] R. Bulla, T. A. Costi, and T. Pruschke, *Numerical renormalization group method for quantum impurity systems*, Review of Modern Physics **80**, 395 (2008). DOI: 10.1103/RevModPhys.80 .395.

[14] T. Maier, M. Jarrell, T. Pruschke, and M. H. Hettler, *Quantum cluster theories*, Review of Modern Physics **77**, 1027 (2005). DOI: 10.1103/RevModPhys.77.1027.

[15] T. Brandes and S. Ketteman, editors, *Anderson localization and its ramifications: disorder, phase coherence and electron correlations* (Sprinter, Berlin, 2003). ISBN: 3540407855. doi:10.1007 /b13139.

[16] J. J. Rehr and R. C. Albers, *Theoretical approaches to x-ray absorption fine structure*, Review of Modern Physics **72**, 621 (2000). DOI: 10.1103/RevModPhys.72.621.

[17] J. J. Rehr, *Theory and calculations of x-ray spectra: XAS, XES, XRS, and NRIXS*, Radiation Physics and Chemistry **75**, 1547 (2006). DOI: 10.1016/j.radphyschem.2005.11.014.

[18] M. L. Cohen, *The evolution of the pseudopotential method for computational materials science* (2007) Talk given at the "13th International Workshop on Computational Physics and Materials Science: Total Energy and Force Methods" (2007). http://sdu .ictp.it/dl/2007/0111_totalenergy/roomM_2007.01.13_09.00-% 09 .59/index.html

[19] M. Imada, A. Fujimori, and Y. Tokura, *Metal-insulator transitions*, Review of Modern Physics **70**, 1039 (1998). DOI: 10 .1103/RevModPhys.70.1039.

[20] Y. Tokura and N. Nagaosa, *Orbital physics in transition-metal oxides*, Science **288**, 462 (2000). DOI: 10.1126/science.288.5465 .462.

[21] D. I. Khomskii and G. A. Sawatzky, *Interplay between spin, charge and orbital degrees of freedom in magnetic oxides*, Solid State Communications **102**, 87 (1997). DOI: 10.1016/S0038 -1098(96)00717-X.

[22] P. Fulde, *Electron Correlations in Molecules and Solids*. (Springer, Berlin, 2002). ISBN: 9783540593645.

[23] P. Fazekas, *Lecture notes on Electron Correlation and Magnetism*. (World Science, Singapore, 1999). ISBN: 9810224745.

[24] E. Pavarini, A. Yamasaki, J. Nuss, and O. K. Andersen, *How chemistry controls electron localization in* $3d^1$ *perovskites: a Wannier-function study*, New Journal of Physics **7**, 188 (2005). DOI: 10.1088/1367-2630/7/1/188.

[25] M. I. Katsnelson, V. Y. Irkhin, L. Chioncel, A. I. Lichtenstein, and R. A. de Groot, *Half-metallic ferromagnets: From band structure to many-body effects*, Review of Modern Physics **80**, 315 (2008). DOI: 10.1103/RevModPhys.80.315.

[26] S. Blügel, T. Brückel, and C. M. Schneider, editors, *Magnetism goes Nano* (Forschungszentrum Jülich, 2005). IFF Spring School 2005. http://hdl.handle.net/2128/560

[27] S. Blügel, G. Gompper, E. Koch, H. Müller-Krumbhaar, R. Spatschek, and R. G. Winkler, editors, *Computational Condensed Matter Physics* (Forschungszentrum Jülich, 2006). IFF Spring School 2006. http://hdl.handle.net/2128/2396

[28] V. I. Anisimov, editor, *Strong coulomb correlations in electronic structure calculations* (Gordon and Breach, Amsterdam, 2000). ISBN: 9056991310.

[29] G. Kotliar, S. Y. Savrasov, K. Haule, V. S. Oudovenko, O. Parcollet, and C. A. Marianetti, *Electronic structure calculations with dynamical mean-field theory*, Review of Modern Physics **78**, 865 (2006). DOI: 10.1103/RevModPhys.78.865.

[30] P. A. M. Dirac, *Quantum mechanics of many-electron systems*, Proceedings of the Royal Society of London – Series A **123**, 714 (1929). http://www.jstor.org/stable/95222. .

[31] P. Hohenberg and W. Kohn, *Inhomogeneous electron gas*, Physical Review **136**, B864 (1964). DOI: 10.1103/PhysRev.136 .B864.

[32] W. Kohn and L. J. Sham, *Self-consistent equations including exchange and correlation effects*, Physical Review **140**, A1133 (1965). DOI: 10.1103/PhysRev.140.A1133.

[33] R. Zeller, *Spin-polarized DFT calculations and magnetism*, in *Computational Nanoscience: Do it yourself!*, edited by J. Grotendorst, S. Blügel, and D. Marx (John von Neumann Institute for Computing, Jülich). http://www.fz-juelich.de/nic-series/volume31/zeller.pdf.

[34] G. Bihlmayer, *Non-collinear magnetism: Exchange parameter and t_c*, in *Computational Nanoscience: Do it yourself!*, edited by J. Grotendorst, S. Blügel, and D. Marx (John von Neumann Institute for Computing, Jülich). http://www.fz-juelich.de/nic-series/volume31/bihlmayer.pdf.

[35] S. Sharma, J. K. Dewhurst, C. Ambrosch-Draxl, S. Kurth, N. Helbig, S. Pittalis, S. Shallcross, L. Nordström, and E. K. U. Gross, *First-principles approach to noncollinear magnetism: Towards spin dynamics*, Physical Review Letters **98**, 196405 (2007). DOI: 10.1103/PhysRevLett.98.196405.

[36] J. P. Perdew and A. Zunger, *Self-interaction correction to density-functional approximations for many-electron systems*, Physical Review B **23**, 5048 (1981). DOI: 10.1103/PhysRevB.23.5048.

[37] E. Runge and E. K. U. Gross, *Density-functional theory for time-dependent systems*, Physical Review Letters **52**, 997 (1984). DOI: 10.1103/PhysRevLett.52.997.

[38] T. Burnus, *Time-Dependent Electron Localization Function* (Berlin, 2004), Diploma thesis, Freie Universität Berlin.

[39] W. Kohn, *Nobel lecture: Electronic structure of matter – wave functions and density functionals*, Review of Modern Physics **71**, 1253 (1999). DOI: 10.1103/RevModPhys.71.1253.

[40] J. P. Perdew and S. Kurth, in *Density functionals: theory and applications*, edited by D. P. Joubert (Springer, Heidelberg, 1998). Available from http://www.physik.fu-berlin.de/~kurth/publ.html.

[41] K. Burke and friends, *The ABC of DFT*. (2003). http://chem.ps.uci.edu/~kieron/dft/.

[42] R. M. Martin, *Electronic Structure*. (Cambridge University Press, 2004). ISBN: 0521782856. doi:10.2277/0521782856. See also http://electronicstructure.org/ and note that a second volume is in preparation.

[43] M. Marques, C. Ullrich, F. Nogueira, A. Rubio, K. Burke, and E. Gross, editors, *Time-Dependent Density Functional Theory* (Springer, Berlin, 2006). ISBN: 9783540354222. doi:10.1007/b11767107.

[44] G. D. Mahan, *Many Particle Physics*. (Springer, Berlin, 2000). ISBN: 0306463385.

[45] A. L. Fetter and J. D. Walecka, *Quantum Theory of Many-Particle Systems*. (Dover Publications, Mineola, NY, 2003). ISBN: 0486428273.

[46] G. Onida, L. Reining, and A. Rubio, *Electronic excitations: density-functional versus many-body Green's-function approaches*, Review of Modern Physics **74**, 601 (2002). DOI: 10.1103/RevModPhys.74.601.

[47] A. Svane and O. Gunnarsson, *Transition-metal oxides in the self-interaction-corrected density-functional formalism*, Physical Review Letters **65**, 1148 (1990). DOI: 10.1103/PhysRevLett.65.1148.

[48] S. Massidda, M. Posternak, and A. Baldereschi, *Hartree-Fock LAPW approach to the electronic properties of periodic systems*, Physical Review B **48**, 5058 (1993). DOI: 10.1103/PhysRevB.48.5058.

[49] O. Gunnarsson, O. K. Andersen, O. Jepsen, and J. Zaanen, *Density-functional calculation of the parameters in the Anderson model: Application to Mn in CdTe*, Physical Review B **39**, 1708 (1989). DOI: 10.1103/PhysRevB.39.1708.

[50] V. I. Anisimov and O. Gunnarsson, *Density-functional calculation of effective coulomb interactions in metals*, Physical Review B **43**, 7570 (1991). DOI: 10.1103/PhysRevB.43.7570.

[51] L. Hedin, *New method for calculating the one-particle Green's function with application to the electron-gas problem*, Physical Review **139**, A796 (1965). DOI: 10.1103/PhysRev.139.A796.

[52] L. Hedin and S. Lundqvist, in *Solid state physics: advances in research and applications. Volume 23*, edited by F. Seitz, D. Turnbull, and H. Ehrenreich (Academic Press, New York).

[53] F. Aryasetiawan, *Self-energy of ferromagnetic nickel in the gw approximation*, Physical Review B **46**, 13051 (1992). DOI: 10 .1103/PhysRevB.46.13051.

[54] V. I. Anisimov, J. Zaanen, and O. K. Andersen, *Band theory and Mott insulators: Hubbard U instead of Stoner I*, Physical Review B **44**, 943 (1991). DOI: 10.1103/PhysRevB.44.943.

[55] V. I. Anisimov, I. V. Solovyev, M. A. Korotin, M. T. Czyżyk, and G. A. Sawatzky, *Density-functional theory and nio photoemission spectra*, Physical Review B **48**, 16929 (1993). DOI: 10.1103 /PhysRevB.48.16929.

[56] A. I. Liechtenstein, V. I. Anisimov, and J. Zaanen, *Density-functional theory and strong interactions: Orbital ordering in Mott-Hubbard insulators*, Physical Review B **52**, R5467 (1995). DOI: 10.1103/PhysRevB.52.R5467.

[57] V. I. Anisimov, F. Aryasetiawan, and A. I. Lichtenstein, *First-principles calculations of the electronic structure and spectra of strongly correlated systems: the LDA+U method*, Journal of Physics: Condensed Matter **9**, 767 (1997). DOI: 10.1088/0953 -8984/9/4/002.

[58] A. Fujimori and F. Minami, *Valence-band photoemission and optical absorption in nickel compounds*, Physical Review B **30**, 957 (1984). DOI: 10.1103/PhysRevB.30.957.

[59] J. van Elp, R. H. Potze, H. Eskes, R. Berger, and G. A. Sawatzky, *Electronic structure of mno*, Physical Review B **44**, 1530 (1991). DOI: 10.1103/PhysRevB.44.1530.

[60] M. C. Gutzwiller, *Effect of correlation on the ferromagnetism of transition metals*, Physical Review Letters **10**, 159 (1963). DOI: 10.1103/PhysRevLett.10.159.

[61] J. Hubbard, *Electron correlations in narrow energy bands*, Proceedings of the Royal Society of London – Series A **276**, 238 (1963). DOI: 10.1098/rspa.1963.0204.

[62] J. Hubbard, *Electron correlations in narrow energy bands. II. The the degenerate band case*, Proceedings of the Royal Society of London – Series A **277**, 237 (1964a). DOI: 10.1098/rspa.1964 .0019.

[63] J. Hubbard, *Electron correlations in narrow energy bands. III. An improved solution*, Proceedings of the Royal Society of London – Series A **281**, 401 (1964b). DOI: 10.1098/rspa.1964.0190.

[64] J. Hubbard, *Electron correlations in narrow energy bands. IV. The atomic representation*, Proceedings of the Royal Society of London – Series A **285**, 242 (1965). DOI: 10.1098/rspa.1965.0124.

[65] J. Kanamori, *Electron correlation and ferromagnetism of transition metals*, Progress of Theoretical Physics **30**, 275 (1963). DOI: 10.1143/PTP.30.275.

[66] G. Kotliar and D. Vollhardt, Physics Today **57**, 53 (March 2004). DOI: 10.1063/1.1712502.

[67] P. W. Anderson, *New approach to the theory of superexchange interactions*, Physical Review **115**, 2 (1959). DOI: 10.1103/PhysRev.115.2.

[68] H. J. Zeiger and G. W. Pratt, *Magnetic interactions in solids*. (Clarendon Press, Oxford, 1973). ISBN: 0198512716.

[69] J. Zaanen, G. A. Sawatzky, and J. W. Allen, *Band gaps and electronic structure of transition-metal compounds*, Physical Review Letters **55**, 418 (1985). DOI: 10.1103/PhysRevLett.55.418.

[70] G. A. Sawatzky, in *Superconductivity : from basic physics to the latest developments*, edited by P. N. Butcher and L. Yu (World Scientific, Singapore).

[71] B. R. Judd, *Operator techniques in atomic spectroscopy*. (McGraw-Hill, New York, 1963). ISBN: 0691059012.

[72] M. R. Pederson, R. A. Heaton, and C. C. Lin, *Local-density hartree–fock theory of electronic states of molecules with self-interaction correction*, The Journal of Physical Chemistry **80**, 1972 (1984). DOI: 10.1063/1.446959.

[73] M. R. Pederson, R. A. Heaton, and C. C. Lin, *Density-functional theory with self-interaction correction: Application to the lithium molecule*, The Journal of Physical Chemistry **82**, 2688 (1985). DOI: 10.1063/1.448266.

Grau, teurer Freund, ist alle Theorie
Und grün des Lebens goldner Baum.
All theory, dear friend, is grey, but the golden tree of actual life springs ever green.

— Johann Wolfgang von Goethe, 1749–1832

2 Principles and application of X-ray absorption spectroscopy

In classical mechanics and every day live, measuring implies to determine the intrinsic state (or ground state) of an object (such as the length of an object or its mass) directly. However, in many cases something else is of interest: the response of the system to a perturbation; a classical, macroscopic example would be the ductility of a material. For microscopic objects, which are governed by quantum mechanics, any measurement influences the system and measuring the ground state itself is impossible. Knowing the ground state of a quantum mechanical system is thus in principle of little use. Yet many properties can be understood from the ground state, which is also both conceptually simpler and easier to calculate. Thus the measured response to a perturbation is used to understand the ground state, which in turn helps to understand and predict the response to other perturbations.

For atoms, molecules and solids the electrons are of main interest; the nuclei can often be regarded as stationary (Born–Oppenheimer approximation) or reacting only slowly (adiabatically) to the changes of the electron density. A natural way to probe the electronic structure is

to use electromagnetic radiation. Using x-ray absorption spectroscopy (XAS), one is able to obtain information about the charge, orbital and spin state. Their interplay determines the interesting electronic and magnetic properties in strongly correlated sytems. Combined with configuration-interaction cluster calculations (see next chapter), XAS also provides information about low-energy excitations. To probe the valence shell of transition-metals *locally* (excitonic), one needs to create a core hole and, therefore, light of the energy of several hundreds of electronvolts (order of nanometres, petaherz, a million wavenumbers). Such light can be conveniently created using synchrotron radiation, which we cover first. Afterwards, we give an introduction into x-ray absorption spectroscopy including linear and circular dichroism and XAS sum rules.

2.1 Synchrotron radiation and other X-ray sources

2.1.1 An historical introduction

If a charged particle such as an electron is deflected or accelerated, electromagnetic radiation is emitted. This phenomenon is known as bremsstrahlung (deceleration radiation) and has been discovered by Nikola Tesla (1856–1943) while performing high-frequency experiments in the 1890s with high-voltage vacuum tubes including Crookes tubes [1–2]. X-rays themselves were discovered by Wilhelm Conrad Röntgen in November 1895 in Würzburg [3]. X-ray tubes remain the primary source for X-rays (or Röntgen rays as they were also called) though another technique supervened in the 1930s: cyclotron radiation and later synchrotron radiation. In cyclotrons, high-energy physicists were studying collisions of subatomic particles; these were accelerated using a fixed-frequency electric field in a homogeneous, constant magnetic field, which causes the particles to stay in circular orbits. The emitted electromagnetic radiation, called cyclotron radiation, was an unwanted, energy-loosing side effect. When the velocity and thus the energy of the electrons is increased, relativistic effects become dominant and bright X-rays are emitted: the synchrotron radiation. The effect was discovered in 1946 by Elder, Gurewitch, Langmuir, and Pollock [4]. In synchrotrons (FIG. 2.1) [5], both the strength of the magnetic field and

Fig. 2.1 (color online) Aerial view of the storage rings of the National Synchrotron Radiation Research Center (NSRRC) in Hsinchu, Taiwan (top left); of the Berliner Elektrontronenspeichering Gesellschaft für Synchrotronstrahlung (BESSY) in Berlin, Germany (bottom left); and of the European Synchrotron Radiation Facility (ESRF) in Grenoble, France (right). Photos taken from http://lightsources.org/; copyright (respectively) © NSRRC; www.euroluftbild.de / BESSY; and ESRF.

the frequency of the electric field are ramped up synchronously during the acceleration of the electrons. As cyclotrons before, synchrotrons were used for high-energy physics such as Betatron at the Lawrence Berkeley National Laboratory, which began operating in 1954; the unwanted X-ray radiation was only used parasitically. Much later in the 1970s the first synchrotron dedicated to X-rays generation was build. Modern synchrotron facilities consist of two rings: the actual synchrotron ring, which is used to accelerate the electrons, and the storage ring, in which the relativistic electrons are injected, after having reached the final velocity. In the storage ring the electrons orbit with constant energy/velocity. Synchrotrons are classified into three generations, depending how the electrons are deflected to obtain the X-ray radiation.

The principle of the first generation of works as described above: The relativistic electron beam is deflected by a so-called bending magnet (or dipole magnet); this produces horizontally polarized photons of essentially all energies up to a maximal energy E_c after which the flux dies off quickly (see FIG. 2.2). Interestingly, the photon beam is not everywhere horizontally polarized: slightly below and above the plane formed by the orbiting electrons the light has a circular component. The second generation of synchrotrons simply increases the number of photons by not deflecting the electrons once but deflecting it laterally several times by an array of magnets such that the electron wiggles through the field and produce a brighter spectrum. The device doing so is called wiggler; it usually consists of permanent magnets arranged in a Halbach array and is inserted in a straight section of the storage ring (thus it is known as insertion device).

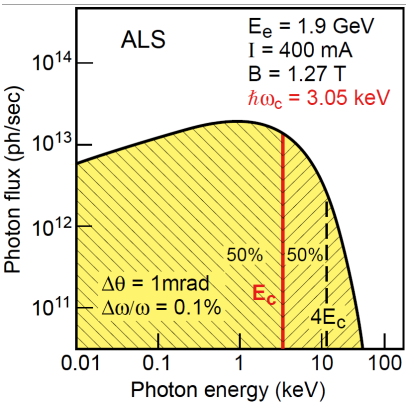

Fig. 2.2 (color online) X-ray spectrum produced with a bending magnet: The flux rises slowly up to the photon energy E_c and then falls off quickly. Taken from http://lightsources.org/; © University of California Berkeley/Advanced Light Source.

The next step, leading to the undulators which are the insertion devices of the third-generation synchrotrons, is to arrange the dipole magnets such that the light produced for each deflection interferes with another to produce a very bright photon beam for a given frequency One big advantage of undulators besides the brilliance is that all polarizations – horizontal, vertical, left and right circular – can be easily produced.

The successor of synchrotrons will be the free electron laser (FEL); while the first small FELs are already operating, larger ones are only under construction (2008). Over the years not only the intensity (or more precisely the brilliance) increased by several orders of magnitude, but also the beam stability, energy resolution, experimental techniques

and theoretical understanding improved. The absorption spectra in this thesis were taken either at bending-magnet or at undulator beamlines.

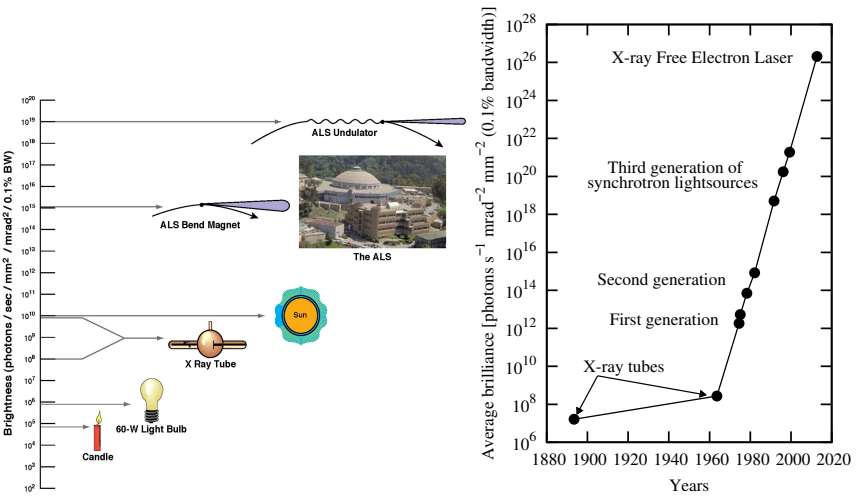

Fig. 2.3 (color online) (a) Brilliance of different light sources from candles to synchrotrons light. (b) The advancement of X-ray light sources (based on Ref. 6). Fig. (a) taken from http://lightsources.org/; © Advanced Light Source.

2.1.2 Brilliance

The important parameter to measure the quality of X-rays is the brilliance [5]; foremost it contains the intensity (at a given energy), i.e. the number of emitted photons (of a certain energy) per time interval (typically, per second). But other parameters are also of importance such as the collimation of the beam, i.e. how much it spreads out horizontally and vertically while propagating (measured in milliradians), or the source area (in millimetres). The spectral shape of the emitted radiation depends on the type of source and might be completely smooth or have peaks at certain energies; therefore the brilliance is given in an energy interval with a (band)width of 0.1% around the chosen energy. Thus the brilliance B is defined as

$$\left[B(E_0)\right] = \left[\frac{\int_{E_0-\Delta E/2}^{E_0+\Delta E/2} N_{\text{Photons}}(E)\,\mathrm{d}E}{t\,A\,\alpha_{\text{horiz}}\alpha_{\text{vert}}}\right] = \frac{1}{\text{s}\cdot\text{mrad}^2\cdot\text{mm}^2}, \tag{2.1}$$

with the bandwidth $\Delta E = 0.1\% \cdot E_0 = 0.001 \cdot E_0$. The advancement of X-ray light sources and a comparison with every-day lightsources can be found in FIG. 2.3.

2.2 Experimental

In principle, absorption measurements are simple: One first measures the intensity (flux) without (or in front of) the sample $I_0(\nu)$ and once after the sample $I(r,\nu)$; knowing the thickness r_0, the frequency-dependent absorption coefficient $\mu(\nu)$ can be easily computed:

$$I(r,\nu) = I_0(\nu)\mathrm{e}^{-\mu(\nu)r} \Rightarrow \mu(\nu) = -r_0 \ln[I(r_0,\nu)/I_0(\nu)]. \tag{2.2}$$

These transmission measurements work well for hard x-rays, which are bulk sensitive. However, using soft X-rays, the light will be already absorbed after few nanometres, making the measurement difficult. Fortunately, one can use also secondary effects for the measurements, namely the relaxation of the excited electrons. The simplest process is that the electron relaxes and the surplus energy is again emitted as light (fluorescence), which can then be picked up by a detector. Fluorescence yield is bulk sensitive and works rather well for dilute samples and thin layers, however, for thick, concentrated samples the spectrum gets serverely distorted due to the so-called 'self-absorption effect' [7–9]. Fluorescence yield can be used for the K edge of carbon, oxygen and fluorine for which the self-absorption effect is small, but it is not negligible for the transition-metal L edges.

There is yet another process: autoionization. Hereby an electron relaxes into the created core hole and with the gained energy another electron is emitted (cf. Auger–Meitner effect, internal photoeffect). However, not all electrons simply escape from the solid but they scatter inelastically, leading to the emission of myriads of secondary electrons of the solid; that way numerous other electrons (which much lower kinetic energy) are emitted. Thus another way to measure the absorption is

by simply measuring all emitted electrons (total electron yield, TEY). The simplest way of doing so is by measuring the sample current (drain current). For TEY in a simple model, one has [10]

$$Y = A \int_0^\infty \mathrm{e}^{-x/(\lambda \cos\theta)} \mathrm{d}x/(\lambda \cos\theta) \mathrm{e}^{-x/d} = Ad/(d + \lambda \cos\theta), \qquad (2.3)$$

where A is the number of electrons produced per photon, θ the incidence angle of the x-rays, λ die absorption length and d the escape depth of the electrons. For $\lambda \approx d$ there are significant saturation effects, while they are negligible for $\lambda \gg d$, which is approximately the case. However, the total-electron-yield method has another drawback: Due to the emission of electrons, the sample charges unless it is conducting enough that the drain current provides enough electrons. And the escape depth of electrons is much smaller than for photons; roughly only the top 30 to 50 Å are probed. Fortunately, most transition-metal compounds are conducting enough to be measurable.

But since the probing depth is limited, the sample must be clean. Thus, the measurements are performed in ultra-high vacuum (pressures around 10^{-10} mbar) and one needs to get rid of the 'dirt' (absorbed water, oxygen, carbon dioxide, etc.) on the sample surface. The latter can be done by cleaving the sample in vacuo, i.e. by cutting the sample with a cleaving knive or for layered materials by simply breaking off a post glued to the top of the sample. The dependence on the quality of the vacuum can be seen by the average time it takes until the sample is covered by a monolayer of atoms [11]: At a pressure of $p = 10^{-6}$ mbar it takes about one second ($t_{\mathrm{mono}} = 1$ s) until the sample is covered by one monolayer ($n_{\mathrm{mono}} = 1$); by contrast, at 10^{-11} mbar it takes about 24 hours for one monolayer to form ($t_{\mathrm{mono}} = n_{mono}\sqrt{2\pi M_{\mathrm{molar}} RT}/pN_A$ with gas constant R, Avogadro number N_A and molar mass M_{molar}). As trivia I want to add that water is most difficult to pump, which makes it difficult to reach 10^{-10} mbar; the solution is to heat the whole chamber to around 130 °C while pumping for a day. To do so, the chamber is laced with heating tapes and then packed with aluminium foil.

More about X-ray experiments can be found in the book by Als-Nielson and McMorrow [5] while for X-ray absorption the publications by Frank de Groot [12–15]and the articles in the "Theo Thole Memorial Issue" [16] provide a good starting point.

The specta shown in this thesis are where recorded in total electron yield at the $L_{2,3}$ edges of $3d$ and $4d$ transition-metal ions.

2.3 X-ray absorption and XAS sum rules

For X-ray absorption spectra an analysis hierarchy exists. The direct approach is to qualitatively extract information from the data itself by looking at their shape and their energy position (by using the knowledge provided via previously taken spectra and from theory). The next step is to use sum rules to extract quantitative information from the spectra, while the third step is to simulate the spectra and – when the calculated spectra match the experiment – to use the result of the calculations. Simulating the spectra confronts one with the problem which method is best and which parameters need to be chosen; the theoretical spectra shown in this thesis have been simulated using configuration-interaction cluster calculations, which is described in the next chapter. But also the sum rules are not without pitfalls as the conditions for which they were derived are not always fulfilled (see below). Nevertheless, sum rules provide effortless insight into a spectrum and thus in the properties of a material. As throughout this thesis, we concentrate on the transitions of electrons from the filled $2p$ orbitals to the partially filled d orbitals of transition-metal ions.

2.3.1 Isotropic x-ray absorption spectroscopy

In X-ray absorption spectroscopy [12–15, 17] light in the x-ray range (approximately 10 to 0.01 nanometres, one hundred eV to tens of keV) is used to excite strongly bound electrons belonging to deep states to weakly bound valence states. In our case, $2p$ transition-metal electrons are excited into the valence band or more precisely in the partially filled d orbitals of this transition-metal ion. These transitions lie in the soft x-ray range of several hundreds of electron volts.[2] The main peaks in the spectrum are labelled in XAS as follows: A letter denotes the shell (main quantum number) from which the electrons stem; the shells are named for historic reasons K ($n = 1$), L ($n = 2$) etc. For a given shell, the peaks are numbered through, starting from the lowest core-hole subshell. L_1 is thus the transition from $2s$ and not well pronounced. L_2 and L_3 stem from $2p$ electrons; this shell is split into two levels with $J = 3/2$ and $J = 1/2$ due to the spin-orbit coupling of the $2p$ state.

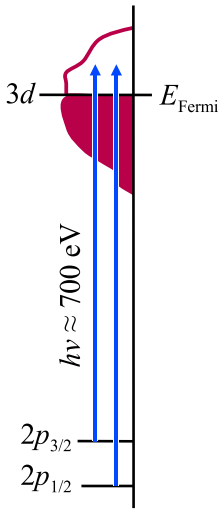

Fig. 2.4 (color online) X-ray absorption scheme for $2p$ to d excitations.

The transition from the $2p$ shell into the d shell is dipole allowed and the transition probability $T_{i\to f}$ follows Fermi's golden rule,

$$T_{i\to f} = \frac{2\pi}{\hbar}|M_{if}|^2\rho_f \text{ with } M_{if} = \langle\Psi|e\vec{\varepsilon}\boldsymbol{r}|\Psi\rangle, \tag{2.4}$$

where M_{if} is the transition matrix element, ρ_f the density of final states; $\vec{\varepsilon}e\boldsymbol{r}$ is the dipole operator with e being the elementary charge and $\vec{\varepsilon}$ (with $\varepsilon^2 = 1$) the polarization of the light. That the transition is dipole allowed immediately implies strong intensities and, due to the dipole-selection rules[3] and the multiplet structure, a high sensitivity to the symmetry of the initial state, including the charge, spin, and orbital state.

In a simple picture (FIG. 2.4) one excites electrons from the spin-orbit split $2p$ states into the d shell, which probes the unoccupied density of states of the ion. However, this simple picture completely

[2] A conversion table for wavelengths and energies is given Appendix C.

[3] $\Delta l = \pm 1$, $\Delta j = 0, \pm 1$, $\Delta m_l = 0, \pm 1$, $\Delta m_s = 0$, $\Delta L = 0, \pm 1$, $\Delta S = 0$, $\Delta J = 0, \pm 1$.

neglects the electron interaction (especially the influence of the core hole). That multiplet effects are important can be seen by comparing L_3 and L_2 edges: In the simple picture their shape should be identical and the ratio should be 2:1. Experimental spectra show that this is usually not the case.

The energy position of the absorption edge is strongly element specific, and its exact position and shape depends on the local electron structure and thus on the valence, spin state and point symmetry. Thus, one can measure for instance in $LaMnCoO_3$ (cf. Chapter 5) the cobalt (Co-$L_{2,3}$) and the manganese ions (Mn-$L_{2,3}$ edges) separately. However, if there are two different sites of the same element, one measures only the sum of the single-site spectra, which reduces the extractable information (cf. $Ca_3Co_2O_6$ in Chapter 4). In some cases, the L absorption edge also overlaps with the K edge of oxygen or the M edge of other ions. (But not for compounds measured for this thesis.) As mentioned above, the exact energy position also depends on the valence: An increase of the valence of the metal ion by one results in a shift of the $L_{2,3}$ XAS spectra to higher energies by 1 eV or more [18]; this shift is a final state effect. By comparing the spectrum of a studied compound with reference spectra of compounds with known valence, the valence of the studied compound can be determined; this effect has been used for several of the studied compounds in this thesis. The spectral shape contains information about the number of hole and the local symmetry; unfortunately, this information is usually not directly accessible due to the complexity of the multiplet structure. However, in some cases one easily sees that, e.g., there are no holes in the t_{2g} orbitals (cf. Figure 6.1). In other cases, one needs to simulate the spectra to understand for instance the influence of the symmetry (cf. Figure 6.2). Note that for the branching ratio a sum rule exists [19–21]which gives access to the spin-orbit operator in the valence state, which is however only rarely used and requires that the L_3 and L_2 manifolds are well separated.

2.3.2 x-ray linear dichroism and sum rules

Using linearly polarized light with a single crystalline sample, one can only excite orbitals with a component in field direction (assuming dipole approximation); e.g. if the light is polarized in z direction

(electric field of the light parallel to z) then only electrons in p_z but not p_x or p_y orbitals are excited.[4] These electrons can only be excited into (empty or partially filled) orbitals which have a component in the same (e.g. z) directions (here: d_{yz}, d_{zx} and $d_{3z^2-r^2}$ but not d_{xy} or $d_{x^2-y^2}$). The transition intensity now depends on the occupation of the final state (i.e. the number of holes in the d orbitals which are dipole allowed for the given polarization of the light). In stead of orbitals, one can also think in terms of electron density and multipole moments.

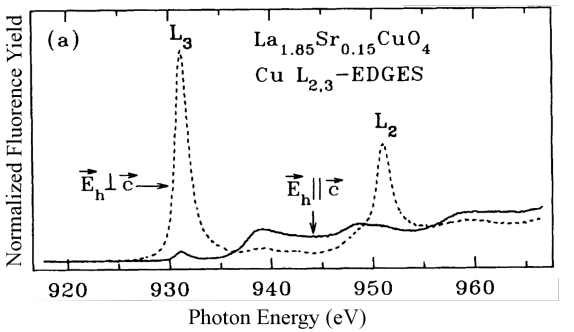

Fig. 2.5 Linear dichroism in $La_{1.85}Sr_{0.15}CuO_4$ with Cu $3d^9$, which has a hole only in the $d_{x^2-y^2}$ orbital. Spectra by C. T. Chen *et al.* [22]. Reprinted with permission. Copyright 1992 by the American Physical Society.

Thus, absorption spectra taken with differently polarized light reveal information about the orbital occupation; the difference between spectra, taken with a different linear polarization, is called linear dichroism, which comes from Greek *dikhroos* (*di-* "twice" + *khros* "colour"). An illustrative example is the layered superconductor $La_{1.85}Sr_{0.15}CuO_4$ (LSCO), which contains a Cu^{2+} ions with $3d^9$ configuration; the copper ion is octahedrally surrounded by oxygens, with a tetragonal distortion such that the out-of-plane axis is longer. One can therefore expect that the $d_{x^2-y^2}$ orbital which points in plane towards the oxygens is highest in energy and thus unoccupied. This is indeed what one can see in the XAS spectra of Figure 2.5.

[4] For the notation and the relation of these real orbitals to spherical harmonics, see Appendix A.

Carra *et al.* derived sum rules for the linear dichroism, which can be used to determine the expectation value of quadrupolar operators [23].

2.3.3 Sum rules for x-ray magnetic circular dichroism

Using circularly polarized light, the excitations are spin-selective; assuming that the spins are parallel/antiparallel aligned to the direction of the light (Poynting vector), the difference (dichroic) spectrum shows the difference between up- and down-spin occupation and gives thus information about the magnetic properties. Contrary to the linear dichroism, no single-crystalline sample are needed, but all spins have to be aligned to the magnetic field; thus the x-ray magnetic circular dichroism (XMCD) is primarily suitable for ferromagnets but also paramagnets can be measured [24]. If the external magnetic field is not strong enough to align all spins, one has to be careful with the analysis and especially with using the following sum rules.

For the orbital moment, Thole *et al.* [25] derived the sum rule

$$\begin{aligned}\langle L_z\rangle = 2\frac{l(l+1)}{c(c+1)-l(l+1)-2}n_{\text{holes}} \\ \times \frac{\int_{\text{edge}}\left[\mu^+(E)-\mu^-(E)\right]\mathrm{d}E}{\int_{\text{edge}}\left[\mu^+(E)+\mu^+(E)+\mu_z(E)\right]\mathrm{d}E},\end{aligned} \tag{2.5}$$

where μ^- and μ^+ denote the spectrum for, respectively, left- and right-circularly polarized light (for a Poynting vector along z), μ_z for z polarized light, l the state subshell (here, d^n, i.e. $l = 2$), c is the core-hole subshell ($c = 1$ for p), and n_{holes} the number of holes. It is $\mu^+(E) + \mu^-(E) + \mu_z(E) \approx \frac{3}{2}[\mu^+(E) + \mu^-(E)]$; the equation can then also be written as

$$\langle L_z\rangle = -2\frac{\int_{L_{2,3}}\Delta\mu(E)\,\mathrm{d}E}{3/2\int_{L_{2,3}}[\mu^+(E)+\mu^-(E)]\mathrm{d}E}n_{\text{holes}}, \tag{2.6}$$

with $\Delta\mu = \mu^+ - \mu^-$.

Carra *et al.* [26] have derived another sum rule to determine the spin $\langle S_z\rangle$ and the magnetic-dipole moment $\langle T_z\rangle$,

$$\frac{\int_{j_+} \Delta\mu \mathrm{d}E - [(c+1)/c] \int_{j_-} \Delta\mu}{\int_{j_+ + j_-} [\mu^+(E) + \mu^-(E) + \mu_z(E)] \, \mathrm{d}E}$$
$$= \frac{l(l+1) - 2 - c(c+1)}{3cn_{\mathrm{holes}}} \langle S_z \rangle \tag{2.7}$$
$$+ \frac{l(l+1)[l(l+1) + 2c(c+1) + 4] - 3(c-1)^2(c+2)^2}{6cl(l+1)n_{\mathrm{holes}}} \langle T_z \rangle,$$

where $j\pm = c \pm 1/2$; which can be simplified for our case to

$$2\langle S_z \rangle + 7\langle T_z \rangle = 3 \frac{\int_{L_3} \Delta\mu \, \mathrm{d}E - 2 \int_{L_2} \Delta\mu \, \mathrm{d}E}{3/2 \int_{L_{2,3}} (\mu^+(E) + \mu^-(E)) \, \mathrm{d}E} n_{\mathrm{holes}}. \tag{2.8}$$

In order to use either sum rules one needs to estimate the denominator, i.e. the volume of the spectrum. XAS spectra show a constant offset plus a so-call edge jump (the "background" is higher after an edge than before); as the interactions regarded for the sum rules do not include these, one needs to substract the background before applying the sum rule. Using the ratio between the orbital and the spin moment avoids this problem. For the spin-sum rule one needs to integrate over the L_3 and L_2 edge separately; this assumes that $j_\pm$ are good quantum numbers, which is especially for the early transition-metal ions not the case. (A note of warning: While for, e.g., Mn-L_{23} spectra splitting the edges is already visually difficult, also for visually well-split edges the $j_\pm$ might be not a good quantum number [27].) Additionally, there is the magnetic dipole moment, which might not be a small number [28]: While octahedral symmetry it can usually be neglected, in trigonal symmetry it can become relevant [27].

2.4 References

[1] N. Tesla, *On the Hurtful Actions of Lenard and Roentgen Tubes*, Electrical Review (1897). http://www.tesla.hu/tesla/articles/18970505.doc.

[2] Wikipedia, *X-ray history* (2007) [Accessed 2007-04-01].

[3] W. C. Röntgen, *Über eine neue Art von Strahlen*, Annalen der Physik **300**, 1 (1898). DOI: 10.1002/andp.18983000102.

[4] F. R. Elder, A. M. Gurewitsch, R. V. Langmuir, and H. C. Pollock, *Radiation from electrons in a synchrotron*, Physical Review **71**, 829 (1947). DOI: 10.1103/PhysRev.71.829.5.

[5] J. Als-Nielsen and D. McMorrow, *Elements of Modern X-Ray Physics*. (Wiley, New York, 2001). ISBN: 0471498580.

[6] Brinkmann, G. R.Materlik, J. Rossbach, and A. Wagner, *Conceptual Design of a 500 GeV e^+/e^- Linear Collider with Integrated X-ray Laser Facility* (1997), DESY REPORT 1997-048, Hamburg.

[7] Z. Tan, J. I. Budnick, and S. M. Heald, *Structural parameter determination in fluorescence exafs of concentrated samples*, Review of Scientific Instruments **60**, 1021 (1989). DOI: 10 .1063/1.1140311.

[8] L. Tröger, D. Arvanitis, K. Baberschke, H. Michaelis, U. Grimm, and E. Zschech, *Full correction of the self-absorption in soft-fluorescence extended x-ray-absorption fine structure*, Physical Review B **46**, 3283 (1992). DOI: 10.1103/PhysRevB.46.3283.

[9] C. H. Booth1 and F. Bridges, *Improved self-absorption correction for fluorescence measurements of extended x-ray absorption fine-structure*, Physica Scripta **T115**, 202 (2005). DOI: 10 .1238/Physica.Topical.115a00202.

[10] B. T. Thole, G. van der Laan, J. C. Fuggle, G. A. Sawatzky, R. C. Karnatak, and J.-M. Esteva, *3d x-ray-absorption lines and the $3d^9 4f^{n+1}$ multiplets of the lanthanides*, Physical Review B **32**, 5107 (1985). DOI: 10.1103/PhysRevB.32.5107.

[11] Wikipedia, *Monozeit* (2008) [Accessed 2008-04-03].

[12] F. M. F. de Groot, Ph.D. thesis, University of Nijmegen, (1991). The thesis and his other publications are available from http:/ /www.anorg.chem.uu.nl/people/staff/FrankdeGroot/publications .% htm.

[13] F. M. F. de Groot, *X-ray absorption of transition metal oxides: An overview of the theoretical approaches*, Journal of Electron Spectroscopy and Related Phenomena **62**, 111 (1993). DOI: 10.1016/0368-2048(93)80009-B.

[14] F. M. F. de Groot, *X-ray absorption and dichroism of transition metals and their compounds*, Journal of Electron Spectroscopy and Related Phenomena **67**, 529 (1994). DOI: 10.1016/0368 -2048(93)02041-J.

[15] F. M. F. de Groot, *Multiplet effects in x-ray spectroscopy*, Coordination Chemistry Reviews **249**, 31 (2005). DOI: 10 .1016/j.ccr.2004.03.018.

[16] See the "Theo Thole Memorial Issue", Journal of Electron Spectroscopy and Related Phenomena **86**, 1 (1997). DOI: 10.1016/S0368-2048(97)00039-X.

[17] R. Stumm von Bordwehr, *A history of x-ray absorption fine structure*, Annales de Physiques **14**, 377 (1989). DOI: 10.1051/anphys:01989001404037700.

[18] C. Mitra, Z. Hu, P. Raychaudhuri, S. Wirth, S. I. Csiszar, H. H. Hsieh, H.-J. Lin, C. T. Chen, and L. H. Tjeng, *Direct observation of electron doping in $La_{0.7}Ce_{0.3}MnO_3$ using x-ray absorption spectroscopy*, Physical Review B **67**, 092404 (2003). DOI: 10.1103/PhysRevB.67.092404.

[19] G. van der Laan and B. T. Thole, *Local probe for spin-orbit interaction*, Physical Review Letters **60**, 1977 (1988). DOI: 10.1103/PhysRevLett.60.1977.

[20] B. T. Thole and G. van der Laan, *Linear relation between x-ray absorption branching ratio and valence-band spin-orbit expectation value*, Physical Review A **38**, 1943 (1988). DOI: 10.1103/PhysRevA.38.1943.

[21] B. T. Thole and G. van der Laan, *Branching ratio in x-ray absorption spectroscopy*, Physical Review B **38**, 3158 (1988). DOI: 10.1103/PhysRevB.38.3158.

[22] C. T. Chen, L. H. Tjeng, J. Kwo, H. L. Kao, P. Rudolf, F. Sette, and R. M. Fleming, *Out-of-plane orbital characters of intrinsic and doped holes in $La_{2-x}Sr_xCuO_4$*, Physical Review Letters **68**, 2543 (1992). DOI: 10.1103/PhysRevLett.68.2543.

[23] P. Carra, H. König, B. T. Thole, and M. Altarelli, *Magnetic x-ray dichroism general features of dipolar and quadrupolar spectra*, Physica B **192**, 182 (1993). DOI: 10.1016/0921-4526(93)90119-Q.

[24] M. W. Haverkort, Z. Hu, J. C. Cezar, T. Burnus, H. Hartmann, M. Reuther, C. Zobel, T. Lorenz, A. Tanaka, N. B. Brookes, H.-H. Hsieh, H.-J. Lin, C.-T. Chen, and L. H. Tjeng, *Spin State Transition in $LaCoO_3$ Studied Using Soft X-ray Absorption Spectroscopy and Magnetic Circular Dichroism*, Physical Review Letters **97**, 176405 (2006). DOI: 10.1103/PhysRevLett.97.176405.

[25] B. T. Thole, P. Carra, F. Sette, and G. van der Laan, *X-ray circular dichroism as a probe of orbital magnetization*, Physical Review Letters **68**, 1943 (1992). DOI: 10.1103/PhysRevLett .68.1943.

[26] P. Carra, B. T. Thole, M. Altarelli, and X. Wang, *X-ray circular dichroism and local magnetic fields*, Physical Review Letters **70**, 694 (1993). DOI: 10.1103/PhysRevLett.70.694.

[27] Y. Teramura, A. Tanaka, and T. Jo, *Effect of Coulomb Interaction on the X-Ray Magnetic Circular Dichroism Spin Sum Rule in 3d Transition Elements*, Journal of the Physical Society of Japan **65**, 1053 (1996). DOI: 10.1143/JPSJ.65.1053.

[28] J. P. Crocombette, B. T. Thole, and F. Jollet, *The importance of the magnetic dipole term in magneto-circular x-ray absorption dichroism for 3d transition metal compounds*, Journal of Physics: Condensed Matter **8**, 4095 (1996). DOI: 10.1088/0953 -8984/8/22/013.

All science is either physics or stamp collecting.
— Ernest Rutherford, 1871–1937

3 Ligand-Field Theory and Cluster Calculations

For nonmetallic solids with rather localized valence electrons, most of the properties can be described by concentrating on a few electrons. This is the case for nonmetallic transition-metal oxides and for soft x-ray absorption spectroscopy as the excitation is excitonic and thus local; here, only the valence d electrons are of interest (plus the $2p$ electrons and hybridizing electrons from the ligands) – all other electrons are enter only as effective potential. One successful numerical technique is the a configuration-interaction (CI) cluster calculation which is essentially restricted on the valence electrons. In this chapter we will look first at the crystal-field and ligand-field theory, which provides by itself a means to understand orbital ordering and spin states. The configuration-interaction cluster calculation is covered next, which makes use of the ligand-field theory.

3.1 Crystal-field and ligand-field theory

The crystal-field theory (CFT) is a purely electrostatic model which goes back to the 1930s and was developed by Bethe [1]and Van Vleck (Ref. 2 and references therein). Hereby, a crystal is not regarded as

a whole but a site it chosen and only the electrostatic influence of the neighbors, regarded as point charges, on the outer shell of the chosen atom is studied. The ligand-field theory (LFT) goes beyond by including the bonding in the coordination complexes. A good introduction into this theory can be found in the book of Schläfer and Gliemann [3], but also in the books of Ballhausen [4], of Sugano, Tanabe and Kamimura [5], of Griffith [6], of Figgis and Hitchman [7], of Gerloch and Slade [8], and less readable but very detailed in the book Abragam and Bleaney [9]. Several inorganic/physical chemistry books have also a section about symmetry and hybridization (see e.g. Ref. 10); additionally, some knowledge about symmetries is useful, but note that only point-group symmetries matter for this theory (see, e.g., 11–12). Finally, since the starting point is a free ion, atomic-physics books provide some basis (e.g. 13–16). In the following we loosely follow the book of Schläfer and Gliemann.

For the case of the Russell–Saunders (or LS) coupling, we denote a state by the symbol ${}^{2S+1}L_J$; hereby $M = 2S + 1$ denotes the spin multiplicity, for $L = 0, 1, 2, \ldots$ the letters $S, P, D, F, G, H, \ldots$ are used and J is the total angular momentum; the Russell–Saunders coupling is a rather good approximation for light elements and assumes that the total momenta $\boldsymbol{S}$, $\boldsymbol{L}$ and $\boldsymbol{J}$ yield good quantum numbers and that the following is true: $\boldsymbol{L} = \sum_i \boldsymbol{l}$, $\boldsymbol{S} = \sum_i \boldsymbol{s}_i$ and $\boldsymbol{J} = \boldsymbol{L} + \boldsymbol{S}$ (i.e. $J \in \{L + S, L + S - 1, \ldots, |L - S|\}$), where $\boldsymbol{s}_i$ and $\boldsymbol{l}_i$ are respectively the spin and angular momentum of a single electron. (For an in-depth description, see the book by Slater [14, Chap. 10].)

As an example, we take Cr^{3+} which has 3 electron in the $3d$ orbitals. For the spin there are two possibilities, namely $S = 1/2$ with $\uparrow\uparrow\downarrow$ ($M = 2$, doublet) and $S = 3/2$ with $\uparrow\uparrow\uparrow$ ($M = 4$, quartet). For the angular momentum, there are in principle the 4 values for the total momentum possible for $\uparrow\uparrow\uparrow$, viz. $L = 0, 1, 2, 3$. However, as the wavefunction must be antisymmetric under interchange of two electrons, only $L = 1$ and $L = 3$ are allowed. This leaves us in case of the quartet with ${}^4F$ and ${}^4P$. In case of the doublet the following configurations are possible: ${}^2P$, $a\,{}^2D$, $b\,{}^2D$, ${}^2F$,${}^2G$ and ${}^2H$ (note that ${}^2D$ appears twice).

The number of possible configurations can be rather large; for d electrons there are 10 [$= 2(2l + 1)$] possibilities to place an atom. Thus for n electrons in a d subshell (d^n) there are $\binom{2(2l+1)}{n} = \binom{10}{n}$ possibilities,

where $\binom{k}{n} = k!/[k!(n-k)!]$ ($k \geq n \geq 0$, otherwise $= 0$) denotes the binominal coefficient. Thus, d^1 and d^9 have 10 configurations, d^2 and d^8 have 45, d^3 and d^7 have 120, d^4 and d^6 have 210, and d^5 has 252.

3.2 The model

In this section we use atomic units in order to make the equations simpler (cf. Appendix E). As mentioned above, in the ligand-field theory one is interested in the electrons which can be assigned to the partially filled subshell of a central ion (e.g. the $3d$ or $4d$ subshells of a transition-metal ion). Hereby the assumption is made that the electrostatic potential of the core and the ligands, i.e. the exchange forces between electrons of the central ion and the ligands can be neglected. The Hamiltonian of N electrons in an subshell can be written as

$$H = \sum_{i=1}^{N} \left(-\frac{1}{2}\nabla_i^2 - \frac{Z^*}{r_i} \right) + \frac{1}{2} \sum_{i=1}^{N} \sum_{\substack{j=1 \\ i \neq j}}^{N} \frac{1}{r_{ij}} + \sum_{i=1}^{N} V(\boldsymbol{r}_i) + \sum_{i=1}^{N} H_{\mathrm{SO}}(i), \tag{3.1}$$

where $-\frac{1}{2}\nabla_i^2$ is the kinetic energy of the ith electron, $-Z^*/r_i$ the potential energy of the ith electron, Z^* is the effective charge of the core (roughly: nuclear charge minus charge of filled shells), $1/r_{ij}$ is the electron–electron interaction of two electrons in the partially filled subshell; $V(\boldsymbol{r}_i)$ denotes the Coulomb interaction between the ith electron and all the ligands, and $H_{\mathrm{SO}}(i)$ is the spin–orbit coupling energy. This Schrödinger equation is too difficult to be solved exactly. One starts by solving the following independent-particle Schrödinger equation

$$H_{0,0}\Phi = \sum_{i=1}^{N} \left(-\frac{1}{2}\nabla_i^2 - \frac{Z^*}{r_i} \right) \Phi = N\varepsilon_{nd}\Phi. \tag{3.2}$$

Here, the Φ are antisymmetrized products of one-electron d functions which are all degenerate and belong to a state of the electron configuration $(nd)^N$ with the energy ε_{nd}, where ε_{nd} is the energy of a single nd electron moving in the effective potential around the core. The

remaining terms of Eq. (3.1) can be regarded as perturbation operator. One can distinguish three cases:

- The weak crystal field, which has the following order in energy: electron–electron interaction > crystal field > spin-orbit coupling,
- the strong crystal field with crystal field > electron–electron interaction > spin–orbit coupling, and
- the strong spin–orbit coupling case with spin-orbit coupling > crystal field > electron–electron interaction.

Unfortunately, in the $3d$ transition-metal compounds, the electron–electron interaction and the crystal-field are of comparable size.

The ligand-field can be calculated as follows. Let $\rho(R)$ denote the charge density of all ligands (but excluding the electron density of the ion of interest), where R denotes the coordinate relative to the central ion; then the crystal-field potential is given by

$$V(\boldsymbol{r}) = \int \frac{\rho(\boldsymbol{R})}{|\boldsymbol{R}-\boldsymbol{r}|}\mathrm{d}^3R. \tag{3.3}$$

We now expand $1/|\boldsymbol{R}-\boldsymbol{r}|$ in spherical harmonics Y_l^m (cf. Appendix A and e.g. [17, pp. 369ff.])

$$V(\boldsymbol{r}) = \sum_{l=0}^{\infty}\sum_{m=-l}^{l}\frac{4\pi}{2l+1}Y_l^m(\theta,\phi)\int\rho(\boldsymbol{R})\frac{r_<^l}{r_>^{l+1}}Y_l^{m*}(\theta,\phi)\,\mathrm{d}^3R, \tag{3.4}$$

where $r_< = \min(R,r)$ and $r_> = \max(R,r)$. Since for $r > R$ the integrand is negligible (in our model, the ligand electron density is vanishingly small near the electrons of the central ion), we have $r_< = r$ and $r_> = R$ and thus

$$V(\boldsymbol{r}) = V(r,\theta,\phi) = \sum_{l=0}^{\infty}\sum_{m=-l}^{l}A_l^m\,r^l\,Y_l^m(\theta,\phi) \tag{3.5}$$

with

$$A_l^m = \frac{4\pi}{2l+1}\int\frac{1}{R^{l+1}}\rho(\boldsymbol{R})Y_l^{m*}(\theta,\phi)\,\mathrm{d}^3R. \tag{3.6}$$

At the first sight $V(\boldsymbol{r})$ contains an infinite series and is thus impossible to solve, fortunately only few terms play a role in the ligand-field theory.

First, if the charge distribution ρ has a particular (point) symmetry, also V needs to have it; i.e. V has to be invariant under all symmetry operations of the to ρ associated symmetry group. (This is generally true.)

Secondly, in the ligand-field theory, V appears as perturbation operator where the wavefunctions are one-electron functions $\phi_{n,l,m} = R_{n,l}(r)Y_l^m(\theta,\phi)$ and thus

$$\langle\phi_{n,l,m}|A_\lambda^\mu\, r^\lambda\, Y_\lambda^\mu|\phi_{n,l,m'}\rangle = A_\lambda^\mu\langle R_{n,l}|r^\lambda|R_n,l\rangle\langle Y_l^m|Y_\lambda^\mu|Y_l^{m'}\rangle. \tag{3.7}$$

Where $\langle Y_l^m|Y_\lambda^\mu|Y_l^{m'}\rangle$ vanishes unless the following conditions are met [18](we assume here that the electrons come from the same subshell)[5]:

- $\lambda \leq 2l$, for d electrons thus: $\lambda \leq 4$
- λ is even

Hence, the potential for d electrons in the approximation of ligand-field theory only consists of

$$V(\boldsymbol{r}) = A_0^0\, r^0 Y_0^0 + \sum_{\mu=-2}^{2} A_2^\mu\, r^2 Y_2^\mu + \sum_{\mu=-4}^{4} A_4^\mu\, r^4 Y_4^m; \tag{3.8}$$

this can be rewritten by defining $B_l^m = (2l+1)/4\pi\, A_l^m\langle r^l\rangle$ and $C_l^m = 4\pi/(2l+1)\, Y_l^m$ as

$$V(\boldsymbol{r}) = B_0^0\, C_0^0 + \sum_{\mu=-2}^{2} B_2^\mu\, C_2^\mu + \sum_{\mu=-4}^{4} B_4^\mu\, C_4^\mu. \tag{3.9}$$

Above potentials [Eq. (3.8) and (3.8)] hold true for all symmetries. For octahedral symmetry (Schönflies: O_h; Hermann-Mauguin: $m3m$, cf. FIG. B.1) the potential must be invariant under all symmetry operations of the O_h point group. The z axis is a C_4 axis, i.e. the potential must be invariant under rotations of $\phi' = \phi + \pi/2$. The only

[5] For $\langle\phi_{n,l,m}|A_\lambda^\mu|\phi_{n,l'm'}\rangle$ the integrals are nonzero only when (a) $|l-l'| \leq \lambda \leq |l+l'|$ and (b) $l+l'+\lambda$ are even.

ϕ dependence is in the exponential $\exp(\mathrm{i}m\phi)$ (cf. Appendix A) and thus A_l^m with $m = 0, \pm 4, \ldots$ are possible. This reduces the potential to

$$V_{O_h}(\boldsymbol{r}) = A_0^0 Y_0^0 + A_2^0 r^2 Y_2^0 + r^4 (A_4^{-4} Y_4^{-4} + A_4^0 Y_4^0 + A_4^4 Y_4^4). \quad (3.10)$$

If one now reflects the coordinate system about the zx plane, i.e. $(x', y', z') = (x, -y, z)$ and sees how the remaining spherical harmonics in Cartesian coordinates (see Appendix A) transform. One then finds $\sigma_{zx} Y_4^{\pm} = Y_4^{\mp 4}$ and thus $A_4^4 = A_4^{-4}$. If one does now a rotation of the coordinate system $C_3(x' = y, y' = z, z' = x)$ one finds that A_2^0 must be zero as for instance for $3z^2 - r^2 = 2z^2 - x^2 - y^2$ the coefficient before the z is different from the one before x and y. This gives the following potential

$$\begin{aligned} V_{O_h}(x, y, z) = A_0^0 Y_0^0 + \sqrt{\frac{9}{4\pi}} r^4 \, r^{-4} \\ \times [A_4^0 \sqrt{\frac{1}{64}} (3x^4 + 3y^4 + 8z^4 + 6x^2y^2 - 24x^2z^2 - 24y^2z^2) \\ + A_4^4 \sqrt{\frac{35}{128}} (2x^4 - 12x^2y^2 + 2y^2)]. \end{aligned} \quad (3.11)$$

If one sets the coefficients for y^4 the same, i.e.

$$3A_4^0 \sqrt{1/64} + 2A_4^4 \sqrt{35/128} = 8A_4^0 \sqrt{1/64} \quad (3.12)$$

or $A_4^4 = \sqrt{5/14} A_4^0$, one obtains

$$V_{O_h}(\boldsymbol{r}) = A_0^0 r^0 Y_0^0 + A_4^0 r^4 [Y_4^0 + \sqrt{5/14} (Y_4^4 + Y_4^{-4})]. \quad (3.13)$$

In the ionic ligand-field theory the charge distribution can be often approximated by the change distribution of the individual ligands assuming point charges or point dipoles [3, pp. 329ff.]. However, this does not work reliably; for this thesis the ionic part of the crystal field has usually been obtained using the total-energy differences of constrained LDA+U calculations or also from the center of gravity of partial density of state coming from LDA+U (or LDA/GGA) calculations. For the hybridization part, i.e. the hopping between the transition-metal d and the ligand oxygen p orbitals, the $V_{pd\sigma}$ and $V_{pd\pi}$ values following to Harrison's rules have been used (sometimes the

uniformly scaled). The matrix elements themselves have been constructed following Slater and Koster and can be found in Appendix B. For lower symmetries the program HYBRID has been used which applies the procedure by Slater and Koster and Harrison's rules for any symmetry; the program is available from the author's homepage.

3.3 Description of d^1 systems

We start with d^1 which is conceptually and numerically simpler as no electron–electron interactions are present (besides the effective Hamiltonian of the ligand field); for simplicity we assume for now that also the spin–orbit coupling is small enough to be ignored, which is approximately valid for (early) $3d$ transition metals. The Schrödinger equation of the unperturbed system is then

$$H_{0,0}\psi = (-\nabla^2 - Z^*/r)\psi = E_{0,0}\psi = \varepsilon_{nd}\psi \tag{3.14}$$

and the perturbation is given by $H' = -V(r)$. The solutions for Eq. (3.14) are the ten wavefunctions

$$\phi_m := \psi_{n,2,m,\sigma} = R_{n,2}(r)Y_1^m(\theta,\phi)\chi_\sigma, \quad m = -2,-1,0,1,2, \tag{3.15}$$

where χ_σ denotes the spin with $\sigma = \pm\frac{1}{2}$ or $\sigma \in \{\alpha,\beta\}$. As the potential is radial, the system has spherical symmetry and gives a ${}^2D$ term. The energy changes are given by the roots ε of the secular determinant $|H' - \mathrm{diag}(\varepsilon)| = 0$ or slightly more verbosely written

$$\left| \begin{pmatrix} H'_{i,\alpha;j\alpha} & H'_{i,\alpha;j\beta} \\ H'_{i,\beta;j\alpha} & H'_{i,\beta;j\beta} \end{pmatrix} - \mathrm{diag}(\varepsilon) \right| = 0, \tag{3.16}$$

where $H'_{i,\sigma;j\sigma'} = \langle\phi_{i,\sigma}|H'|\phi_{j,\sigma'}\rangle$ and $\mathrm{diag}(\varepsilon)$ is a matrix with ε on the diagonal and zero elsewhere. Since H' does not operate on the spin, we have $H'_{i,\alpha;j\alpha} = H'_{i,\beta;j\beta} = H'_{i,j}$ and $H'_{i\alpha;j\beta} = H'_{i\beta;j\alpha} = 0$.

3.3.1 Octahedral (O_h) field

By symmetry considerations one knows that in an octahedral field the fivefold (orbitally) degenerate D term splits into a doubly degenerate

E_g term[6] and a three-fold degenerate T_{2g} state. An appropriate basis is

$$\begin{aligned}
E_g &\begin{cases} \phi_1 = \psi_{n,2,0} & = e_g^a = d_{3z^2-r^2} R_{n,2} \\ \phi_2 = \frac{1}{\sqrt{2}}(\psi_{n,2,2} + \psi_{n,2,-2}) & = e_g^b = d_{x^2-y^2} R_{n,2} \end{cases} \\
T_{2g} &\begin{cases} \phi_3 = -\frac{\mathrm{i}}{\sqrt{2}}(\psi_{n,2,2} - \psi_{n,2,-2}) & = t_{2g}^0 = d_{xy} R_{n,2} \\ \phi_4 = \frac{\mathrm{i}}{\sqrt{2}}(\psi_{n,2,1} + \psi_{n,2,-1}) & = t_{2g}^+ = d_{yz} R_{n,2} \ . \\ \phi_5 = -\frac{1}{\sqrt{2}}(\psi_{n,2,1} - \psi_{n,2,-1}) & = t_{2g}^- = d_{zx} R_{n,2} \end{cases}
\end{aligned} \tag{3.17}$$

We can now write down the matrix elements $H_{i,j} = \langle \phi_i | H | \phi_j \rangle$. The off-diagonal terms which connect E_g states with T_{2g} vanish as $\{e_g^a, e_g^b\}$ and $\{t_{2g}^0, t_{2g}^\pm\}$ belong to different irreducible representations of the symmetry group of H'. Furthermore, the other off-diagonal elements vanish since ϕ_i and ϕ_j, belonging to the irreducible representation of H', transform as different columns of the representation matrices. Thus the matrix is

$$H'_{O_h} = \begin{pmatrix} H_{1,1} & 0 & 0 & 0 & 0 \\ 0 & H_{2,2} & 0 & 0 & 0 \\ 0 & 0 & H_{3,3} & 0 & 0 \\ 0 & 0 & 0 & H_{4,4} & 0 \\ 0 & 0 & 0 & 0 & H_{5,5} \end{pmatrix}, \tag{3.18}$$

for which the roots of the scular matrix are simply $\varepsilon_i = H_{i,i}$. Furthermore, the symmetry tells us that the energy of the E_g and, respectively, of the T_{2g} states is the same. One can now plug in the definition of H', abbreviate $\langle r^l \rangle = \langle R_{n,2}(r) | r^l | R_{n,2} \rangle$ and calculate the integrals over three spherical harmonics explicitly. The result is then

[6] We use the Mulliken symbols [19–22]throughout; they are related to the Bethe symbols [1, 23]as follows. Mulliken A_1 = Bethe Γ_1 (degeneracy: 1), $A_2 = \Gamma_2$ (1), $E = \Gamma_3$ (2), $T_1 = \Gamma_4$ (3), $T_2 = \Gamma_5$ (3). Mulliken symbols: A denotes a state which is symmetric and B one which is antisymmetric with respect to the principal C_n axis. The subscripts 1 and 2 (for A and B) denote, respectively, no sign change (1) or a sign change (2) upon rotation about the center of the atom; g (gerade, symmetric) and u (ungerade, antisymmetric) denote, respectively, no sign change (g) or a sign change (u) upon inversion through the center of the atom. Prime ($'$) and double prime ($''$) denote symmetry ($'$) and antisymmetry ($''$) with respect to a horizontal symmetry plane σ_h. (σ stands for Spiegelebene [mirror plane].)

$$\varepsilon(E_g) = -\frac{1}{2\sqrt{\pi}}\langle r^0\rangle A_0^0 - 6\frac{1}{14\sqrt{\pi}}\langle r^4\rangle A_4^0$$
$$\varepsilon(T_{2g}) = -\frac{1}{2\sqrt{\pi}}\langle r^0\rangle A_0^0 + 4\frac{1}{14\sqrt{\pi}}\langle r^4\rangle A_4^0. \tag{3.19}$$

The crystal-field splitting betwixt the E_g and the T_{2g} states is thus given by $\Delta = 10Dq = E(E_g) - E(T_{2g}) = -10/(14\sqrt{\pi})A_4^0$ with $\Delta > 0$. Thus, the potential in Eq. (3.13) can be written as

$$V_{O_h}(r) = -A_0^0\langle r^0\rangle Y_0^0 - \frac{7\sqrt{\pi}}{5}\Delta\,\langle r^4\rangle[Y_4^0 + \sqrt{5/14}(Y_4^4 + Y_4^{-4})] \tag{3.20}$$

or, using $B_l^m := A_l^m\langle r^l\rangle$ and $C_l^m(\theta,\phi) = \sqrt{4\pi/(2k+1)}Y_l^m(\theta,\phi)$, as

$$\begin{aligned} V_{O_h}(r) &= -\frac{1}{2\sqrt{\pi}}B_0^0C_0^0 + \frac{21}{10}\Delta[C_4^0 + \sqrt{5/14}(C_4^4 + C_4^{-4})] \\ &= -\frac{1}{2\sqrt{\pi}}B_0^0C_0^0 + 21Dq[C_4^0 + \sqrt{5/14}(C_4^4 + C_4^{-4})] \end{aligned} \tag{3.21}$$

In cubic symmetry (with eight ligands), $A_{0,0}^{(\mathrm{cube})} = \frac{4}{3}A_{0,0}^{(\mathrm{oct})}$ and $A_{4,0}^{(\mathrm{cube})} = -\frac{8}{9}A_{4,0}^{(\mathrm{oct})}$. And for a tetrahedron (T_d) $A_{0,0}^{(\mathrm{tetr})} = \frac{2}{3}A_{0,0}^{(\mathrm{oct})}$ and $A_{4,0}^{(\mathrm{tetr})} = -\frac{4}{9}A_{4,0}^{(\mathrm{oct})}$.

3.3.2 Tetragonal (D_{4h}) symmetry

In tetragonal symmetry, the octahedral E_g states split into two nondegenerate states, namely B_{1g} and A_{1g}, and the triply degenerate octahedral T_{2g} state splits into a doubly degenerate E_g and a nondegenerate B_{2g} state. We continue to use the same basis $\{\phi_i\}$ [cf. Eq. (3.17)] as before; the fivefold orbitally degenerate D term now splits into three nondegenerate terms A_{1g} (ϕ_1, $d_{3z^2-r^2}$), B_{1g} (ϕ_2, $d_{x^2-y^2}$), B_{2g} (ϕ_3, d_{xy}) and a doubly degenerated E_g term (ϕ_4/d_{yz} and ϕ_5/d_{zx}). The matrix is again diagonal. In total, one obtains the following energies

$$
\begin{aligned}
\varepsilon(B_{1g}) &= \varepsilon_{0,\text{oct.}} + \varepsilon_{0,\text{D}_{4\text{h}}} + 6Dq + 2Ds - Dt \\
&= \varepsilon_{0,\text{D}_{4\text{h}}} + \frac{3}{5}\Delta + \frac{1}{2}\Delta_{e_g} \\
\varepsilon(A_{1g}) &= \varepsilon_{0,\text{oct.}} + \varepsilon_{0,\text{D}_{4\text{h}}} + 6Dq - 2Ds - 6Dt \\
&= \varepsilon_{0,\text{D}_{4\text{h}}} + \frac{3}{5}\Delta - \frac{1}{2}\Delta_{e_g} \\
\varepsilon(B_{2g}) &= \varepsilon_{0,\text{oct.}} + \varepsilon_{0,\text{D}_{4\text{h}}} - 4Dq + 2Ds - Dt \\
&= \varepsilon_{0,\text{D}_{4\text{h}}} - \frac{2}{5}\Delta + \frac{1}{2}\Delta_{t_{2g}} \\
\varepsilon(E_g) &= \varepsilon_{0,\text{oct.}} + \varepsilon_{0,\text{D}_{4\text{h}}} - 4Dq - Ds + 4Dt \\
&= \varepsilon_{0,\text{D}_{4\text{h}}} - \frac{2}{5}\Delta - \frac{1}{2}\Delta_{t_{2g}}
\end{aligned}
\tag{3.22}
$$

and the following potential

$$
V(\boldsymbol{r}) = B_0^0 C_0^0 - 7Ds\, C_2^0 + 21(Dq - Dt)C_4^0 + 21Dq\sqrt{\frac{5}{14}}(C_4^4 + C_4^{-4}). \tag{3.23}
$$

Note: With this definition, $10Dq$ is the difference between the B_{1g} ($d_{x^2-y^2}$) and the B_{2g} (d_{xy}) state and not the weighted difference between the B_{1g}/A_{1g} (Oh: E_g) and the B_{2g}/E_g (Oh: T_{2g}) states; the same is true for the potential shown below for the orthorhombic symmetry.

3.3.3 Orthorhombic (D_{2h}) symmetry

In orthorhombic (D_{2h}; mmm) symmetry, the tetragonal E_g state splits further, additionally the Hamilton operator no longer diagonal for the basis ϕ_i as the ϕ_1 ($d_{3z^2-r^2}$) and ϕ_2 ($d_{x^2-y^2}$) states are mixed by the mixing parameter Dv. The states are given by [24]

$$\begin{aligned}
\varepsilon(B_{1g}) &= \varepsilon_{0,\text{oct.}} + \varepsilon_{0,\text{D}_{4\text{h}}} + 6Dq + 2Ds - \frac{7}{2}Dt + \frac{1}{2}\sqrt{\Gamma} \\
\varepsilon(A_{1g}) &= \varepsilon_{0,\text{oct.}} + \varepsilon_{0,\text{D}_{4\text{h}}} + 6Dq + 2Ds - \frac{7}{2}Dt - \frac{1}{2}\sqrt{\Gamma} \\
\varepsilon(B_{2g}(xy)) &= \varepsilon_{0,\text{oct.}} + \varepsilon_{0,\text{D}_{4\text{h}}} - 4Dq + 2Ds - Dt \\
&= \varepsilon_{0,\text{D}_{4\text{h}}} - \frac{2}{5}\Delta + \frac{1}{2}\Delta_{t_{2g}} \\
\varepsilon(B_{2g}(zx)) &= \varepsilon_{0,\text{oct.}} + \varepsilon_{0,\text{D}_{4\text{h}}} - 4Dq + Ds + 4Dt + Du \\
&= \varepsilon_{0,\text{D}_{4\text{h}}} - \frac{2}{5}\Delta - \frac{1}{2}\Delta_{t_{2g}} + \frac{1}{2}\Delta_{e_g} \qquad (3.24) \\
\varepsilon(B_{2g}(yz)) &= \varepsilon_{0,\text{oct.}} + \varepsilon_{0,\text{D}_{4\text{h}}} - 4Dq + Ds + 4Dt - Du \\
&= \varepsilon_{0,\text{D}_{4\text{h}}} - \frac{2}{5}\Delta - \frac{1}{2}\Delta_{t_{2g}} - \frac{1}{2}\Delta_{e_g} \qquad (3.25)
\end{aligned}$$

with

$$\Gamma = (4Ds + 5Dt)^2 + (2Dv)^2. \qquad (3.26)$$

The potential is then given by

$$\begin{aligned}
V(\boldsymbol{r}) = B_0^0 C_0^0 &+ \left(\frac{1}{2}\sqrt{6}Du - 2\sqrt{2}Dv\right)(C_2^2 + C_2^{-2}) + 21(Dq - Dt)C_4^0 \\
&+ \left(3\frac{2}{5}Du + \frac{6}{5}Dv\right)(C_4^2 + C_4^{-2}) \\
&+ 21\sqrt{5}14Dq(C_4^4 + C_4^{-4}). \qquad (3.27)
\end{aligned}$$

3.3.4 Trigonal (D_{3d}) symmetry

In the trigonal symmetry D_{3d} ($\overline{3}m$) exist a dihedral/diagonal mirrorplane. There are several possibilities to align the triangles (see FIG. 3.1).

Contrary to the above symmetries, O_h, D_{4h}, and D_{2h}, a basis of spherical harmonics is also useful; we use the notation $d_l := Y_2^l$ in the following. In a trigonal symmetry, the following terms exist: An E_g ("E_g^σ", here denoted as $E_g^{(h)}$, h for high in energy) doublet consisting of

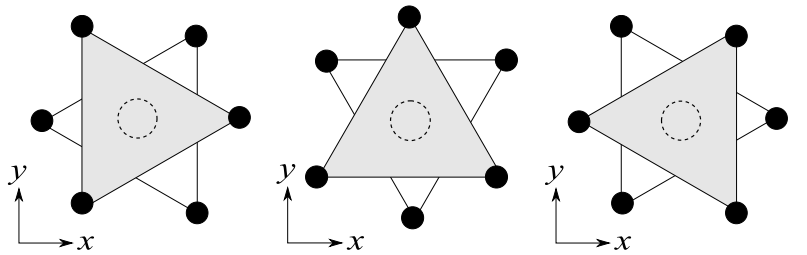

(a) (b) (c)

Fig. 3.1 In trigonal symmetry, one has the choice for orientating the transition-metal–ligand complex.

$d_{\pm 1}$ (d_{zx}, d_{yz}) orbitals, another doubly degenerate E_g ("E_g^{π}", $E_g^{(l)}$, l for low) term consisting of $d_{\pm 2}$ (d_{xy}, $d_{x^2-y^2}$), and an A_{1g} term consisting of the d_0 ($d_{3z^2-r^2}$) orbital [4, 8, 24–25].

In the week-field case ($D\sigma$ and $D\tau$ small, i.e. no mixing between the two E_g terms), the energies are then given by

$$\begin{aligned}
\varepsilon(E_g^{(h)}) &= \varepsilon_0 + 6Dq + 2D\sigma - D\tau \\
&= \varepsilon_0 + \frac{3}{5}\Delta_{12} - \frac{1}{5}\Delta_{02} \\
\varepsilon(E_g^{(l)}) &= \varepsilon_0 - 4Dq - D\sigma + 4D\tau \\
&= \varepsilon_0 - \frac{2}{5}\Delta_{12} - \frac{1}{5}\Delta_{02} \\
\varepsilon(A_{1g}) &= \varepsilon_0 - 4Dq - 2D\sigma - 6D\tau \\
&= \varepsilon_0 - \frac{2}{5}\Delta_{12} + \frac{4}{5}\Delta_{02}, \qquad (3.28)
\end{aligned}$$

where the splitting is either parameterized by $\Delta_{12} = \varepsilon(E_g^{(h)}) - \varepsilon(E_g^{(l)})$ [splitting between the higher-lying $E_g^{(h)}$ $d_{\pm 1}$ states and $E_g^{(l)}$ ($d_{\pm 2}$)] and $\Delta_{02} = \varepsilon(A_{1g}) - \varepsilon(E_g^{(l)})$, or, classically, by $D\sigma$ and $D\tau$ (see Ballhausen [4]). In the general case, there is a mixing V_{mix} between the two E_g states and the Hamiltonian is no longer diagonal. For the two E_g states one thus has the following Hamiltonians

$$H_{e_g} = \varepsilon_0 + Dq + \frac{1}{2}D\sigma + \frac{3}{2}D\tau + \begin{pmatrix} 5Dq + \frac{5}{6}D\tau - \frac{1}{2}D\sigma & \sqrt{2}D\sigma - \frac{5}{3}\sqrt{2}D\tau \\ \sqrt{2}D\sigma - \frac{5}{3}\sqrt{2}D\tau & -5Dq - \frac{5}{6}D\tau + \frac{1}{2}D\sigma \end{pmatrix}$$

or alternatively

$$H_{e_g} = \begin{pmatrix} E_g^{(h)} & V_{\mathrm{mix}} \\ V_{\mathrm{mix}} & E_g^{(l)} \end{pmatrix}. \tag{3.29}$$

Diagonalizing the Hamiltonian and inserting the definitions for Δ_{02} and Δ_{12} yields

$$\begin{aligned} \varepsilon(E_g^{(h)}) &= \varepsilon_0 + Dq + \frac{1}{2}D\sigma + \frac{3}{2}D\tau + \sqrt{\Gamma_{e_g}} \\ &= \varepsilon_0 + \frac{1}{2}\left(E_g^{(1)} + E_g^{(2)} + \sqrt{(E_g^{(1)} - E_g^{(2)})^2 + 4V_{\mathrm{mix}}}\right) \\ &= \varepsilon_0 + \frac{1}{10}(\Delta_{12} + 5\sqrt{\Delta_{12}^2 + 4V_{\mathrm{mix}}^2}) - \frac{1}{5}\Delta_{02} \\ \varepsilon(E_g^{(l)}) &= \varepsilon_0 + Dq + \frac{1}{2}D\sigma + \frac{3}{2}D\tau - \sqrt{\Gamma_{e_g}} \\ &= \varepsilon_0 + \frac{1}{2}\left(E_g^{(1)} + E_g^{(2)} - \sqrt{(E_g^{(1)} - E_g^{(2)})^2 + 4V_{\mathrm{mix}}}\right) \\ &= \varepsilon_0 + \frac{1}{10}(\Delta_{12} - 5\sqrt{\Delta_{12}^2 + 4V_{\mathrm{mix}}^2}) - \frac{1}{5}\Delta_{02} \\ \varepsilon(A_{1g}) &= \varepsilon_0 - 4Dq - 2D\sigma - 6D\tau \\ &= \varepsilon_0 - \frac{2}{5}\Delta_{12} + \frac{4}{5}\Delta_{02} \end{aligned} \tag{3.30}$$

with $\Gamma_{e_g} = 25Dq^2 + \frac{1}{4}(3D\sigma - 5D\tau)^2 + Dq(\frac{25}{3}D\tau - 5D\sigma)$. The potential is then given by

$$V_{D_{3d}} = B_0^0 C_0^0 + B_2^0 C_2^0 + B_4^0 C_4^0 + B_4^3 (C_4^3 - C_4^{-3}). \tag{3.31}$$

That the other coefficients B_l^m vanish, comes from the three-fold axis along z; the ϕ dependence of spherical harmonics is $\mathrm{e}^{\mathrm{i}m\phi}$ and thus the invariance of the potential under symmetry operations is only fulfilled

for $m = 0, \pm 3$. For the alignment of the trigonal prism as shown in Figure 3.1(a), one obtains the following parameters:

$$\begin{aligned}
B_2^0 &= -7D\sigma = \varepsilon(A_{1g}) - \varepsilon(E_g^{(l)}) - 2\sqrt{2}V_{\mathrm{mix}} \\
&= \frac{1}{2}\left(2\Delta_{02} - \Delta_{12} - 4\sqrt{2}V_{\mathrm{mix}} + \sqrt{\Delta_{12}^2 + 5V_{\mathrm{mix}}}\right) \\
B_4^0 &= -14(Dq + \frac{3}{2}D\tau) = \frac{1}{5}[9\varepsilon(A_{1g}) - 2\varepsilon(E_g^{(l)}) - 7\varepsilon(E_g^{(h)})] + 2\sqrt{2}V_{\mathrm{mix}} \\
&= \frac{1}{10}\left(18\Delta_{02} - 9\Delta_{12} + 20\sqrt{2}V_{\mathrm{mix}} - 5\sqrt{\Delta_{12}^2 + 5V_{\mathrm{mix}}}\right) \\
B_4^3 &= -14\sqrt{\frac{10}{7}}Dq = \sqrt{\frac{7}{5}}[\sqrt{2}\big(\varepsilon(E_g^{(l)} - \varepsilon(E_g^{(h)})\big) - V_{\mathrm{mix}}] \\
&= -\sqrt{\frac{7}{5}}\left(V_{\mathrm{mix}} + \sqrt{2(\Delta_{12}^2 + 5V_{\mathrm{mix}})}\right). \qquad (3.32)
\end{aligned}$$

If one rotates the triangles about the z axis by, respectively, 90° or 180°, the parameters change as follows: For 90° [Figure 3.1(b)] B_4^3 becomes purely imaginary ($B_4^{3,(90^\circ)} = \mathrm{i}B_4^{3,(0^\circ)}$) and for 180° [Figure 3.1(c)] B_4^3 becomes positive ($B_4^{3,(180^\circ)} = -B_4^{3,(0^\circ)}$).

3.4 Description of d^N systems

We assume again that the spin–orbit operator might be neglected. The noninteracting Hamiltonian is now $H = \sum_{i=1}^{N}(-\frac{1}{2}\nabla_i^2 - Z^*/r_i)$ and the energy is $E = N\varepsilon_{nd}$; the perturbation operator now also includes the electron–electron interaction $\sum_{i<j} 1/r_{i,j}$. For an in-depth description including all d^2 to d^9 configurations, see Ref. [3].

The wavefunctions are constructed from Slater determinants and a term described by ${}^{2S+1}L$ can be described by a wavefunction $\Psi(L, M_L, S, M_S)$. For a d^2 system one finds the following terms and associated energies

$$\begin{aligned}
\Delta E(^1S) &= A + 14B + 7C \\
\Delta E(^1D) &= A - 3B + 2C \\
\Delta E(^1G) &= A + 4B + 2C \\
\Delta E(^3P) &= A + 7B \\
\Delta E(^3F) &= A - 8B
\end{aligned} \tag{3.33}$$

where A, B, C are Racah parameters [26–27], which can also be expressed in Slater integrals [28–29]

$$A = F_0 - 49F_4 = F^0 - \frac{1}{9}F^4 = F^0 - \frac{49}{441}F^4 \tag{3.34}$$

$$B = F_2 - 5F_4 = \frac{1}{49}F^2 - \frac{5}{441}F^4 = \frac{9}{441}F^2 - \frac{5}{441}F^4 \tag{3.35}$$

$$C = 35F_4 = \frac{35}{441}F^4 = \frac{5}{63}F^4. \tag{3.36}$$

Numerical values for the Slater integrals can be obtained from atomic Hartree–Fock calculations [13–14]such as Cowan's RCN [30]. Note that Hartree–Fock overestimates the Slater integrals slightly and for F_0 often much.[7]

The states listed above split in ligand fields; for an octahedral field one obtains the states

$$\begin{aligned}
^1S &\rightarrow^1 A_{1g} \\
^1D &\rightarrow^1 E_g \oplus {}^1T_{2g} \\
^1G &\rightarrow^1 A_{1g} \oplus {}^1E_g \oplus {}^1T_{1g} + {}^1T_{2g} \\
^3P &\rightarrow^3 T_{1g} \\
^3F &\rightarrow^3 A_{2g} \oplus {}^3T_{1g} \oplus {}^3T_{2g}
\end{aligned} \tag{3.37}$$

The term-diagrams in dependence of the crystal-field splitting can be shown in form of Tanabe-Sugano diagrams; all possible d^n depending

[7] Cf. [13, p.464] and references therein: "Appropriate scale range from about 0.7 to 0.8 for neutral atoms to about 0.9 or 0.95 for highly ionized atoms". The problem is that using configuration interaction (CI), only a limited number of CI can be included explicitly; trying to tackle this perturbatively is hampered by slow convergence [31–32]. This empirical correction has been justified quantitatively [33–34].

on an octahedral crystal-field splitting can be found in the book by Sugano, Tanabe and Kamimura [5]; for lower lower symmetries they can be found in the book by König and Kremer [35].

3.5 Configuration-interaction calculations

Configuration interaction (CI) is a post-Hartree–Fock linear variation method, which takes correlations into account. Usually, CI is used as an all-electron method and is thus computationally quite expensive. By contrast, the CI cluster calculations, used for calculating the X-ray absorption spectra in this thesis, are restricted to the valence electrons (d shell) plus the hybridizing/binding ligand oxygens (effectively 10 electrons) and the $2p$ core states involved in the XAS, which makes the calculations fast but no longer fully ab initio; but more to this later.

Hartree–Fock, on which CI is based, is a variational technique using antisymmetrized products one-electron wavefunctions to solve variationally a Schrödinger equation. The wavefunction $\psi(\boldsymbol{r}_1, \ldots, \boldsymbol{r}_N)$ is constructed from a Slater determinant of the one-electron wavefunctions $\phi_i(\boldsymbol{r})$ as follows

$$\phi(\boldsymbol{r}_1, \ldots, \boldsymbol{r}_N) = \begin{vmatrix} \phi_1(\boldsymbol{r}_1) & \cdots & \phi_1(\boldsymbol{r}_N) \\ \vdots & \ddots & \vdots \\ \phi_N(\boldsymbol{r}_1) & \cdots & \phi_N(\boldsymbol{r}_N) \end{vmatrix}. \tag{3.38}$$

The Hartree–Fock Hamiltonian for N electrons and nuclei indexed by α is given by

$$H = \sum_{i=1}^{N} \left[-\frac{1}{2}\nabla_i^2 - \sum_{\alpha} \frac{Z_\alpha}{r_{i\alpha}} \right] + \sum_{\substack{j=1 \\ j<i}} [2J_j(r_i) - K_j(i)], \tag{3.39}$$

where the first term is the kinetic energy and the potential produced by the nuclei (often called external potential); the second term J is the Coulomb operator and the third one, K, the exchange operator. The last two form together the Fock operator. It is

$$\begin{aligned} J_j(\boldsymbol{r})\psi(\boldsymbol{r}) &= \psi(\boldsymbol{r}) \int |\phi_j(\boldsymbol{r}')|^2 \frac{1}{|\boldsymbol{r}' - \boldsymbol{r}|} \, \mathrm{d}^3 r' \\ K_j(\boldsymbol{r}_i)\psi(\boldsymbol{r}) &= \phi_j(\boldsymbol{r}) \int \frac{\phi_j^*(r')\psi(r')}{|\boldsymbol{r}' - \boldsymbol{r}|} \, \mathrm{d}^3 r'. \end{aligned} \tag{3.40}$$

According to the Rayleigh–Ritz principle, the true energy E_0 of a system described by a Hamiltonian H is always lower than (or equally low as) the expection value of $\langle\Psi|H|\Psi\rangle$ where Ψ is an arbitrary normalized wave function; this principle is used in Hartree–Fock calculations (as in the density-functional calculations). The equation Eq. (3.39) equation is solved iteratively (self-consistent field method).

The advantage of Hartree–Fock is that it is self-interaction free (the term is present in both J and $-K$ can cancels thus; this is a problem of many DFT functionals), it is also systematically improvable. On the negative side is the relative big computational demand (compared with e.g. LDA calculations) and that correlation effects are neglected; to cure the latter issue, post-Hartree–Fock techniques such as Møller-Plesset (MP) perturbation theory, multi-configurational self-consistent field, configuration interaction have been derived. (Another alternative is density-functional theory using LDA, GGA, meta-GGA, or hybrid functionals.)

In the configuration interaction method [36]excited Slater configurations are included as well. Hartree–Fock already yields, by construction, the best single Slater-determinant wavefunction, thus one needs to go to multi-determinant trial functions to improve the result. In the following, S denotes singly, D doubly, and T triply excited determinants, measured relative to the HF configuration. The CI wavefunction can be then written as

$$\Psi_{\mathrm{CI}} = a_0\Phi_{\mathrm{SCF}} + \sum_S a_S\Phi_S + \sum_D a_D\Phi_D + \sum_T a_T\Phi_T \cdots = \sum_i a_i\Phi_i, \tag{3.41}$$

where Φ_{SCF} is the best Hartree–Fock (single-determinant) wavefunction. The CI wavefunction has to be minimized under the constraint that the wavefunction remains normalized. (See, e.g., Ref. 36 for more on quantum chemistry methods including CI, MP, truncated CI, direct CI, etc.)

3.6 Configuration-interaction cluster calculation

For calculating x-ray absorption spectra at transition-metal L edges, it suffices to take only few electrons into account, namely the valence d electrons and the $2p$ electrons. For the details of the spectra the

multiplet structure plays a major role whereas the exact absolute energy of the spectrum is of lesser interest. (At least for calculations, experimentally the relative energy position can be used to the determine the valence and is thus of importance.) Therefore, the idea is to describe the d (and $2p$) electrons well using multi-Slater determinants, but approximate the rest of the ion by an effective potential.

The input file in the CI cluster calculation program thus consists of

- the (ionic) crystal-field potential, i.e. the coefficients of the expansion in spherical harmonics,
- a similar term for the hybridization with the ligand oxygens (see Appendix B), also expanded in spherical harmonics,
- the Slater parameters F^2 and F^4 to describe the d electrons and the F^2, G^1 and G^2 parameters describing the $2p$ electrons of created the core hole,
- the spin-orbit coupling parameter ξ (also written als ζ) for the d and for the $2p$ states,
- the charge-transfer energy Δ, and
- the on-site Coulomb U for the d orbitals and for d–$2p$.

The Slater parameters and the spin-orbit coupling can be obtained from Hartree–Fock calculations (here, the RCN by Cowan has been used [30]); the Slater parameters have typically reduced to 80% as the calculated value is too large [13, p.464]. The hybridization values are based on Harrison's rule following the description by Slater and Koster (see Appendix B), and the ionic crystal-field has been obtained from either constrained LDA+U calculations or from the center-of-gravity of the partial density of states.

When calculated with hybridization, several configurations[8] have to be taken into account:

$$\Psi = \alpha_n |d^n\rangle + \alpha_{n+1} |d^{n+1}\underline{L}\rangle + \alpha_{n+2} |d^{n+2}\underline{L}^2\rangle + \cdots, \tag{3.42}$$

[8] One should not confuse "configuration" here. In configuration interaction one uses a linear combination of configuration-state functions (CSF), whereas with respect to hybridization one talks about the electron configuration. The CI cluster calculations always use many CSF, but for ionic calculations only one electronic configuration.

where $\underline{L}$ denotes a ligand whole and $\sum_i \alpha_i^2 = 1$.

3.7 References

[1] H. Bethe, *Termaufspaltung in Kristallen*, Annalen der Physik **395**, 133 (1929). DOI: 10.1002/andp.19293950202. .

[2] J. H. V. Vleck, *Quantum mechanics-the key to understanding magnetism*, Review of Modern Physics **50**, 181 (1978). DOI: 10.1103/RevModPhys.50.181.

[3] H. L. Schläfer and G. Gliemann, *Basic principles of ligand field theory*. (Wiley, London, 1969).

[4] C. J. Ballhausen, *Introduction to Ligand Field Theory*. (McGraw-Hill, New York, 1962).

[5] S. Sugano, Y. Tanabe, and H. Kamimura, *Multiplets of transition-metal ions in crystals*. (Academic Press, New York, 1970).

[6] J. S. Griffith, *The theory of transition-metal ions*. (Cambridge University Press, Cambridge, 1971).

[7] B. N. Figgis and M. A. Hitchman, *Ligand Field Theory and Its Applications*. (Wiley-VCH, New York, 2000). ISBN: 9780471317760.

[8] M. Gerloch and R. C. Slade, *Ligand-field parameters*. (Cambridge Univ. Press, London, 1973). ISBN: 0521201373.

[9] A. Abragam and B. Bleaney, *Electron paramagnetic resonance of transition ions*. (Clarendon, Oxford, 1970a). ISBN: 0198512503.

[10] P. Atkins and J. de Paula, *Atkins' Physical Chemistry*. (Oxford University Press, Oxford, 2006).

[11] M. El-Batanouny and F. Wooten, *Symmetry and Condensed Matter Physics*. (Cambridge University Press, Cambridge, 2008).

[12] P. W. M. Jacobs, *Group Theory with Applications in Chemical Physics*. (Cambridge University Press, Cambridge, 2005). ISBN: 0521642507.

[13] R. D. Cowan, *The theory of atomic structure and spectra*. (University of California, Berkeley, 1981).

[14] J. C. Slater, *Quantum Theory of Atomic Structure*. (McGraw-Hill, New York, 1960).

[15] G. Czycholl, *Theoretische Festkörperphysik*. (Springer, Berlin, 2008). ISBN: 9783540747895. doi:10.1007/978-3-540-74790-1. See also the script by Müller-Hartmann, *Theoretische Festkörperphysik*, http://www.thp.uni-koeln.de/thphysik/fkp2.ps.gz.

[16] B. Bransden and C. Joachain, *Physics of atoms and molecules*. (Prentice, New York, 2003). ISBN: 058235692X.

[17] H. Eyring, J. Walter, and G. E. Kimball, *Quantum Chemistry*. (Wiley, London, 1938).

[18] J. A. Gaunt, *The triplets of helium*, Philosophical Transactions of the Royal Society of London, Series A **228**, 151 (1929). DOI: 10.1098/rsta.1929.0004.

[19] R. S. Mulliken, *Electronic structures of polyatomic molecules and valence. vi. on the method of molecular orbitals*, The Journal of Chemical Physics **3**, 375 (1935a). DOI: 10.1063/1.1749683.

[20] R. S. Mulliken, *Electronic structures of polyatomic molecules. vii. ammonia and water type molecules and their derivatives*, The Journal of Chemical Physics **3**, 506 (1935b). DOI: 10.1063/1.1749715.

[21] R. S. Mulliken, *Electronic structures of polyatomic molecules. ix. methane, ethane, ethylene, acetylene*, The Journal of Chemical Physics **3**, 517 (1935c). DOI: 10.1063/1.1749717.

[22] R. S. Mulliken, *Electronic structures of molecules xii. electroaffinity and molecular orbitals, polyatomic applications*, The Journal of Chemical Physics **3**, 386 (1935d). DOI: 10.1063/1.1749732.

[23] H. Bethe, *Zur Theorie des Zeemaneffektes an den Salzen der seltenen Erden*, Zeitschrift für Physik **60**, 218 (1930). DOI: 10.1007/BF01339827.

[24] M. W. Haverkort, Ph.D. thesis, Universität zu Köln, (2005). arXiv:cond-mat/0505214

[25] J. L. M. Gerloch, G. G. Phillips, and P. N. Quested, *Magnetic properties of trigonally distorted octahedral iron(ii) complexes*, Journal of the Chemical Society A **1970**, 1941 (1970). DOI: 10.1039/J19700001941.

[26] G. Racah, *Theory of complex spectra. ii*, Physical Review **62**, 438 (1942). DOI: 10.1103/PhysRev.62.438.

[27] G. Racah, *Theory of complex spectra. iii*, Physical Review **63**, 367 (1943). DOI: 10.1103/PhysRev.63.367.

[28] J. C. Slater, *The theory of complex spectra*, Physical Review **34**, 1293 (1929). DOI: 10.1103/PhysRev.34.1293.

[29] G. H. Shortley, *The theory of complex spectra*, Physical Review **40**, 185 (1932). DOI: 10.1103/PhysRev.40.185.

[30] Cowan's [13]RCN program can be obtained from ftp://aphysics.lanl.gov/pub/cowan/. For the documentation see http://www.ucd.ie/speclab/Cowandocs/ and http://www-troja.fjfi.cvut.cz/~ladi/ncowan/cowread.html.

[31] J. C. Morrison and K. Rajnak, *Many-body calculations for the heavy atoms*, Physical Review A **4**, 536 (1971). DOI: 10.1103/PhysRevA.4.536.

[32] J. C. Morrison, *Effect of core polarization upon the $f - f$ interactions of rare-earth and actinide ions*, Physical Review A **6**, 643 (1972). DOI: 10.1103/PhysRevA.6.643.

[33] K. Rajnak and B. G. Wybourne, *Configuration interaction effects in ln configurations*, Physical Review **132**, 280 (1963). DOI: 10.1103/PhysRev.132.280.

[34] B. G. Wybourne, *Generalization of the "Linear Theory" of configuration interaction*, Physical Review **137**, A364 (1965). DOI: 10.1103/PhysRev.137.A364.

[35] E. König and S. Kremer, *Ligand field energy diagrams*. (Plenum Press, New York, 1977). ISBN: 0306309467.

[36] F. Jensen, *Introduction to Computational Chemistry*. (Wiley, Chichester, 1999). ISBN: 047198425.

4 Valence, spin, and orbital state of Co ions in one-dimensional $Ca_3Co_2O_6$

Results published as: Tobias Burnus, Zhiwei Hu, Maurits W. Haverkort, Júlio C. Cezar, Delphine Flahaut, Vincent Hardy, Antoine Maignan, Nicholas B. Brookes, Arata Tanaka, Hui-Huang Hsieh, Hong-Ji Lin, Chien-Te Chen, and L. Hao Tjeng Physical Review B **74**, 245111 (2006).
DOI: 10.1103/PhysRevB.74.245111 OAI: arXiv:cond-mat/0611545

THE one-dimensional $Ca_3Co_2O_6$ has attracted great interest in recent years due to the observation of the stair-step jumps in the magnetization at regular intervals of the applied magnetic field [1–9]. The rhombohedral structure of this compound consists of $[Co_2O_6]_\infty$ chains running along the c axis of the hexagonal unit cell [10]. In each chain, CoO_6 octahedra alternate with CoO_6 trigonal prisms. The magnetism is Ising-like and directed along the Co chains with large magnetic moments of $4.8\mu_B$ per formula unit [11–12]. The intra-chain coupling is ferromagnetic with a spin-freeze at $T_{SF} = 7$ K and the chains couple antiferromagneticly with a Néel temperature of $T_N = 25$K [11].

Based on density-functional-theory calculations, Vidya *et al.* claimed a low-spin (LS) Co^{4+}_{oct} and a high-spin (HS) Co^{2+}_{trig} state for $Ca_3Co_2O_6$ [13]. However, other experimental and theoretical works have proposed a Co^{3+} valence state at both the octahedral and trigonal Co sites, with the Co_{oct} LS ($S = 0$) and the Co_{trig} HS ($S = 2$) state [14–18]. The Ising character of the magnetism is also subject of discussion. Dai and Whangbo *et al.* found from their band structure calculations that the spin-orbit-inactive d_0 orbital lies lowest of all Co_{trig} crystal-field levels [17, 19], and had to invoke excited states in their attempt to explain the Ising magnetism. Wu *et al.* [18], on the other hand, calculated that it is the spin-orbit-active d_2 orbital which lies lowest, giving a very different picture for the Ising magnetism.

In this chapter we have applied soft-x-ray absorption spectroscopy (XAS) and magnetic circular dichroism (XMCD) at the Co-$L_{2,3}$ edges to resolve the Co valence, spin and orbital state issue in $Ca_3Co_2O_6$. We have also carried out detailed configuration-interaction cluster

calculations to analyze the spectra. We found that the Co ions are all in the 3+ state, that the Co_{oct} are non-magnetic, and that the Co^{3+}_{trig} carry a $1.7\mu_B$ orbital moment. We clarify the orbital occupation issue and the origin of the Ising magnetism.

The $Ca_3Co_2O_6$ single crystals were grown by heating a mixture of $Ca_3Co_4O_9$ and K_2CO_3 in a weight ratio of 1:7 at 950 °C for 50 h in an alumina crucible in air. The cooling was performed in two steps, first down to 930 °C at a rate of 10 °C/h and then down to room temperature at 100 °C/h [8]. The Co-$L_{2,3}$ XAS spectra of $Ca_3Co_2O_6$ and of CoO and $EuCoO_3$ (Ref. 20) as references were recorded at the Dragon beamline of the National Synchrotron Radiation Research Center (NSRRC) in Taiwan with an energy resolution of 0.3 eV. The first sharp peak at 777 eV of photon energy at the Co-L_3 edge of CoO was used for energy calibration, which enabled us to achieve better than 0.05 eV accuracy in the relative energy alignment. The XMCD spectra were collected at the ID08 beamline of the European Synchrotron Radiation Facility (ESRF) in Grenoble with a resolution of 0.25 eV and a degree of circular polarization close to 100% in a magnetic field of 5.5 Tesla with the sample kept at approximately 15–20 K, using a dedicated superconducting magnet setup from Oxford Instruments. The Poynting vector of the photons and the magnetic field were both parallel to the c axis. The single-domain $Ca_3Co_2O_6$ crystal used for the XMCD experiment was needle-shaped with a dimension of $0.2 \times 0.2 \times 10$ mm^3 for $a \times b \times c$. Clean sample areas were obtained by cleaving the crystals *in situ* in chambers with base pressures in the low 10^{-10} mbar range. The Co $L_{2,3}$ spectra were recorded using the total-electron-yield method (TEY).

Figure 4.1 shows the Co-$L_{2,3}$ XAS spectrum of $Ca_3Co_2O_6$ together with that of CoO and $EuCoO_3$. CoO serves here as a 2+ reference and $EuCoO_3$ as a LS 3+ reference [20]. One can see first of all that the 2+ spectrum (CoO) contains peaks which are 2 or more eV lower in energy than the main peak of the 3+ spectrum ($EuCoO_3$). It is well known that x-ray absorption spectra at the transition-metal $L_{2,3}$ edges are highly sensitive to the valence state. An increase of the valence of the metal ion by one results in a shift of the $L_{2,3}$ XAS spectra to higher energies by 1 eV or more [21]. This shift is due to a final state effect in the x-ray absorption process. The energy difference between a $3d^n$ ($3d^7$ for Co^{2+}) and a $3d^{n-1}$ ($3d^6$ for Co^{3+}) configuration is $\Delta E =$

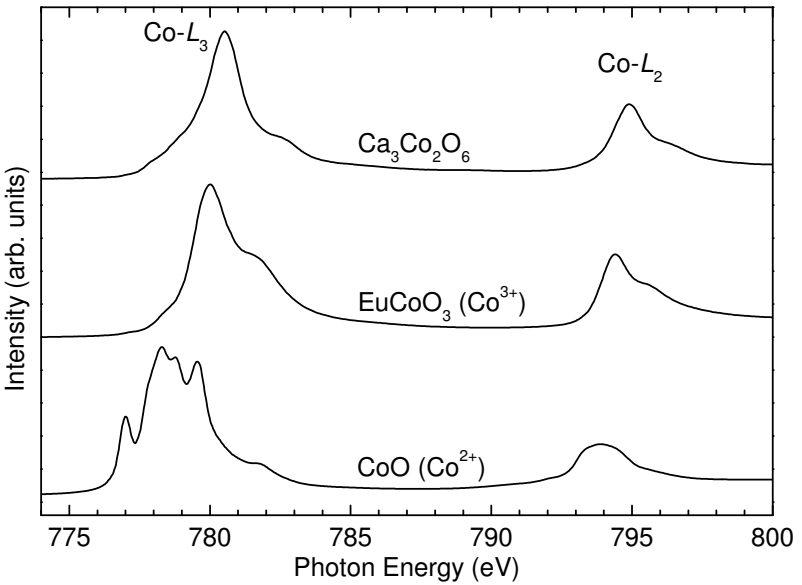

Fig. 4.1 Co-$L_{2,3}$ XAS spectra of $Ca_3Co_2O_6$, CoO, and $EuCoO_3$.

$E(2p^6 3d^{n-1} \rightarrow 2p^5 3d^n) - E(2p^6 3d^n \rightarrow 2p^5 3d^{n+1}) \approx U_{pd} - U_{dd} \approx 1$–2 eV, where U_{dd} is the Coulomb repulsion energy between two $3d$ electrons and U_{pd} the one between a $3d$ electron and the $2p$ core hole.

One can observe from FIG. 4.1 that the $Ca_3Co_2O_6$ spectrum has no features at the low-energy side, which otherwise could have indicated the presence of Co^{2+} species like in CoO. Instead, the spectrum has a much closer resemblance to that of Co^{3+}, like in $EuCoO_3$. This means that one can safely rule out the Co^{2+}/Co^{4+} scenario [13]. In other words, the XAS experiment reveals unambiguously that both the Co_{oct} and the Co_{trig} ions are in the 3+ valence state. This result supports the analysis of the Co $2p$ core-level x-ray photoemission spectra [15]and band-structure calculations [16, 18].

In order to resolve the spin-state issue, we now resort to XMCD. The top part (a) of FIG. 4.2 depicts Co-$L_{2,3}$ XAS spectra taken with circularly polarized light with the photon spin parallel (solid line, μ^+) and antiparallel (dashed line, μ^-) aligned to the magnetic field. The quantization axis z has been chosen to be parallel to the c axis, which

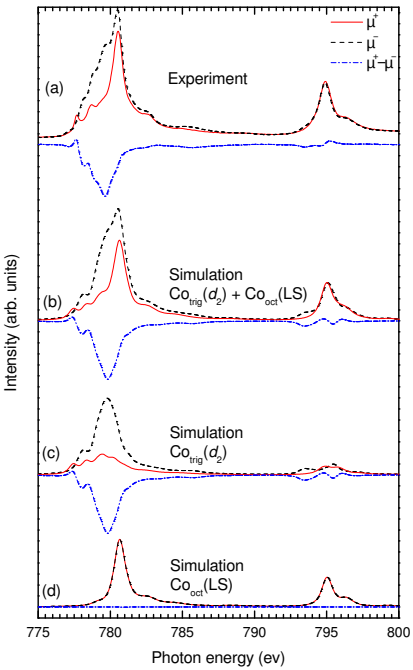

Fig. 4.2 (color online) (a) Measured soft-x-ray absorption spectra with parallel (μ^+, solid line) and antiparallel (μ^-, dashed line) alignment between photon spin and magnetic field, together with the difference spectrum ($\mu^+ - \mu^-$, dash-dotted); (b) Simulated sum spectra assuming a doubly occupied d_2 orbital for the Co_{trig} and low-spin (LS) Co_{oct} ions; (c) and (d) Contribution of the Co_{trig} and Co_{oct} ions to the simulated sum spectra.

is the easy magnetization axis [3]. One can clearly observe large differences between the spectra using these two alignments. The difference spectrum, i.e. the XMCD spectrum, is also shown (dash-dotted line, $\mu^+ - \mu^-$). Using the well-known XMCD sum rule developed by Thole *et al.* [22],

$$L_z = \frac{4}{3}\frac{\int[\mu^+(E) - \mu^-(E)]\,\mathrm{d}E}{\int[\mu^+(E) + \mu^-(E)]\,\mathrm{d}E}(10 - N_e), \tag{4.1}$$

where N_e is the number of the Co d electrons, we can extract directly the orbital (L_z) contribution to the magnetic moment without the need to do detailed modeling. Assuming an average Co $3d$ occupation number of about $N_e = 6.5$ electrons (estimated for a HS Co^{3+} oxide [23] and also to be justified below by cluster calculations) we find a value of $1.2\mu_B$ for the L_z, which is a very large number indicating that the ground state is strongly spin-orbit active.

To extract more detailed information concerning the spin and orbital states from the Co $L_{2,3}$ XAS spectra, we have carried out simulations for the XMCD spectra using the well-proved configuration-interaction (CI) cluster model [24–26]. The method uses for each Co site a CoO_6 cluster which includes the full atomic multiplet theory and the local effects of the solid. It accounts for the intra-atomic $3d$–$3d$ and $2p$–$3d$ Coulomb interactions, the atomic $2p$ and $3d$ spin-orbit couplings, the O $2p$–Co $3d$ hybridization, and the proper local crystal-field parameters. In the configuration-interaction cluster calculation we describe the ground state by the configurations

$$\Psi = \alpha_6|d^6\rangle + \alpha_7|d^7\underline{L}\rangle + \alpha_8|d^8\underline{L}^2\rangle + \alpha_9|d^9\underline{L}^3\rangle, \tag{4.2}$$

where $\underline{L}$ denotes a ligand hole and $\sum_{i=6}^{9}\alpha_i^2 = 1$ [27–28]. The transition-metal electron occupation is then given by

$$N_e = 6\alpha_6^2 + 7\alpha_7^2 + 8\alpha_8^2 + 9\alpha_9^2. \tag{4.3}$$

The simulations have been carried out using the program XTLS 8.3 [24].

In octahedral symmetry the $3d$ orbitals split up in the well-known e_g and t_{2g} levels; the splitting is given by $10Dq$. In a trigonal prismatic environment, however, it is found that the $x^2 - y^2$ is degenerate with the xy, and the yz with zx orbital [17–18]. In the presence of the spin-orbit coupling, it is then better to use the complex orbitals d_0, d_2/d_{-2}, and d_1/d_{-1}. Band structure calculations indicate that the d_1/d_{-1} band is split off from the d_0 and d_2/d_{-2} bands by about 1 eV, while the d_0 and d_2/d_{-2} bands are almost degenerate [17–18]. Critical for the magnetism and for the line shape of the simulated spectra are the crystal field parameter $10Dq$ for the $Co_{oct}O_6$ cluster and the crystal field parameter for the splitting between the nearly degenerate d_0 and d_2 orbitals of the $Co_{trig}O_6$ cluster. $10Dq$ needs to be critically

tuned since this is set to determine whether Co_{oct}–O_6 cluster is in the LS or HS state [29]. The trigonal prism crystal field has also to be fine tuned since it determines whether the d_2 or the d_0 lies lowest, and thus the magnitude of the orbital moment and strength of the magnetocrystalline anisotropy as we will show below. Tuning of these parameters will be done by establishing which of the simulated spectra reproduce the experimentally observed ones.

As a starting point, we make the assumption that the Co_{oct} ion is in the LS state, based on the observation that the average Co_{oct}-O bond length of 1.916 Å in this material [10] is shorter than the 1.925 Å in $LaCoO_3$ at 5 K, which is known to be LS [30]. With such a short length, the Co ion is subjected to a large enough $10Dq$, sufficient to stabilize the non-magnetic LS state [29–30] for Co^{3+}_{oct} ions in $Ca_3Co_2O_6$. With this starting point, the magnetism and the XMCD signal have to originate from the Co_{trig} ions. This is quite plausible since with the extremely large Co_{trig}–O average bond length of 2.062 Å[10], which is much larger than 1.961 Å for $LaCoO_3$ at 1000 K [30], one can expect that the crystal field is small enough to stabilize the HS state [29]. Based on the observation that the orbital contribution to the magnetic moment is extremely large, we take the d_2 *ansatz* for the Co_{trig} and not the d_0. In the CI calculation, the parameters for the multipole part of the Coulomb interactions were given by the Hartree-Fock values, while the monopole parts (U_{dd}, U_{pd}) were estimated from photoemission experiments on Co^{3+} materials [31]. The one-electron parameters such as the O $2p$–Co $3d$ charge-transfer energies and integrals were estimated from band-structure results [17–19]. The charge-transfer energy is given by $\Delta = E(d^6) - E(d^7\underline{L}) = 1.5$ eV, the d–d Coulomb repulsion by $U_{dd} = 5.5$ eV and of p–d of the excited Co by $U_{\underline{p}d} = 7.0$ eV; the Slater integrals have been reduced to 80% of their Hartree-Fock value. An exchange field of $H_{ex} = 3$ meV has been used. For the Co_{trig} ions the ionic crystal splittings are $\Delta E^{ionic}_{d_1/d_2} = 0.9$ eV and $\Delta E^{ionic}_{d_0/d_2} = 0.05$ eV taken from band-structure calculation [18]; the hybridization is $V^{hyb}_{d_1} = 1.88$ eV, $V^{hyb}_{d_0} = 1.28$ eV, and $V^{hyb}_{d_2} = 1.25$ eV. For Co_{oct} ions $pd\sigma = -1.44$ eV and $pd\pi = 0.63$ eV was used. With this set of parameters we have found a LS–HS transition for Co_{oct} at $10Dq = 0.65$ eV. Here we used $10Dq = 0.8$ eV, based on band-structure calculation, which is the same value as for $EuCoO_3$ known as a LS Co^{3+} oxide [20].

The results of these simulations are given by curves (b) in FIG. 4.2, together with a break-down into the separate contributions of the Co_{trig} (curves c) and Co_{oct} (curves d) ions. One can clearly observe that the simulations (curves b) reproduce the experimental spectra quite well. All major and minor peaks in the individual experimental XAS (μ^+, μ^-) and XMCD ($\mu^+ - \mu^-$) spectra (curves a) are present in the simulations (curves b). It is almost needless to remark that the entire simulated XMCD signal is coming from the HS Co_{trig} ions (curves c), since we started with a nonmagnetic LS Co_{oct} (curves d). In the simulation, we find $S_z = 1.8\mu_B$ and $L_z = 1.7\mu_B$, giving a total magnetic moment of $2S_z + L_z = 5.3\mu_B$ per formula unit. Due to strong hybridization between Co $3d$ and O $2p$, the $3d$ occupation numbers of the Co_{trig} ions and the Co_{oct} are 6.3 and 6.8, respectively, giving on average 6.5 electrons as used for the sum rules. The calculated total moment from the simulation compares reasonably well with the $4.8\mu_B$ value from direct magnetization measurements [6, 12]. Yet, the simulated L_z value ($1.7\mu_B$) is appreciably larger than the one derived from the experiment using the XMCD sum rule ($1.2\mu_B$). However, looking more closely at the simulated and experimental XMCD spectra, we can clearly see that the XMCD spectra have very similar line shapes and that the distinction is mainly in the amplitude, i.e. a matter of scaling. This indicates that the discrepancy in the L_z determination might be caused by the fact that the sample is not fully magnetized in our experiment. According to magnetization measurements one can only achieve 90% of the saturation magnetization at 5.5 T [12]. In addition, slight misalignment of the sample together with the high magnetocrystalline anisotropy may account for some further reduction of the experimental value.

Having established that the d_2/LS scenario for the Co_{trig}/Co_{oct} ions explains well the experimental spectra, we now investigate the sensitivity of our analysis. For this we change the *ansatz* for the Co_{trig} ion: we now put the d_0 orbital to be energetically lower than the d_2 [32]. The result is shown in FIG. 4.3, in which the simulated XMCD spectrum (b) is compared with the experimental one (a). One can unambiguously recognize large discrepancies in the line shapes, not only in the L_3 region (777–785 eV), where the simulated XMCD signal has much less amplitude, but also in the L_2 (792–797 eV), where now an XMCD signal is calculated while it is practically absent in

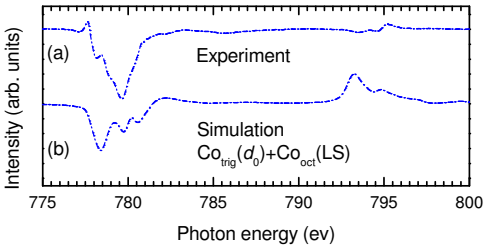

Fig. 4.3 (color online) (a) Measured soft-x-ray magnetic circular dichroism spectrum (XMCD, $\mu^+ - \mu^-$); (b) Simulated XMCD spectrum assuming a doubly occupied d_0 orbital for the Co_{trig} and low-spin (LS) Co_{oct} ions.

the experiment. Using the XMCD sum rule [22], we can relate these discrepancies also directly to the fact that the d_0 *ansatz* essentially does not carry an orbital moment.

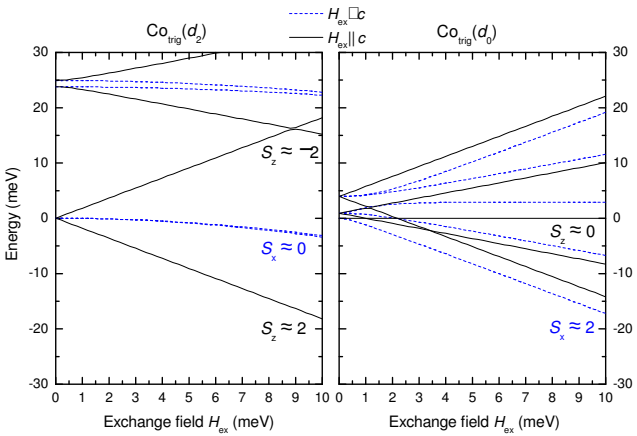

Fig. 4.4 (color online) Total-energy level diagram for the Co_{trig} ion as a function of the exchange field H_{ex} along the z direction (c axis, solid lines) and along the x direction (perpendicular to the c axis, dashed lines), with (left panel) the d_2 and (right panel) the d_0 orbital doubly occupied.

The success of the cluster method for the analysis of both the high-energy spectroscopies and the ground-state magnetic moments provides confidence for its use to investigate the magnetocrystalline anisotropy in this material. We have calculated the total energy of the $Co_{trig}O_6$

cluster as a function of the exchange field H_{ex}, directed either along the z axis (the c axis or the one-dimensional chain) or along the x axis (perpendicular to the c axis). The results for the d_2 *ansatz* are plotted in the left panel of FIG. 4.4. It is evident that the lowest state gains energy when H_{ex} is along z and very little to nothing for H_{ex} along x. This demonstrates directly that the magnetocrystalline anisotropy should be large and directed along the z, consistent with the experimental observation that the magnetization parallel to c is almost sixfold of the one perpendicular c (at 12 K and 5.5 T) [3] and with the Ising nature of the magnetism. We note that the lowest curve in the figure shows an energy gain with a rate twice that of H_{ex} (along z), meaning that S_z is close to $2\mu_B$ which in turn is consistent with the HS ($S = 2$) nature of the $\mathrm{Co_{trig}}$ ion.

We have also analyzed the magnetocrystalline anisotropy of the $\mathrm{Co_{trig}O_6}$ cluster using the d_0 *ansatz*. The right panel of FIG. 4.4 reveals that the total energy decreases for both directions of H_{ex}, but now with the important distinction that the energy for H_{ex} along x is always lower than for H_{ex} along z. This implies that the easy-magnetization axis should be perpendicular to the z axis, which is not consistent with the experimental facts. Also this contradiction thus effectively falsifies the d_0 *ansatz* [17, 19].

To conclude, using soft x-ray absorption spectroscopy and the magnetic circular dichroism therein at the Co-$L_{2,3}$ edges we have experimentally determined that both Co ions in $\mathrm{Ca_3Co_2O_6}$ are 3+, with the $\mathrm{Co_{trig}}$ ion in the high-spin state and the $\mathrm{Co_{oct}}$ in the nonmagnetic state. The $\mathrm{Co_{trig}}$ ion carries an anomalously large orbital moment of $1.7\mu_B$ which we have been able to relate to the double occupation of the d_2 orbital. In addition, the detailed analysis of the spectral line shapes together with that of the magnetocrystalline anisotropy firmly establishes that the d_2 orbital lies lowest in energy [18] and not the d_0 [17, 19]This in turn also demonstrates that a proper incorporation of the spin-orbit interaction is required for the *ab-initio* calculation of the delicate electronic structure of this material.

1 References

[1] S. Aasland, H. Fjellvåg, and B. Hauback, *Magnetic properties of the one-dimensional $Ca_3Co_2O_6$*, Solid State Communications **101**, 187 (1997). DOI: 10.1016/S0038-1098(96)00531-5.

[2] H. Kageyama, K. Yoshimura, K. Kosuge, H. Mitamura, and T. Goto, *Field-Induced Magnetic Transitions in the One-Dimensional Compound $Ca_3Co_2O_6$*, Journal of the Physical Society of Japan **66**, 1607 (1997a). DOI: 10.1143/JPSJ.66 .1607.

[3] H. Kageyama, K. Yoshimura, K. Kosuge, M. Azuma, M. Takano, H. Mitamura, and T. Goto, *Magnetic Anisotropy of Ca 3Co 2O 6 with Ferromagnetic Ising Chains*, Journal of the Physical Society of Japan **66**, 3996 (1997b). DOI: 10.1143 /JPSJ.66.3996.

[4] A. Maignan, C. Michel, A. C. Masset, C. Martin, and B. Raveau, *Single crystal study of the one dimensional $Ca_3Co_2O_6$ compound: five stable configurations for the Ising triangular lattice*, Eur. Phys. J. B **15**, 657 (2000). DOI: 10.1007/PL00011051.

[5] Y. B. Kudasov, *Steplike Magnetization in a Spin-Chain System: $Ca_3Co_2O_6$*, Physical Review Letters **96**, 027212 (2006). DOI: 10.1103/PhysRevLett.96.027212.

[6] V. Hardy, M. R. Lees, O. A. Petrenko, D. M. Paul, D. Flahaut, S. Hebert, and A. Maignan, *Temperature and time dependence of the field-driven magnetization steps in $Ca_3Co_2O_6$ single crystals*, Physical Review B **70**, 064424 (2004a). DOI: 10.1103 /PhysRevB.70.064424.

[7] D. Flahaut, A. Maignan, S. Hébert, C. Martin, R. Retoux, and V. Hardy, *Chromium site selective substitution in $Ca_3Co_2O_6$: Influence on the magnetic properties of an Ising-like triangular lattice*, Physical Review B **70**, 094418 (2004). DOI: 10.1103 /PhysRevB.70.094418.

[8] V. Hardy, D. Flahaut, M. R. Lees, and O. A. Petrenko, *Magnetic quantum tunneling in $Ca_3Co_2O_6$ studied by ac susceptibility: Temperature and magnetic-field dependence of the spin-relaxation time*, Physical Review B **70**, 214439 (2004b). DOI: 10.1103/PhysRevB.70.214439.

[9] O. Petrenko, J. Wooldridge, M. Lees, P. Manuel, and V. Hardy, *Single crystal neutron diffraction study of the magnetisation process in $Ca_3Co_2O_6$*, Eur. Phys. J. B **47**, 79 (2005). DOI: 10 .1140/epjb/e2005-00308-y.

[10] H. Fjellvåg, E. Gulbrandsen, S. Aasland, A. Olsen, and B. C. Hauback, *Crystal Structure and Possible Charge Ordering in One-Dimensional $Ca_3Co_2O_6$*, J. Solid State Chem. **124**, 190 (1996). DOI: 10.1006/jssc.1996.0224.

[11] V. Hardy, S. Lambert, M. R. Lees, and D. M. Paul, *Specific heat and magnetization study on single crystals of the frustrated quasi-one-dimensional oxide Ca_3Co_2O*, Physical Review B **68**, 014424 (2003). DOI: 10.1103/PhysRevB.68.014424.

[12] A. Maignan, V. Hardy, S. Hebert, M. Drillon, M. Lees, O. Petrenko, D. M. Paul, and D. Khomskii, *Quantum Tunneling of the Magnetization in the Ising Chain Compound $Ca_3Co_2O_6$*, J. Mater. Chem. **14**, 1231 (2004). DOI: 10.1039/b316717h.

[13] R. Vidya, P. Ravindran, H. Fjellvåg, A. Kjekshus, and O. Eriksson, *Tailor-Made Electronic and Magnetic Properties in One-Dimensional Pure and Y-Substituted $Ca_3Co_2O_6$*, Physical Review Letters **91**, 186404 (2003). DOI: 10.1103/PhysRevLett .91.186404.

[14] E. V. Sampathkumaran, N. Fujiwara, S. Rayaprol, P. K. Madhu, and Y. Uwatoko, *Magnetic behavior of Co ions in the exotic spin-chain compound $Ca_3Co_2O_6$ from ^{59}Co NMR studies*, Physical Review B **70**, 014437 (2004). DOI: 10.1103/PhysRevB.70 .014437.

[15] K. Takubo, T. Mizokawa, S. Hirata, J.-Y. Son, A. Fujimori, D. Topwal, D. D. Sarma, S. Rayaprol, and E.-V. Sampathkumaran, *Electronic structure of Ca_3CoXO_6 (X = Co, Rh, Ir) studied by x-ray photoemission spectroscopy*, Physical Review B **71**, 073406 (2005). DOI: 10.1103/PhysRevB.71.073406.

[16] V. Eyert, C. Laschinger, T. Kopp, and R. Frésard, *Extended moment formation and magnetic ordering in the trigonal chain compound $Ca_3Co_2O_6$*, Chem. Phys. Lett. **385**, 249 (2004). DOI: 10.1016/j.cplett.2003.12.105.

[17] M.-H. Whangbo, D. Dai, H.-J. Koo, and S. Jobic, *Investigations of the oxidation states and spin distributions in $Ca_3Co_2O_6$ and Ca_3CoRhO_6 by spin-polarized electronic band structure calculations*, Solid State Communications **125**, 413 (2003). DOI: 10 .1016/S0038-1098(02)00872-4.

[18] Hua Wu, M. W. Haverkort, Z. Hu, D. I. Khomskii, and L. H. Tjeng, *Nature of magnetism in $Ca_3Co_2O_6$*, Physical Review Letters **95**, 186401 (2005). DOI: 10.1103/PhysRevLett.95.186401.

[19] D. Dai and M.-H. Whangbo, *Analysis of the uniaxial magnetic properties of high-spin d^6 ions at trigonal prism and linear two-coordinate sites: Uniaxial magnetic properties of $Ca_3Co_2O_6$ and $Fe[C(SiMe_3)_3]_2$*, Inorg. Chem. **44**, 4407 (2005). DOI: 10.1021/ic050185g.

[20] Z. Hu, H. Wu, M. W. Haverkort, H. H. Hsieh, H.-J. Lin, T. Lorenz, J. Baier, A. Reichl, I. Bonn, C. Felser, A. Tanaka, C. T. Chen, and L. H. Tjeng, *Different look at the spin state of Co^{3+} ions in a CoO_5 pyramidal coordination*, Physical Review Letters **92**, 207402 (2004). DOI: 10.1103/PhysRevLett.92.207402.

[21] C. Mitra, Z. Hu, P. Raychaudhuri, S. Wirth, S. I. Csiszar, H. H. Hsieh, H.-J. Lin, C. T. Chen, and L. H. Tjeng, *Direct observation of electron doping in $La_{0.7}Ce_{0.3}MnO_3$ using x-ray absorption spectroscopy*, Physical Review B **67**, 092404 (2003). DOI: 10.1103/PhysRevB.67.092404.

[22] B. T. Thole, P. Carra, F. Sette, and G. van der Laan, *X-ray circular dichroism as a probe of orbital magnetization*, Physical Review Letters **68**, 1943 (1992). DOI: 10.1103/PhysRevLett.68.1943.

[23] T. Saitoh, T. Mizokawa, A. Fujimori, M. Abbate, Y. Takeda, and M. Takano, *Electronic structure and temperature-induced paramagnetism in $lacoo_3$*, Physical Review B **55**, 4257 (1997). DOI: 10.1103/PhysRevB.55.4257.

[24] A. Tanaka and T. Jo, *Resonant 3d, 3p and 3s photoemission in transition metal oxides predicted at 2p threshold*, Journal of the Physical Society of Japan **63**, 2788 (1994). DOI: 10.1143/JPSJ.63.2788.

[25] F. M. F. de Groot, *X-ray absorption and dichroism of transition metals and their compounds*, Journal of Electron Spectroscopy and Related Phenomena **67**, 529 (1994). DOI: 10.1016/0368-2048(93)02041-J.

[26] See the "Theo Thole Memorial Issue", Journal of Electron Spectroscopy and Related Phenomena **86**, 1 (1997). DOI: 10.1016/S0368-2048(97)00039-X.

[27] T. Saitoh, A. E. Bocquet, T. Mizokawa, and A. Fujimori, *Systematic variation of the electronic structure of* 3*d transition-metal compounds*, Physical Review B **52**, 7934 (1995). DOI: 10.1103/PhysRevB.52.7934.

[28] Z. Hu, C. Mazumdar, G. Kaindl, F. M. F. de Groot, S. A. Warda, and D. Reinen, *Valence electron distribution in* $La_2Li_{1/2}Cu_{1/2}O_4$, $Nd_2Li_{1/2}Ni_{1/2}O_4$, *and* $La_2Li_{1/2}Co_{1/2}O_4$, Chem. Phys. Lett. **297**, 321 (1998). DOI: 10.1016/S0009-2614(98)01135-X.

[29] J. B. Goodenough, in *Progress in Solid State Chemistry, Vol. 5*, edited by H. Reiss (Pergamon Press, Oxford), p. 145.

[30] P. G. Radaelli and S.-W. Cheong, *Structural phenomena associated with the spin-state transition in* $lacoo_3$, Physical Review B **66**, 094408 (2002). DOI: 10.1103/PhysRevB.66.094408.

[31] A. E. Bocquet, T. Mizokawa, K. Morikawa, A. Fujimori, S. R. Barman, K. Maiti, D. D. Sarma, Y. Tokura, and M. Onoda, *Electronic structure of early 3d-transition-metal oxides by analysis of the 2p core-level photoemission spectra*, Physical Review B **53**, 1161 (1996). DOI: 10.1103/PhysRevB.53.1161.

[32] $\Delta E^{\mathrm{total}}_{d_2/d_0} = 0.102\mathrm{eV}$ with an exchange field of $H_{\mathrm{ex}} = 3\mathrm{meV}$, $H_{\mathrm{ex}} || c$.

5 Local electronic structure and magnetic properties of $LaMn_{0.5}Co_{0.5}O_3$ studied by x-ray absorption and magnetic circular dichroism spectroscopy

Results published in: Tobias Burnus, Zhiwei Hu, Hui-Huang Hsieh, V. L. Joseph Joly, P. A. Joy, Maurits W. Haverkort, Hua Wu, Arata Tanaka, Hong-Ji Lin, Chien-Te Chen, and L. Hao Tjeng
Physical Review B **77**, 125124 (2008).
DOI: 10.1103/PhysRevB.77.125124 OAI: arXiv:0709.3243

THE manganites continue to attract considerable attention from the solid state physics and chemistry community over the last five decades because of their spectacular material properties [1–4]. The parent compound $LaMnO_3$ is an A-type antiferromagnetic insulator with orthorhombic perovskite crystal structure. Replacing La by Sr, Ca or Ba results in multifarious electronic and magnetic properties including the transformation into a ferromagnetic state accompanied by a metal-insulator transition and the occurrence of colossal magnetoresistance [5–6]. Substitution of the magnetic Mn ions by Co also yields ferromagnetism in the $LaMn_{1-x}Co_xO_3$ series. The Curie temperature reaches a maximum for $x = 0.5$ ($T_C = 220$–240 K) [7–11]. This should be contrasted with the end member of this series, namely the rhombohedral $LaCoO_3$, which is a nonmagnetic insulator at low temperatures, showing yet the well-known spin-state transition at higher temperatures which by itself is subject of five decades of intensive study [7, 9, 12].

Explaining the appearance of ferromagnetism in the manganites by Co substitution is, however, not a trivial issue. Assuming that ordering of the Co and Mn ions had not been achieved for the $x = 0.5$ composition, Goodenough *et al.* concluded early on that the ferromagnetism is generated by Mn^{3+}–O–Mn^{3+} superexchange interactions [7]. On the other hand, later magnetic susceptibility and Mn NMR studies suggested that it is the exchange interaction involving the ordering of

Co^{2+}–Mn^{4+} transition-metal ions which causes the ferromagnetism in $LaMn_{0.5}Co_{0.5}O_3$ [8–9, 13–17].

Only few high-energy spectroscopic studies are reported for the Co substituted manganites. Using soft-x-ray absorption spectroscopy (XAS), Park *et al.* found in their low Co compositions that the Co ions are divalent, favoring a Mn^{3+}–Mn^{4+} double-exchange mechanism for the ferromagnetism [18]. Extrapolating this Co divalent result to the $x = 0.5$ composition would provide support to the suggestion that the ferromagnetism therein is caused by the Co^{2+}–Mn^{4+} exchange interaction. However, no XAS data have been reported so far for this $x = 0.5$ composition. Using K-edge XAS, Toulemonde *et al.* revealed that the Co ion is also divalent in their hole doped and Co substituted manganite [19]. Yet, these results for the low Co limit have been questioned by van Elp, who claimed that the Co ions should be in the intermediate-spin trivalent state rather than in the high-spin divalent state [20].

Further discussion is also raised by the work of Joy and coworkers [21–22], who have synthesized two different single phases of $LaMn_{0.5}Co_{0.5}O_3$ and inferred from a combination of magnetic susceptibility and x-ray photoelectron spectroscopy measurements that the phase with the higher T_C contains high-spin Mn^{3+} and low-spin Co^{3+} ions, while the lower T_C phase has Co^{2+} and Mn^{4+}. Very recently, however, long-range charge ordering has been observed in neutron diffraction experiments by Bull *et al.* [23] and Troyanchuk *et al.* [24] on the high-T_C phase, pointing towards the Co^{2+}–Mn^{4+} scenario. Also, the most recent magnetic susceptibility and K-edge XAS data by Kyômen *et al.* favor the presence of essentially Co^{2+}–Mn^{4+} at low temperatures [25]. The issue of Mn/Co ordering including the possible coexistence of ordered and disordered regions remains one of the important topics [11, 26–27]. Interesting is that the magnetization of polycrystalline samples of $LaCo_{0.5}Mn_{0.5}O_3$ does not saturate in magnetic fields up to 7 T [16], and that there are indications for a large magnetic anisotropy [24].

On the theoretical side, not much work has been carried out so far. A relatively early band-structure study by Yang *et al.* on the $LaMn_{0.5}Co_{0.5}O_3$ system predicted a half-metallic behavior with a magnetic moment of $3.01\mu_B$ for Mn and $0.54\mu_B$ for Co ions, suggesting Mn^{3+}–Co^{3+} valence states [28]. This study, however, was performed

before the existence of the charge-ordered crystal structure was reported [23–24].

Here, we present our experimental study of the local electronic structure of $LaMn_{0.5}Co_{0.5}O_3$ both for the high- and low-T_C phases using the element-specific XAS and x-ray magnetic circular dichroism (XMCD) at the Co-$L_{2,3}$ and Mn-$L_{2,3}$ edges, i.e., transitions from the $2p$ core to the $3d$ valence orbitals. Our objective is not only to establish the valence and spin states of the Co and Mn ions but also to investigate the possible presence of an orbital moment associated with a Co^{2+} ion, in which case the material should have a large magnetocrystalline anisotropy and a nontrivial temperature dependence of its magnetic susceptibility.

In XAS and XMCD we make use of the fact that the Coulomb interaction of the $2p$ core hole with the $3d$ electrons is much larger than the $3d$ band width, so that the absorption process is strongly excitonic and therefore well understood in terms of atomiclike transitions to multiplet-split final states [29–31]. Unique to soft-x-ray absorption is that the dipole selection rules are very effective in determining which of the $2p^5 3d^{n+1}$ final states can be reached and with what intensity, starting from a particular $2p^6 3d^n$ initial state ($n = 7$ for Co^{2+}, $n = 6$ for Co^{3+}, $n = 4$ for Mn^{3+}, and $n = 3$ for Mn^{4+}). This makes the technique an extremely sensitive local probe, ideal to study the valence [32–33] and spin [12, 34–38] character as well as the orbital contribution to the magnetic moment [39–41] of the ground or initial state.

The two single-phase $LaMn_{0.5}Co_{0.5}O_3$ polycrystalline samples were synthesized as described previously [21–22, 42] and the single phase nature of the two phases (low-T_C phase and high-T_C phase) were confirmed by temperature dependent magnetization measurements. These measurements showed a single sharp magnetic transition at $T_C = 225$ K (called high-T_C phase) for the sample synthesized at 700 °C and a sharp transition at $T_C = 150$ K (called low-T_C phase) for the sample synthesized at 1300 °C. On the other hand, more than one magnetic transition or broad magnetic transitions were observed for samples synthesized at other temperatures indicating their mixed phase behavior, as described in Ref. 42. The magnetization at 5 K in a field of 5 T is 50.4 emu/g for the high-T_C phase and 42.4 emu/g for the low-T_C phase. The Co- and Mn-$L_{2,3}$ XAS and XMCD spectra were recorded at the Dragon beamline of the National Synchrotron Radiation Research

Center (NSRRC) in Taiwan with an energy resolution of 0.25 eV. The sharp peak at 777.8 eV of the Co-L_3 edge of single crystalline CoO and at 640 eV of the Mn-L_3 of single crystalline MnO were used for energy calibration. The isotropic XAS spectra were measured at room temperature, whereas the XMCD spectra at both the Co-$L_{2,3}$ and the Mn-$L_{2,3}$ edges were measured at 135 K in a 1 T magnetic field with approximately 80% circularly polarized light. The magnetic field makes an angle of 30° with respect to the Poynting vector of the soft x-rays. The spectra were recorded using the total electron yield method (by measuring the sample drain current) in a chamber with a base pressure of 2×10^{-10} mbar. Clean sample areas were obtained by cleaving the polycrystals *in situ*.

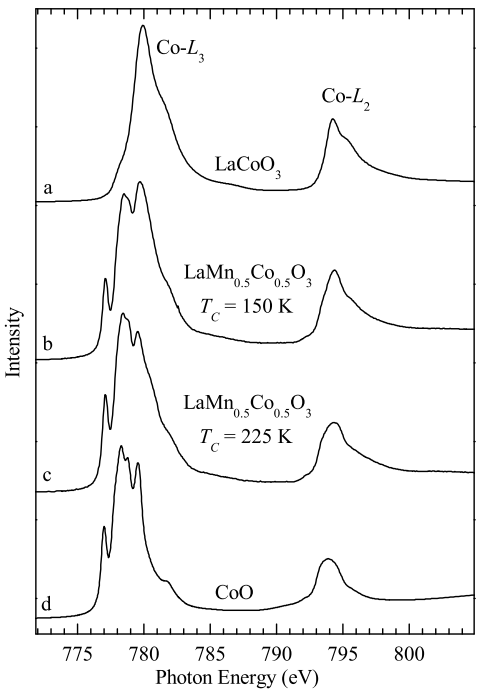

Fig. 5.1 Co-$L_{2,3}$ XAS spectra of (a) $LaCoO_3$ as a Co^{3+} reference, of the $LaMn_{0.5}Co_{0.5}O_3$ samples with (b) T_C = 150 K and (c) T_C = 225 K, and (d) of CoO as a Co^{2+} reference.

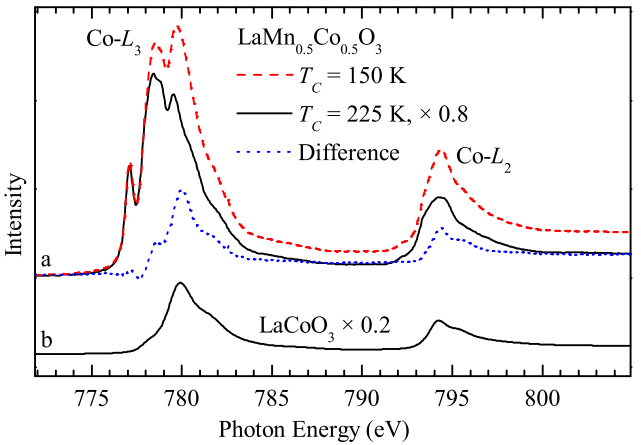

Fig. 5.2 (color online) Co-$L_{2,3}$ XAS spectra of (a) the $LaMn_{0.5}Co_{0.5}O_3$ samples with T_C = 225 K (solid curve) and T_C = 150 K (dashed curve), their difference (dotted curve), and (b) of $LaCoO_3$ as Co^{3+} reference.

Figure 5.1 shows the Co-$L_{2,3}$ XAS spectra of $LaMn_{0.5}Co_{0.5}O_3$ for both the high-T_C [curve (c)] and the low-T_C phase [curve (b)]. The spectra were taken at room temperature. For comparison, the spectrum of $LaCoO_3$ in the low-temperature nonmagnetic state [curve (a)] is included as a low-spin trivalent Co reference and also of CoO (curve d) as a divalent Co reference. The spectra are dominated by the Co $2p$ core-hole spin-orbit coupling which splits the spectrum roughly in two parts, namely the L_3 ($h\nu \approx$ 777–780 eV) and L_2 ($h\nu \approx$ 793–796 eV) white lines regions. The line shape of the spectrum depends strongly on the multiplet structure given by the Co $3d$–$3d$ and $2p$–$3d$ Coulomb and exchange interactions, as well as by the local crystal fields and the hybridization with the O $2p$ ligands.

Important is that XAS spectra are highly sensitive to the valence state: an increase of the valence state of the metal ion by one causes a shift of the XAS $L_{2,3}$ spectra by one or more eV toward higher energies [32–33]. This shift is due to a final state effect in the x-ray absorption process. The energy difference between a $3d^n$ ($3d^7$ for Co^{2+}) and a $3d^{n-1}$ ($3d^6$ for Co^{3+}) configuration is $\Delta E = E(2p^6 3d^{n-1} \rightarrow 2p^5 3d^n) - E(2p^6 3d^n \rightarrow 2p^5 3d^{n+1}) \approx U_{\underline{p}d} - U_{dd} \approx$ 1–2 eV, where U_{dd} is the Coulomb repulsion energy between two $3d$ electrons and $U_{\underline{p}d}$ the one between a $3d$

electron and the $2p$ core hole. In FIG. 5.1 we see a shift of the center of gravity of the L_3 white line to higher photon energies by approximately 1.5 eV in going from CoO to $LaCoO_3$. The energy position and the spectral shape of the high-T_C phase of $LaMn_{0.5}Co_{0.5}O_3$ is very similar to that of CoO, indicating an essentially divalent state of the Co ions.

While the spectral features of the low-T_C phase of $LaMn_{0.5}Co_{0.5}O_3$ are also very similar to those of CoO and the high-T_C phase as far as the low-energy side of the L_3 white line is concerned, this is no longer true for the high-energy side. The spectral weight at about 780 eV is increased when one compares the high-T_C with the low-T_C phase, and this increase is revealed more clearly by curves (a) of FIG. 5.2. It is natural to associate this increase with the presence of Co^{3+} species since the $LaCoO_3$ spectrum has its main peak also at 780 eV. In order to verify this in a more quantitative manner, we rescaled the spectrum of the high-T_C phase with respect to that of the low-T_C phase and calculate their difference. We find that a rescaling factor of about 0.8 results in a difference spectrum (dotted curve of FIG. 5.2) which resembles very much the spectrum of $LaCoO_3$. This in turn may be taken as an indication that the low-T_C phase has about 20% of its Co ions in the low-spin trivalent state. This result contradicts the reports in Refs. 21 and 22 which suggested that it was the high-T_C sample which contained trivalent Co ions. The different result coming from the x-ray photoemission (XPS) study [22] could be due to the following reason: Unlike XAS in which the multiplet structure of the Co-$L_{2,3}$ spectra is very characteristic for the Co valence, the XPS yields rather broad and featureless Co $2p$ core-level spectra with very little distinction between Co^{2+} and Co^{3+}. To use XPS core-level shifts to determine the valence state of insulating materials is also not so straight forward due to the fact that the chemical potential with respect to the valence or conduction band edges is not well defined. The present finding of the presence of low-spin Co^{3+} species naturally explains why the low-T_C sample has less than the optimal T_C: the nonmagnetic ions suppress strongly the spin-spin coupling between neighboring metal ions.

Figure 5.3 shows the room temperature Mn-$L_{2,3}$ XAS spectra of the low-T_C $LaMn_{0.5}Co_{0.5}O_3$ [curve (a)] and the high-T_C $LaMn_{0.5}Co_{0.5}O_3$ [curve (b)] together with $LaMnO_3$ as a trivalent Mn reference [curve (c)] and MnO as a divalent Mn reference [curve (d)]. Again we see

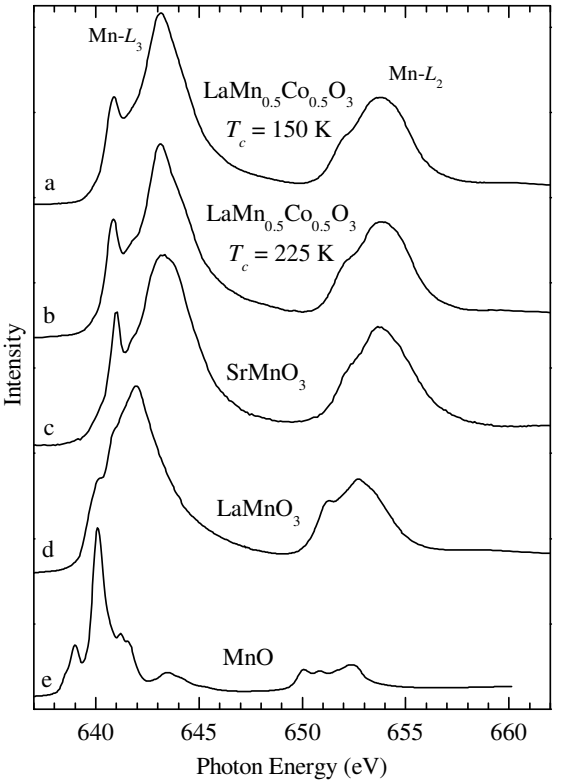

Fig. 5.3 Mn-$L_{2,3}$ XAS spectra of the $LaMn_{0.5}Co_{0.5}O_3$ sample with (a) T_C = 150 K and (b) T_C = 225 K together with (c) $SrMnO_3$ (Mn^{4+}, taken from Ref. 43), (d) $LaMnO_3$ (Mn^{3+}) and (e) MnO (Mn^{2+}) for comparison.

a gradual shift of the center of gravity of the L_3 white line to higher energies from MnO to $LaMnO_3$ and further to $SrMnO_3$, reflecting the increase of the Mn valence state from 2+ via 3+ to 4+. The Mn-$L_{2,3}$ spectrum of the high-T_C $LaMn_{0.5}Co_{0.5}O_3$ samples is similar to that of $SrMnO_3$ and $LaMn_{0.5}Ni_{0.5}O_3$ [44], in which a Ni^{2+}/Mn^{4+} valence state was found. The Mn-$L_{2,3}$ XAS spectrum thus reveals an essentially Mn^{4+} state in the high-T_C $LaMn_{0.5}Co_{0.5}O_3$, consistent with the observation of the Co^{2+} valence in the Co-$L_{2,3}$ XAS spectra above, i.e. fulfilling the charge balance requirement.

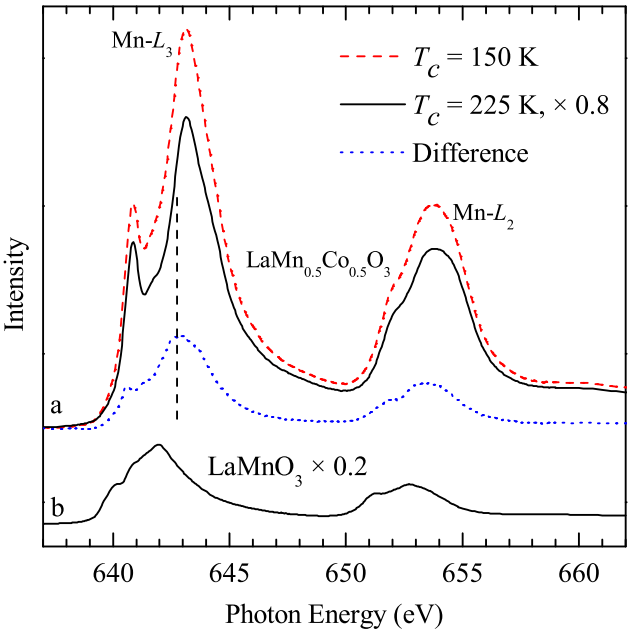

Fig. 5.4 (color online) Mn-$L_{2,3}$ XAS spectra of (a) the two $LaMn_{0.5}Co_{0.5}O_3$ samples with T_C = 150 K (dashed curve), T_C = 225 K (solid curve) and their difference (dotted curve), and (b) $LaMnO_3$ (Mn^{3+}) for comparison.

To investigate whether the presence of Co^{3+} species in the low-T_C $LaMn_{0.5}Co_{0.5}O_3$ is also accompanied by the occurrence of Mn^{3+} ions as charge compensation, we have carried out a similar analysis as for the Co spectra. Figure 5.4 shows the low-T_C spectrum (dashed curve) and the high-T_C one (solid curve) rescaled to 80% of low T_C. Their difference spectrum is shown as the dotted curve. We find that the line shape resembles very much that of the high-T_C sample itself, suggesting that most of the Mn in the low-T_C sample are also tetravalent. This in turn would imply that the low-T_C sample has to have excess of oxygen to account for the presence of the Co^{3+} species. Nevertheless, a closer look reveals that the energy position of the difference spectrum lies between that of the Mn^{4+} and the Mn^{3+} spectra, and that the valley at 641–642 eV, at which energy a typical Mn^{3+} system like $LaMnO_3$ has its maximum, is not so deep. This suggests that in the

low-T_C sample, there are also some Mn^{3+} ions or strongly hybridized Mn^{3+} and Mn^{4+} ions. Such a charge compensation for the Co^{3+} could indicate that the ordering of the Mn and Co ions is less than perfect, so that the dislocated Co ions in the Mn^{4+} positions would have smaller metal-oxygen distances, leading to the stabilization of the low-spin trivalent state of the Co.

Having established the valences of the Co and Mn ions, we now focus our attention on their magnetic properties. In the top panel (a) of FIG. 5.5, we present the XMCD spectra at the Co-$L_{2,3}$ edges of the high-T_C $LaMn_{0.5}Co_{0.5}O_3$ taken at 135 K. The spectra μ^+ (solid curve) and μ^- (dashed curve) stand, respectively, for parallel and antiparallel alignments between the photon spin and the magnetic field. One can clearly observe large differences between the two spectra with the different alignments. The difference spectrum, $\Delta\mu = \mu^+ - \mu^-$, i.e. the XMCD spectrum, is also shown (dotted curve). In the bottom panel (b) of FIG. 5.5 we show the XMCD spectra at the Mn-$L_{2,3}$ edges. Also here we can observe a large XMCD signal. It is important to note that the XMCD is largely negative at both the Co and the Mn L_3 edges, indicating that the Co^{2+} and Mn^{4+} ions are aligned ferromagnetically.

Very interesting about the XMCD at the Co-$L_{2,3}$ edges is that it is almost zero at the L_2 while it is largely negative at the L_3. This is a direct indication that the orbital contribution (L_z, $m_{\rm orb}$) to the Co magnetic moment must be large. In making this statement, we effectively used the XMCD sum rule derived by Thole *et al.* [39], in which the ratio between the energy-integrated XMCD signal and the energy-integrated isotropic spectra gives a direct value for L_z. Nevertheless, for a quantitative analysis it is preferred to extract experimentally the L_z/S_z ratio by making use of an approximate XMCD sum rule developed by Carra *et al.* [45] for the spin contribution ($2S_z$, $m_{\rm spin}$) to the magnetic moment. This is more reliable than extracting the individual values for L_z and S_z since one no longer needs to make corrections for an incomplete magnetization, due to, for example, possible strong magnetocrystalline anisotropy in a polycrystalline material. The sum rules of Thole *et al.* [39] and Carra *et al.* [45] give for the $m_{\rm orb}/m_{\rm spin}$ or $L_z/2S_z$,

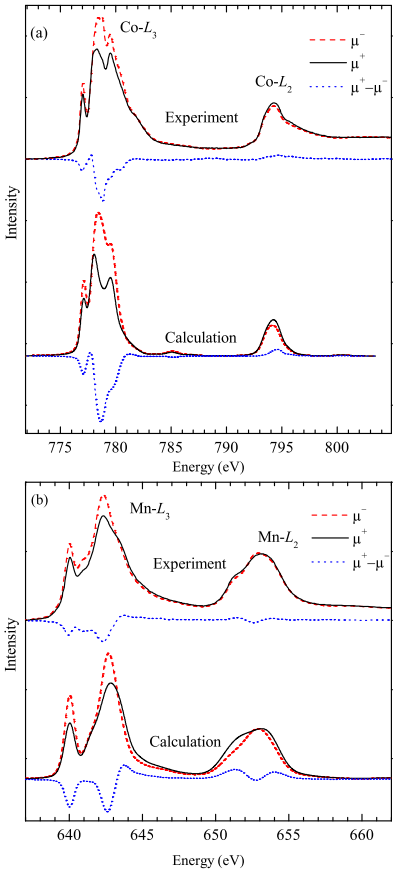

Fig. 5.5 (color online) Co-$L_{2,3}$ (*a*) and Mn-$L_{2,3}$ (*b*) spectra of $LaMn_{0.5}Co_{0.5}O_3$ taken with circularly polarized x-rays at 135 K. The photon spin was aligned parallel (μ^+, solid) and antiparallel (μ^-, dashed) to the 1 T magnetic field, respectively; the difference spectra is shown as dotted curve. Top: measured spectra. Bottom: simulated spectra.

$$\frac{m_{\mathrm{orb}}}{m_{\mathrm{spin}}} = \frac{L_z}{2S_z + 7T_z} = \frac{2}{3}\frac{\int_{L_3}\Delta\mu(E)\,\mathrm{d}E + \int_{L_2}\Delta\mu(E)\,\mathrm{d}E}{\int_{L_3}\Delta\mu(E)\,\mathrm{d}E - 2\int_{L_2}\Delta\mu(E)\,\mathrm{d}E}, \tag{5.1}$$

where T_z denotes the magnetic dipole moment. This T_z for ions in octahedral symmetry is a small number and negligible compared to S_z [46–47]. Using this equation, we extract $m_{\mathrm{orb}}/m_{\mathrm{spin}} = 0.47$ out of our Co-$L_{2,3}$ XMCD spectrum. This is a large value and is in fact close to the value of 0.57 for CoO [49], a compound well known for the important role of the spin-orbit interaction for its magnetic and structural properties [50–59]. The unquenched orbital moment is closely related to the open t_{2g} shell of the $3d^7$ configuration [60–61].

Applying the sum rules for the Mn-$L_{2,3}$ XMCD spectra, we obtain $m_{\mathrm{orb}}/m_{\mathrm{spin}} = 0.09$. This means that the orbital moment for the Mn^{4+} ions is nearly quenched. Indeed, for the $3d^3$ configuration in the Mn^{4+} compounds, the majority t_{2g} shell is fully occupied and thus a practically quenched orbital moment is to be expected.

To critically check our findings concerning the local electronic structure of the Co and Mn ions, we will explicitly simulate the experimental XMCD spectra using the configuration interaction cluster model [29–31]. The method uses a CoO_6 and MnO_6 cluster, respectively, which includes the full atomic multiplet theory and the local effects of the solid. It accounts for the intra-atomic $3d$–$3d$ and $2p$–$3d$ Coulomb interactions, the atomic $2p$ and $3d$ spin-orbit couplings, the oxygen $2p$–$3d$ hybridization, and local crystal field parameters. Parameters for the multipole part of the Coulomb interactions were given by the Hartree-Fock values [29], while the monopole parts (U_{dd}, U_{pd}) as well as the oxygen $2p$–$3d$ charge transfer energies were determined from photoemission experiments on typical Co^{2+} and Mn^{4+} compounds [62]. The one-electron parameters such as the oxygen $2p$–$3d$ and oxygen $2p$–oxygen $2p$ transfer integrals were extracted from band-structure calculations [63] within the local-density approximation (LDA) using the low-temperature crystal structure of the high-T_C phase [24]. The simulations have been carried out using the XTLS 8.3 program [29] with the parameters given in Ref. 64.

Important for the local electronic structure of the Co^{2+} ion is its local t_{2g} crystal field scheme. This together with the spin-orbit interaction

determines to a large extent its magnetic properties. To extract the crystal field parameters needed as input for the cluster model, we have performed constrained LDA+U calculations [63] without the spin-orbit interaction. We find that the $zx + xy$ orbital lies lowest, while the yz is located 22 meV and the $zx - xy$ 27 meV higher. Here, we made use of local coordinates in which the z direction is along the long Co–O bond (2.078 Å), the y along the second-longest bond (2.026 Å), and the x along the short bond (1.997 Å). The cluster model finds the easy axis of the magnetization to lie in the yz direction with a single-ion anisotropy energy of about 0.5–1.5 meV, i.e., larger than can be achieved by the applied magnetic field. Since we are dealing with a polycrystalline sample, the sum of spectra taken with the light coming from all directions has to be calculated; we approximated this by summing two calculated spectra: one for light with the Poynting vector along the yz axis and one with the Poynting vector perpendicular to this. The exchange field direction is kept along the yz in both cases.

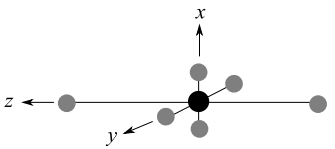

Fig. 5.6 Local coordinate system

In good approximation the local symmetry of of the octrahedron is orthorhombic D_{2h}, which allows one to use the crystal-field as defined in Section 3.3.3; the used local coordinate system can be seen in FIG. 5.6; the bond lengths are Co–O_x = 1.997 Å, Co–O_y = 2.026 Å, and Co–O_z = 2.078 Å. If one now creates a crystal-field, one-electron energy diagram, see FIG. 5.7, using the crystal-field splittings from the LDA calculation, one sees that usual D_{2h} splittings. Note, however, that the lowest two states are mixed. The eigenenergies of these states are

$$E(3x^2 - r^2) = \frac{3}{5}\Delta_{\mathrm{CF}} + \frac{1}{2}\Delta_{e_g}$$

$$E(x^2 - y^2) = \frac{3}{5}\Delta_{\mathrm{CF}} - \frac{1}{2}\Delta_{e_g}$$

$$E(zx - xy) = -\frac{2}{5}\Delta_{\mathrm{CF}} + \Delta_3$$

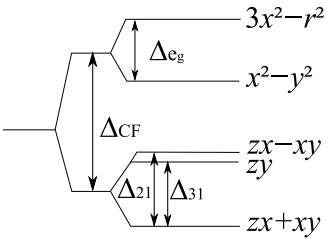

Fig. 5.7 Crystal-field spitting

$$E(zy) = -\frac{2}{5}\Delta_{\mathrm{CF}} + \Delta_2$$
$$E(zx+xy) = -\frac{2}{5}\Delta_{\mathrm{CF}} + \Delta_1, \qquad (5.2)$$

where $\Delta_{21} = \Delta_2 - \Delta_1 = 22$ meV and $\Delta_{31} = 27$ meV according to LDA+U.

The results of the cluster model calculations are included in FIG. 5.5, in the top panel (a) for the Co $L_{2,3}$ edges and the bottom panel (b) for the Mn. One can see that the line shapes of the experimental Co and Mn spectra are well explained by the simulations: all the characteristic features are reproduced. We would like to remark that the experimental XMCD spectra (dotted curves) are in general about 30% smaller than the simulated XMCD spectra (dotted curves). This is due to the fact that the experimental spectra were *not* corrected for the incomplete degree of circular polarization ($\approx$80%) of the beamline, nor for the fact that magnetic field makes an angle of 30° with respect to the Poynting vector of the light, nor for the reduction of the magnetization at 135 K at which the sample was measured – compared to the calculation which were done at 0 K. From these simulations we thus can safely conclude that our interpretation for the Co and Mn valences and magnetic moments is sound.

Our finding of a large orbital contribution to the Co magnetic moment has important implications for the interpretation of the magnetic susceptibility data. In most of the studies published so far, one tried to extract magnetic quantum numbers from the magnetic susceptibility data using the Curie or Curie-Weiss law by finding a temperature region in which the inverse of the magnetic susceptibility is linear with temperature. One usually takes the high temperature region. We will

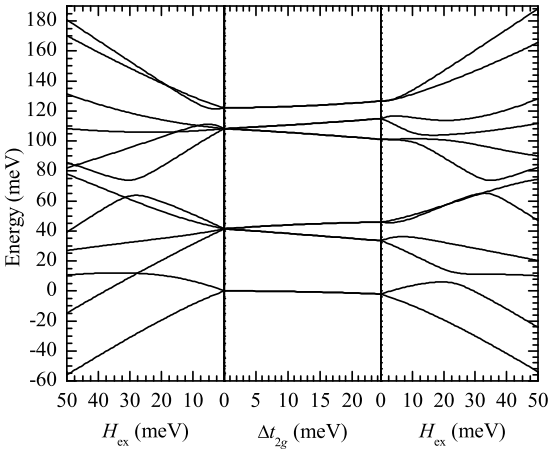

Fig. 5.8 Energy level diagram of the Co^{2+} ion (left panel) in a cubic field depending on the strength of the exchange field H_{ex}, (middle panel) the effect of lowering the symmetry [$\Delta e_g = 4\Delta t_{2g} = 4(E_{zx-xy,yz} - E_{zx+xy})$], and (right panel) the low-symmetry energy splitting depending on H_{ex}.

show below that this standard procedure will *not* provide the magnetic quantum numbers relevant for the ground state of this material.

The fact that the $3d$ spin-orbit interaction in this Co material is "active" has as a consequence that the energy difference between the ground state and the first excited state will be of the order of the spin-orbit splitting ζ, which is about 66 meV for the Co^{2+} ion. We have illustrated this in FIG. 5.8 which shows the energy level diagram of the Co^{2+} ion, both in cubic symmetry (left panel) and in the low-temperature and ferromagnetic state of the $LaMn_{0.5}Co_{0.5}O_3$ system (right panel) where we have used the crystal field scheme as described above.

To demonstrate the consequences of the presence of such a set of low lying excited states, we calculated the magnetic susceptibility χ of the Co^{2+} in cubic symmetry for an applied magnetic field of 0.01 T and without an exchange field. The results are presented in FIG. 5.9 where we depict also the (apparent) effective magnetic moment μ_{eff} [μ^2_{eff} is defined here as $3k_B$ divided by the temperature derivative of $1/\chi(T)$] and the (apparent) Weiss temperature Θ [Θ is defined here as the intercept of the tangent to the $1/\chi(T)$ curve with the abscissa].

One can clearly observe that $1/\chi(T)$ is not linear with temperature for temperatures between $T_C = 225$ K and roughly 800 K. Only for temperatures higher than 800 K, one can find a Curie-Weiss-like behavior, but then the (apparent) Weiss temperature has nothing to do with magnetic correlations since they were not included in this single ion calculations. Instead, the (apparent) Weiss temperature merely reflects the fact that the first excited states are thermally populated. This means in turn that one cannot directly extract the relevant *ground* state quantum numbers from the high temperature region.

In principle, one could hope to find a Curie-Weiss behavior by focusing on the very low temperature region only, e.g., below 50 K, but there one has to take into account that there is a very large van Vleck contribution to the magnetic susceptibility due to the fact that the first excited states are lying very close, i.e., in the range of the spin-orbit splitting. The extrapolation to $T = 0$ K would then give the real value for μ_{eff} of the ground state. In the case of $LaMn_{0.5}Co_{0.5}O_3$, however, the presence of ferromagnetism, which already sets in at 225 K, will completely dominate the magnetic susceptibility and thus hinder the determination of μ_{eff} of the ground state using this procedure. Obviously, one can determine in principle the magnetic moments in a ferromagnet from the saturation magnetization, but apparently this is the issue for $LaMn_{0.5}Co_{0.5}O_3$ where one is debating about the importance of Mn/Co disorder and its relationship to reduced magnetizations and less than optimal Curie temperatures.

Another often used "magnetic" technique to determine the moments in this ferromagnetic material is neutron scattering. Troyanchuk *et al.* found a mean value of $2.5\mu_B$ per formula unit ($LaCo_{0.5}Mn_{0.5}O_3$) [24]. The authors claimed that this is in good agreement with the Co^{2+}–Mn^{4+} scenario. Indeed, assuming spin-only moments as is generally done (but which is not correct as shown above), one would already expect $3\mu_B$ for a Co^{2+} ion and $3\mu_B$ for a Mn^{4+} ion, totaling to $6\mu_B$, i.e. $3\mu_B$/f.u., which is somewhat larger than the experimental finding and which can be understood consistently if one assumes that the Co–Mn ordering in their sample is not perfect. It is important to note that the low-spin Co^{3+}–Mn^{3+} scenario can be ruled out since this yields only $2\mu_B$/f.u., i.e., too low to explain the experiment. Nevertheless, a Co^{3+}–Mn^{3+} scenario in which the Co^{3+} ion is in the intermediate

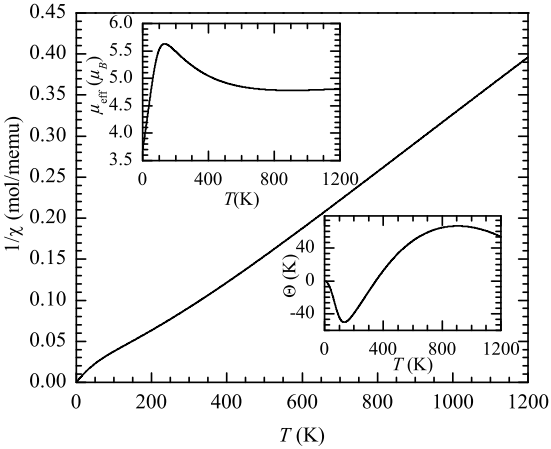

Fig. 5.9 Calculated inverse susceptibility for a single Co^{2+} ion in a cubic crystal field; (top inset) the (apparent) effective moment μ_{eff} and (bottom inset) the (apparent) Weiss temperature Θ as defined in the text.

($S = 1$) or high spin state ($S = 2$) cannot be excluded on the basis of the moments measured by the neutrons alone [12, 38].

Our cluster model calculations based on the XAS and XMCD spectra reveal that the Co^{2+} ion has $m_{\text{spin}} = 2.12\mu_B$ and $m_{\text{orb}} = 0.99\mu_B$ and that the Mn^{4+} has $m_{\text{spin}} = 2.84\mu_B$ and $m_{\text{orb}} = 0.02\mu_B$, totaling to $2.99\mu_B$/f.u. This is not inconsistent with the magnetization results of Asai *et al.* [16], if we make an extrapolation to higher magnetic fields as to estimate the saturated total moment. Our result is larger than the neutron results, but also not inconsistent if one is willing to accept that there is an appreciable amount of Co–Mn disorder in the neutron sample. Crucial is that our XAS and XMCD spectra rule out *all* the Co^{3+}–Mn^{3+} scenarios: (1) our Co $L_{2,3}$ spectra give a positive match with those of Co^{2+} compounds, while they do not fit those of low-spin Co^{3+} and high-spin Co^{3+} compounds [12, 38]; (2) our Mn $L_{2,3}$ spectra are very similar to those of Mn^{4+} compounds, and very dissimilar to those of Mn^{3+}.

To summarize, we have utilized an element-specific spectroscopic technique, namely, soft-x-ray absorption and magnetic circular dichroism spectroscopy, to unravel the local electronic structure of $LaMn_{0.5}Co_{0.5}O_3$

system. We have firmly established the high-spin Co^{2+}–Mn^{4+} scenario. We have found a very large orbital contribution to the Co magnetic moment, implying a nontrivial temperature dependence for the magnetic susceptibility. We also have revealed that samples with lower Curie temperatures contain low-spin nonmagnetic Co^{3+} ions.

1 References

[1] G. H. Jonker and J. H. van Santen, *Ferromagnetic compounds of manganese with perovskite structure*, Physica **16**, 337 (1950). DOI: 10.1016/0031-8914(50)90033-4.

[2] J. Volger, *Further experimental investigations on some ferromagnetic oxidic compounds of manganese with perovskite structure*, Physica **20**, 49 (1954). DOI: 10.1016/S0031-8914(54)80015-2.

[3] A. P. Ramirez, *Colossal magnetoresistance*, Journal of Physics: Condensed Matter **9**, 8171 (1997). DOI: 10.1088/0953-8984/9/39/005.

[4] M. Imada, A. Fujimori, and Y. Tokura, *Metal-insulator transitions*, Review of Modern Physics **70**, 1039 (1998). DOI: 10.1103/RevModPhys.70.1039.

[5] R. von Helmolt, J. Wecker, B. Holzapfel, L. Schultz, and K. Samwer, *Giant negative magnetoresistance in perovskitelike $La_{2/3}Ba_{1/3}MnO_x$ ferromagnetic films*, Physical Review Letters **71**, 2331 (1993). DOI: 10.1103/PhysRevLett.71.2331.

[6] S. Jin, T. H. Tiefel, M. McCormack, R. A. Fastnacht, R. Ramesh, and L. H. Chen, *Thousandfold Change in Resistivity in Magnetoresistive La-Ca-Mn-O Films*, Science **264**, 413 (1994). DOI: 10.1126/science.264.5157.413.

[7] J. B. Goodenough, A. Wold, R. J. Arnott, and N. Menyuk, *Relationship Between Crystal Symmetry and Magnetic Properties of Ionic Compounds Containing Mn^{3+}*, Physical Review **124**, 373 (1961). DOI: 10.1103/PhysRev.124.373.

[8] G. Blasse, *Ferromagnetic interactions in non-metallic perovskites*, Journal of Physics and Chemistry of Solids **26**, 1969 (1965). DOI: 10.1016/0022-3697(65)90231-3.

[9] G. H. Jonker, *Magnetic and Semiconducting Properties of Perovskites Containing Manganese and Cobalt*, Journal of Applied Physics **37**, 1424 (1966). DOI: 10.1063/1.1708498.

[10] S. Hébert, C. Martin, A. Maignan, R. Retoux, M. Hervieu, N. Nguyen, and B. Raveau, *Induced ferromagnetism in $LaMnO_3$ by Mn-site substitution: The major role of Mn mixed valency*, Physical Review B **65**, 104420 (2002). DOI: 10.1103/PhysRevB.65.104420.

[11] R. I. Dass and J. B. Goodenough, *Multiple magnetic phases of $La_2CoMnO_{6-\delta}$ ($0 \leq \delta \leq 0.05$)*, Physical Review B **67**, 014401 (2003). DOI: 10.1103/PhysRevB.67.014401.

[12] M. W. Haverkort, Z. Hu, J. C. Cezar, T. Burnus, H. Hartmann, M. Reuther, C. Zobel, T. Lorenz, A. Tanaka, N. B. Brookes, H.-H. Hsieh, H.-J. Lin, C.-T. Chen, and L. H. Tjeng, *Spin State Transition in $LaCoO_3$ Studied Using Soft X-ray Absorption Spectroscopy and Magnetic Circular Dichroism*, Physical Review Letters **97**, 176405 (2006). DOI: 10.1103/PhysRevLett.97.176405.

[13] N. Nishimori, K. Asai, and M. Mizoguchi, *NMR Study on the Supertransferred Hyperfine Magnetic Field at ^{55}Mn in Ferromagnetic Perovskites $La(Co_{1-x}Mg_x)_{0.5}Mn_{0.5}O_3$*, Journal of the Physical Society of Japan **64**, 1326 (1995). DOI: 10.1143/JPSJ.64.1326.

[14] I. O. Troyanchuk, N. V. Samsonenko, N. V. Kasper, H. Szymczak, and A. Nabialek, *Magnetic ordering in perovskites containing manganese and cobalt*, Journal of Physics: Condensed Matter **9**, 8287 (1997b). DOI: 10.1088/0953-8984/9/39/013.

[15] I. O. Troyanchuk, N. V. Samsonenko, A. Nabiaiek, and H. Szymczak, *Magnetic interactions and phase transitions in the Co- and Ni-doped manganites*, Journal of Magnetism and Magnetic Materials **168**, 309 (1997a). DOI: 10.1016/S0304-8853(96)00702-0.

[16] K. Asai, K. Fujiyoshi, N. Nishimori, Y. Satoh, Y. Kobayashi, and M. Mizoguchi, *Magnetic Properties of $REMe_0.5Mn_0.5O_3$ (RE = Rare Earth Element, Me = Ni, Co)*, Journal of the Physical Society of Japan **67**, 4218 (1998). DOI: 10.1143/JPSJ.67.4218.

[17] I. O. Troyanchuk, L. S. Lobanovsky, D. D. Khalyavin, S. N. Pastushonok, and H. Szymczak, *Magnetic and magnetotransport properties of Co-doped manganites with perovskite structure*, Journal of Magnetism and Magnetic Materials **210**, 63 (2000). DOI: 10.1016/S0304-8853(99)00620-4.

[18] J.-H. Park, S.-W. Cheong, and C. T. Chen, *Double-exchange ferromagnetism in* $La(Mn_{1-x}Co_x)O_3$, Physical Review B **55**, 11072 (1997). DOI: 10.1103/PhysRevB.55.11072.

[19] O. Toulemonde, F. Studer, A. Barnabé, A. Maignan, C. Martin, and B. Raveau, *Charge states of transition metal in "Cr, Co and Ni" doped* $Ln_{0.5}Ca_{0.5}MnO_3$ *CMR manganites*, Eur. Phys. J. B **4**, 159 (1998). DOI: 10.1007/s100510050364.

[20] J. van Elp, *Comment on "Double-exchange ferromagnetism in* $La(Mn_{1-x}Co_x)O_3$*"*, Physical Review B **60**, 7649 (1999). DOI: 10.1103/PhysRevB.60.7649.

[21] P. A. Joy, Y. B. Khollam, and S. K. Date, *Spin states of Mn and Co in* $LaMn_{0.5}Co_{0.5}O_3$, Physical Review B **62**, 8608 (2000b). DOI: 10.1103/PhysRevB.62.8608.

[22] V. L. Joseph Joly, P. A. Joy, S. K. Date, and C. S. Gopinath, *The origin of ferromagnetism in the two different phases of* $LaMn_{0.5}Co_{0.5}O_3$*: evidence from x-ray photoelectron spectroscopic studies*, Journal of Physics: Condensed Matter **13**, 649 (2001c). DOI: 10.1088/0953-8984/13/4/311.

[23] C. L. Bull, D. Gleeson, and K. S. Knight, *Determination of B-site ordering and structural transformations in the mixed transition metal perovskites* La_2CoMnO_6 *and* La_2NiMnO_6, Journal of Physics: Condensed Matter **15**, 4927 (2003). DOI: 10.1088/0953-8984/15/29/304.

[24] I. O. Troyanchuk, A. P. Sazonov, H. Szymczak, D. M. Többens, and H. Gamari-Seale, *Phase separation in* $La_{2-x}A_xCoMnO_6$ *(*$A = Ca$ *and Sr) perovskites*, Journal of Experimental and Theoretical Physics **99**, 363 (2004). DOI: 10.1134/1.1800193.

[25] T. Kyômen, R. Yamazaki, and M. Itoh, *Correlation between Magnetic Properties and Mn/Co Atomic Order in* $LaMn_{0.5}Co_{0.5}O_{3+\delta}$*. I. Secon d-Order Nature in Mn/Co Atomic Ordering and Valence State*, Chemistry of Materials **15**, 4798 (2003). DOI: 10.1021/cm0302781.

[26] T. Kyômen, R. Yamazaki, and M. Itoh, *Correlation between Magnetic Properties and Mn/Co Atomic Order in $LaMn_{0.5}Co_{0.5}O_{3+\delta}$. 2. Magne tic and Calorimetric Properties*, Chemistry of Materials **16**, 179 (2004). DOI: 10.1021/cm030279t.

[27] C. Autret, K. K. z. J Hejtmánek, M. Marysko, Z. Jirák, M. Dlouhá, and S. Vratislav, *Electric transport and magnetic properties of perovskites $LaMn_{1-x}Co_xO_3$ up to 900 K*, Journal of Physics: Condensed Matter **17**, 1601 (2005). DOI: 10.1088/0953-8984/17/10/015.

[28] Z. Yang, L. Ye, and X. Xie, *Electronic and magnetic properties of the perovskite oxides: $LaMn_{1-x}Co_xO_3$*, Physical Review B **59**, 7051 (1999). DOI: 10.1103/PhysRevB.59.7051.

[29] A. Tanaka and T. Jo, *Resonant 3d, 3p and 3s photoemission in transition metal oxides predicted at 2p threshold*, Journal of the Physical Society of Japan **63**, 2788 (1994). DOI: 10.1143/JPSJ.63.2788.

[30] F. M. F. de Groot, *X-ray absorption and dichroism of transition metals and their compounds*, Journal of Electron Spectroscopy and Related Phenomena **67**, 529 (1994). DOI: 10.1016/0368-2048(93)02041-J.

[31] See the "Theo Thole Memorial Issue", Journal of Electron Spectroscopy and Related Phenomena **86**, 1 (1997). DOI: 10.1016/S0368-2048(97)00039-X.

[32] C. T. Chen and F. Sette, *High resolution soft x-ray spectroscopies with the dragon beamline*, Physica Scripta **T31**, 119 (1990). DOI: 10.1088/0031-8949/1990/T31/016.

[33] C. Mitra, Z. Hu, P. Raychaudhuri, S. Wirth, S. I. Csiszar, H. H. Hsieh, H.-J. Lin, C. T. Chen, and L. H. Tjeng, *Direct observation of electron doping in $La_{0.7}Ce_{0.3}MnO_3$ using x-ray absorption spectroscopy*, Physical Review B **67**, 092404 (2003). DOI: 10.1103/PhysRevB.67.092404.

[34] G. van der Laan and B. T. Thole, *Local probe for spin-orbit interaction*, Physical Review Letters **60**, 1977 (1988). DOI: 10.1103/PhysRevLett.60.1977.

[35] B. T. Thole and G. van der Laan, *Linear relation between x-ray absorption branching ratio and valence-band spin-orbit expectation value*, Physical Review A **38**, 1943 (1988). DOI: 10.1103/PhysRevA.38.1943.

[36] C. Cartier dit Moulin, P. Rudolf, A. M. Flank, and C. T. Chen, *Spin transition evidenced by soft x-ray absorption spectroscopy*, The Journal of Physical Chemistry **96**, 6196 (1992). DOI: 10 .1021/j100194a021.

[37] H. F. Pen, L. H. Tjeng, E. Pellegrin, F. M. F. de Groot, G. A. Sawatzky, M. A. van Veenendaal, and C. T. Chen, *Phase transition in $LiVO_2$ studied by near-edge x-ray-absorption spectroscopy*, Physical Review B **55**, 15500 (1997). DOI: 10.1103 /PhysRevB.55.15500.

[38] Z. Hu, H. Wu, M. W. Haverkort, H. H. Hsieh, H.-J. Lin, T. Lorenz, J. Baier, A. Reichl, I. Bonn, C. Felser, A. Tanaka, C. T. Chen, and L. H. Tjeng, *Different look at the spin state of Co^{3+} ions in a CoO_5 pyramidal coordination*, Physical Review Letters **92**, 207402 (2004). DOI: 10.1103/PhysRevLett.92.207402.

[39] B. T. Thole, P. Carra, F. Sette, and G. van der Laan, *X-ray circular dichroism as a probe of orbital magnetization*, Physical Review Letters **68**, 1943 (1992). DOI: 10.1103/PhysRevLett .68.1943.

[40] C. T. Chen, Y. U. Idzerda, H.-J. Lin, N. V. Smith, G. Meigs, E. Chaban, G. H. Ho, E. Pellegrin, and F. Sette, *Experimental confirmation of the x-ray magnetic circular dichroism sum rules for iron and cobalt*, Physical Review Letters **75**, 152 (1995). DOI: 10.1103/PhysRevLett.75.152.

[41] T. Burnus, Z. Hu, M. W. Haverkort, J. C. Cezar, D. Flahaut, V. Hardy, A. Maignan, N. B. Brookes, A. Tanaka, H.-H. Hsieh, H.-J. Lin, C.-T. Chen, and L. H. Tjeng, *Valence, spin, and orbital state of Co ions in one-dimensional $Ca_3Co_2O_6$: An x-ray absorption and magnetic circular dichroism study*, Physical Review B **74**, 245111 (2006). DOI: 10.1103/PhysRevB.74 .245111.

[42] P. A. Joy, Y. B. Khollam, S. N. Patole, and S. K. Date, *Low-temperature synthesis of single phase $LaMn_{0.5}Co_{0.5}O_3$*, Materials Letters **46**, 261 (2000a). DOI: 10.1016/S0167-577X(00) 00182-8.

[43] R. K. Sahu, Z. Hu, M. L. Rao, S. S. Manoharan, T. Schmidt, B. Richter, M. Knupfer, M. Golden, J. Fink, and C. M. Schneider, *X-ray absorption spectra at the ru and mn $l_{2,3}$ edges and long-range ferromagnetism in $srru_{1-x}mn_xo_3$ solid solutions* ($0 \leq x \leq 0.5$), Physical Review B **66**, 144415 (2002). DOI: 10 .1103/PhysRevB.66.144415.

[44] M. C. Sánchez, J. García, J. Blasco, G. Subías, and J. Perez-Cacho, *Local electronic and geometrical structure of $LaNi_{1-x}Mn_xO_{3+\delta}$ perovskites determined by x-ray-absorption spectroscopy*, Physical Review B **65**, 144409 (2002). DOI: 10 .1103/PhysRevB.65.144409.

[45] P. Carra, B. T. Thole, M. Altarelli, and X. Wang, *X-ray circular dichroism and local magnetic fields*, Physical Review Letters **70**, 694 (1993). DOI: 10.1103/PhysRevLett.70.694.

[46] Y. Teramura, A. Tanaka, and T. Jo, *Effect of Coulomb Interaction on the X-Ray Magnetic Circular Dichroism Spin Sum Rule in 3d Transition Elements*, Journal of the Physical Society of Japan **65**, 1053 (1996). DOI: 10.1143/JPSJ.65.1053.

[47] T_z needs not to be small at the surface, see Crocombette *et al.*, Ref. 48. With a probing depth of ≈ 40 Å, however, the contribution of the surface is a small fraction of that of the bulk, so that ignoring T_z in determining $m_{\rm orb}/m_{\rm spin}$ leads to errors not larger a few percent.

[48] J. P. Crocombette, B. T. Thole, and F. Jollet, *The importance of the magnetic dipole term in magneto-circular x-ray absorption dichroism for 3d transition metal compounds*, Journal of Physics: Condensed Matter **8**, 4095 (1996). DOI: 10.1088/0953 -8984/8/22/013.

[49] G. Ghiringhelli, L. H. Tjeng, A. Tanaka, O. Tjernberg, T. Mizokawa, J. L. de Boer, and N. B. Brookes, *3d spin-orbit photoemission spectrum of nonferromagnetic materials: The test cases of CoO and Cu*, Physical Review B **66**, 075101 (2002). DOI: 10.1103/PhysRevB.66.075101.

[50] C. G. Shull, W. A. Strauser, and E. O. Wollan, *Neutron diffraction by paramagnetic and antiferromagnetic substances*, Physical Review **83**, 333 (1951). DOI: 10.1103/PhysRev.83.333.

[51] Y.-Y. Li, *Magnetic moment arrangements and magnetocrystalline deformations in antiferromagnetic compounds*, Physical Review **100**, 627 (1955). DOI: 10.1103/PhysRev.100.627.

[52] W. L. Roth, *Magnetic Structures of MnO, FeO, CoO, and NiO*, Physical Review **110**, 1333 (1958). DOI: 10.1103/PhysRev.110 .1333.

[53] B. van Laar, *Multi-Spin-Axis Structure for CoO*, Physical Review **138**, A584 (1965). DOI: 10.1103/PhysRev.138.A584.

[54] D. C. Khan and R. A. Erickson, *Magnetic Form Factor of Co^{++} Ion in Cobaltous Oxide*, Physical Review B **1**, 2243 (1970). DOI: 10.1103/PhysRevB.1.2243.

[55] M. D. Rechtin, S. C. Moss, and B. L. Averbach, *Influence of Lattice Contraction on Long-Range Order in CoO Near T_N*, Physical Review Letters **24**, 1485 (1970). DOI: 10.1103 /PhysRevLett.24.1485.

[56] W. Jauch, M. Reehuis, H. J. Bleif, F. Kubanek, and P. Pattison, *Crystallographic symmetry and magnetic structure of CoO*, Physical Review B **64**, 052102 (2001). DOI: 10.1103 /PhysRevB.64.052102.

[57] J. Kanamori, *Theory of the Magnetic Properties of Ferrous and Cobaltous Oxides, I*, Progress of Theoretical Physics **17**, 177 (1957). DOI: 10.1143/PTP.17.177.

[58] T. Nagamiya and K. Motizuki, *Theory of the Magnetic Scattering of Neutrons by CoO*, Review of Modern Physics **30**, 89 (1958). DOI: 10.1103/RevModPhys.30.89.

[59] T. Shishidou and T. Jo, *Antiferromagnetic Structure in CoO*, Journal of the Physical Society of Japan **67**, 2637 (1998). DOI: 10.1143/JPSJ.67.2637.

[60] C. J. Ballhausen, *Introduction to Ligand Field Theory*. (McGraw-Hill, New York, 1962).

[61] S. I. Csiszar, M. W. Haverkort, Z. Hu, A. Tanaka, H. H. Hsieh, H.-J. Lin, C. T. Chen, T. Hibma, and L. H. Tjeng, *Controlling orbital moment and spin orientation in CoO layers by strain*, Physical Review Letters **95**, 187205 (2005). DOI: 10.1103 /PhysRevLett.95.187205.

[62] A. E. Bocquet, T. Mizokawa, K. Morikawa, A. Fujimori, S. R. Barman, K. Maiti, D. D. Sarma, Y. Tokura, and M. Onoda, *Electronic structure of early 3d-transition-metal oxides by analysis of the 2p core-level photoemission spectra*, Physical Review B **53**, 1161 (1996). DOI: 10.1103/PhysRevB.53.1161.

[63] Hua Wu *et al.* (unpublished). (unpublished).

[64] Parameters CoO_6 cluster: $U_{3d3d} = 6.5$ eV, $U_{3d2p} = 8.2$ eV, $\Delta = 5.5$ eV, $T_{pp} = 0.7$ eV, $\Delta_{\mathrm{CF}}^{\mathrm{ionic}} = 450$ meV, $\Delta_{t_{2g}}^{\mathrm{ionic}} = 24.5$ meV, $\Delta_{zx-xy,yz}^{\mathrm{ionic}} = 5$ meV, $\Delta_{e_g}^{\mathrm{ionic}} = 88$ meV, $V_{pd\sigma} = -1.24$ eV, $V_{pd\pi} = 0.572$ eV, $H_{\mathrm{ex}} = 6.5$ meV, and $B_{\mathrm{ext}}^{\mathrm{eff}} = \cos 30^\circ \times 1$ T. Hartree-Fock results have been used for the Slater integrals, which were reduced to (F_{dd}^2) 90%, (F_{dd}^4) 100%, and (F_p^2, G_{pd}^1, G_{pd}^3) 0.95%. Parameters MnO_6 cluster: $U_{3d3d} = 5.0$ eV, $U_{3d2p} = 6.0$ eV, $\Delta = -3.0$ eV, $T_{pp} = 0.7$ eV, $\Delta_{\mathrm{CF}}^{\mathrm{ionic}} = 0.95$ eV, $V_{pd\sigma} = -1.6$ eV, $V_{pd\pi} = 0.74$ eV, $H_{\mathrm{ex}}6.5$ meV, and $B_{\mathrm{ext}}^{\mathrm{eff}} = \cos 30^\circ \times 1$ T. The Slater integrals were reduced to to 70%.

6 X-ray absorption and x-ray magnetic dichroism study on Ca_3CoRhO_6 and Ca_3FeRhO_6

Results published in: T. Burnus, Z. Hu, Hua Wu, J. C. Cezar, S. Niitaka, H. Takagi, C. F. Chang, N. B. Brookes, H.-J. Lin, L. Y. Jang, A. Tanaka, K. S. Liang, C. T. Chen, L. H. Tjeng, Physical Review B **77**, 205111 (2008).
DOI: 10.1103/PhysRevB.77.205111 OAI: arXiv:0803.0293

1 Introduction

THE quasi one-dimensional transition-metal oxides Ca_3ABO_6 (A = Fe, Co, Ni, ...; B = Co, Rh, Ir, ...) have attracted a lot of interest in recent years because of their unique electronic and magnetic properties [1–13]. The structure of Ca_3ABO_6 contains one-dimensional (1D) chains consisting of alternating face-sharing AO_6 trigonal prisms and BO_6 octahedra. Each chain is surrounded by six parallel neighboring chains forming a triangular lattice in the basal plane. Peculiar magnetic and electronic behaviors are expected to be related to geometric frustration in such a triangle lattice with antiferromagnetic (AFM) interchain interaction and Ising-like ferromagnetic (FM) intrachain coupling. $Ca_3Co_2O_6$, which realizes such a situation, shows stair-step jumps in the magnetization at regular intervals of the applied magnetic field of $M_s/3$, suggesting ferrimagnetic spin alignment. It has a saturation magnetization of $M_s = 4.8\mu_B$ per formula unit at around 4 T [14]. Studies on the temperature and magnetic-field dependence of the characteristic spin-relaxation time suggest quantum tunneling of the magnetization similar to single-molecular magnets [15]. An applied magnetic field induces a large negative magnetoresistance, apparently not related to the three-dimensional magnetic ordering [11]. Band-structure calculations using the local-spin-density approximation plus Hubbard U (LSDA+U) predicted that the Co^{3+} ion at the trigonal site, being in the high-spin (HS) state ($S = 2$), has a giant orbital moment of $1.57\mu_B$ due to the occupation of minority-spin d_2 orbital, while the

Co^{3+} ion at the octahedral site is in the low-spin (LS) state ($S = 0$) [16]. An x-ray absorption and magnetic circular dichroism study at the Co-$L_{2,3}$ edge has confirmed this prediction [17]. Both studies explain well the Ising nature of the magnetism of $Ca_3Co_2O_6$.

Ca_3CoRhO_6 and Ca_3FeRhO_6 have the same crystal structure as $Ca_3Co_2O_6$, but different magnetic and electronic properties: Neutron diffraction and magnetization measurements also indicated intrachain-FM and interchain-AFM interactions in Ca_3CoRhO_6 like in $Ca_3Co_2O_6$ [7]. In contrast, susceptibility data on Ca_3FeRhO_6 reveal a single transition into a three-dimensional AFM [5, 18]. Although Ca_3CoRhO_6 has a similar magnetic structure as $Ca_3Co_2O_6$, it exhibits considerable differences in the characteristic temperatures in the magnetic susceptibility. The high-temperature limit of the magnetic susceptibility shows a Curie-Weiss behavior with a positive Weiss temperature of 150 K for Ca_3CoRhO_6 [5], while 30 K was found for $Ca_3Co_2O_6$ [2–3]. The measured magnetic susceptibility undergoes two transitions at $T_{c_1} = 90$ K and $T_{c_2} = 25$ K for Ca_3CoRhO_6, and at $T_{c_1} = 24$ K and $T_{c_2} = 12$ K for $Ca_3Co_2O_6$ [3, 5, 7–8, 12, 18], which were attributed to FM-intrachain and AFM-interchain coupling, respectively. In contrast, Ca_3FeRhO_6 has an AFM ordering below $T_N = 12$ K [5, 18–19]. Unlike $Ca_3Co_2O_6$, there is only one plateau at 4 T and no saturation even at 18 T in the magnetization of Ca_3CoRhO_6 at 70 K [7]. A partially disordered state in Ca_3CoRhO_6 has been inferred by the previous work of Niitaka *et al.* [8]

In order to understand the contrasting magnetic properties of Ca_3CoRhO_6 and Ca_3FeRhO_6, and, particularly, the type and origin of the intrachain magnetic coupling of these quasi 1D systems, the valence, spin, and orbital states have to be clarified. However, these issues have been contradictorily discussed in previous theoretical and experimental studies. The general-gradient-approximated (GGA) density-functional band calculations [20] suggest a Co^{3+}/Rh^{3+} state in Ca_3CoRhO_6, while LSDA+U calculations with inclusion of the spin-orbit coupling favor a Co^{2+}/Rh^{4+} state and, again, a giant orbital moment due to the occupation of minority-spin d_0 and d_2 orbitals [21]. Neutron diffraction experiments on Ca_3CoRhO_6 [8, 22] suggest the Co^{3+}/Rh^{3+} state. However, based on the magnetic susceptibility [5] and x-ray photoemission spectroscopy [23] the Co^{2+}/Rh^{4+} state was proposed. For Ca_3FeRhO_6, the Fe^{2+}/Rh^{4+} state was suggested in a magnetic susceptibility study

[5], whereas Mössbauer spectroscopy indicates a Fe^{3+} state [19], and thus Rh^{3+}.

In order to settle the above issues, in this chapter we first clarify the valence state of the Rh, Co, and Fe ions in Ca_3CoRhO_6 and Ca_3FeRhO_6 using x-ray absorption spectroscopy (XAS) at the $L_{2,3}$ edges of Rh, Co, and Fe. We reveal a valence state of Co^{2+}/Rh^{4+} in Ca_3CoRhO_6 and of Fe^{3+}/Rh^{3+} in Ca_3FeRhO_6. Then, we investigate the orbital occupation and magnetic properties using x-ray magnetic circular dichroism (XMCD) experiments at the Co-$L_{2,3}$ edge of Ca_3CoRhO_6. We find a minority-spin d_0d_2 occupation for the HS Co^{2+} ground state and, thus, a giant orbital moment of about $1.7\mu_B$. As will be seen below, our results account well for the previous experiments.

2 Experimental

Polycrystalline samples were synthesized by a solid-state reaction and characterized by x-ray diffraction to be single phase [5]. The Rh-$L_{2,3}$ XAS spectra were measured at the NSRRC 15B beamline in Taiwan, which is equipped with a double-Si(111) crystal monochromator for photon energies above 2 keV. The photon-energy resolution at the Rh-$L_{2,3}$ edge ($h\nu \approx 3000$–3150 eV) was set to 0.6 eV. The Fe-$L_{2,3}$ XAS spectrum of Ca_3FeRhO_6 was measured at the NSRRC Dragon beamline with a photon-energy resolution of 0.25 eV. The main peak at 709 eV of the Fe-L_3 edge of single crystalline Fe_2O_3 was used for energy calibration. The Co-$L_{2,3}$ XAS and XMCD spectra of Ca_3CoRhO_6 were recorded at the ID8 beamline of ESRF in Grenoble with a photon-energy resolution of 0.2 eV. The sharp peak at 777.8 eV of the Co-L_3 edge of single crystalline CoO was used for energy calibration. The Co-$L_{2,3}$ XMCD spectra were recorded in a magnetic field of 5.5 T; the photons were close to fully circularly polarized. The sample pellets were cleaved *in situ* in order to obtain a clean surface. The pressure was below 5×10^{-10} mbar during the measurements. All data were recorded in total-electron-yield mode. The Rh-$L_{2,3}$ and Fe-$L_{2,3}$ XAS spectra were measured at room temperature and the Co-$L_{2,3}$ XAS and XMCD spectra at 50 K.

3 XAS and valence state

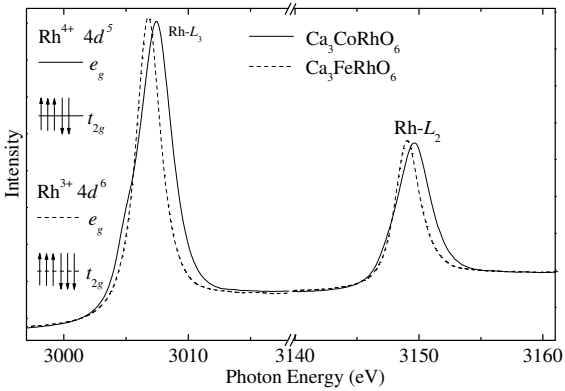

Fig. 6.1 The Rh-$L_{2,3}$ XAS spectra of Ca_3CoRhO_6 and Ca_3FeRhO_6 and a schematic energy level diagram for Rh^{3+} 4d^6 and Rh^{4+} 4d^5 configurations in octahedral symmetry.

We first concentrate on the valence of the rhodium ions in both studied compounds. For 4*d* transition-metal oxides, the XAS spectrum at the $L_{2,3}$ edge reflects basically the unoccupied t_{2g}- and e_g-related peaks in the O_h symmetry. This is due to the larger band-like character and the stronger crystal-field interaction of the 4*d* states as well as due to the weaker intra-atomic interactions as compared with 3*d* transition-metal oxides, where intra-atomic multiplet interactions are dominant [24–25]. The intra-atomic multiplet and spin-orbit interactions in 4*d* elements only modify the relative intensity of the t_{2g}- and e_g-related peaks. Figure 6.1 shows the XAS spectra at the Rh-$L_{2,3}$ edges of Ca_3FeRhO_6 (dashed line) and Ca_3CoRhO_6 (solid line). The Rh-$L_{2,3}$ spectrum shows a simple, single-peaked structure at both Rh-L_2 and Rh-L_3 edges for Ca_3FeRhO_6, while an additional low-energy shoulder is observed for Ca_3CoRhO_6. Furthermore, the peak in the Ca_3CoRhO_6 spectrum is shifted by 0.8 eV to higher energies compared to that of the Ca_3FeRhO_6.

The single-peaked spectral structure for Ca_3FeRhO_6 indicates Rh^{3+} ($4d^6$) with completely filled t_{2g} orbitals, i.e. only transitions from the 2*p* core levels to the e_g states are possible. The results are in agreement with Mössbauer spectroscopy [19]. The shift to higher energies from

Ca_3FeRhO_6 to Ca_3CoRhO_6 reflects the increase in the Rh valence from Rh^{3+} to Rh^{4+} as we can learn from previous studies on $4d$ transition-metal compounds [24–27]. Furthermore, for Ca_3CoRhO_6 the spectrum shows a weak low-energy shoulder, which is weaker at the Rh-L_2 edge than at the Rh-L_3 edge. This shoulder can be attributed to transitions from the $2p$ core levels to the t_{2g} state, reflecting a $4d^5$ configuration with one hole at the t_{2g} state. Such spectral features were found earlier for Ru^{3+} in $Ru(NH_4)_3Cl_6$ [24, 28]. Detailed calculations reveal that the multiplet and spin-orbit interactions suppress the t_{2g}-related peak at the L_2 edge for a $4d^5$ configuration [24–27]. Thus, we find a Rh^{4+} ($4d^5$) state for Ca_3CoRhO_6. Having determined a Rh^{3+} state in Ca_3FeRhO_6 and a Rh^{4+} state in Ca_3CoRhO_6, we turn to the Fe-$L_{2,3}$ and the Co-$L_{2,3}$ XAS spectra to further confirm the Fe^{3+} state and the Co^{2+} state, as expected for charge balance.

Figure 6.2 shows the experimental Fe-$L_{2,3}$ XAS spectra of (g) Ca_3FeRhO_6, along with those of (a) single crystalline Fe_2O_3 as a Fe^{3+} reference and of (j) FeO, taken from Ref. 29, as a Fe^{2+} reference. Additionally, calculated spectra for different symmetries using purely ionic (i.e. without Fe $3d$–O $2p$ hybridization) crystal-field multiplet calculations [24, 30–32] are shown. It is well known that an increase of the valence state of the $3d$ transition-metal ion by one causes a shift of the XAS $L_{2,3}$ spectra by about one eV towards higher energies [33–35]. The main peak of the Fe L_3 structure of the Ca_3FeRhO_6 lies 0.8 eV above the main peak of the divalent reference FeO and only slightly lower in energy than the one of Fe_2O_3 (Fe^{3+}). This indicates trivalent iron ions in Ca_3FeRhO_6. The slightly lower energy shift of Ca_3FeRhO_6 relative to Fe_2O_3 can be attributed to the weak trigonal crystal field in the former as compared an octahedral field in the later, as we will show below.

The experimental spectra of the reference compounds, curve (a) for Fe_2O_3 and curve (j) for FeO, can be well understood using the multiplet calculations. For Fe_2O_3 we find a good simulation taking a Fe^{3+} ion in an octahedral symmetry with a t_{2g}–e_g splitting of 1.6 eV, which is depicted in curve (b) in Fig. 2. For FeO, a good match with the experiment can be found for the Fe^{2+} in an octahedral environment with a splitting of 0.9 eV, see curve (i). The weaker crystal field in FeO, compared with Fe_2O_3, is consistent due to its larger Fe–O bond length.

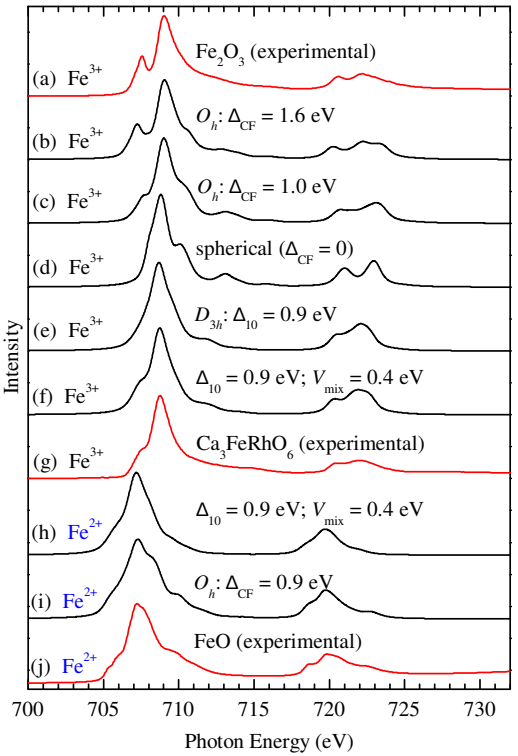

Fig. 6.2 (color online) Experimental XAS spectra at the Fe-$L_{2,3}$ edge of (a) Fe_2O_3 (Fe^{3+}), (g) Ca_3FeRhO_6, and (j) FeO (Fe^{2+}), taken from Park [29], together with simulated spectra (b, c) in O_h, (d) spherical, and (e, f) D_{3h} symmetry for Fe^{3+} and simulated spectra in (h) D_{3h} and (i) O_h symmetry for Fe^{2+}. The simulated spectra have been broadend by a Gaussian with a half width at half maximum (HWHM) of 0.2 eV and Lorentzian with HWHM 0.3 eV.

In order to understand the experimental Fe $L_{2,3}$ spectrum of Ca_3FeRhO_6, we first return to the Fe_2O_3 spectrum. When we reduce the t_{2g}–e_g splitting from 1.6 eV (curve b) via 1.0 eV (curve c) to 0.0 eV (curve d), we observe that the the low-energy shoulder becomes washed out, while the high-energy shoulder becomes more pronounced [30]. Going further to a trigonal crystal field, the high-energy shoulder looses its intensity as shown in curve (e) for a splitting of 0.9 eV between $d_{\pm 1}$

(d_{yz}/d_{zx}) and $d_0/d_{\pm 2}$ ($d_{3z^2-r^2}/d_{xy}/d_{x^2-y^2}$). The experimental Fe-$L_{2,3}$ XAS spectrum of Ca_3FeRhO_6 in FIG. 6.2(g) can be well reproduced with this trigonal crystal field of 0.9 eV and in addition a mixing parameter $V_{\mathrm{mix}} = 0.4$ eV, which mixes the $d_{\pm 2}$ with the $d_{\mp 1}$ orbitals; the result for this Fe with the $3d^5$ high-spin configuration is presented in curve (f).

We note that curve (f) has been generated with the Fe in the trivalent state. As a check, we have also tried to fit the experimental spectrum of Ca_3FeRhO_6 using a divalent Fe ansatz. However, the simulation does not match, as is illustrated in curve (h), in which we have used the same trigonal crystal field splitting of 0.9 eV and mixing parameter of 0.4 eV. To conclude, the Fe-$L_{2,3}$ and Rh-$L_{2,3}$ XAS spectra of Ca_3FeRhO_6 firmly establish the Fe^{3+}/Rh^{3+} scenario.

For the Ca_3CoRhO_6 system, the Rh-$L_{2,3}$ XAS spectra suggest that the Rh ions are tetravalent, implying that the Co ions should be divalent. To confirm this Co^{2+}/Rh^{4+} scenario we have to study explicitly the valence of the Co ion. FIG. 6.3 shows the Co-$L_{2,3}$ XAS spectra of Ca_3CoRhO_6 together with CoO as a Co^{2+} and $Ca_3Co_2O_6$ as a Co^{3+} reference [17]. Again we see a shift to higher energies from CoO to $Ca_3Co_2O_6$ by about one eV. The Ca_3CoRhO_6 spectrum lies at the same energy position as the CoO spectrum confirming the Co^{2+}/Rh^{4+} scenario [21] and ruling out the Co^{3+}/Rh^{3+} scenario [20]. The result is fully consistent with the above finding from the Rh-$L_{2,3}$ edge of Ca_3CoRhO_6 and in agreement with previous results from x-ray photoemission spectroscopy [23].

4 XMCD and orbital occupation/moment

After determining the valence states of Rh, Fe, and Co ions we turn our attention to the orbital occupation and magnetic properties of the Co^{2+} ion at the trigonal-prism site. This is motivated by the consideration that Co^{2+} ions may have a large orbital moment [36], whose size depends on details of the crystal field, while the high-spin Fe^{3+} ($3d^5$) and low-spin Rh^{3+} ($4d^6$) ions in Ca_3FeRhO_6 have a closed subshell without orbital degrees of freedom and thus no orbital moment.

In trigonal-prism symmetry the $3d$ orbitals are split into $d_{\pm 1}$, d_0, and $d_{\pm 2}$ states, see FIG. 6.4. In terms of one-electron levels, the $d_{\pm 1}$ orbitals lie highest in energy, while the lower lying d_0, and $d_{\pm 2}$ usually are

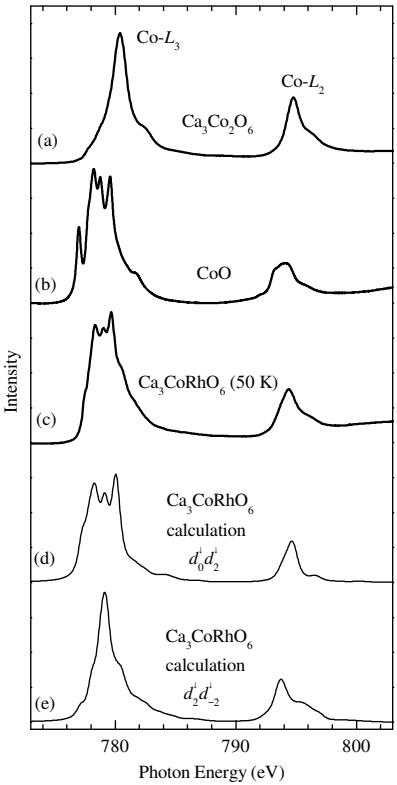

Fig. 6.3 The Co-$L_{2,3}$ spectra of (a) $Ca_3Co_2O_6$ (Co^{3+}), (b) CoO (Co^{2+}), and (c) Ca_3CoRhO_6. The simulated spectra of high-spin Co^{2+} ($3d^7$) in trigonal prismatic symmetry are shown in (d) for a d_0d_2 and in (e) for a d_2d_{-2} minority-spin orbital occupation.

nearly degenerate. For a Co^{3+} d^6 system, it is *a priori* not obvious from band structure calculations to say which of these low lying orbitals gets occupied. Details, such as the inclusion of the spin-orbit interaction, can become crucial. Indeed, for $Ca_3Co_2O_6$, it was found from LDA+U calculations [16] and confirmed by XMCD measurements [17] that the spin-orbit interaction is crucial to stabilize the occupation of the d_2 orbital, thereby giving rise to giant orbital moments and Ising-type

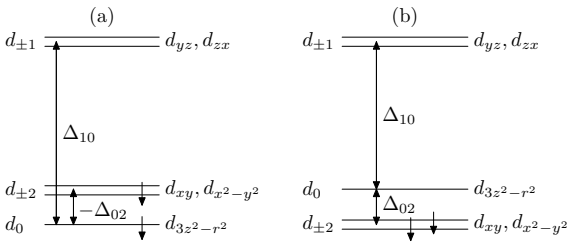

Fig. 6.4 Scheme of the two possible $3d$ occupations for a high-spin Co^{2+} ion in trigonal prismatic symmetry, ignoring the five up spins. (a) The $d_0 d_2$ minority-spin occupation allows for a large orbital magnetic moment, whereas (b) for $d_2 d_{-2}$ the orbital moment vanishes.

magnetism. For a Co^{2+} d^7 ion, however, the situation is quite different. As we will explain below, the double occupation of the $d_0 d_2$ orbitals is energetically much more favored than that of the $d_2 d_{-2}$: the energy difference could be of order 1 eV while the d_0 and $d_{\pm2}$ by themselves could be degenerate on a one-electron level. The consequences are straightforward: the double occupation of $d_0 d_2$, see FIG. 6.4(a), should lead to a large orbital moment of $2\mu_B$ (neglecting covalent effects) and Ising type of magnetism with the magnetization direction fixed along the chains [7, 21]. In contrast, the $d_2 d_{-2}$, see FIG. 6.4(b), would have given a quenched orbital moment.

In order to experimentally establish that the Co^{2+} ion has the $d_0 d_2$ configuration, we have performed an XMCD study at the Co-$L_{2,3}$ edges of Ca_3CoRhO_6. Fig. FIG. 6.5 shows the Co-$L_{2,3}$ XMCD spectrum of Ca_3CoRhO_6 taken at 50 K under 5.5 T. The spectra were taken, respectively, with the photon spin parallel (μ^+, dotted curve) and antiparallel (μ^-, solid curve) to the magnetic field. One can clearly observe large differences between the two spectra with the different alignments. Their difference, $\mu^+ - \mu^-$, is the XMCD spectrum (dashed curve). An important feature of XMCD experiments is that there are sum rules, developed by Thole and Carra *et al.* [37–38], to determine the ratio between the orbital ($m_{\rm orb} = L_z$) and spin ($m_{\rm spin} = 2S_z$) contributions to the magnetic moment, namely

$$\frac{m_{\rm orb}}{m_{\rm spin}} = \frac{2}{3}\frac{\Delta L_3 + \Delta L_2}{\Delta L_3 - 2\Delta L_2}, \tag{6.1}$$

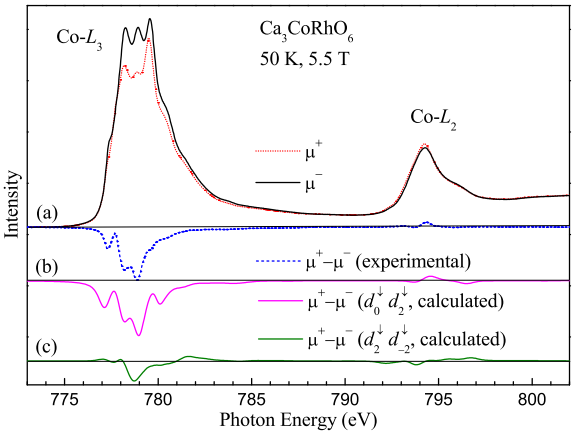

Fig. 6.5 (color online) (a) Measured soft x-ray absorption spectra with parallel (μ^+, dotted curve) and antiparallel (μ^-, solid curve) alignment between photon spin and magnetic field, together with their difference (XMCD) spectrum ($\mu^+ - \mu^-$, dashed curve); simulated XMCD spectra for (b) d_0d_2 and (c) d_2d_{-2} minority-spin occupation of the high-spin Co^{2+}.

here, ΔL_3 and ΔL_2 are the energy integrals of the L_3 and L_2 XMCD intensity. The advantage of these sum rules is that one needs not to do any simulations of the spectra to obtain the desired quantum numbers. In our particular case, we can immediately recognize the presence of a large orbital moment in FIG. 6.5(a), since there is a large net (negative) integrated XMCD spectral weight. Using Eq. (6.1) we find $m_{\rm orb}/m_{\rm spin} = 0.63$. Since the Co^{2+} ion is quite ionic, $m_{\rm spin}$ is very close to the expected ionic value of $3\mu_B$. For example, our LDA+U calculations yield $2.72\mu_B$ for the Co^{2+} ion ($2.64\mu_B$ for LDA) and Whangbo *et al.* obtained $2.71\mu_B$ from GGA calculations [20]. Using a value of $2.7\mu_B$ for the spin moment, we estimate $m_{\rm orb} = 1.7\mu_B$, in nice agreement with our LDA+U result of $1.69\mu_B$, for the d_0d_2 minority-spin orbital occupation [21].

To critically check our experimental and previous LDA+U results [21] regarding the d_0d_2 orbital occupation and the giant orbital moment, we explicitly simulate the experimental XMCD spectra using a charge-transfer configuration-interaction cluster calculation [31, 39], which includes not only the full atomic multiplet theory and the local effects of the solid, but also the oxygen $2p$–cobalt $3d$ hybridization. The results

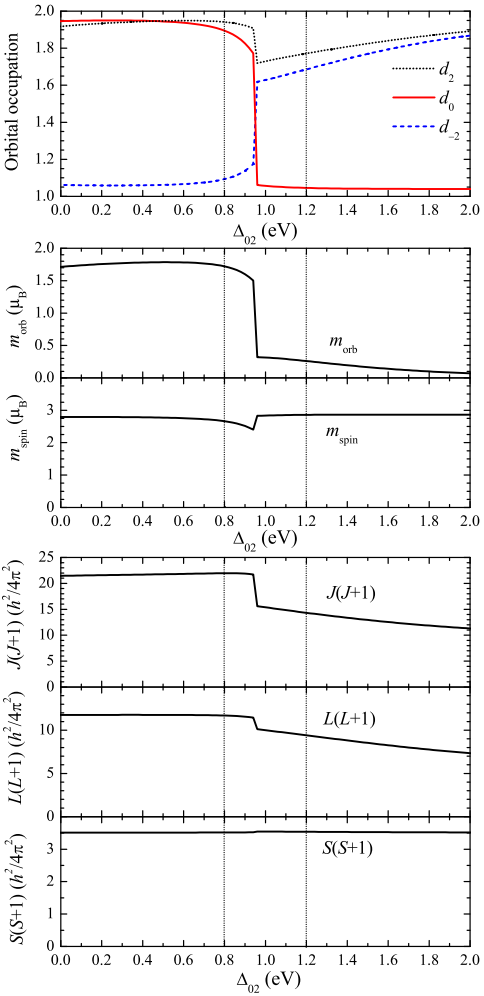

Fig. 6.6 (color online) Top panel: Occupation number of the d_0, d_2, and d_{-2} orbitals as function of the d_0–$d_{\pm 2}$ splitting Δ_{02} [FIG. 6.4(b)]. Middle panel: Orbital and spin moments ($m_{\rm orb}$ and $m_{\rm spin}$) as function of Δ_{02}. Bottom panel: $J(J+1)$, $L(L+1)$, and $S(S+1)$ as function of Δ_{02}.

of the calculated Co-$L_{2,3}$ XAS and XMCD spectra are presented in FIGS. 6.3(d) and 6.5(b), respectively. We can clearly observe that

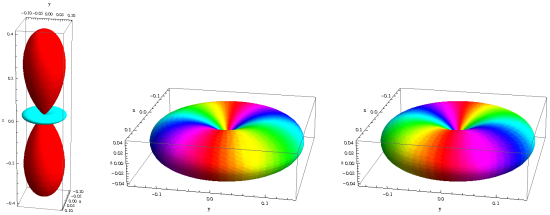

Fig. 6.7 (color online) Electron distribution of the d_0, $_2$ and d_{-2} orbitals.

the simulations reproduce the experimental spectra very well. The parameters [40] used are those which indeed give the d_0d_2 orbital occupation for the ground state. The magnetic quantum numbers found are $m_{\rm orb} = 1.65\mu_B$ and $m_{\rm spin} = 2.46\mu_B$, yielding $m_{\rm orb}/m_{\rm spin} = 0.67$ and a total Co magnetic moment of $4.11\mu_B$. With the Rh in the $S = 1/2$ tetravalent state, the total magnetic moment per formula unit should be around $5\mu_B$. This is not inconsistent with the results of the high-field magnetization study by Niitaka *et al.* [7]: they found a total moment of $4.05\mu_B$, but there the saturation of the magnetization has not yet been reached even under 18.7 Tesla. This can now be understood since the magnetocrystalline anisotropy, associated with the active spin-orbit coupling, is extremely strong and makes it difficult to fully magnetize a powder sample as was used in their study.

We also have simulated the spectra for the d_2d_{-2} scenario. These are depicted in FIG. 6.3(e) for the XAS and FIG. 6.5(c) for the XMCD. It is obvious that the experimental spectra are not reproduced. The simulated line shapes are very different from the experimental ones and the integral of the simulated XMCD spectrum yields a vanishing orbital moment. We therefore can safely conclude that the ground state of this material is not d_2d_{-2}. For completeness we mention that the magnetic quantum numbers found for this d_2d_{-2} ansatz are $m_{\rm orb} = 0.20\mu_B$ and $m_{\rm spin} = 2.86\mu_B$, yielding $m_{\rm orb}/m_{\rm spin} = 0.07$ and a total Co magnetic moment of $3.06\mu_B$.

5 Stability of the d_0d_2 state

Having established that the ground state of Ca_3CoRhO_6 has the Co^{2+} d^7 ion in the doubly occupied d_0d_2 orbital configuration and not in

the d_2d_{-2}, it is interesting to study its stability in more detail. As already mentioned above, for a Co^{3+} d^6 ion, the d_0 and $d_{\pm2}$ states can be energetically very close to each other. For a Co^{2+} d^7 ion, however, the d_0d_2 and d_2d_{-2} states are very much different in energy. This is illustrated in the top panel of FIG. 6.6, in which we have calculated the occupation numbers of the d_0, d_2, and d_{-2} orbitals as a function of Δ_{02}, the one-electron level splitting between the d_0 and $d_{\pm2}$ orbitals. The d_0d_2 ground state which gives the best simulation to the experimental XAS and XMCD spectra was obtained with $\Delta_{02} \approx 0.4$ eV. We can observe that the d_0d_2 situation is quite stable for a wide range of Δ_{02} values, certainly up to 0.8 eV. With a transition region between $\Delta_{02} = 0.8$–1.2 eV, we find a stable d_2d_{-2} situation only for Δ_{02} values larger than 1.2 eV. (For the d_2d_{-2} simulations above we have used $\Delta_{02} = 1.4$ eV.) This is a very large number indeed, and it can be traced back to the multiplet character of the on-site Coulomb interactions: an occupation of d_2d_{-2} means a much stronger overlap of the electron clouds as compared to the case for a d_0d_2; this can be seen in FIG. 6.7 where the electron distribution of these orbitals is shown. This results in a higher repulsion energy, which is not a small quantity in view of the atomic-like values of the F^2 and F^4 Slater integrals determining the multiplet splitting [31, 41].

In the middle panel of FIG. 6.6 we also show the expectation values for m_{orb} and m_{spin} when varying Δ_{02}. Again we clearly observe that the large orbital-moment situation is quite stable. To quench the orbital moment one would need much higher Δ_{02} values. Important is that the spin state does not change here. Bottom panel of FIG. 6.6 demonstrates that the high-spin state of the Co^{2+} ion is not affected by Δ_{02}: the expectation value $\langle S^2 \rangle$ remains constant throughout at a value consistent with an essentially $S = 3/2$ state. Obviously, the L^2 and J^2 quantum numbers are strongly affected by Δ_{02}.

6 Conclusion

To summarize, the Rh-$L_{2,3}$, Co-$L_{2,3}$ and Fe-$L_{2,3}$ XAS measurements indicate Co^{2+}/Rh^{4+} in Ca_3CoRhO_6 and Fe^{3+}/Rh^{3+} in Ca_3FeRhO_6. The magnetic properties of Ca_3FeRhO_6 are relatively simple as both the HS Fe^{3+} and LS Rh^{3+} ions have a closed subshell and thus no orbital degrees of freedom and no orbital moment. The weak intrachain

AFM coupling between the HS Fe ions can be understood in terms of the normal superexchange via the intermediate non-magnetic O–Rh–O complex. For Ca_3CoRhO_6, the combined experimental and theoretical study of the Co-$L_{2,3}$ XAS and XMCD spectra reveals a giant orbital moment of about $1.7\mu_B$. This large orbital moment is connected with the minority-spin d_0d_2 occupation for HS Co^{2+} ($3d^7$) ions in the peculiar trigonal prismatic coordination. The high FM ordering temperature in Ca_3CoRhO_6, compared with that of $Ca_3Co_2O_6$, can be attributed to the distinct octahedral sites (which mediate the Co–Co magnetic coupling): the magnetic Rh^{4+} ion ($S = 1/2$) in the former and the nonmagnetic Co^{3+} ion ($S = 0$) in the latter.

7 References

[1] H. Fjellvåg, E. Gulbrandsen, S. Aasland, A. Olsen, and B. C. Hauback, *Crystal Structure and Possible Charge Ordering in One-Dimensional $Ca_3Co_2O_6$*, J. Solid State Chem. **124**, 190 (1996). DOI: 10.1006/jssc.1996.0224.

[2] S. Aasland, H. Fjellvåg, and B. Hauback, *Magnetic properties of the one-dimensional $Ca_3Co_2O_6$*, Solid State Communications **101**, 187 (1997). DOI: 10.1016/S0038-1098(96)00531-5.

[3] H. Kageyama, K. Yoshimura, K. Kosuge, H. Mitamura, and T. Goto, *Field-Induced Magnetic Transitions in the One-Dimensional Compound $Ca_3Co_2O_6$*, Journal of the Physical Society of Japan **66**, 1607 (1997a). DOI: 10.1143/JPSJ.66.1607.

[4] H. Kageyama, K. Yoshimura, K. Kosuge, M. Azuma, M. Takano, H. Mitamura, and T. Goto, *Magnetic Anisotropy of Ca 3Co 2O 6 with Ferromagnetic Ising Chains*, Journal of the Physical Society of Japan **66**, 3996 (1997b). DOI: 10.1143/JPSJ.66.3996.

[5] S. Niitaka, H. Kageyama, M. Kato, K. Yoshimura, and K. Kosuge, *Synthesis, crystal structure, and magnetic properties of new one-dimensional oxides Ca_3CoRhO_6 and Ca_3FeRhO_6*, J. Solid State Chem. **146**, 137 (1999). DOI: 10.1006/jssc.1999.8319.

[6] A. Maignan, C. Michel, A. C. Masset, C. Martin, and B. Raveau, *Single crystal study of the one dimensional $Ca_3Co_2O_6$ compound: five stable configurations for the Ising triangular lattice*, Eur. Phys. J. B **15**, 657 (2000). DOI: 10.1007/PL00011051.

[7] S. Niitaka, H. Kageyama, K. Yoshimura, K. Kosuge, S. Kawano, N. Aso, A. Mitsuda, H. Mitamura, and T. Goto, *High-field magnetization and neutron diffraction studies of one-dimensional compound Ca_3CoRhO_6*, Journal of the Physical Society of Japan **70**, 1222 (2001). DOI: 10.1143/JPSJ.70.1222.

[8] S. Niitaka, K. Yoshimura, K. Kosuge, M. Nishi, and K. Kakurai, *Partially Disordered Antiferromagnetic Phase in Ca_3CoRhO_6*, Physical Review Letters **87**, 177202 (2001). DOI: 10.1103 /PhysRevLett.87.177202.

[9] B. Martínez, V. Laukhin, M. Hernando, J. Fontcuberta, M. Parras, and J. M. González-Calbet, *Enhancement of antiferromagnetic coupling in the quasi-one-dimensional $Ca_3Co_2O_6$ ferrimagnet*, Physical Review B **64**, 012417 (2001). DOI: 10.1103 /PhysRevB.64.012417.

[10] E. V. Sampathkumaran and A. Niazi, *Superparamagnetic-like ac susceptibility behavior in the partially disordered antiferromagnetic compound Ca_3CoRhO_6*, Physical Review B **65**, 180401 (2002). DOI: 10.1103/PhysRevB.65.180401.

[11] B. Raquet, M. N. Baibich, J. M. Broto, H. Rakoto, S. Lambert, and A. Maignan, *Hopping conductivity in one-dimensional $Ca_3Co_2O_6$ single crystals*, Physical Review B **65**, 104442 (2002). DOI: 10.1103/PhysRevB.65.104442.

[12] V. Hardy, S. Lambert, M. R. Lees, and D. M. Paul, *Specific heat and magnetization study on single crystals of the frustrated quasi-one-dimensional oxide Ca_3Co_2O*, Physical Review B **68**, 014424 (2003). DOI: 10.1103/PhysRevB.68.014424.

[13] X. Yao, S. Dong, K. Xia, P. Li, and J.-M. Liu, *Spin persistence in an antiferromagnetic triangular Ising lattice under a magnetic field*, Physical Review B **76**, 024435 (2007). DOI: 10.1103 /PhysRevB.76.024435.

[14] A. Maignan, V. Hardy, S. Hebert, M. Drillon, M. Lees, O. Petrenko, D. M. Paul, and D. Khomskii, *Quantum Tunneling of the Magnetization in the Ising Chain Compound $Ca_3Co_2O_6$*, J. Mater. Chem. **14**, 1231 (2004). DOI: 10.1039/b316717h.

[15] V. Hardy, D. Flahaut, M. R. Lees, and O. A. Petrenko, *Magnetic quantum tunneling in $Ca_3Co_2O_6$ studied by ac susceptibility: Temperature and magnetic-field dependence of the spin-relaxation time*, Physical Review B **70**, 214439 (2004b). DOI: 10.1103/PhysRevB.70.214439.

[16] Hua Wu, M. W. Haverkort, Z. Hu, D. I. Khomskii, and L. H. Tjeng, *Nature of magnetism in $Ca_3Co_2O_6$*, Physical Review Letters **95**, 186401 (2005). DOI: 10.1103/PhysRevLett.95.186401.

[17] T. Burnus, Z. Hu, M. W. Haverkort, J. C. Cezar, D. Flahaut, V. Hardy, A. Maignan, N. B. Brookes, A. Tanaka, H.-H. Hsieh, H.-J. Lin, C.-T. Chen, and L. H. Tjeng, *Valence, spin, and orbital state of Co ions in one-dimensional $Ca_3Co_2O_6$: An x-ray absorption and magnetic circular dichroism study*, Physical Review B **74**, 245111 (2006). DOI: 10.1103/PhysRevB.74 .245111.

[18] M. J. Davis, M. D. Smith, and H.-C. zur Loye, *Crystal growth, structural characterization and magnetic properties of Ca_3CuRhO_6, $Ca_3Co_{1.34}Rh_{0.66}O_6$ and Ca_3FeRhO_6*, J. Solid State Chem. **173**, 122 (2003). DOI: 10.1016/S0022-4596(03) 00102-6.

[19] S. Niitaka, K. Yoshimura, K. Kosuge, K. Mibu, H. Mitamura, and T. Goto, *Magnetic and ^{57}Fe Mössbauer studies of Ca_3FeRhO_6*, Journal of Magnetism and Magnetic Materials **260**, 48 (2003). DOI: 10.1016/S0304-8853(02)00102-6.

[20] M.-H. Whangbo, D. Dai, H.-J. Koo, and S. Jobic, *Investigations of the oxidation states and spin distributions in $Ca_3Co_2O_6$ and Ca_3CoRhO_6 by spin-polarized electronic band structure calculations*, Solid State Communications **125**, 413 (2003). DOI: 10 .1016/S0038-1098(02)00872-4.

[21] H. Wu, Z. Hu, D. I. Khomskii, and L. H. Tjeng, *Insulating state and the importance of the spin-orbit coupling in Ca_3CoRhO_6*, Physical Review B **75**, 245118 (2007). DOI: 10.1103/PhysRevB.75.245118.

[22] M. Loewenhaupt, W. Schäfer, A. Niazi, and E. V. Sampathkumaran, *Evidence for the coexistence of low-dimensional magnetism and long-range order in Ca_3CoRhO_6*, Europhysics Letters **63**, 374 (2003). DOI: 10.1209/epl/i2003-00542-5.

[23] K. Takubo, T. Mizokawa, S. Hirata, J.-Y. Son, A. Fujimori, D. Topwal, D. D. Sarma, S. Rayaprol, and E.-V. Sampathkumaran, *Electronic structure of Ca_3CoXO_6 (X = Co, Rh, Ir) studied by x-ray photoemission spectroscopy*, Physical Review B **71**, 073406 (2005). DOI: 10.1103/PhysRevB.71.073406.

[24] F. M. F. de Groot, *X-ray absorption and dichroism of transition metals and their compounds*, Journal of Electron Spectroscopy and Related Phenomena **67**, 529 (1994). DOI: 10.1016/0368-2048(93)02041-J.

[25] Z. Hu, H. von Lips, M. S. Golden, J. Fink, G. Kaindl, F. M. F. de Groot, S. Ebbinghaus, and A. Reller, *Multiplet effects in the Ru-$L_{2,3}$ x-ray-absorption spectra of Ru(IV) and Ru(V) compounds*, Physical Review B **61**, 5262 (2000). DOI: 10.1103/PhysRevB.61.5262.

[26] Z. Hu, M. S. Golden, S. G. Ebbinghaus, M. Knupfer, J. Fink, F. M. F. de Groot, and G. Kaindl, *The distribution of the doped holes in $La_{2-x}Sr_xCu_{1-y}Cu_yO_{4-\delta}$*, Chemical Physics **282**, 451 (2002). DOI: 10.1016/S0301-0104(02)00729-2.

[27] R. K. Sahu, Z. Hu, M. L. Rao, S. S. Manoharan, T. Schmidt, B. Richter, M. Knupfer, M. Golden, J. Fink, and C. M. Schneider, *X-ray absorption spectra at the ru and mn $l_{2,3}$ edges and long-range ferromagnetism in $srru_{1-x}mn_xo_3$ solid solutions* ($0 \leq x \leq 0.5$), Physical Review B **66**, 144415 (2002). DOI: 10.1103/PhysRevB.66.144415.

[28] T. K. Sham, *X-ray absorption spectra of ruthenium L edges in $Ru(NH_3)_6Cl_3$*, Journal of the American Chemical Society **105**, 2269 (1983). DOI: 10.1021/ja00346a028.

[29] J.-H. Park, Ph.D. thesis, University of Michigan, (1994).

[30] F. M. F. de Groot, J. C. Fuggle, B. T. Thole, and G. A. Sawatzky, *2p x-ray absorption of 3d transition-metal compounds: An atomic multiplet description including the crystal field*, Physical Review B **42**, 5459 (1990). DOI: 10.1103/PhysRevB.42.5459.

[31] A. Tanaka and T. Jo, *Resonant 3d, 3p and 3s photoemission in transition metal oxides predicted at 2p threshold*, Journal of the Physical Society of Japan **63**, 2788 (1994). DOI: 10.1143/JPSJ.63.2788.

[32] See the "Theo Thole Memorial Issue", Journal of Electron Spectroscopy and Related Phenomena **86**, 1 (1997). DOI: 10.1016/S0368-2048(97)00039-X.

[33] C. T. Chen and F. Sette, *High resolution soft x-ray spectroscopies with the dragon beamline*, Physica Scripta **T31**, 119 (1990). DOI: 10.1088/0031-8949/1990/T31/016.

[34] C. Mitra, Z. Hu, P. Raychaudhuri, S. Wirth, S. I. Csiszar, H. H. Hsieh, H.-J. Lin, C. T. Chen, and L. H. Tjeng, *Direct observation of electron doping in $La_{0.7}Ce_{0.3}MnO_3$ using x-ray absorption spectroscopy*, Physical Review B **67**, 092404 (2003). DOI: 10.1103/PhysRevB.67.092404.

[35] T. Burnus, Z. Hu, H. H. Hsieh, V. L. J. Joly, P. A. Joy, M. W. Haverkort, H. Wu, A. Tanaka, H.-J. Lin, C. T. Chen, and L. H. Tjeng, *Local electronic structure and magnetic properties of $LaMn_{0.5}Co_{0.5}O_3$ studied by x-ray absorption and magnetic circular dichroism spectroscopy*, Physical Review B **77**, 125124 (2008). DOI: 10.1103/PhysRevB.77.125124.

[36] G. Ghiringhelli, L. H. Tjeng, A. Tanaka, O. Tjernberg, T. Mizokawa, J. L. de Boer, and N. B. Brookes, *3d spin-orbit photoemission spectrum of nonferromagnetic materials: The test cases of CoO and Cu*, Physical Review B **66**, 075101 (2002). DOI: 10.1103/PhysRevB.66.075101.

[37] B. T. Thole, P. Carra, F. Sette, and G. van der Laan, *X-ray circular dichroism as a probe of orbital magnetization*, Physical Review Letters **68**, 1943 (1992). DOI: 10.1103/PhysRevLett.68.1943.

[38] P. Carra, B. T. Thole, M. Altarelli, and X. Wang, *X-ray circular dichroism and local magnetic fields*, Physical Review Letters **70**, 694 (1993). DOI: 10.1103/PhysRevLett.70.694.

[39] J. Okamoto, K. Mamiya, S.-I. Fujimori, T. Okane, Y. Saitoh, Y. Muramatsu, K. Yoshii, A. Fujimori, A. Tanaka, M. Abbate, T. Koide, S. Ishiwata, S. Kawasaki, and M. Takano, *Antiferromagnetic-to-ferromagnetic transition induced by diluted Co in $SrFe_{1-x}Co_xO_3$: Magnetic circular x-ray dichroism study*, Physical Review B **71**, 104401 (2005). DOI: 10.1103/PhysRevB.71.104401.

[40] Parameters (in eV). $U_{3d,3d} = 5$, $U_{2\underline{p},3d} = 6.5$, $\Delta = 4$, $\Delta_{10}^{\text{ionic}} = 0.65$, $V_{\text{mix}}^{\text{ionic}} = -0.2$, $V_{pd\sigma} = -1.024$, $H_{\text{ex}} = 0.045$. The Slater integrals were reduced to 80% of their Hartree-Fock value. $\Delta_{02}^{\text{ionic}} = 0.4$ ($d_0 d_2$ scenario), $\Delta_{02}^{\text{ionic}} = 1.4$ ($d_2 d_{-2}$). The simulated spectra have been broadend by a Gaussian with HWHM 0.2 eV and Lorentzian with HWHM 0.2 eV.

[41] E. Antonides, E. C. Janse, and G. A. Sawatzky, *LMM Auger spectra of Cu, Zn, Ga, and Ge. I. Transition probabilities, term splittings, and effective Coulomb interaction*, Physical Review B **15**, 1669 (1977). DOI: 10.1103/PhysRevB.15.1669.

7 Orbitally driven spin-singlet dimerization in $S = 1$ $La_4Ru_2O_{10}$

Results published in: Hua Wu, Zhiwei Hu, Tobias Burnus, Jonathan D. Denlinger, Peter G. Khalifah, David G. Mandrus, Ling-Yun Jang, Hui-Huang Hsieh, Arata Tanaka, Keng S. Liang, Jim W. Allen, Robert J. Cava, Daniel I. Khomskii, and L. Hao Tjeng
Physical Review Letters **96**, 256402 (2006).
DOI: 10.1103/PhysRevLett.96.256402 OAI: arXiv:cond-mat/0606445

One of the most intriguing aspects of transition-metal materials is the wide variety and richness of their physical properties [1]. Although conceptually clean and beautiful, theoretical simplifications in terms of a Heisenberg model or a single-band Hubbard model turn out to be inadequate [2]. It now becomes more and more clear that a full identification of the relevant orbital and spin degrees of freedom of the ions involved is needed to understand, for instance, the colossal magnetoresistance behavior in the manganates [3–7], magnetization reversals, and metal-insulator transitions in early transition-metal oxides [8–12], as well as the formation of spin gaps in non-one-dimensional $S = \frac{1}{2}$ systems [13–16].

Very recently Khalifah *et al.* [17] synthesized the semiconducting quasi two-dimensional $La_4Ru_2O_{10}$ compound and discovered that this system undergoes a strong first-order structural transition at $T_s = 160$ K (see FIG. 7.1), accompanied by a rare $4d$ orbital ordering and spin-gap opening. Their interpretation of these phenomena was that the Ru^{4+} ion transforms from the usual $t_{2g\uparrow}^3 t_{2g\downarrow}^1$ low-spin state with $S = 1$ to an $t_{2g\uparrow}^2 t_{2g\downarrow}^2$ "ultralow" spin state with $S = 0$, caused by a sufficiently strong crystal-field splitting (CFS) of the Ru-$4d$ t_{2g} levels due to the lattice distortion below T_s.

However, already soon after that, it was also hypothesized by Khalifah *et al.*, based on unpublished standard band-structure calculations, that a chemical bond may be formed associated with the orbital ordering. Here, we report on an x-ray absorption spectroscopy (XAS) study in which we reveal that the Ru^{4+} ions remain in the $S = 1$ spin state

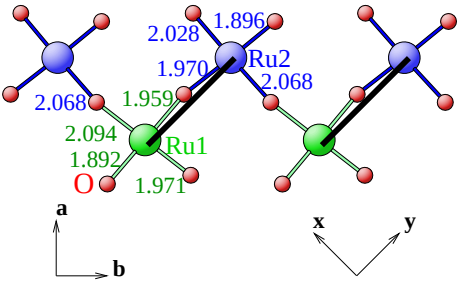

Fig. 7.1 (color online) The main block of the low-temperature (20 K) triclinic crystal structure of $La_4Ru_2O_{10}$ shown in the crystallographic *ab* plane: the two-dimensional Ru–O network consisting of distorted RuO_6 octahedra extends along the *c* axis (not shown, pointing into paper plane) and *b* axis with corrugation. The Ru–O bond lengths are marked in units of Å, and those out of the *ab* plane (not shown) are 2.046 and 2.057 Å for Ru1, and 2.046 and 2.082 Å for Ru2. The spin-singlet dimers are marked by black solid bars. The local orthogonal coordinate system (*xyz*) is used in our band calculations with *z* parallel to *c* and *y* (*x*) along the short (long) Ru1–Ru2 direction. The high-temperature monoclinic structure (not shown) above $T_s = 160$ K has equal Ru–Ru distances along the *x* and *y* directions: Ru1 and Ru2 are equivalent.

across T_s. This directly points to the possibility that $La_4Ru_2O_{10}$ is in fact a novel system in which the spin-gap opening is due to a singlet-dimer formation in a non-one-dimensional and $S > \frac{1}{2}$ material. We find using local-spin-density approximation + Hubbard U (LSDA + U) band-structure calculations that the distinct orbital ordering involves a significant anisotropy of the antiferromagnetic exchange couplings, indicating indeed the formation of Ru ($S = 1$)–Ru ($S = 1$) singlet dimers.

Floating zone crystals were grown in a NEC SC-M15HD image furnace using rods with a 1:1 or 4:5 ratio of La:Ru which had been prereacted and sintered in air at 1250 °C. A small (1–2 atm) overpressure of oxygen aided the growth, and the power was dynamically increased during the run to compensate for absorption by the copious amounts of evaporated Ru. Sizeable crystals could only be obtained using seed crystals. X-ray diffraction confirmed both the macroscopic phase purity and the universal presence of two twin domains. The

XAS measurements were performed at the Taiwan NSRRC 15B beam line, equipped with a double-Si(111)-crystal monochromator, delivering photons from 2 keV and up. The spectra were recorded using the total-electron-yield method in a chamber with a base pressure in the low 10^{-10} mbar range. Clean sample areas were obtained by cleaving the crystals *in situ*. The photon-energy resolution at the Ru-$L_{2,3}$ edges ($h\nu \approx 2.9$ keV) was set at 0.6 eV. Strong polarization-dependent O-K XAS spectra [18] verify the high sample quality.

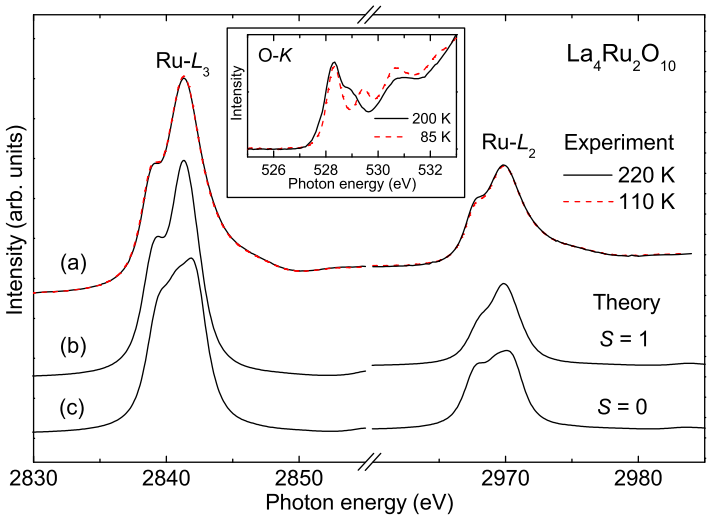

Fig. 7.2 (color online) (a) Experimental Ru-$L_{2,3}$ XAS spectra of $La_4Ru_2O_{10}$ measured at 220 and 110 K, i.e., above and below $T_s = 160$ K. (b) Theoretical simulations for the Ru^{4+} ion in the $S = 1$ high-temperature phase at 220 K, $S = 1$ low-temperature phase at 110 K, and $S = 0$. The inset shows O-K spectra measured at 200 and 85 K from [18].

The top curves of FIG. 7.2 depict the Ru-$L_{2,3}$ XAS spectra of $La_4Ru_2O_{10}$ taken at 220 K (solid line) and 110 K (dashed line). The spectral-line shapes depend strongly on the multiplet structure given by the Ru-4d–4d and -2p–4d Coulomb and exchange interactions, as well as by the local CFS and the hybridization with the O 2p ligands. Unique to XAS

is that the dipole selection rules are very effective in determining which of the $2p^5 4d^{n+1}$ final states can be reached and with what intensity, starting from a particular $2p^6 4d^n$ initial state ($n = 4$ for Ru^{4+}) [19–20]. This makes the technique extremely sensitive to the quantum numbers of the initial state [21–22].

The essence of the Ru-$L_{2,3}$ XAS spectra in FIG. 7.2 is that there is only a very small change across T_s, suggesting that the local electronic and spin state of the Ru^{4+} ion in the high-temperature (HT) and low-temperature (LT) phases are quite similar. This seems surprising in view of the fact that we observed considerable modifications in the O-K XAS spectra in going from 200 K (solid line) to 85 K (dashed line) as shown in the inset of FIG. 7.2 [18]. Since these O-K spectra are known to be sensitive to band-structure effects [19], their modifications are fully consistent with the strong changes in the crystal structure as seen in neutron diffraction [17], confirming the good quality of our samples.

To extract quantitative information on the CFS and spin state from the Ru spectra, we have performed simulations using the successful configuration-interaction cluster model [19–20, 23]. The calculations have been carried out for a RuO_6 cluster in the proper HT and LT local coordination using the XTLS 8.3 program [23]. Parameters for the multipole part of the Coulomb interactions were set standardly at 80% of the Hartree-Fock values [23], while the monopole parts (U_{dd}, U_{pd}) were taken from Ca_2RuO_4 [24–26]. The O $2p$–Ru $4d$ charge-transfer energy was estimated from LDA calculations (see below), and the O $2p$–Ru $4d$ transfer integrals and their distance dependence from Harrison's relations [27]. The local CFS parameters are to be determined from the comparison between the simulations and the experimental spectra.

The bottom curves of FIG. 7.2 show the simulations for both the HT and LT phases. We found optimal fits (solid and dashed lines) if the Ru $4d$ xz orbital is set at about 100–150 meV (HT) and 200–300 meV (LT) lower in energy than the essentially degenerate (within 50 meV) yz and xy orbitals [28]. These numbers refer to total energies calculated including the CFS and covalency but without spin-orbit interaction. Important is that the cluster calculation indeed finds the $S = 1$ state for both the HT and LT phases, which is a direct consequence of the fact that in both phases the xz orbital is essentially doubly occupied while the yz and xy are each singly occupied. We also have carried

out calculations for the Ru ion in the artificial $S = 0$ state by changing the CFS parameter such that the xz orbital lies above the degenerate yz and xy orbitals [28]. As shown in FIG. 7.2, the simulated spectrum disagrees with the experiment. So we can rule out that the spin-gap opening is due to a local spin-state transition [17].

To confirm our XAS-derived conclusions and, more importantly, to get in-depth understanding of the nature of the spin-gap state below T_s, we performed systematic LDA and LSDA + U band-structure calculations [29], by using the full-potential augmented-plane-waves plus local-orbital method [30]. We took the neutron crystal structure data at 20 K and 298 K [17]. The muffin-tin sphere radii are chosen to be 2.8, 2.0, and 1.5 Bohr for La, Ru, and O atoms, respectively. $U = 3$ eV and Hund's rule exchange $J_H = 0.5$ eV ($U_{\text{eff}} = 2.5$ eV) are used for Ru $4d$ electrons, which are common for ruthenates [24–25, 31–32].

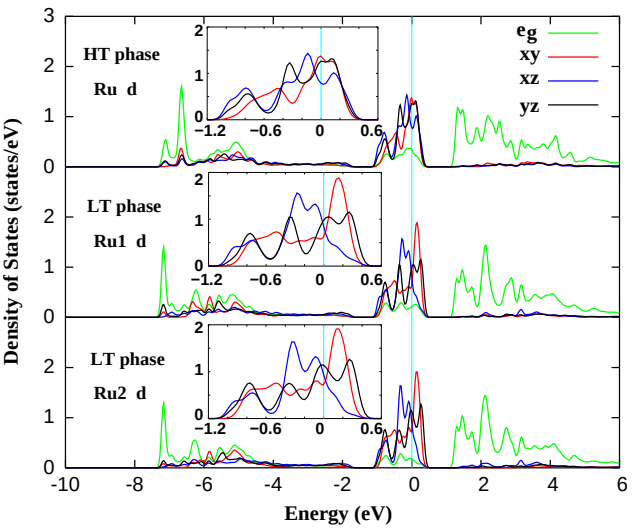

Fig. 7.3 (color online) LDA density of states of the Ru $4d$ orbitals in the high-temperature (HT, upper panel) and low-temperature (LT, middle and lower panels) phases. The insets show a close-up of the t_{2g} (xy, xz, and yz) states in the vicinity of the Fermi level set at 0 eV.

Figure 7.3 shows the Ru $4d$ density of states (DOS) calculated using the LDA for the nonmagnetic (NM) state. The inset shows a close-up of the t_{2g} levels and a calculation of the first moments supports the XAS analysis: for both the HT and LT phases, the xz orbital lies lowest and the splitting Δ'_{CF} between the higher lying yz and xy orbitals is less than 50 meV. It is the magnitude of this Δ'_{CF} relative to J_H which determines the spin state of the Ru^{4+} ion. To make a crude estimate: the $S_{\mathrm{CF}} = 1$ state ($xz^{\uparrow\downarrow}yz^{\uparrow}xy^{\uparrow}$) carries the Hund's stabilization energy of $3J_H$, whereas the $S_{\mathrm{CF}} = 0$ state ($xz^{\uparrow\downarrow}yz^{\uparrow\downarrow}$) has a total stabilization energy of $2J_H$ plus Δ'_{CF}. Assuming that 0.5 eV is a reasonable estimate for J_H, one must expect that a Δ'_{CF} of 0.05 eV is far from sufficient to obtain the $S_{\mathrm{CF}} = 0$ state. Obviously this is what the XAS experiments have revealed. Moreover, our LDA calculations also find that the ferromagnetic (FM) as well as the antiferromagnetic (AF) solution are more stable than the NM one, giving further support that the $S_{\mathrm{CF}} = 0$ is unfavorable. This was also found recently by LDA calculations of Eyert *et al.* [33].

Table 7.1 LSDA + U results for the total energy (per formula unit and relative to the lowest solution) and band gap in the low-temperature phase of $La_4Ru_2O_{10}$, calculated for the nonmagnetic (NM), ferromagnetic (FM), and three types of antiferromagnetic (AF) solutions. The exchange constants are found to be $J_x = 1.5$ meV, $J_y = 65.5$ meV, and $J_z = 4.5$ meV.

State	Exchange	Energy (meV)	Gap (eV)
NM	$\cdots$	775	$\cdots$
FM	$J_x + J_y + 2J_z$	152	$\cdots$
AF_{xyz}	$-J_x - J_y - 2J_z$	0	0.5
AF_{xy}	$-J_x - J_y + 2J_z$	18	0.3
AF_{yz}	$J_x - J_y - 2J_z$	3	0.4

The LDA results as shown in FIG. 7.3 predict a metallic state for both the HT and LT phases, and this is in strong disagreement with the observed semiconducting behavior with a gap of about 0.3 eV [17]. One should note, however, that the Fermi level is located in a narrow Ru t_{2g} band with no more than 1.5 eV width. This signals that modest electron correlation effects at the Ru sites will already be able to turn this material into a Mott insulator.We therefore set

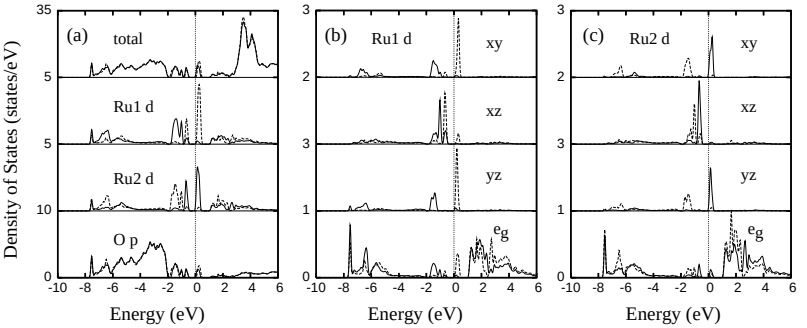

Fig. 7.4 Density of states (DOS) of the $La_4Ru_2O_{10}$ in the antiferromagnetic low-temperature phase calculated using LSDA + U. (a) Total DOS per formula unit, the 4d states of the two inequivalent Ru^{4+} ions, and the $2p$ states of all the ten oxygens; (b) orbitally resolved $4d$ states of Ru1 and (c) of Ru2. The solid (dashed) curves denote the up(down)-spin channels.

out to do LSDA + U calculations for the LT phase and found that a band gap of about 0.5 eV is indeed opened in the Ru t_{2g} band as can be seen from FIG. 7.4(a). Within the LSDA + U mean-field approach, the lowest state of this insulator is AF and is labeled as AF_{xyz} in TABLE 7.1 to indicate the AF alignment with the nearest neighbors along the x, y, and z directions (FIG. 7.1). The Ru^{4+} spin moment inside the muffin-tin sphere is about $1.2\mu_B$, confirming the XAS result that the spin state is $S = 1$ but not $S = 0$.

It is important to look now at the orbital character of the AF_{xyz} solution. Figures 7.4(b) and 7.4(c) show the orbitally resolved DOS of the AF aligned Ru1 and Ru2 ions. One can clearly see for each of the ions that the xy and yz orbitals (with the spins parallel) are singly occupied while the xz are doubly occupied. This double occupation is due to the Ru–O bonds being elongated along the x direction, see FIG. 7.1. We thus find an orbital ordered state which is different from the originally proposed doubly occupied xy and xz ($S = 0$) state [17].

As a result, the half-filled xy and yz orbitals are magnetically active. To explain the formation of the spin gap in the LT phase, it is crucial to identify the relevant exchange interactions in this system. We therefore have calculated other magnetic configurations: the FM and two more types of AF solutions, namely AF_{xy} and AF_{yz}. The $2\times La_4Ru_2O_{10}$ unit cell is used for all solutions, except for AF_{yz} where

the $4\times$ $La_4Ru_2O_{10}$ unit cell is taken with the doubling along the b direction (see FIG. 7.1).We also studied the NM solution, and confirmed that this is much higher in energy than the AF_{xyz}, by 775 meV per formula unit (TABLE 7.1). The NM solution is metallic, the FM half-metallic, and all AF insulating. The Ru^{4+} spin moment is $1.2 \pm 0.1\mu_B$ for all magnetic solutions.

The relative energies of the different magnetic states allow us to estimate the exchange constants J_x, J_y, and J_z along the x, y, and z directions (FIG. 7.1), respectively. With the FM being 130–150 meV higher in energy than the AF solutions, we thus have very large AF exchange interactions in this system. As listed in TABLE 7.1, we find $J_x = 1.5$ meV, $J_y = 65.5$ meV, and $J_z = 4.5$ meV. The significant anisotropy is related to the fact that *both* the xy and yz orbitals contribute to the exchange coupling along the y direction having the *short* Ru–O–Ru distance, while *only* the xy or yz orbital contributes to the x or z direction, respectively, having the *long* Ru–O–Ru distance. Hence we can consider the LT phase of $La_4Ru_2O_{10}$ as practically consisting of strongly coupled Ru–Ru dimers with weak interdimer coupling, or at most as two-leg ladders with $J_{\text{rung}} = J_y = 65.5$ meV and $J_{\text{leg}} = J_z = 4.5$ meV, with weak interladder coupling of 1.5 meV. Those rather well isolated Ru–Ru dimers or rungs will have the singlet ground state [34]. This explains naturally the appearance of a spin gap in the LT phase, which, according to our calculations, should be about 60 meV, in reasonable agreement with the measured value of 40 meV [17]. The dimer character of the spin gap seems also to agree with the results of the single-crystal neutron scattering [35].

To summarize, XAS measurements revealed that the Ru^{4+} ions in $La_4Ru_2O_{10}$ remain in the $S = 1$ spin state across the structural phase transition and spin-gap formation. LSDA + U calculations provided support for this finding and identified the distinct orbital ordering accompanying the structural transition. Crucial is that with LSDA + U we were able to estimate the intersite antiferromagnetic exchange interactions and found them to be highly anisotropic. This brought us to the conclusion that the spin-gap opening is due to the formation of Ru–Ru singlet dimers. Such a transition is rather unusual since $La_4Ru_2O_{10}$ is a two-dimensional $S = 1$ system; it is largely driven by orbital ordering which amplifies the importance of orbital physics in correlated systems.

1 References

[1] M. Imada, A. Fujimori, and Y. Tokura, *Metal-insulator transitions*, Review of Modern Physics **70**, 1039 (1998). DOI: 10 .1103/RevModPhys.70.1039.

[2] Y. Tokura and N. Nagaosa, *Orbital physics in transition-metal oxides*, Science **288**, 462 (2000). DOI: 10.1126/science.288 .5465.462.

[3] A. P. Ramirez, *Colossal magnetoresistance*, Journal of Physics: Condensed Matter **9**, 8171 (1997). DOI: 10.1088/0953-8984/9 /39/005.

[4] D. I. Khomskii and G. A. Sawatzky, *Interplay between spin, charge and orbital degrees of freedom in magnetic oxides*, Solid State Communications **102**, 87 (1997). DOI: 10.1016/S0038 -1098(96)00717-X.

[5] T. Mizokawa and A. Fujimori, *Unrestricted Hartree-Fock study of transition-metal oxides: Spin and orbital ordering in perovskite-type lattice*, Physical Review B **51**, 12880 (1995). DOI: 10.1103 /PhysRevB.51.12880.

[6] T. Mizokawa and A. Fujimori, *Electronic structure and orbital ordering in perovskite-type* 3*d transition-metal oxides studied by Hartree-Fock band-structure calculations*, Physical Review B **54**, 5368 (1996). DOI: 10.1103/PhysRevB.54.5368.

[7] T. Mizokawa and A. Fujimori, *Spin, charge, and orbital ordering in mn perovskite oxides studied by model Hartree-Fock calculations*, Physical Review B **56**, R493 (1997). DOI: http://link .aps.org/abstract/PRB/v56/pR493.

[8] Y. Ren, T. T. M. Palstra, D. I. Khomskii, E. Pellegrin, A. A. Nugroho, A. A. Menovsky, and G. A. Sawatzky, *Temperature-induced magnetization reversal in a* YVO_3 *single crystal*, Nature (London) **396**, 441 (1998). DOI: 10.1038/24802.

[9] G. R. Blake, T. T. M. Palstra, Y. Ren, A. A. Nugroho, and A. A. Menovsky, *Transition between orbital orderings in* YVO_3, Physical Review Letters **87**, 245501 (2001). DOI: 10.1103 /PhysRevLett.87.245501.

[10] C. Ulrich, G. Khaliullin, J. Sirker, M. Reehuis, M. Ohl, S. Miyasaka, Y. Tokura, and B. Keimer, *Magnetic neutron scattering study of YVO_3: Evidence for an orbital peierls state*, Physical Review Letters **91**, 257202 (2003). DOI: 10.1103/PhysRevLett .91.257202.

[11] J.-H. Park, L. H. Tjeng, A. Tanaka, J. W. Allen, C. T. Chen, P. Metcalf, J. M. Honig, F. M. F. de Groot, and G. A. Sawatzky, *Spin and orbital occupation and phase transitions in V_2O_3*, Physical Review B **61**, 11506 (2000). DOI: 10.1103/PhysRevB .61.11506.

[12] M. W. Haverkort, Z. Hu, A. Tanaka, W. Reichelt, S. V. Streltsov, M. A. Korotin, V. I. Anisimov, H. H. Hsieh, H.-J. Lin, C. T. Chen, D. I. Khomskii, and L. H. Tjeng, *Orbital-assisted metal-insulator transition in VO_2*, Physical Review Letters **95**, 196404 (2005). DOI: 10.1103/PhysRevLett.95.196404.

[13] M. Isobe, E. Ninomiya, A. N. Vasil'ev, and Y. Ueda, *Novel phase transition in spin-1/2 linear chain systems: $NaTiSi_2O_6$ and $LiTiSi_2O_6$*, Journal of the Physical Society of Japan **71**, 1423 (2002). DOI: 10.1143/JPSJ.71.1423.

[14] P. G. Radaelli, Y. Horibe, M. J. Gutmann, H. Ishibashi, C. H. Chen, R. M. Ibberson, Y. Koyama, Y.-S. Hor, V. Kiryukhin, and S.-W. Cheong, *Formation of isomorphic Ir^{3+} and Ir^{4+} octamers and spin dimerization in the spinel $CuIr_2S_4$*, Nature (London) **416**, 155 (2002). DOI: 10.1038/416155a.

[15] M. Schmidt, W. R. II, P. G. Radaelli, K. Refson, N. M. Harrison, and S. W. Cheong, *Spin singlet formation in $MgTi_2O_4$: Evidence of a helical dimerization pattern*, Physical Review Letters **92**, 056402 (2004). DOI: 10.1103/PhysRevLett.92.056402.

[16] D. I. Khomskii and T. Mizokawa, *Orbitally induced peierls state in spinels*, Physical Review Letters **94**, 156402 (2005). DOI: 10.1103/PhysRevLett.94.156402.

[17] P. Khalifah, R. Osborn, Q. Huang, H. W. Zandbergen, R. Jin, Y. Liu, D. Mandrus, and R. J. Cava, *Orbital ordering transition in $La_4Ru_2O_{10}$*, Science **297**, 2237 (2002). DOI: 10.1126/science .1075556.

[18] J. D. Denlinger (to be published).

[19] F. M. F. de Groot, *X-ray absorption and dichroism of transition metals and their compounds*, Journal of Electron Spectroscopy and Related Phenomena **67**, 529 (1994). DOI: 10.1016/0368-2048(93)02041-J.

[20] See the "Theo Thole Memorial Issue", Journal of Electron Spectroscopy and Related Phenomena **86**, 1 (1997). DOI: 10.1016/S0368-2048(97)00039-X.

[21] Z. Hu, H. von Lips, M. S. Golden, J. Fink, G. Kaindl, F. M. F. de Groot, S. Ebbinghaus, and A. Reller, *Multiplet effects in the Ru-$L_{2,3}$ x-ray-absorption spectra of Ru(IV) and Ru(V) compounds*, Physical Review B **61**, 5262 (2000). DOI: 10.1103/PhysRevB.61.5262.

[22] Z. Hu, H. Wu, M. W. Haverkort, H. H. Hsieh, H.-J. Lin, T. Lorenz, J. Baier, A. Reichl, I. Bonn, C. Felser, A. Tanaka, C. T. Chen, and L. H. Tjeng, *Different look at the spin state of Co^{3+} ions in a CoO_5 pyramidal coordination*, Physical Review Letters **92**, 207402 (2004). DOI: 10.1103/PhysRevLett.92.207402.

[23] A. Tanaka and T. Jo, *Resonant 3d, 3p and 3s photoemission in transition metal oxides predicted at 2p threshold*, Journal of the Physical Society of Japan **63**, 2788 (1994). DOI: 10.1143/JPSJ.63.2788.

[24] T. Mizokawa, L. H. Tjeng, G. A. Sawatzky, G. Ghiringhelli, O. Tjernberg, N. B. Brookes, H. Fukazawa, S. Nakatsuji, and Y. Maeno, *Spin-orbit coupling in the Mott insulator Ca_2RuO_4*, Physical Review Letters **87**, 077202 (2001). DOI: 10.1103/PhysRevLett.87.077202.

[25] T. Mizokawa, L. H. Tjeng, H.-J. Lin, C. T. Chen, S. Schuppler, S. Nakatsuji, H. Fukazawa, and Y. Maeno, *Orbital state and metal-insulator transition in $Ca_{2-x}Sr_xRuO_4$ ($x = 0.0$ and 0.09) studied by x-ray absorption spectroscopy*, Physical Review B **69**, 132410 (2004). DOI: 10.1103/PhysRevB.69.132410.

[26] Both $La_4Ru_2O_{10}$ and Ca_2RuO_4 are two dimensional and have almost the same octahedral $\langle Ru^{4+}–O\rangle$ bond lengths and similar t_{2g} bandwidths of about 1.5 eV.

[27] W. A. Harrison, *Electronic Structure and the Properties of Solids: The Physics of the Chemical Bond*. (Dover, New York, 1989). ISBN: 0486660214.

[28] Parameters for RuO_6 cluster [eV]: $U_{dd} = 3.0$, $U_{cd} = 2.0$, $\Delta = 2.0$, $pd\sigma = -2.1$ for 2.01 Å, $10Dq = 1.9$, $Dt = 0.04$, $Du = 0.04$, $Dv = 0.00$, $\zeta = 60\%$ of Hartree-Fock value; $Ds = -0.03$ ($S = 1$, HT), -0.06 ($S = 1$, LT), $+0.90$ ($S = 0$, LT).

[29] V. I. Anisimov, I. V. Solovyev, M. A. Korotin, M. T. Czyżyk, and G. A. Sawatzky, *Density-functional theory and nio photoemission spectra*, Physical Review B **48**, 16929 (1993). DOI: 10 .1103/PhysRevB.48.16929.

[30] P. Blaha *et al.* http://www.wien2k.at.

[31] Z. Fang, N. Nagaosa, and K. Terakura, *Orbital-dependent phase control in* $Ca_{2-x}Sr_xRuO_4$ *(*$0 \leq x \leq 0.5$*)*, Physical Review B **69**, 045116 (2004). DOI: 10.1103/PhysRevB.69.045116.

[32] Using a larger Hubbard $U = 5$ eV does not change the spin-singlet dimer picture at all, but gives a too large band gap of 1.1 eV.

[33] V. Eyert, S. G. Ebbinghaus, and T. Kopp, *Orbital ordering and spin-ladder formation in* La_2RuO_5, Physical Review Letters **96**, 256401 (2006). DOI: 10.1103/PhysRevLett.96.256401.

[34] Inclusion of the spin-orbit coupling does not affect our conclusions: the xz orbital in the LT phase being lower than the yz and xy by the CFS of ≈ 300 meV together with the band formation make the weaker spin-orbit coupling of ≈ 150 meV to be less operative. The exchange constants change by less than 5 meV and the orbital moment is small, not more than about $0.2\mu_B$.

[35] R. Osborn (private communication).

8 $Ca_{2-x}Sr_xRuO_4$

The measurements and calculations have been performed together with Zhiwei Hu. The experiments have been done at NSRRC in collaboration with T. T. Tran and T. Mizokawa and with support of Hui-Huang Hsieh (Chung Cheng Institute of Technology, National Defense University), Ling-Yun Jang (NSRRC), and Keng S. Liang (NSRRC), and at BESSY with Frank Schäfers and Marcel Mertin. The samples were prepared by Satoru Nakatsuji and Yoshiteru Maeno. The results were discussed with Maurits W. Haverkort and L. Hao Tjeng. The spectra were calculated using the XTLS program of Arata Tanaka.

THE class of $Ca_{2-x}Sr_xRuO_4$ systems shows a rich phase diagram [1–8]. The most prominent member is the Sr_2RuO_4, which becomes superconducting at 0.93 K [9–10]. Sr_2RuO_4 contains of layers of octahedra and its structure (space group $I4/mmm$) closely resembles the original high-T_c superconductors; it is probably a triplet paired superconductor [9–10] and the pairing mechanism is believed to be at least partially of magnetic origin [11–16]. The other end member of this series is the antiferromagnetic Mott insulator Ca_2RuO_4 [3–5, 7, 17–19].

As FIG. 8.1 shows, the $I4/mmm$ structure retains for $x = 2$ down to $x = 1.5$. Then the unit cell is doubled with space group $I4_1/acd$; going from $x = 1.5$ to $x = 0.5$ the octahedra rotate about the c axis up to 12.8° for $x = 0.5$; while the compounds remain paramagnetic metals in this region, there is a critical enhancement of susceptibility towards $x = 0.5$ [5]. For $x < 0.5$ the octahedra start to tilt (T phase). For $0.2 < x < 0.5$ $Ca_{2-x}Sr_xRuO_4$ exhibits metamagnetic and near $x = 0.5$ even an almost ferromagnetic state [1, 5, 20–21]. For $x < 0.2$ the tilts are ordered into the spacegroup $Pbca$ with a maximal tilt at low temperature near 12°. $Ca_{2-x}Sr_xRuO_4$ is metallic for $x > 0.2$ and for high temperatures. For $x < 0.2$ an insulating phase appears; the associated metal-insulator transition-temperature rises for smaller x, reaching $T_{MI} = 260$ K for $x = 0$. At low temperatures the insulating phase is antiferromagnetic. Note that Sr has only a larger ionic radius as Ca but the same valence.

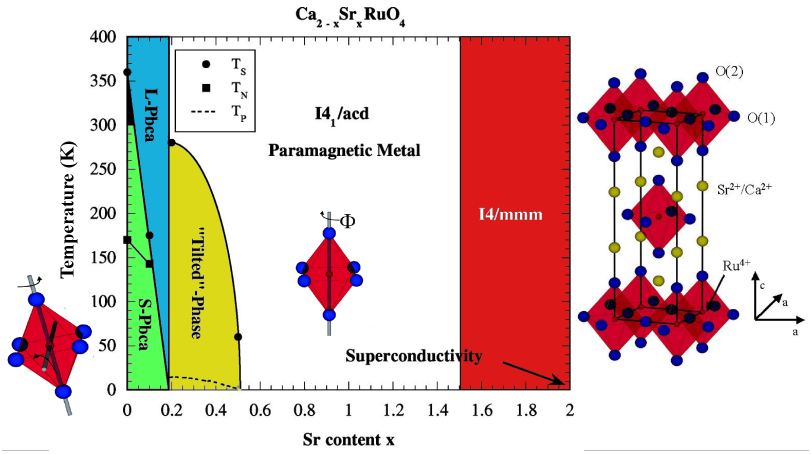

Fig. 8.1 (color online) Phase diagram of $Ca_{2-x}Sr_xRuO_4$, including the different structural and magnetic phases; the only nonmetallic phase is the antiferromagnetic S-*Pbca*. The L- and S-*Pbca* denote, respectively, elongated and compressed octahedra. Figure taken from Steffens [22]; the phase diagram has been taken from Fried *et al.* [1]. (Reprinted with permission. Copyright 2001 by the American Physical Society.)

8.1 Ca_2RuO_4

In Ca_2RuO_4 the ruthenium ion is tetravalent ($4d^4$) and due to the large t_{2g}–e_g crystal-field splitting, all four electrons are in the t_{2g} subshell; the spin state is thus $S = 1$. At low temperature (11 K), the octahedra is flat (compressed) with an in-plane Ru–O distances of 2.02 Å and an out-of-plane (apical) distance of 1.97 Å. When increasing the temperature the apical/in-plane distance ratio changes gradually; at room temperature the octahedron is almost regular (1.99 Å) while for 400 K it is elongated (in plane 1.95 Å, apical 2.04 Å) [3–4]. This structural change is associated with magnetic and electronic changes. Below the Néel temperature of $T_N \approx 110$ K the calcium ruthenate is an antiferromagnetic insulator with magnetization in b direction [4]; between 110 K and 360 K it is a paramagnetic insulator. It then undergoes a metal-insulator transition to become a paramagnetic metal for temperatures above 360 K. Ca_4RuO_4 has an optical gap of $E_{\text{gap}} = 0.5$ eV [23], which is ten times as big as one naïvely expects from the metal-insulator temperature, i.e. $E_{\text{gap}} \approx k_B T_{\text{MIT}}$. This is simliar to V_2O_3, VO_2, and Ti_2O_3, where the gap is also one order

of magnetude larger than $k_B T_{\mathrm{MIT}}$ [24–25]. There the metal-insulator transition is accompanied by dramatic changes of the spin and orbital structure, which one can therefore also expect for Ca_2RuO_4. In the Hubbard model, it depends on the ratio between electron repulsion U and band width W whether a material is a Mott insulator or a metal. However, the effective U and W depend in turn strongly on the spin and orbital structure.

8.1.1 Orbital occupation

The temperature-dependent structural changes are accompanied by large changes in the orbital occupation. These changes have indeed be found in a x-ray absorption study at the oxygen K edge of Ca_2RuO_4 [26–27]. However, extracting the orbital occupation of the Ru $4d$ from the O-K edge is a rather indirect method and there are discussions in literature about these numbers and their accuracy [26–28].

We therefore performed XAS measurements at the Ru-$L_{2,3}$ edge. These were done at the Taiwan NSRRC 15B beam line, equipped with a double-Si(111)-crystal monochromator, delivering photons from 2 keV and up. Additionally, we performed a temperature-dependence measurement at the KMC-1 beamline at BESSY. The spectra were recorded using the total-electron-yield method in a chamber with a base pressure in the low 10^{-10} mbar range. Clean sample areas were obtained by cleaving the crystals in situ. The photon-energy resolution at the Ru-$L_{2,3}$ edges ($h\nu \approx 2.9$ keV) was set at 0.6 eV.

Figure 8.2 shows the Ru-$L_{2,3}$ spectra measured with the electric field E polarized perpendicular to the c axis (dashed curve) and almost parallel to the c axis[9] (solid curve). The difference between the two directions, the linear dichroism, reduces going from 78 K to 300 K and then reverses for 380 K. At 78 K the octahedra are flat, therefore one expects that the xy is occupied and lower in energy than the yz and zx orbitals. If one looks at the first peak (A) at both L_3 and L_2 edge, one sees that the $E||c$ one is higher and thus contains more

[9] The sample surface is perpendicular to the c axis (easy cleavage plane as calcium ruthenate is layered). In order to measures $E||c$, the x-rays hit the sample at grazing incidence (70°); for consistency, the same angle is used for $E \perp c$. To do so, the sample is mounted on a wedge. As the intensity is proportional to $\cos^2$, the measurement has an error of about $\cos^2 20° \approx 10$ %.

holes as expected. (The first peak (A) can be associated with the t_{2g} orbitals and the second, larger peak (B) with the e_g orbitals; note that the presence multiplets, a mixing of states due to spin-orbit coupling, and ligand hybridization reduce the simplicity of the analysis.) For room temperature (295 K) the octahedra are almost regular, which can also be seen in the spectra. And for the metallic 380 K the octahedra are elongated and the $E \perp c$ peak is now higher, indicating a hole in xy. The less pronounced peak can be attributed to the less localized electrons in the metallic state.

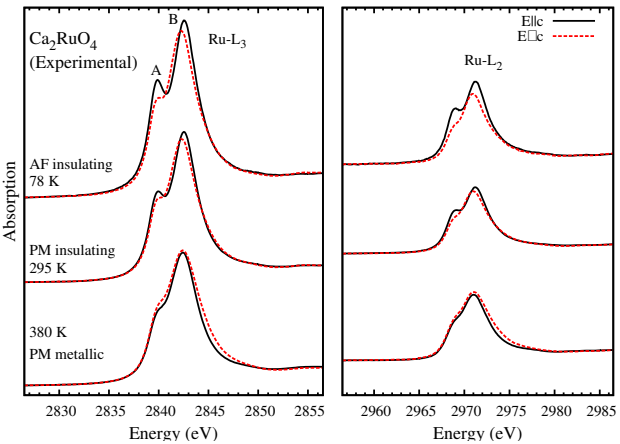

Fig. 8.2 (color online) Ru-$L_{2,3}$ XAS spectra of Ca_2RuO_4 taken with the electric field parallel (solid curve) and perpendicular (dashed curve) to the c axis in the antiferromagnetic insulating phase at 78 K, in the paramagnetic insulating phase at 295 K, and in the metallic paramagnetic phase at 380 K.

Besides the detailed spectra in all three phases (antiferromagnetic insulating, paramagnetic insulating, and paramagnetic metallic), the temperature dependence of the spectra is useful. The most prominent change when changing the temperature is the peak (A) of the L_3 edge for light polarized along the c axis (cf. FIG. 8.2). We have monitored the detailed temperature depencence of peak A across the three phases at BESSY. The result is shown in FIG. 8.3, where the curve is given by the height of the first peak normalized by the height of the second. One sees a gradual change with a small jump at the Néel temperature,

and around the metal-insulator transition at 380 K a big jump occurs and a hysteresis is recognizable. The gradual change below T_{MIT} is typical for correlated insulators with active-spin orbit coupling [29].

Using resonant x-ray diffraction an additional phase was observed at 260 K, which has been attributed to orbital ordering [30]. While the ordering itself cannot be measured in XAS due to the averaging over all Ru sites, one may expect a change of the orbital occupation and thus in the XAS spectra upon the appearance of the orbital ordering. However, in FIG. 8.2 the lineshape around 260 K shows no particularities.

The spectra above (FIGS. 8.2 and 8.3) and the result of previous O-K edge XAS study [26–27] show dramatic changes of the orbtial occupation while the changes in the crystal structure are comparably small. Especially large are the changes in the orbital occupation across the metal-insulator transition. (See also TABLE 8.1 in the following section.)

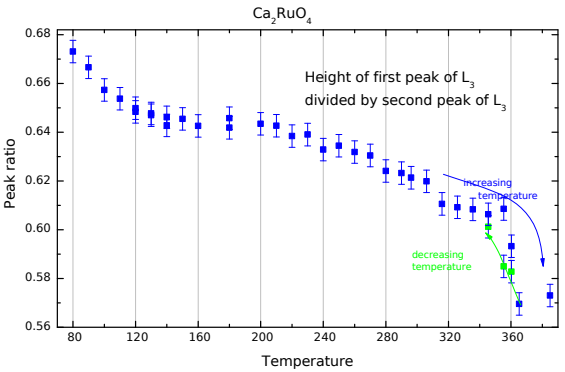

Fig. 8.3 (color online) Temperature-dependence of the Ru-L_3 edge; the curve shows the ratio of the first peak of the L_3 edge divided by the main peak for light polarized in c direction.

The gradual change of the orbital occupation, visible in the change of of the ratio curve of FIG. 8.3, could indicate that the spin-orbit coupling in Ca_2RuO_4 plays a role. If one compares the CI cluster calculation with and without spin-orbit coupling (see FIG. 8.5), one sees that without spin-orbit coupling the relative intensity of the $E \perp c$ spectrum at

the L_3 edge is strongly suppressed and peak (A) at the L_2 edge is enhanced. Only with spin-obrit coupling the experimental spectra can be reproduced. This result is in line with Mizokawa *et al.* [26]: They showed using spin-resolved circularly polarized photoemission spectroscopy that a substantial orbital angular moment is induced and estimated $\langle \sum_i l_x^i \cdot s_x^i \rangle \approx -0.28$, which is comparable to the value of CoO where an orbital moment of about $1\mu_B$ was found.[10] This result is in line with our configuration-interaction cluster calculations, but in contrast to DFT calculations which show that for the band structure the spin-orbit coupling does not seem to play an important role [31].

8.1.2 Calculation

We used configuration-interaction cluster calculations to simulated the XAS spectra (FIG. 8.2); the preliminarly simulated spectra are shown in FIG. 8.4, which match the experimental spectra quite well. (See Note 32 for the used parameters.) From the calculations, the orbital occupation numbers can be extracted, see TABLE 8.1; the numbers match the expectations from the crystal structure.

8.2 $Ca_{1.91}Sr_{0.91}RuO_4$

Upon substitution of calcium by strontium, the metal-insulator transition temperature decreases quickly whereas the Néel temperature decreases much slower. For $x = 0.09$ both transitions occur approximately simultaneously at $T = 155$ K. If one compares the XAS spectra of $Ca_{1.91}Sr_{0.09}RuO_4$ (FIG. 8.6) at 78 K with those of Ca_2RuO_4 (FIG. 8.2), one sees that the spectra lie between the 78 K and 295 K spectra of Ca_2RuO_4. And the room-temperature spectrum of $x = 0.09$ resembles the 380 K spectrum of Ca_2RuO_4.

[10] Preliminary results of us show for the metallic Sr_2RuO_4 similary high values for $\langle \sum_i l_x^i \cdot s_x^i \rangle$. These spin-resolved measurements where done at ID8 at the ESRF together with Nicholas Brookes; however, the count rates was rather low and thus the result has a rather large error bar and is not reliable.

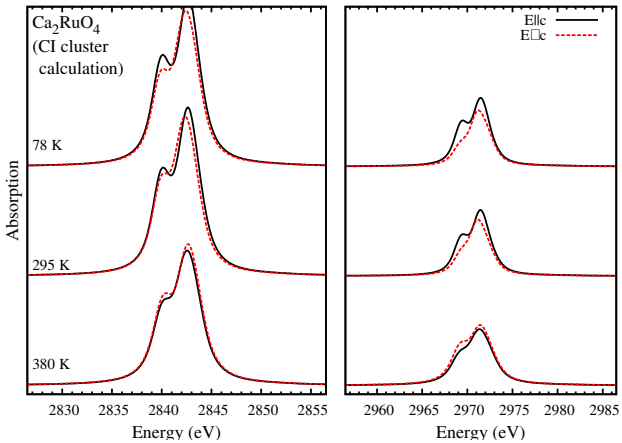

Fig. 8.4 (color online) Simulated Ru-$L_{2,3}$ XAS spectra of Ca_2RuO_4 for the antiferromagnetic (78 K), paramagnetic insulating (295 K), and the paramagnetic metallic phase (380 K).

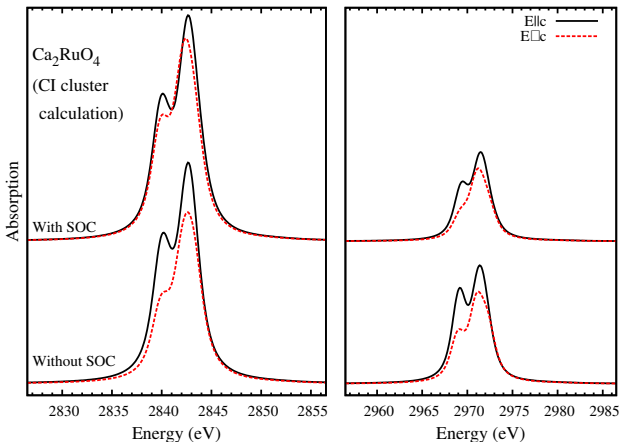

Fig. 8.5 (color online) Simulated Ru-$L_{2,3}$ XAS spectra of Ca_2RuO_4 for the antiferromagnetic (78 K) phase including and without spin-orbit coupling.

8.3 The effective moment $\tilde{J}$ problem

In Ca_2RuO_4 the ruthenium ion is formally (i.e. ignoring hybridization) 4+ and is therefore in a $4d^4$ state. Assuming non-distorted octahedral

Table 8.1 Hole occupations as determined via configuration-interaction cluster calculation from the experimental Ru-$L_{2,3}$ XAS for Ca_2RuO_4.

Hole occupation	xy	yz	zx
Antiferromagnetic insulating, 78 K	0.34	0.84	0.84
Paramagnetic insulating, 295 K	0.45	0.79	0.79
Paramagnetic metal, 380 K	0.83	0.58	0.59

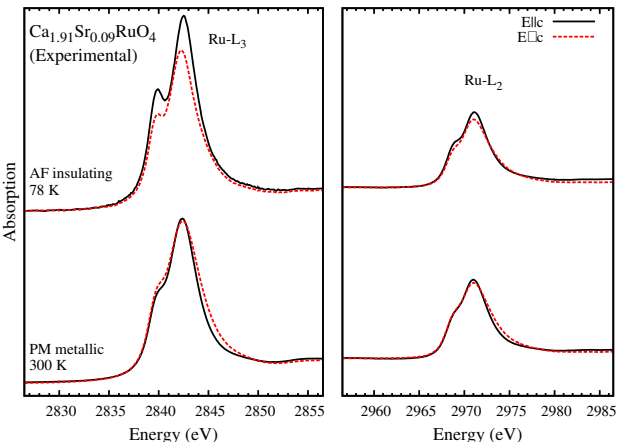

Fig. 8.6 (color online) Ru-$L_{2,3}$ XAS spectra of $Ca_{1.91}Sr_{0.09}RuO_4$ taken with the electric field parallel (solid curve) and perpendicular (dashed curve) to the c axis in the antiferromagnetic insulating phase at 78 K and in the metallic paramagnetic phase at 300 K.

symmetry (O_h, $m3m$), the states split into the doubly degenerated, higher-lying e_g (Γ_3) and the triply degenerated, lower-lying t_{2g} (Γ_5) states. As the crystal-field splitting between the t_{2g} and e_g levels is large in the 4d transition metal Ru, it suffices to only regard to the t_{2g} subshell. Within the t_{2g} one has the same matrix elements as in the $L = 1$ state of p orbitals and thus one can define an effective orbital moment $\tilde{L}$ by projecting L on the t_{2g} manifold, i.e. $\langle L \rangle_{t_{2g}} = \alpha \tilde{L}$, where α depends on the detailed structure of the t_{2g} and is here $\alpha = -1$ [33].[11] The spin-orbit splitting is given by $H_{\mathrm{SO}} = \lambda \left(\langle \boldsymbol{L} \rangle_{t_{2g}} \cdot \boldsymbol{S} \right) =$

[11] The $\alpha = -1$ is valid for a t_{2g} (Γ_5) triplet originating in a D term and can be understood as follows. $d_1 = -(d_{zx} + \mathrm{i}d_{yz})/\sqrt{2}$. As the p_x, p_y, p_z transform under O like d_{yz}, d_{zx}, d_{xy} [33, pp 632ff], one can replace $d_{zx} + \mathrm{i}d_{yz}$ by $p_y + \mathrm{i}p_x$. It is $p_x = -(p_1 - p_{-1})/\sqrt{2}$

$\alpha\lambda(\tilde{\boldsymbol{L}} \cdot \boldsymbol{S}) = \tilde{\lambda}(\tilde{\boldsymbol{L}} \cdot \boldsymbol{S})$ [33, pp 832ff]. In our case, we thus have $\tilde{L} = 1$, $S = 1$ and $\tilde{\lambda} = -\lambda$. As the subshell is more than half filled, one expects $J = |L + S|$. However, as the sign of $\tilde{\lambda}$ is reversed, one needs to calculate $\tilde{J} = |\tilde{L} - S| = 0$, which means that the ground state is a singlet and a singlet is nonmagnetic.

This contrasts with an ordered moment of $1.3\mu_B$ (aligned along the b axis) as determined by Braden *et al.* using neutrons [4]. Susceptibility measurements (FIGS. 8.7 and 8.8) by Cao *et al.* [34] determined a Néel temperature T_N of 110 K and a relatively low saturation magnetization of $M_{\text{sat}} \approx 0.4\mu_B$/Ru using a magnetic field of up to 30 T (at 5 K). (For Ru $S = 1$ one would expect $M_{\text{sat}} \approx 2\mu_B$/Ru.) Above T_N the susceptibility M/H is "unusual, almost linear with increasing T" [34]; a Curie-Weiss fit yields an unrealistic effective moment of about $4\mu_B$/Ru – much higher than $\approx 2.8\mu_B$/Ru expected for Ru^{4+} with $S = 1$. Also according to the magnetisation measurement the moment lies in the a-b plane. Regarding the susceptibility data, one should, however, be careful with the interpretation: If a material has a large magnetocrystalline anisotropy, as in this case, the Curie–Weiss law gives misleading results (see Chapter 5 and Ref. 35). (Additionally, as on can see in FIG. 8.8 the saturation magnetization can usually not be reached for antiferromagnets.)

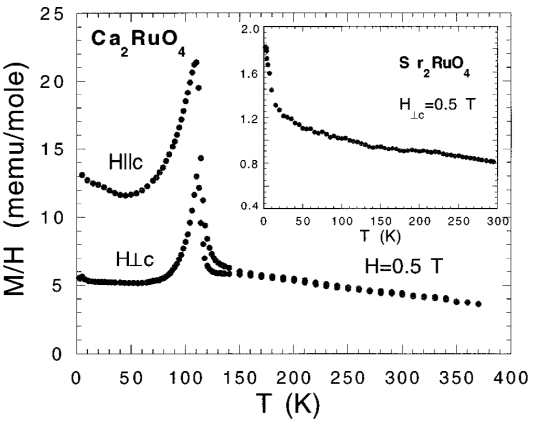

Fig. 8.7 Magnetic susceptibility along two principal directions for single-crystal Ca_2RuO_4. The inset shows the susceptibility of Sr_2RuO_4; note the much smaller susceptibility scale than for Ca_2RuO_4. Figure taken from Cao *et al.* [34].

and $p_y = \mathrm{i}(p_1 + p_{-1})/\sqrt{2}$ and thus $d_1 \mathrel{\widehat{=}} -(p_y + \mathrm{i}p_x)/\sqrt{2} = -\mathrm{i}p_{-1}$, i.e. d_1 corresponds to p_{-1}. (Hereby is $d_1 = Y_2^1$ and $p_1 = Y_1^1$.)

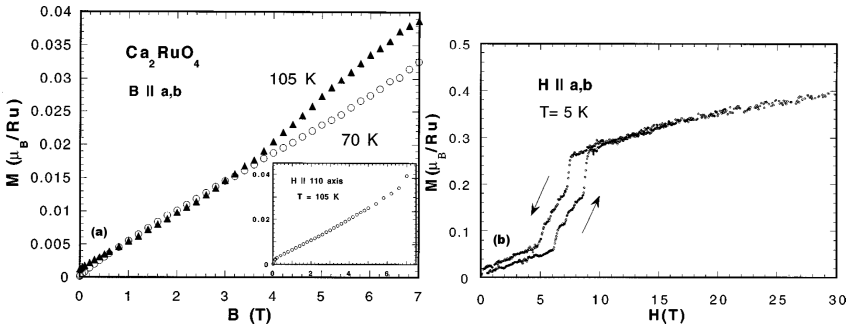

Fig. 8.8 (a) Magnetization versus applied field along the in-plane direction for two temperatures. The inset shows comparable data for the [110] direction. The break in M vs H at 3.5 T for $T = 105$ K is probably a spin reorientation transition. (b) Very high field $M(H)$ showing a hysteretic metamagnetic transition at about 9 T. The magnetization by $H = 30$ T is well below the value (≈ 1.4–$1.8\mu_B$/Ru) expected for the $S = 1$ $4d^4$ configuration for Ru^{4+}. Figure taken from Cao *et al.* [34].

8.3.1 In octahedral symmetry

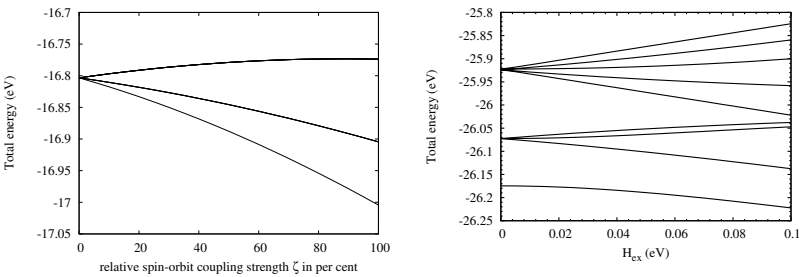

Fig. 8.9 (a) Energy-level diagram showing the splitting of the lowest 9 states in octahedral symmetry with the spin-orbit coupling (SOC) ζ (relative to the Hartree–Fock value). The nine-fold degenerated state splits into a singlet, triplet and quintet. (b) The levels are further split using an exchange-field $H_{\rm ex}$.

In octahedral symmetry without spin-orbit coupling and without any external magnetic B or internal exchange field $H_{\rm ex}$, the ground state is nine-fold degenerated. If the spin-orbit coupling is turned on, the states split [see FIG. 8.9(a)] three states – a singlet ground state and a triplet and quintet excited state. The degeneracy of the latter states can

be seen when an exchange field is applied (FIG. 8.9(b)). Figure 8.10 depicts the lowest nine isotropic XAS spectra with spin-orbit coupling but without exchange field; here, the triplet is 99.9 meV higher in energy than the ground state. This energy difference of about 100 meV ($\approx$ 1160 K) is rather large compared with e.g. the Néel temperature of T_N = 110 K ($\approx$ 9.5 eV) and while the exchange-field reduces the energy gap between singlet and triplet, it still remains relatively large.

For the configuration-interaction cluster calculation, the following settings have been used: Δ_{CF} = 1.6eV, U_{4d4d} = 5eV, U_{4d2p} = 4 eV, Δ = 0, t_{pp} = 0.7 eV, Slater-integral reduction to 70% of their Hartree-Fock value, Hybridization V_{e_g} = 4.37 eV and $V_{t_{2g}}$ = 2.38 eV (115% of Harrison's rule). Broadening: Γ_{Lorenz} = 0.4, Γ_{Gauss}: 0.7 at the L_3 and 0.5 at the L_2 edge.)

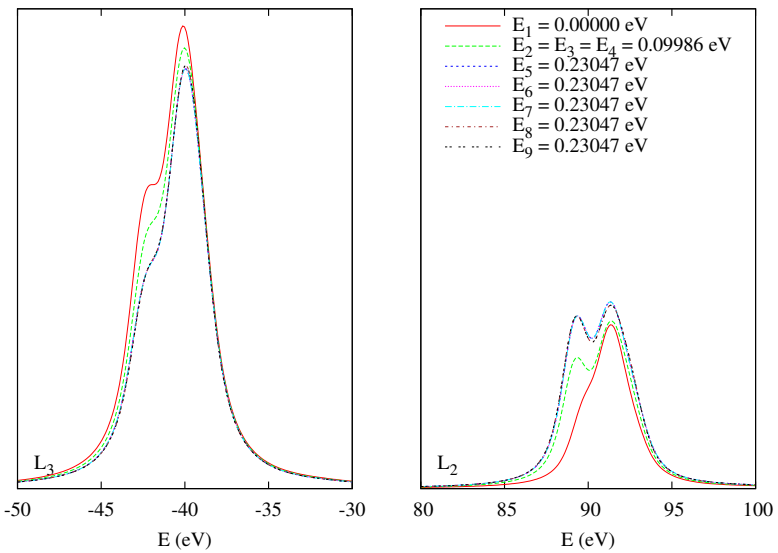

Fig. 8.10 (color online) Calculated lowest nive spectra in octaheral symmetry (Δ_{CF} = 1.6 eV) with spin-orbit coupling and without exchange field. One obtains one spectrum for the singlet, three identical ones for the a triplet, and five identicial a quintet.

8.3.2 In tetragonal symmetry

If one now changes the c/a ratio, the octahedron is in tetragonal symmetry (D_{4h}, $4mm$), the t_{2g} state splits into a doubly degenerated

e_g state and as non-degenerate b_{2g} state. Figure 8.11 shows the energy-level diagram in dependence of the Δt_{2g} splitting; rather arbitrarily the Δe_g splitting has been chosen as $\Delta e_g = 3\Delta t_{2g}$. As the calculation shows, also a tetragonal distrotion does not help to reduce the gap significantly.

However, already a relative small exchange field is able to generate a magnetic moment in the singlet ground state as one can see in FIG. 8.12 (cf. also Ref. 36); the increase in moment is accompanied by an orbital occpuation change from 1.68 to 1.77 for xy and a decrease of yz/zx from 1.22 to 1.18 in going from $H_{\mathrm{ex}} = 0$ to 100 meV, at the same time the energy distance between the ground-state singlet and the first excited state increases from 64 to 117 meV. The calculation has been done in D_{4h} symmetry with the 77 K parameters shown in Note 32. Hereby the exchange-field is a simplistic approach to include the intersite interaction. The proper way is to take band formation into account; this can be mimicked by doing multi-site cluster calculations.

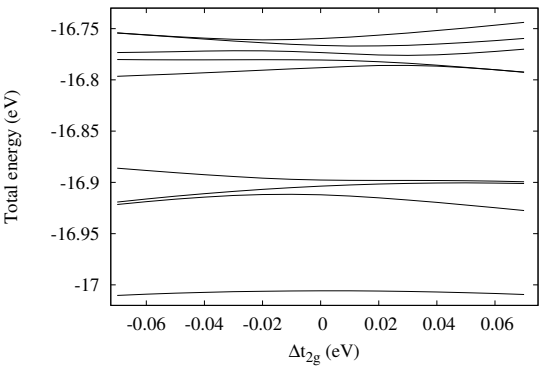

Fig. 8.11 Energy-level diagram depending on the tetragonal distortion Δt_{2g} with $\Delta e_g = 3\Delta t_{2g}$ and an exchange field of 15 meV.

8.4 Conclusion

We have shown that the ruthenium orbital occupation of Ca_2RuO_4 changes strongly with temperature, especially across the metal-insulator transition; large changes could also be observed for $Ca_{1.91}Sr_{0.09}RuO_4$.

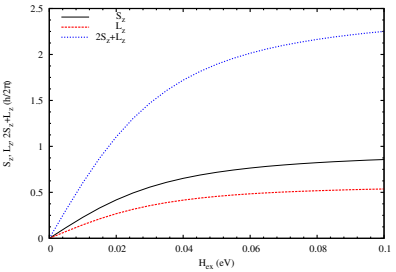

Fig. 8.12 (color online) Spin and orbital moment, and magnetization $|M_z| = 2S_z + L_z$ of the ground state in dependence of the exchange field.

The changes in the orbital (and spin) correlations in turn are responsible for the large gap compared with the comparibly small metal-insulator transition temperature. The temperature dependence shows magnetostriction effects, which indicate that spin-orbit coupling is active. The cluster-calculation is able to nicely reproduce the spectra, however, the issue that the lowest state in the calculation is a nonmagnetic singlet state whereas Ca_2RuO_4 is an antiferromagnet is not fully solved, even though that through an exchange field the ground state becomes magnetic. The effects of band formation should be included and multi-cluster calculation should be done to further investigate this issue, which might also help to understand the metamagnetism in $Ca_{2-x}Sr_xRuO_4$.

8.5 References

[1] O. Friedt, M. Braden, G. André, P. Adelmann, S. Nakatsuji, and Y. Maeno, *Structural and magnetic aspects of the metal-insulator transition in $Ca_{2-x}Sr_xRuO_4$*, Physical Review B **63**, 174432 (2001). DOI: 10.1103/PhysRevB.63.174432.

[2] O. Friedt, Ph.D. thesis, Université Paris XI, Paris, (2003). http://www-llb.cea.fr/theses/friedt_2003.pdf

[3] O. Friedt, P. Steffens, M. Braden, Y. Sidis, S. Nakatsuji, and Y. Maeno, *Strongly enhanced magnetic fluctuations in a large-mass layered ruthenate*, Physical Review Letters **93**, 147404 (2004). DOI: 10.1103/PhysRevLett.93.147404.

[4] M. Braden, G. André, S. Nakatsuji, and Y. Maeno, *Crystal and magnetic structure of Ca_2RuO_4: Magnetoelastic coupling and the metal-insulator transition*, Physical Review B **58**, 847 (1998). DOI: 10.1103/PhysRevB.58.847.

[5] S. Nakatsuji and Y. Maeno, *Quasi-two-dimensional Mott transition system $Ca_{2-x}Sr_xRuO_4$*, Physical Review Letters **84**, 2666 (2000b). DOI: 10.1103/PhysRevLett.84.2666.

[6] M. Braden, W. Reichardt, S. Nishizaki, Y. Mori, and Y. Maeno, *Structural stability of Sr_2RuO_4*, Physical Review B **57**, 1236 (1998). DOI: 10.1103/PhysRevB.57.1236.

[7] S. Nakatsuji and Y. Maeno, *Switching of magnetic coupling by a structural symmetry change near the Mott transition in $Ca_{2-x}Sr_xRuO_4$*, Physical Review B **62**, 6458 (2000a). DOI: 10 .1103/PhysRevB.62.6458.

[8] D. J. Singh, *Magnetism in the ruthenates*, in *Electronic Structure and Magnetism of Complex Materials*, edited by D. J. Singh and D. A. Papaconstantopoulos (Springer, Berlin), p. 298.

[9] Y. Maeno, H. Hashimoto, K. Yoshida, S. Nishizaki, T. Fujita, J. G. Bednorz, and F. Lichtenberg, *Superconductivity in a layered perovskite without copper*, Nature (London) **372**, 532 (2002). DOI: 10.1038/372532a0.

[10] T. M. Rice and M. Sigrist, *Sr2RuO4: an electronic analogue of ^3He?*, Journal of Physics: Condensed Matter **7**, L643 (1995). DOI: 10.1088/0953-8984/7/47/002.

[11] I. I. Mazin and D. J. Singh, *Ferromagnetic spin fluctuation induced superconductivity in Sr_2RuO_4*, Physical Review Letters **79**, 733 (1997). DOI: 10.1103/PhysRevLett.79.733.

[12] I. I. Mazin and D. J. Singh, *Competitions in layered ruthenates: Ferromagnetism versus antiferromagnetism and triplet versus singlet pairing*, Physical Review Letters **82**, 4324 (1999). DOI: 10.1103/PhysRevLett.82.4324.

[13] Y. Kitaoka, K. Ishida, K. Asayama, S. Ikeda, S. Nishizaki, Y. Maenob, K. Yoshida, and T. Fujita, *Spin fluctuation and unconventional pairing in Sr_2RuO_4*, Physica C **282-287**, 210 (1997). DOI: 10.1016/S0921-4534(97)00202-5.

[14] L. Tewordt, *Collective order parameter modes and spin fluctuations for spin-triplet superconducting state in Sr2RuO4*, Physical Review Letters **83**, 1007 (1999). DOI: 10.1103/PhysRevLett.83.1007.

[15] H. Mukuda, K. Ishida, Y. Kitaoka, K. Asayama, Z. Mao, Y. Mori, and Y. Maeno, *Novel character of spin fluctuations in spin-triplet superconductor Sr_2RuO_4: ^{17}O-NMR study*, Journal of the Physical Society of Japan **67**, 3945 (1998). DOI: 10.1143/JPSJ.67.3945.

[16] E. V. Kuz'min, S. G. Ovchinnikov, and I. O. Baklanov, *Comparison of superconductivity in Sr_2RuO_4 and copper oxides*, Phys. Rev. B **61**, 15392 (2000). DOI: 10.1103/PhysRevB.61.15392.

[17] S. Nakatsuji, Shin-ichi Ikeda, and Y. Maeno, *Ca_2RuO_4: New Mott insulators of layered ruthenate*, Journal of the Physical Society of Japan **66**, 1868 (1997). DOI: 10.1143/JPSJ.66.1868.

[18] A. V. Puchkov, M. C. Schabel, D. N. Basov, T. Startseva, G. Cao, T. Timusk, and Z.-X. Shen, *Layered ruthenium oxides: From band metal to Mott insulator*, Physical Review Letters **81**, 2747 (1998). DOI: 10.1103/PhysRevLett.81.2747.

[19] G. Cao, S. McCall, M. Shepard, J. E. Crow, and R. P. Guertin, *Thermal, magnetic, and transport properties of single-crystal $Sr_{1-x}Ca_xRuO_3$ ($0 < \sim x < \sim 1$)*, Physical Review B **56**, 321 (1997). DOI: 10.1103/PhysRevB.56.321.

[20] S. Nakatsuji, D. Hall, L. Balicas, Z. Fisk, K. Sugahara, M. Yoshioka, and Y. Maeno, *Heavy-mass fermi liquid near a ferromagnetic instability in layered ruthenates*, Physical Review Letters **90**, 137202 (2003). DOI: 10.1103/PhysRevLett.90.137202.

[21] L. Balicas, S. Nakatsujia, D. Hall, Z. Fisk, and Y. Maeno, *Metamagnetism in $Ca_{2-x}Sr_xRuO_4$ in the verge of the Mott transition*, Physica B **246-347**, 344 (2004). DOI: 10.1016/j.physb.2004.01.103.

[22] P. Steffens, *Struktur und Magnetismus in $Ca_{2-x}Sr_xRuO_4$* (2003), Diploma thesis, University of Cologne.

[23] J. H. Jung, Z. Fang, J. P. He, Y. Kaneko, Y. Okimoto, and Y. Tokura, *Change of Electronic Structure in Ca_2RuO_4 Induced by Orbital Ordering*, Physical Review Letters **91**, 056403 (2003). DOI: 10.1103/PhysRevLett.91.056403.

[24] J.-H. Park, L. H. Tjeng, A. Tanaka, J. W. Allen, C. T. Chen, P. Metcalf, J. M. Honig, F. M. F. de Groot, and G. A. Sawatzky, *Spin and orbital occupation and phase transitions in* V_2O_3, Physical Review B **61**, 11506 (2000). DOI: 10.1103/PhysRevB .61.11506.

[25] M. W. Haverkort, Z. Hu, A. Tanaka, W. Reichelt, S. V. Streltsov, M. A. Korotin, V. I. Anisimov, H. H. Hsieh, H.-J. Lin, C. T. Chen, D. I. Khomskii, and L. H. Tjeng, *Orbital-assisted metal-insulator transition in* VO_2, Physical Review Letters **95**, 196404 (2005). DOI: 10.1103/PhysRevLett.95.196404.

[26] T. Mizokawa, L. H. Tjeng, G. A. Sawatzky, G. Ghiringhelli, O. Tjernberg, N. B. Brookes, H. Fukazawa, S. Nakatsuji, and Y. Maeno, *Spin-orbit coupling in the Mott insulator* Ca_2RuO_4, Physical Review Letters **87**, 077202 (2001). DOI: 10.1103 /PhysRevLett.87.077202.

[27] T. Mizokawa, L. H. Tjeng, H.-J. Lin, C. T. Chen, S. Schuppler, S. Nakatsuji, H. Fukazawa, and Y. Maeno, *Orbital state and metal-insulator transition in* $Ca_{2-x}Sr_xRuO_4$ *(*$x = 0.0$ *and* 0.09*) studied by x-ray absorption spectroscopy*, Physical Review B **69**, 132410 (2004). DOI: 10.1103/PhysRevB.69.132410.

[28] Z. Fang, K. Terakura, and N. Nagaosa, *Orbital physics in ruthenates: first-principles studies*, New Journal of Physics **7**, 66. DOI: 10.1088/1367-2630/7/1/066.

[29] S. I. Csiszar, M. W. Haverkort, Z. Hu, A. Tanaka, H. H. Hsieh, H.-J. Lin, C. T. Chen, T. Hibma, and L. H. Tjeng, *Controlling orbital moment and spin orientation in CoO layers by strain*, Physical Review Letters **95**, 187205 (2005). DOI: 10.1103 /PhysRevLett.95.187205.

[30] I. Zegkinoglou, J. Strempfer, C. S. Nelson, J. P. Hill, J. Chakhalian, C. Bernhard, J. C. Lang, G. Srajer, H. Fukazawa, S. Nakatsuji, Y. Maeno, and B. Keimer, *Orbital ordering transition in* Ca_2RuO_4 *observed with resonant x-ray diffraction*, Physical Review Letters **95**, 136401 (2005). DOI: 10.1103/PhysRevLett .95.136401.

[31] Z. Fang, N. Nagaosa, and K. Terakura, *Orbital-dependent phase control in* $Ca_{2-x}Sr_xRuO_4$ *(*$0 \leq x \leq 0.5$*)*, Physical Review B **69**, 045116 (2004). DOI: 10.1103/PhysRevB.69.045116.

[32] Parameters (in eV). For $T = 78$ K: $U_{4d,4d} = 5$, $U_{2p,4d} = 4$, $\Delta = 0$, $10Dq = 1.68$, $Ds = -0.125$, $Dt = -0.045$, $H_{\mathrm{ex}} = 0.010$, $V_{a_{1g}}^{\mathrm{hyb}} = V_{b_{1g}}^{\mathrm{hyb}} = 4.37$, $V_{e_g}^{\mathrm{hyb}} = 2.48$, $V_{b_{2g}}^{\mathrm{hyb}} = 2.38$, $T_{pp} = 0.7$. For 295K: $10Dq = 1.6$, $Dt = -0.048$, $V_{a_{1g}}^{\mathrm{hyb}} = V_{b_{1g}}^{\mathrm{hyb}} = 4.37$, $V_{e_g}^{\mathrm{hyb}} = V_{b_{2g}}^{\mathrm{hyb}} = 2.5$. For 380K: $\Delta = -1$ $10Dq = 1.6$ $Ds = 0.050$, $Dt = 0.020$ $V_{a_{1g}}^{\mathrm{hyb}} = V_{b_{1g}}^{\mathrm{hyb}} = 4.81$, $V_{e_g}^{\mathrm{hyb}} = 2.38 = V_{b_{2g}}^{\mathrm{hyb}} = 2.38$. The Slater integrals have been reduced to 70% of their Hartree–Fock value. The spectra have been broadend by a Voigt function using a Gaussian with half width at half maximum (HWHM) of $\Gamma_G = 0.4$ eV and of a Lorentzian with HWHM Γ_L of 0.7 (L_3, 78 K and 295 K), 0.5 (L_2; 78 K and 295 K), and 0.8 (380 K)..

[33] A. Abragam and B. Bleaney, *Electron paramagnetic resonance of transition ions*. (Clarendon, Oxford, 1970b). ISBN: 0198512503. pp. 480, 632f, 832ff, 372f, 403ff.

[34] G. Cao, S. McCall, M. Shepard, and J. E. Crow, *Magnetic and transport properties of single-crystal Ca_2RuO_4: Relationship to superconducting Sr_2RuO_4*, Physical Review B **56**, R2916 (1997). DOI: 10.1103/PhysRevB.56.R2916.

[35] N. Hollmann, M. W. Haverkort, M. Cwik, M. Benomar, M. Reuther, A. Tanaka, and T. Lorenz, *Anisotropic susceptibility of $La_{2-x}Sr_xCoO_4$ related to the spin states of cobalt*, New Journal of Physics **10**, 023018 (2008). DOI: 10.1088/1367-2630/10/2/023018.

[36] B. R. Cooper and O. Vogt, *Singlet ground state magnetism*, Journal de Physique Colloques **32**, C1-958 (1971). DOI: 10.1051/jphyscol:19711343.

All good things must come to an end. — Proverb

9 Summary

PROPERTIES of transition-metal compounds are governed by the interplay of charge, spin, and orbital degrees of freedom and show a wealth of intriguing properties. To understand the underlying physics, the detailed electronic structure needs to be known and understood. For this thesis, $3d$ and $4d$ transition-metal oxides were studied, using x-ray absorption spectroscopy (XAS) combined with calculations, to improve their understanding of the valence, spin, and orbital physics. The following result were obtained.

The valence, spin, and orbital state of the Co ions in the one-dimensional cobaltate $Ca_3Co_2O_6$ were investigated using x-ray absorption and x-ray magnetic circular dichroism at the Co-$L_{2,3}$ edges. The Co ions at both the octahedral Co_{oct} and trigonal Co_{trig} sites are found to be in a 3+ state. From the analysis of the dichroism we established a low-spin state for the Co_{oct} and a high-spin state with an anomalously large orbital moment of $1.7\mu_B$ at the Co^{3+}_{trig} ions. This large orbital moment along the c-axis chain and the unusually large magnetocrystalline anisotropy can be traced back to the double occupancy of the d_2 orbital in trigonal crystal field.

Ca_3CoRhO_6 and Ca_3FeRhO_6 have the same crystal structure as $Ca_3Co_2O_6$; while Ca_3CoRhO_6 also has ferromagnetic intrachain coupling, Ca_3FeRhO_6 is antiferromagnetic. Using XAS at the Rh-$L_{2,3}$, Co-$L_{2,3}$, and Fe-$L_{2,3}$ edges, we find a valence state of Co^{2+}/Rh^{4+} in Ca_3CoRhO_6 and of Fe^{3+}/Rh^{3+} in Ca_3FeRhO_6. X-ray magnetic circular dichroism spectroscopy at the Co-$L_{2,3}$ edge of Ca_3CoRhO_6 reveals a giant orbital moment of about $1.7\mu_B$, which can be attributed to the occupation of the minority-spin d_0d_2 orbital state of the high-spin Co^{2+} ($3d^7$) ions in trigonal prismatic coordination. This active role of the spin-orbit coupling explains the strong magnetocrystalline anisotropy and Ising-like magnetism of Ca_3CoRhO_6. Thus as in $Ca_3Co_2O_6$ the orbital occupation maximizes the orbital moment by only occupying one of the d_2/d_{-2} orbitals. However, the details are different as Ca_3CoRhO_6 has one extra minority spin electron and the stability of the d_0d_2 configuration over the d_2d_{-2} is largely increased due to the electron–electron interaction.

Another cobaltate, the ferromagnetic $LaMn_{0.5}Co_{0.5}O_3$, was studied: We found a high-spin Co^{2+}-Mn^{4+} valence state for samples with the optimal Curie temperature. We discovered that samples with lower Curie temperatures contain low-spin nonmagnetic Co^{3+} ions. Using soft-x-ray magnetic circular dichroism, we established that the Co^{2+} and Mn^{4+} ions are ferromagnetically aligned. We also revealed that the Co^{2+} ions have a large orbital moment: $m_{\mathrm{orb}}/m_{\mathrm{spin}} \approx 0.47$. Together with model calculations, this suggests the presence of a large magnetocrystalline anisotropy in the material and predicts a nontrivial temperature dependence for the magnetic susceptibility.

Besides cobaltates, also ruthenates were investigated. For Ca_2RuO_4 we have shown that the ruthenium orbital occupation changes strongly with temperature, especially across the metal-insulator transition; large changes could also be observed for $Ca_{1.91}Sr_{0.09}RuO_4$. The changes in the orbital (and spin) correlations in turn are responsible for the large gap compared with the comparibly small metal-insulator transition temperature. The temperature dependence shows magnetostriction effects, which indicate that spin-orbit coupling is active. The cluster-calculation is able to nicely reproduce the spectra, however, there remains the issue that the lowest state in the calculation is a nonmagnetic singlet state and only with an exchange field a magnetic moment is present.

Orbital-occupation changes play also a major role for the properties of $La_4Ru_2O_{10}$. Using x-ray absorption spectroscopy at the Ru-$L_{2,3}$ edge we revealed that the Ru^{4+} ions remain in the $S = 1$ spin state across the rare 4*d*-orbital ordering transition and spin-gap formation. We identify a distinct orbital ordering with a significant anisotropy of the antiferromagnetic exchange couplings. We conclude that $La_4Ru_2O_{10}$ appears to be a novel material in which the orbital physics drives the formation of spin-singlet dimers in a quasi-two-dimensional $S = 1$ system.

The determination of the correct crystal field and the hybridization is essential for the configuration-interaction cluster calculations and thus for all the results presented here (cf. Appendix B for the hybridization calculations).

Es irrt der Mensch, so lang er strebt.
— Johann Wolfgang von Goethe, 1749–1832

10 Zusammenfassung

Die Ladungs-, Spin- und orbitalen Freiheitsgrade sind verantwortlich für den vielfältigen Eigenschaften der Übergangsmetallverbindungen. Um die zugrunde liegende Physik zu verstehen, muß die genaue elektronische Struktur bekannt und verstanden sein. In dieser Arbeit wurden 3*d*- und 4*d*-Übergangsmetalloxide mittels Röntgenabsorptionspektroskopie (XAS) und numerischen Rechnungen untersucht, um deren Ladungs-, Spin- und orbitale Physik besser zu verstehen. Folgende Ergebnise wurden dabei erzielt.

Valenz-, Spin- und orbitale Zustände der Cobaltionen im eindimensionalen Cobaltat $Ca_3Co_2O_6$ wurden mittels Röntgenabsorptionspektroskopie und magnetischem Röntgenzirkulardichroismus an den Co-$L_{2,3}$-Kanten untersucht. Sowohl die Cobaltionen an den trigonalen (Co_{trig}) als auch die an den oktahedralen (Co_{oct}) Gitterplätzen haben eine Oxidationszahl von 3+. Durch Analyse des Dichroismus wurde ein niedriger Spinzustand für das Co_{oct} und ein hoher Spinzustand für Co_{trig} bestimmt, wobei letzteres Ion ein ungewöhnlich großes orbitales Moment von $1{,}7\mu_B$ aufweist. Dieses ist entlang der *c*-Achse orientiert und zeigt ein ungewöhnlich große magnetische Kristallanisotropie; dies kann auf die doppelte Besetzung der d_2-Orbitale im trigonalen Feld zurückgeführt werden.

Ca_3CoRhO_6 und Ca_3FeRhO_6 besitzen dieselbe Kristallstruktur wie $Ca_3Co_2O_6$, wobei ersteres ebenfalls eine ferromagnetische Kopplung entlang der Cobaltkette zeigt wohingegen Ca_3FeRhO_6 ein Antiferromagnet ist. Mittels XAS an den Rh-$L_{2,3}$-, Co-$L_{2,3}$- und Fe-$L_{2,3}$-Kanten konnte die Valenzzustände Co^{2+}/Rh^{4+} für Ca_3CoRhO_6 bzw. Fe^{3+}/Rh^{3+} für Ca_3FeRhO_6 bestimmt werden. Die Zirkulardichroismus-Messungen an den Co-$L_{2,3}$-Kanten ergeben ein riesiges orbitales Moment von $1{,}7\mu_B$, welches zurückführbar ist auf die doppelte Besetzung der $d_0 d_{-2}$ Minoritätsspin-Orbitale des trigonalen Co^{2+} ($3d^7$), welches im Hochspinzustand ist. Die aktive Rolle des Spin-Bahnkopplung erklärt die starke magnetische Kristallanisotropie und den Isingartigen Magnetismus in Ca_3CoRhO_6. Somit wird wie in $Ca_3Co_2O_6$ das orbitale Moment

durch die orbitale Besetzung maximiert, wobei Ca_3CoRhO_6 ein zusätzliches Minoritätsspin-Elektron besitzt und durch die Elektron-Elektron-Wechselwirkung die Stabilität des $d_0 d_2$ stark erhöht gegenüber einer $d_2 d_{-2}$ Besetzung ist.

Als weiteres Cobaltat wurde das ferromagnetische $LaMn_{0.5}Co_{0.5}O_3$ untersucht; hierbei wurde für Proben mit optimaler Curie-Temperatur ein hoher Co Spinzustand mit Co^{2+}-Mn^{4+} gefunden. Es zeigte sich, daß Proben mit niedriger Curie-Temperatur nichtmagnetische Co^3+ im niedrigen Spinzustand enhielten. Mittels magnetischem Zirkulardichroismus wurde festgestellt, daß die Co^{2+} und Mn^{2+} ferromagnetisch ausgerichtet sind. Weiterhin zeigte sich, daß die Co^{+3}-Ionen ein großes orbitales Moment besitzen, da $m_{\mathrm{orb}}/m_{\mathrm{spin}} \approx 0.47$. Zusammen mit Modellrechnungen weist dies auf eine große magnetische Kristallanisotropie hin und auf eine nicht triviale Temperaraturabhängigkeit der magnetischen Suszeptibilität.

Neben den Cobaltverbindungen wurden auch Ruthenate untersucht. Für Ca_2RuO_4 zeigte es sich, daß eine starke Temperaturabhängigkeit der orbitalen Besetzung der Rutheniumionen, insbesondere beim Metall-Isolatorübergang; ähnlich große Änderungen wurden bei $Ca_{1.91}Sr_{0.09}RuO_4$ gefunden. Die Änderungen in den orbitalen (und Spin)korrelationen sind ihrerseits für die im Vergleich zur Metall-Isolator-Übergangstemperatur große Bandlücke verantwortlich. Die Temperaturabhängigkeit zeigt Magnetostriktionseffekte, die auf eine aktive Spin-Bahnwechselwirkung hindeuten. Die Klusterrechnungen[12] reproduzieren die Spektren gut, allerdings bleibt als Problem, daß der Grundzustand ein nicht magnetisches Singulet ist und nur mittels des Austauschfeldes ein magnetisches Moment vorhanden ist.

Orbitale Besetzungsänderungen spielen auch eine große Rolle bei den Eigenschaften von $La_4Ru_2O_{10}$. Mittels Röntgenabsorptionsspektropie an der Ru-$L_{2,3}$-Kante konnte gezeigt werden, daß die Ru^{4+}-Ionen während des seltenen 4*d*-orbitalen Ordnungsübergangs mit Spinlückenformation im $S = 1$-Zustand bleiben, wobei wir eine ausgeprägte orbitale Ordnung mit beträchtlicher Anisotropie der antiferromagnetischen Austauschkopplung feststellen konnten. Somit scheint $La_4Ru_2O_{10}$ ein neuartiges Material zu sein, in dem die orbitale Physik zur Bildung von

[12] Das Wort Kluster, verwandt mit dem englischen „Cluster“ und mit Klunt und Klump, gibt es tatsächlich im Norddeutschen und ist in den Wörterbüchern von Adelung, Grimm, Mensing und Mackensen nachgewiesen. Beispiel: Ein Kluster Heidelbeeren.

Spinsingulet-Dimeren in einem quasi zweidimensionalen $S = 1$-System führt.

Die Bestimmung des richtigen Kristallfeld- und Hybridisierungsparameter ist essentiel für die Konfigurationsinteractions-Klusterrechnungen und somit für die in dieser Arbeit gezeigten Ergebnisse (vgl. Anhang B zur Bestimmung der Hybridisierungsparameter).

Mathematics is an experimental science, and definitions do not come first, but later on.

— Oliver Heaviside, 1850–1925

A Spherical harmonics

SPHERICAL harmonics (sometimes also called surface harmonics) play a major role in quantum mechanics. In this chapter we first introduce the Legendre polynomials, then we show some properties of spherical harmonics and list the lowest ones explicitly. Thereafter, linear combinations yielding real functions are given.

A.1 Legendre polynomials

Legendre polynomials,[13] also known as Legendre functions of the first kind, Legendre coefficients or zonal harmonics, are solutions to the Legendre differential equation, namely

$$(1-x^2)\frac{\mathrm{d}^2y}{\mathrm{d}x^2} - 2x\frac{\mathrm{d}y}{\mathrm{d}x} + n(n+1)y = 0 \tag{A.1}$$

or rewritten

$$\frac{\mathrm{d}}{\mathrm{d}x}\left((1-x^2)\frac{\mathrm{d}y}{\mathrm{d}x}\right) + n(n+1) = 0. \tag{A.2}$$

The Legendre polynomial $P_n(z)$ can be defined as contour integral,

$$P_n(z) = \frac{1}{2\pi\mathrm{i}}\oint (1-2tz)^{-1/2} + t^{-n-1}\,\mathrm{d}t. \tag{A.3}$$

The Rodrigues representation provides the formula

$$P_n(z) = \frac{1}{2^n n!}\frac{\mathrm{d}^n(z^2-1)^n}{\mathrm{d}z^n}. \tag{A.4}$$

The Legendre polynomials satisfy the orthonormality relation

$$\int_{-1}^{1} P_n(z)P_m(z)\,\mathrm{d}z = \frac{2\delta_{nm}}{2n+1}. \tag{A.5}$$

[13] See also (Bronsteĭn, 2003, Arfken, 1985, Weisstein, 2006a and Abramowitz, 1984).

The Legendre differential equation can be enhanced to give the associated Legendre differential equation, namely

$$\frac{\mathrm{d}}{\mathrm{d}x}\left((1-x^2)\frac{\mathrm{d}y}{\mathrm{d}x}\right)+\left(l(l+1)-\frac{m^2}{1-x^2}\right)y=0 \tag{A.6}$$

or rewritten

$$(1-x^2)\frac{\mathrm{d}^2y}{\mathrm{d}x^2}-2x\frac{\mathrm{d}y}{\mathrm{d}x}+\left(l(l+1)-\frac{m^2}{1-x^2}\right)y=0. \tag{A.7}$$

The solutions $P_l^m(x)$ are called associated Legendre polynomials for integer l and associated Legendre functions of the first kind for non-integer l. The complete solution is $y = C_1P_l^m(x) + C_2Q_l^m(x)$ where $Q_l^m(x)$ is a Legendre function of the second kind.

We are only interested in the associated Legendre polynomials, which are given for l being a positive integer and $m = 0, 1, 2, \ldots$ as

$$P_l^m(x)=(-1)^m(1-x^2)^{m/2}\frac{\mathrm{d}^m}{\mathrm{d}x^m}P_l(x)=\frac{(-1)^m}{2^l l!}(1-x^2)^{2/m}\frac{\mathrm{d}^{l+m}}{\mathrm{d}x^{l+m}}(x^2-1)^l. \tag{A.8}$$

For negative m, the associated Legendre polynomials are defined by

$$P_l^{-m}(x)=(-1)^m\frac{(l-m)!}{(l+m)!}P_l^m(x), \tag{A.9}$$

note, however, that some authors omit the Condon-Shortley phase $(-1)^m$. The associated Legendre polynomials also fulfil an orthonormality relation.

A.2 Spherical harmonics

The spherical harmonics are the angular portion of the solution to Laplace's equation in spherical coordinates where azimuthal symmetry is not present.[14] Spherical harmonics satisfy the spherical harmonic differential equation, which is given by the angular part of Laplace's equation in spherical coordinates.

The spherical harmonic is defined as

[14] See (Weisstein, 2006b) and citations given in previous footnote.

$$Y_l^m(\theta,\phi) := \sqrt{\frac{2l+1}{4\pi}\frac{(l-m)!}{(l+m)!}} P_l^m(\cos\theta)\mathrm{e}^{\mathrm{i}m\phi}, \tag{A.10}$$

where θ is the polar coordinate with $\theta \in [0,\pi]$ and ϕ is the azimuthal (longitudinal) coordinate with $\phi \in [0,2\pi]$. Spherical harmonics fulfil the orthonormality relation; i.e.

$$\int Y_l^m(\theta,\phi)\overline{Y}_{l'}^{m'}(\theta,\phi)\,\mathrm{d}\Omega = \int_0^{2\pi}\int_0^{\pi} Y_l^m(\theta,\phi)\overline{Y}_{l'}^{m'}(\theta,\phi)\,\sin\theta\,\mathrm{d}\theta\mathrm{d}\phi = \delta_{ll'}\delta_{mm'}, \tag{A.11}$$

where $\overline{Y}$ denotes the complex conjugated. Spherical harmonics obey

$$\begin{aligned} Y_l^{-l}(\theta,\phi) &= \frac{1}{2^l l!}\sin^l\theta\,\mathrm{e}^{-\mathrm{i}l\phi}, \\ Y_l^0(\theta,\phi) &= \sqrt{\frac{2l+1}{4\pi}}P_l(\cos\theta), \\ Y_l^{-m}(\theta,\phi) &= (-1)^m\overline{Y}_l^m(\theta,\phi). \end{aligned}$$

Integrals of the spherical harmonics are given by

$$\begin{aligned} &\int_0^{2\pi}\int_0^{\pi} Y_{l_1}^{m_1}(\theta,\phi)Y_{l_2}^{m_2}(\theta,\phi)Y_{l_3}^{m_3}(\theta,\phi)\sin\theta\,\mathrm{d}\theta\,\mathrm{d}\phi \\ &= \sqrt{\frac{(2l_1+1)(2l_2+1)(2l_3+1)}{4\pi}}\begin{pmatrix} l_1 & l_2 & l_3 \\ 0 & 0 & 0 \end{pmatrix}\begin{pmatrix} l_1 & l_2 & l_3 \\ m_1 & m_2 & m_3 \end{pmatrix}, \end{aligned}$$

where $\begin{pmatrix} l_1 & l_2 & l_3 \\ m_1 & m_2 & m_3 \end{pmatrix}$ is a Wigner $3j$ symbol.

A.3 Explicit values for spherical harmonics

We list in the following some explicit functions for the lowest spherical harmonics.

Y_0^0	$\frac{1}{2\sqrt{\pi}}$
Y_1^0	$\frac{1}{2}\sqrt{\frac{3}{\pi}}\cos\theta$

$Y_1^{\pm 1}$	$\mp\frac{1}{2}\sqrt{\frac{3}{2\pi}}\sin\theta \mathrm{e}^{\pm \mathrm{i}\phi}$
Y_2^0	$\frac{1}{4}\sqrt{\frac{5}{\pi}}(3\cos^2\theta - 1)$
$Y_2^{\pm 1}$	$\mp\frac{1}{2}\sqrt{\frac{15}{2\pi}}\cos\theta\sin\theta \mathrm{e}^{\pm \mathrm{i}\phi}$
$Y_2^{\pm 2}$	$\frac{1}{4}\sqrt{\frac{15}{2\pi}}\sin^2\theta \mathrm{e}^{\pm 2\mathrm{i}\phi}$
Y_3^0	$\frac{1}{4}\sqrt{\frac{7}{\pi}}(5\cos^3\theta - 3\cos\theta)$
$Y_3^{\pm 1}$	$\mp\frac{1}{8}\sqrt{\frac{21}{\pi}}(5\cos^2\theta - 1)\sin\theta \mathrm{e}^{\pm \mathrm{i}\phi}$
$Y_3^{\pm 2}$	$\frac{1}{4}\sqrt{\frac{105}{2\pi}}\cos\theta\sin^2\theta \mathrm{e}^{\pm 2\mathrm{i}\phi}$
$Y_3^{\pm 3}$	$\mp\frac{1}{8}\sqrt{\frac{35}{\pi}}\sin^3\theta \mathrm{e}^{\pm 3\mathrm{i}\phi}$
Y_4^0	$\frac{3}{16\sqrt{\pi}}(35\cos^4\theta - 30\cos^2\theta + 3)$
$Y_4^{\pm 1}$	$\mp\frac{3}{8}\sqrt{\frac{5}{\pi}}\cos\theta\sin\theta\,(7\cos^2\theta + 3)\mathrm{e}^{\pm \mathrm{i}\phi}$
$Y_4^{\pm 2}$	$\frac{3}{8}\sqrt{\frac{5}{2\pi}}\sin^2\theta\,(7\cos\theta - 1)\mathrm{e}^{\pm 2\mathrm{i}\phi}$
$Y_4^{\pm 3}$	$\mp\frac{3}{8}\sqrt{\frac{35}{\pi}}\cos\theta\sin^3\theta\,\mathrm{e}^{\pm 3\mathrm{i}\phi}$
$Y_4^{\pm 4}$	$\frac{3}{16}\sqrt{\frac{35}{2\pi}}\sin^4\theta\,\mathrm{e}^{\pm 4\mathrm{i}\phi}$

In Cartesian coordinates we have

$$\mathrm{e}^{\pm \mathrm{i}m\phi} = \left(\frac{x \pm \mathrm{i}y}{\sqrt{x^2+y^2}}\right)^m,$$

$$\theta = \sin^{-1}\left(\sqrt{\frac{x^2+y^2}{x^2+y^2+z^2}}\right)$$

$$= \cos^{-1}\left(\frac{z}{\sqrt{x^2+y^2+z^2}}\right)$$

and hence

Y_0^0	$\frac{1}{2}\frac{1}{\sqrt{\pi}}$
Y_1^0	$\frac{1}{2}\sqrt{\frac{3}{\pi}}\frac{z}{\sqrt{x^2+y^2+z^2}}$

$Y_1^{\pm 1}$	$\mp\frac{1}{2}\sqrt{\frac{3}{2\pi}}\frac{x\pm \mathrm{i}y}{\sqrt{x^2+y^2+z^2}}$
Y_2^0	$\frac{1}{4}\sqrt{\frac{5}{\pi}}\left(\frac{3z^2}{x^2+y^2+z^2}-1\right)$
$Y_2^{\pm 1}$	$\mp\frac{1}{2}\sqrt{\frac{15}{2\pi}}\frac{z(x\pm \mathrm{i}y)}{x^2+y^2+z^2}$
$Y_2^{\pm 2}$	$\frac{1}{4}\sqrt{\frac{15}{2\pi}}\frac{(x\pm \mathrm{i}y)^2}{x^2+y^2+z^2}$
Y_3^0	$\frac{1}{4}\sqrt{\frac{7}{\pi}}\frac{z}{\sqrt{x^2+y^2+z^2}}(\frac{5z^2}{x^2+y^2+z^2}-3)$
$Y_3^{\pm 1}$	$\mp\frac{1}{8}\sqrt{\frac{21}{\pi}}\left(\frac{5z^2}{x^2+y^2+z^2}-1\right)\frac{x\pm \mathrm{i}y}{\sqrt{x^2+y^2+z^2}}$
$Y_3^{\pm 2}$	$\frac{1}{4}\sqrt{\frac{105}{2\pi}}\frac{z(x\pm \mathrm{i}y)^2}{(x^2+y^2+z^2)^{3/2}}$
$Y_3^{\pm 3}$	$\mp\frac{1}{8}\sqrt{\frac{35}{\pi}}\frac{(x\pm \mathrm{i}y)^3}{(x^2+y^2+z^2)^{3/2}}$
Y_4^0	$\frac{3}{16\sqrt{\pi}}\left(\frac{35z^4}{(x^2+y^2+z^2)^2}-\frac{30z^2}{x^2+y^2+z^2}+3\right)$
$Y_4^{\pm 1}$	$\mp\frac{3}{8}\sqrt{\frac{5}{\pi}}\frac{z(x\pm \mathrm{i}y)}{x^2+y^2+z^2}\left(\frac{7z^2}{x^2+y^2+z^2}+3\right)$
$Y_4^{\pm 2}$	$\frac{3}{8}\sqrt{\frac{5}{2\pi}}\frac{(x\pm \mathrm{i}y)^2}{x^2+y^2+z^2}\left(\frac{7z}{x^2+y^2+z^2}-1\right)$
$Y_4^{\pm 3}$	$\mp\frac{3}{8}\sqrt{\frac{35}{\pi}}\frac{z(x\pm \mathrm{i}y)^3}{(x^2+y^2+z^2)^2}$
$Y_4^{\pm 4}$	$\frac{3}{16}\sqrt{\frac{35}{2\pi}}\frac{(x\pm \mathrm{i}y)^4}{(x^2+y^2+z^2)^2}$

Note that $\sqrt{x^2+y^2+z^2}=r$.

A.4 Real combinations of spherical harmonics

More convenient that the complex spherical harmonics are the following linear combinations which are real functions; additionally, they form a good basis in octahedral point symmetry.

s	Y_0^0	$\frac{1}{2}\frac{1}{\sqrt{\pi}}$	$\frac{1}{2}\frac{1}{\sqrt{\pi}}$
p_z	Y_1^0	$\frac{1}{2}\sqrt{\frac{3}{\pi}}\cos\theta$	$\frac{1}{2}\sqrt{\frac{3}{\pi}}\frac{z}{r}$
p_x	$-\frac{1}{\sqrt{2}}(Y_1^1-Y_1^{-1})$	$\frac{1}{2}\sqrt{\frac{3}{\pi}}\sin\theta\cos\phi$	$\frac{1}{2}\sqrt{\frac{3}{\pi}}\frac{x}{r}$
p_y	$\frac{\mathrm{i}}{\sqrt{2}}(Y_1^1+Y_1^{-1})$	$\frac{1}{2}\sqrt{\frac{3}{\pi}}\sin\theta\sin\phi$	$\frac{1}{2}\sqrt{\frac{3}{\pi}}\frac{y}{r}$

$d_{3z^2-r^2}$	Y_2^0	$\frac{1}{4}\sqrt{\frac{5}{\pi}}(3\cos^2\theta-1)$	$\frac{1}{4}\sqrt{\frac{5}{\pi}}\frac{3z^2-r^2}{r^2}$
d_{zx}	$-\frac{1}{\sqrt{2}}(Y_2^1-Y_2^{-1})$	$\frac{1}{2}\sqrt{\frac{15}{\pi}}\sin 2\theta\cos\phi$	$\frac{1}{2}\sqrt{\frac{15}{\pi}}\frac{zx}{r^2}$
d_{yz}	$\frac{\mathrm{i}}{\sqrt{2}}(Y_2^1+Y_2^{-1})$	$\frac{1}{2}\sqrt{\frac{15}{\pi}}\sin 2\theta\sin\phi$	$\frac{1}{2}\sqrt{\frac{15}{\pi}}\frac{yz}{r^2}$
d_{xy}	$-\frac{\mathrm{i}}{\sqrt{2}}(Y_2^2-Y_2^{-2})$	$\frac{1}{4}\sqrt{\frac{15}{\pi}}\sin^2\theta\sin 2\phi$	$\frac{1}{4}\sqrt{\frac{15}{\pi}}\frac{xy}{r^2}$
$d_{x^2-y^2}$	$\frac{1}{\sqrt{2}}(Y_2^2+Y_2^{-2})$	$\frac{1}{4}\sqrt{\frac{15}{\pi}}\sin^2\theta\cos 2\phi$	$\frac{1}{4}\sqrt{\frac{15}{\pi}}\frac{x^2-y^2}{r^2}$
$f_{5z^3-3zr^2}$	Y_3^0	$\frac{1}{4}\sqrt{\frac{7}{2\pi}}(5\cos^3\theta-3\cos\theta)$	$\frac{1}{4}\sqrt{\frac{7}{\pi}}\frac{5z^3-3zr^2}{r^3}$
$f_{5xz^2-xr^2}$	$-\frac{1}{\sqrt{2}}(Y_3^1-Y_3^{-1})$	$\frac{1}{16}\sqrt{\frac{21}{2\pi}}(5\sin 3\theta+\sin\theta)\cos\phi$	$\frac{1}{4}\sqrt{\frac{21}{2\pi}}\frac{5xz^2-xr^2}{r^3}$
$f_{5yz^2-yr^2}$	$\frac{\mathrm{i}}{\sqrt{2}}(Y_3^1+Y_3^{-1})$	$\frac{1}{8}\sqrt{\frac{21}{2\pi}}(5\cos 2\theta+3)\sin\theta\sin\phi$	$\frac{1}{4}\sqrt{\frac{21}{2\pi}}\frac{5yz^2-yr^2}{r^3}$
f_{xyz}	$\frac{-\mathrm{i}}{\sqrt{2}}(Y_3^2-Y_3^{-2})$	$\frac{1}{4}\sqrt{\frac{105}{\pi}}\cos\theta\sin^2\theta\sin 2\phi$	$\frac{1}{8}\sqrt{\frac{105}{\pi}}\frac{xyz}{r^3}$
$f_{(x^2-y^2)z}$	$\frac{1}{\sqrt{2}}(Y_3^2+Y_3^{-2})$	$\frac{1}{4}\sqrt{\frac{105}{\pi}}\cos\theta\sin^2\theta\cos 2\phi$	$\frac{1}{4}\sqrt{\frac{105}{\pi}}\frac{(x^2-y^2)z}{r^3}$
$f_{x^3-3xy^2}$	$\frac{-1}{\sqrt{2}}(Y_3^3-Y_3^{-3})$	$\frac{1}{4}\sqrt{\frac{35}{2\pi}}\sin^3\theta\cos 3\phi$	$\sqrt{\frac{35}{2\pi}}\frac{x^3-3xy^2}{r^3}$
$f_{y^3-3x^2y}$	$\frac{\mathrm{i}}{\sqrt{2}}(Y_3^3+Y_3^{-3})$	$\frac{1}{4}\sqrt{\frac{35}{2\pi}}\sin^3\theta\sin 3\phi$	$\sqrt{\frac{35}{2\pi}}\frac{y^3-x^2y}{r^3}$

A.5 References

[1] I. N. Bronsteĭn, *Handbook of Mathematics*. (Springer, Berlin, 2003). ISBN: 3540434917.

[2] G. Arfken, *Mathematical Methods for Physicists*. (Academic Press, Orlando, FL, 1985).

[3] E. W. Weisstein, *Legendre Polynomial* (2006a), MathWorld – A Wolfram Web Resource, http://mathworld.wolfram.com/LegendrePolynomial.html.

[4] M. Abramowitz and I. A. Stegun, editors, *Pocketbook of Mathematical Functions* (Harri Deutsch, Frankfurt, 1984). ISBN: 3871448184.

[5] E. W. Weisstein, *Spherical Harmonic* (2006b), MathWorld – A Wolfram Web Resource, http://mathworld.wolfram.com/SphericalHarmonic.html.

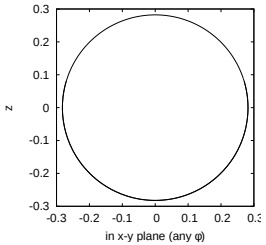

$s = Y_0^0$

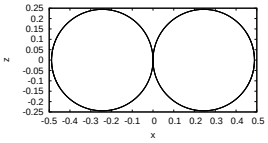

$p_x\ (\phi = 0)$

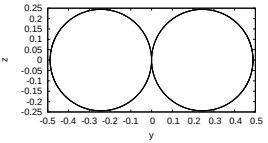

$p_y\ (\phi = \frac{1}{2}\pi)$

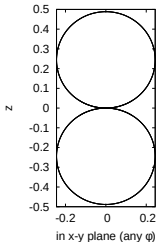

$p_z = Y_1^0$

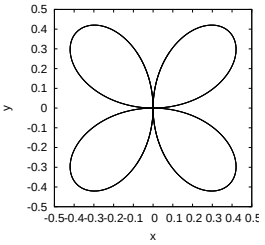

$d_{xy}\ (\theta = \frac{1}{2}\pi)$

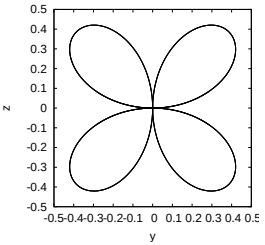

$d_{yz}\ (\phi = \frac{1}{2}\pi)$

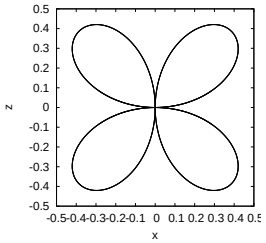

$d_{zx}\ (\phi = 0)$

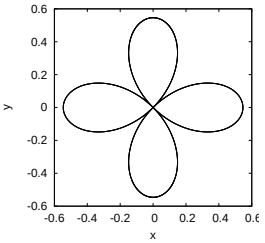

$d_{x^2-y^2}\ (\theta = \frac{1}{2}\pi)$

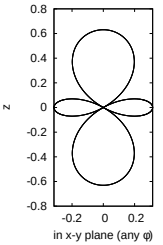

$d_{3z^2-r^2} = Y_1^0$

Fig. A.1 Real combinations of spherical-harmonics (part one).

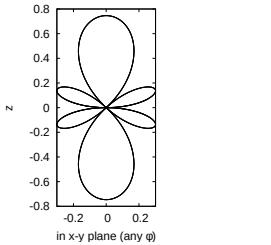

$f_{5z^3-4zr^2} = Y_3^0$

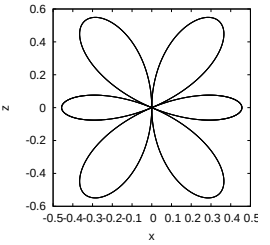

$f_{5z^2x-xr^2}$ $(\phi = 0)$

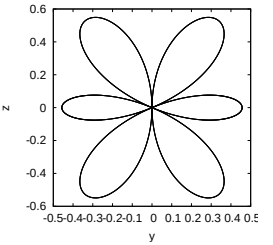

$f_{5yz^2-yr^2}$ $(\phi = \frac{1}{2}\pi)$

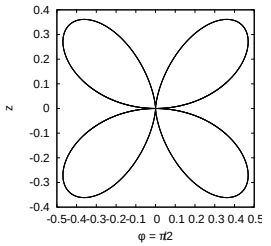

f_{xyz} $(\phi = \frac{1}{4}\pi)$

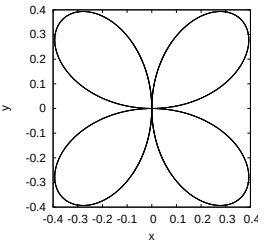

f_{xyz} $(\theta = \frac{1}{4}\pi)$

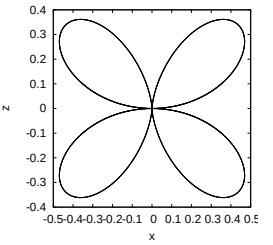

$f_{(x^2-y^2)z}$ $(\phi = 0)$

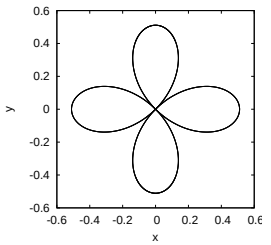

$f_{(x^2-y^2)z}$ $(\theta = \frac{1}{4}\pi)$

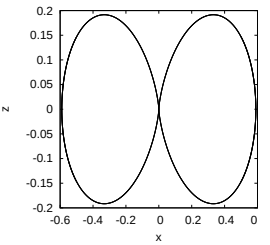

$f_{x^3-3xy^2}$ $(\phi = 0)$

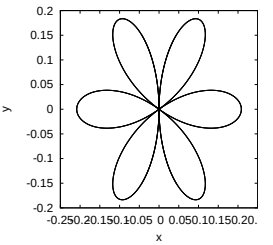

$f_{x^3-3xy^2}$ $(\theta = \frac{1}{4}\pi)$

Fig. A.2 Real combinations of spherical-harmonics (part two).

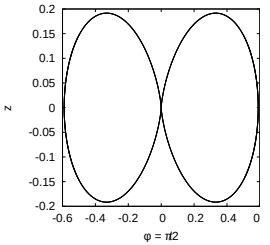

$f_{y^3-3x^2y}$ $(\phi = \frac{1}{2}\pi)$

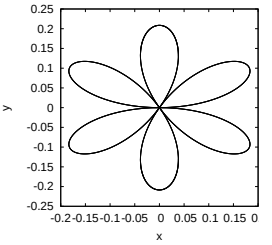

$f_{y^3-3x^2y}$ $(\theta = 0)$

Fig. A.3 Real combinations of spherical-harmonics (part three).

The theoretical oriented scientist cannot be envied, because nature, i.e. the experiment, is a relentless and not very friendly judge of his work. In the best case scenario it only says "maybe" to a theory, but never "yes" and in most cases "no". If an experiment agrees with theory it means "perhaps" for the latter. If it does not agree it means "no". Almost any theory will experience a "no" at one point in time – most theories very soon after they have been developed. — Albert Einstein, 1879–1955

B Hybridization

As written in Chapter 3, the hybridization of the transition-metal d states with the surrounding ions (the ligands) is in some cases quite important. In this section we construct the hybridization Hamiltonians explicitly for different symmetries. Note that on the author's homepage the Fortran program HYBRID is available, which does the following calculations numerically for any symmetry and which also produces the coefficients to be used with Tanaka's XTLS program [1].

The total Hamiltonian consists of the static Coulomb field of all the ions in the crystal at the site of the transition-metal ion of interest, and of the hopping between the transition-metal ion and ligands plus of the oxygen–oxygen hybridization; one obtains in total a Hamiltonian as follows:

$$\begin{aligned} H &:= \begin{pmatrix} \text{ionic crystal field of TM} & \text{TM–ligand hybridization} \\ \text{ligand–TM hybridization} & \text{ligand–ligand hybridization} \end{pmatrix}. \\ &= \begin{pmatrix} H_{1,1} & H_{1,2} \\ H_{2,1} & H_{2,2} \end{pmatrix} \end{aligned} \tag{B.1}$$

At $H_{1,1}$ one has the ionic crystal field; if one only takes the d electrons into account – as we will do in this chapter –, one usually makes $H_{1,1}$ tracefree (i.e. the mean energy of the d orbitals is zero). In octahedral (also called cubic; Schönflies: O_h; Hermann-Mauguin: $m3m$) symmetry[15] the ionic part has the following form[16]

[15] For point groups, see e.g. http://www.phys.ncl.ac.uk/staff/njpg/symmetry/. See also Section 3.3.1.

$$H^{\mathrm{Oh}}_{1,1} := \begin{array}{c} \\ d_{xy} \\ d_{yz} \\ d_{zx} \\ d_{x^2-y^2} \\ d_{3z^2-r^2} \end{array} \begin{array}{c} \begin{array}{ccccc} d_{xy} & d_{yz} & d_{zx} & d_{x^2-y2} & d_{3z^2-r^2} \end{array} \\ \begin{pmatrix} -4Dq & 0 & 0 & 0 & 0 \\ 0 & -4Dq & 0 & 0 & 0 \\ 0 & 0 & -4Dq & 0 & 0 \\ 0 & 0 & 0 & 6Dq & 0 \\ 0 & 0 & 0 & 0 & 6Dq \end{pmatrix} \end{array}, \tag{B.2}$$

where $10Dq = \Delta_{3,5}$ is the splitting between the t_{2g} (Γ_5) and e_g (Γ_3) states. The $H_{2,2}$ describes the ligand (i.e. the oxygens), consisting of the energy offset compared to the transition metal (i.e. tr $H_{1,1}$), the charge transfer energy Δ, and the hybridization between oxygen atoms ($V_{pp\sigma}$, $V_{pp\pi}$).

To determine the transition-metal–ligand hybridization we use the equations by J. C. Slater and G. F. Koster [2]; see also in the book of Harrison [3] and for f and g orbitals in the article by Sharma [4]. These contain the Slater–Koster parameters $V_{pd\sigma}$ and $V_{pd\pi}$, which can be either approximated using W. A. Harrison's rules [3]or, more reliably, come out of tight-binding fits to *ab-inito* band-structure calculations. The Slater–Koster equations are based on direction cosins. We choose the transition–metal ion as origin and use the vector $(l\hat{\boldsymbol{x}}, m\hat{\boldsymbol{y}}, n\hat{\boldsymbol{z}})$, where $\hat{\boldsymbol{x}}$, $\hat{\boldsymbol{y}}$ and $\hat{\boldsymbol{z}}$ are unit vectors, we can reach any ligand; note that equations assume that $l^2 + m^2 + n^2 = 1$.

B.1 Octahedral symmetry

We are now ready to to do an actual calculation. We use the following labelling: first oxygen $\mathrm{O_I}$ is at $(l = -1, m = 0, n = 0)$, second at $(1, 0, 0)$ etc. (see Fig. B.1 for the complete set). For p_x–d_{xy} hybridization one finds $E_{x,xy} = \sqrt{3}l^2 m V_{pd\sigma} + m(1-2l^2)V_{pd\pi}$ (see Ref. 2 and Section B.6). Thus only for ligands III and IV we obtain a nonvanishing energy, namely $E^{\mathrm{III}}_{x,xy} = -V_{\mathrm{pd}\pi}$ and $E^{\mathrm{IV}}_{x,xy} = V_{\mathrm{pd}\pi}$. To obtain $E_{y,yz}$ and $E_{z,zx}$ one simply permutes $E_{x,xy}$, i.e. $(x, l) \to (y, m) \to (z, n) \to (x, l)$ etc. For the other equations, see Slater–Koster's article [2] or Section B.6.

[16] We have choose the following order: xy, yz, zx, $x^2 - y^2$ and $3z^2 - r^2$. In the literature one finds also yz, zx, xy, $x^2 - y^2$ and $3z^2 - r^2$, and other permutations as there is unfortunately no unique natural order; this makes quick comparing of different publications difficult. Fortunately, the final result is independent of this choise.

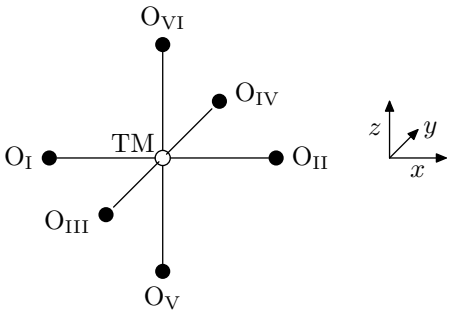

Fig. B.1 Used coordinate system. TM denotes the transition-metal ion, the O the surrounding ligands.

Continuing this tedious work, we get the following matrix

$$H_{1,2}^{O_h} = (H_{2,1}^{O_h})^\dagger$$

$$= \begin{array}{c} \\ \mathrm{O_I}\colon p_x \\ \mathrm{O_I}\colon p_y \\ \mathrm{O_I}\colon p_z \\ \mathrm{O_{II}}\colon p_x \\ \mathrm{O_{II}}\colon p_y \\ \mathrm{O_{II}}\colon p_z \\ \mathrm{O_{III}}\colon p_x \\ \mathrm{O_{III}}\colon p_y \\ \mathrm{O_{III}}\colon p_z \\ \mathrm{O_{IV}}\colon p_x \\ \mathrm{O_{IV}}\colon p_y \\ \mathrm{O_{IV}}\colon p_z \\ \mathrm{O_V}\colon p_x \\ \mathrm{O_V}\colon p_y \\ \mathrm{O_V}\colon p_z \\ \mathrm{O_{VI}}\colon p_x \\ \mathrm{O_{VI}}\colon p_y \\ \mathrm{O_{VI}}\colon p_z \end{array} \begin{array}{c} \begin{array}{ccccc} d_{xy} & d_{yz} & d_{zx} & d_{x^2-y^2} & d_{3z^2-r^2} \end{array} \\ \begin{pmatrix} 0 & 0 & 0 & -\frac{1}{2}\sqrt{3}V_{pd\sigma} & \frac{1}{2}V_{pd\sigma} \\ -V_{pd\pi} & 0 & 0 & 0 & 0 \\ 0 & 0 & -V_{pd\pi} & 0 & 0 \\ 0 & 0 & 0 & \frac{1}{2}\sqrt{3}V_{pd\sigma} & -\frac{1}{2}V_{pd\sigma} \\ V_{pd\pi} & 0 & 0 & 0 & 0 \\ 0 & 0 & V_{pd\pi} & 0 & 0 \\ -V_{pd\pi} & 0 & 0 & 0 & 0 \\ 0 & 0 & 0 & \frac{1}{2}\sqrt{3}V_{pd\sigma} & \frac{1}{2}V_{pd\sigma} \\ 0 & -V_{pd\pi} & 0 & 0 & 0 \\ V_{pd\pi} & 0 & 0 & 0 & 0 \\ 0 & 0 & 0 & -\frac{1}{2}\sqrt{3}V_{pd\sigma} & -\frac{1}{2}V_{pd\sigma} \\ 0 & V_{pd\pi} & 0 & 0 & 0 \\ 0 & -V_{pd\pi} & 0 & 0 & 0 \\ 0 & 0 & 0 & 0 & -V_{pd\sigma} \\ 0 & 0 & V_{pd\pi} & 0 & 0 \\ 0 & V_{pd\pi} & 0 & 0 & 0 \\ 0 & 0 & 0 & 0 & V_{pd\sigma} \end{pmatrix} \end{array}.$$

Next, we would like to split the 5×18 matrix $H_{1,2}$ into a 5×5 matrix of binding orbitals and a 13×5 nonbinding null space. This we do with a unitary transformation U, which leaves $H_{1,1}$ invariant but transforms $H_{1,2} = H_{2,1}^{\dagger}$ (and inevitably $H_{2,2}$); in addition, U should make the 5×5 matrix as diagonal as possible. For the transition-metal–ligand hybridization part of the matrix $\tilde{H} = U^{\dagger} H U$, we obtain

$$\tilde{H}_{2,1} = \tilde{H}_{1,2}^{\dagger}$$

$$= \begin{array}{c} \\ Ld_{xy} \\ Ld_{yz} \\ Ld_{zx} \\ Ld_{x^2-y^2} \\ Ld_{3z^2-r^2} \end{array} \begin{array}{c} \begin{array}{ccccc} d_{xy} & d_{yz} & d_{zx} & d_{x^2-y2} & d_{3z^2-r^2} \end{array} \\ \begin{pmatrix} 2V_{pd\pi} & 0 & 0 & 0 & 0 \\ 0 & 2V_{pd\pi} & 0 & 0 & 0 \\ 0 & & 2V_{pd\pi} & 0 & 0 \\ 0 & 0 & 0 & -\sqrt{3}V_{pd\sigma} & 0 \\ 0 & 0 & 0 & 0 & -\sqrt{3}V_{pd\sigma} \end{pmatrix} \end{array},$$

where $V_{pd\sigma} < 0$ is the distance-dependent σ-binding and $V_{pd\pi}$ the π-binding hybridization. One sees immediately that in octahedral symmetry the e_g (Γ_3) orbital are purly σ bound whereas the t_{2g} (Γ_5) are π bound. Using the vectors $|d_{xy}\rangle = |Ld_{xy}\rangle = (1,0,0,0,0)$ etc., one can write this as the known

$$\begin{aligned} V_{xy} &:= \langle d_{xy}|H_{1,2}|d_{xy}\rangle &&= 2V_{pd\pi}, \\ V_{yz} &:= \langle d_{yz}|H_{1,2}|d_{yz}\rangle &&= 2V_{pd\pi}, \\ V_{zy} &:= \langle d_{zx}|H_{1,2}|d_{zx}\rangle &&= 2V_{pd\pi}, \\ V_{x^2-y^2} &:= \langle d_{x^2-y^2}|H_{1,2}|d_{x^2-y^2}\rangle &&= -\sqrt{3}V_{pd\sigma}, \\ V_{3z^2-r^2} &:= \langle d_{3z^2-r^2}|H_{1,2}|d_{3z^2-r^2}\rangle &&= -\sqrt{3}V_{pd\sigma}. \end{aligned} \tag{B.3}$$

B.2 Tetragonal and orthorhombic symmetry

Fortunately, it is trivial to modify the matrix $H_{1,2}$ for tetragonal (D_{4h}; $4mm$) and orthorhombic (D_{2h}; mmm) point symmetry. We start with the orthorhombic symmetry. Here, we need to replace the universal $V_{pd\sigma}$ by $V_{pd\sigma,x}$, $V_{pd\sigma,y}$ and $V_{pd\sigma,z}$ as the bond lengths are different in the x, y and z direction; analogously for $V_{pd\pi}$. The new $H_{1,2}$ has now the following form

$H_{1,2}^{D_{2h}} = (H_{2,1}^{D_{2h}})^\dagger$

$$
= \begin{array}{c} \\ \mathrm{O_I}\colon p_x \\ \mathrm{O_I}\colon p_y \\ \mathrm{O_I}\colon p_z \\ \mathrm{O_{II}}\colon p_x \\ \mathrm{O_{II}}\colon p_y \\ \mathrm{O_{II}}\colon p_z \\ \mathrm{O_{III}}\colon p_x \\ \mathrm{O_{III}}\colon p_y \\ \mathrm{O_{III}}\colon p_z \\ \mathrm{O_{IV}}\colon p_x \\ \mathrm{O_{IV}}\colon p_y \\ \mathrm{O_{IV}}\colon p_z \\ \mathrm{O_V}\colon p_x \\ \mathrm{O_V}\colon p_y \\ \mathrm{O_V}\colon p_z \\ \mathrm{O_{VI}}\colon p_x \\ \mathrm{O_{VI}}\colon p_y \\ \mathrm{O_{VI}}\colon p_z \end{array}
\begin{array}{c}
\begin{array}{ccccc} d_{xy} & d_{yz} & d_{zx} & d_{x^2-y^2} & d_{3z^2-r^2} \end{array} \\
\begin{pmatrix}
0 & 0 & 0 & -\frac{1}{2}\sqrt{3}V_{pd\sigma,x} & \frac{1}{2}V_{pd\sigma,x} \\
-V_{pd\pi,x} & 0 & 0 & 0 & 0 \\
0 & 0 & -V_{pd\pi,x} & 0 & 0 \\
0 & 0 & 0 & \frac{1}{2}\sqrt{3}V_{pd\sigma,x} & -\frac{1}{2}V_{pd\sigma,x} \\
V_{pd\pi,x} & 0 & 0 & 0 & 0 \\
0 & 0 & V_{pd\pi,x} & 0 & 0 \\
-V_{pd\pi,y} & 0 & 0 & 0 & 0 \\
0 & 0 & 0 & \frac{1}{2}\sqrt{3}V_{pd\sigma,y} & \frac{1}{2}V_{pd\sigma,y} \\
0 & -V_{pd\pi,y} & 0 & 0 & 0 \\
V_{pd\pi,y} & 0 & 0 & 0 & 0 \\
0 & 0 & 0 & -\frac{1}{2}\sqrt{3}V_{pd\sigma,y} & -\frac{1}{2}V_{pd\sigma,y} \\
0 & V_{pd\pi,y} & 0 & 0 & 0 \\
0 & 0 & -V_{pd\pi,z} & 0 & 0 \\
0 & -V_{pd\pi,z} & 0 & 0 & 0 \\
0 & 0 & 0 & 0 & -V_{pd\sigma,z} \\
0 & 0 & V_{pd\pi,z} & 0 & 0 \\
0 & V_{pd\pi,z} & 0 & 0 & 0 \\
0 & 0 & 0 & 0 & V_{pd\sigma,z}
\end{pmatrix}
\end{array}.
$$

After a lengthier calculation (or few seconds of Mathematica crunching) one obtains

$$
\begin{aligned}
V_{xy} &= \sqrt{2(V_{pd\pi,x}^2 + V_{pd\pi,y}^2)}, \\
V_{yz} &= \sqrt{2(V_{pd\pi,y}^2 + V_{pd\pi,z}^2)}, \\
V_{zy} &= \sqrt{2(V_{pd\pi,z}^2 + V_{pd\pi,x}^2)}, \\
V_{x^2-y^2} &= \sqrt{\frac{3}{2}(V_{pd\sigma,x}^2 + V_{pd\sigma,y}^2)}
\end{aligned}
$$

$$V_{3z^2-r^2} = \sqrt{2}\left(\frac{V_{pd\sigma,z}^2}{\sqrt{V_{pd\sigma,z}^2 + V_{pd\sigma,x}^2 V_{pd\sigma,y}^2/(V_{pd\sigma,x}^2 + V_{pd\sigma,y}^2)}}\right. \tag{B.4}$$

$$\left. + \frac{V_{pd\sigma,x}^2 V_{pd\sigma,y}^2}{\sqrt{(V_{pd\sigma,x}^2 + V_{pd\sigma,y}^2)[V_{pd\sigma,y}^2 V_{pd\sigma,z}^2 + V_{pd\sigma,x}^2 (V_{pd\sigma,y}^2 V_{pd\sigma,z}^2)]}}\right),$$

plus a mixing term

$$\langle L d_{x^2-y^2} | \tilde{H} | d_{3z^2-r^2} \rangle = \frac{-V_{pd\sigma,x}^2 + V_{pd\sigma,y}^2}{\sqrt{2(V_{pd\sigma,x}^2 + V_{pd\sigma,y}^2)}}.$$

Note that while H is hermitian, $H_{1,2} = H_{2,1}^{\dagger}$ are triangular matrices due to the particular choice of finding the bonding and antibonding ligand orbitals (QR decomposition and finding the null space via single-value decomposition [5]); in order to have a symmetric $H_{1,2}$ matrix, which is needed when using the equations in Section B.5, one needs to use of a rotation matrix R with

$$R_{2,2} = \begin{pmatrix} 1 & 0 & 0 & 0 & 0 \\ 0 & 1 & 0 & 0 & 0 \\ 0 & 0 & 1 & 0 & 0 \\ 0 & 0 & 0 & \cos\phi & \sin\phi \\ 0 & 0 & 0 & -\sin\phi & \cos\phi \end{pmatrix}, \tag{B.5}$$

$R_{1,1}$ being a identity matrix and $R_{1,2} = R_{2,1}$ a null matrix.

For tetragonal symmetry (D_{4h}) the mixing term vanishes, and V_{xy} and $V_{x^2-y^2}$ simplify to their octahedral form. The complicated $V_{3z^2-r^2}^2$ term simplifies to

$$V_{3z^2-r^2} = \frac{2V_{pd\sigma,z}^2}{\sqrt{2V_{pd\sigma,z}^2 + V_{pd\sigma,x/y}^2}} + \frac{V_{pd\sigma,x/y}^4}{\sqrt{V_{pd\sigma,x/y}^6 + 2V_{pd\sigma,x/y}^4 V_{pd\sigma,z}^2}}. \tag{B.6}$$

If all $V_{pd\sigma}$ and $V_{pd\pi}$ are equal, one obtains as expected the result for an octahedral field as derived above.

B.3 Trigonal symmetry

We now have a look at trigonal (D_{3d}, $\overline{3}m$) symmetry. (For hexagonal symmetry, D_{3h} or $\overline{6}m2$, see next section.) Here, we have to start constructing a completely new matrix. We place again the transition-metal ion at the origin. The absolute value of z component of the vector to the ligands be c and the component in the x-y plane be a. We require as usual that the distances between transition-metal ion and each ligand is one, i.e. $1 = a^2 + c^2$. For the first ligand (see Fig. B.2) we obtain in-plane $\frac{1}{2}\sqrt{3} = \cos 30° = x/a$ and $\frac{1}{2} = \sin 30° = y/a$, where 30° is half of the triangular angle $180°/3 = 60°$. Contrary to octahedral or tetrahedral symmetry, there is no natural choice for the coordinates. In the following, the following coordinates are used:

$$
\begin{aligned}
\mathrm{O_I} &: \Big(-\frac{\sqrt{3}}{2}a, \quad \frac{1}{2}a, \; -c\Big),\\
\mathrm{O_{II}} &: \Big(-\frac{\sqrt{3}}{2}a, \; -\frac{1}{2}a, \quad c\Big),\\
\mathrm{O_{III}} &: \Big(\frac{\sqrt{3}}{2}a, \quad \frac{1}{2}a, \; -c\Big),\\
\mathrm{O_{IV}} &: \Big(\frac{\sqrt{3}}{2}a, \quad -\frac{1}{2}a, \quad c\Big),\\
\mathrm{O_V} &: \Big(0, \qquad -a, \quad -c\Big),\\
\mathrm{O_{VI}} &: \Big(0, \qquad a, \qquad c\Big).
\end{aligned}
$$

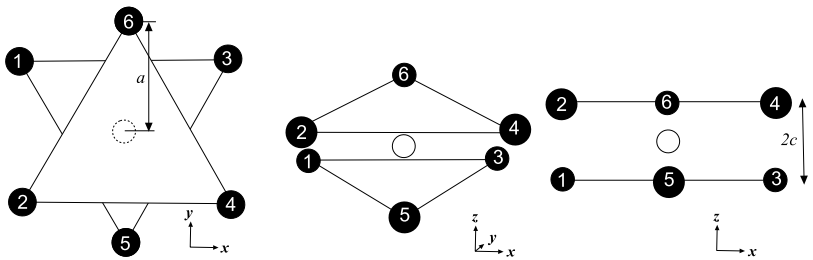

Fig. B.2 Trigonal symmetry ($D_{3d}, \overline{3}m$) – used coordinate system

As the equations are too long to print them in a matrix, we now write them down ligand by ligand. We start with the fifth and sixth ligand as there the equations are easier; we have $(l, m, n) = (0, \mp a, \mp c)$, respectively, and thus

$$
\begin{aligned}
V_{x,xy}^{\mathrm{V/VI}} &= \mp a V_{pd\pi} \\
V_{x,yz}^{\mathrm{V/VI}} &= 0 \\
V_{x,zx}^{\mathrm{V/VI}} &= \mp c V_{pd\pi} \\
V_{x,x^2-y^2}^{\mathrm{V/VI}} &= 0 \\
V_{x,3z^2-r^2}^{\mathrm{V/VI}} &= 0 \\
V_{y,xy}^{\mathrm{V/VI}} &= 0 \\
V_{y,yz}^{\mathrm{V/VI}} &= \sqrt{3} a^2 (\mp c) V_{pd\sigma} \mp c(1-2a^2) V_{pd\pi} \\
V_{y,zx}^{\mathrm{V/VI}} &= 0 \\
V_{y,x^2-y^2}^{\mathrm{V/VI}} &= \frac{1}{2}\sqrt{3} (\mp a)(-a^2) V_{pd\sigma} \pm a(1-a^2) V_{pd\pi} \\
V_{y,3z^2-r^2}^{\mathrm{V/VI}} &= \mp a (c^2 - \frac{1}{2} a^2) V_{pd\sigma} \mp a c^2 V_{pd\pi}
\end{aligned}
$$

$$
\begin{aligned}
V_{z,xy}^{\mathrm{V/VI}} &= 0 \\
V_{z,yz}^{\mathrm{V/VI}} &= \sqrt{3} c^2 (\mp a) V_{pd\sigma} \mp a(1-2n^2) V_{pd\pi} \\
V_{z,zx}^{\mathrm{V/VI}} &= 0 \\
V_{z,x^2-y^2}^{\mathrm{V/VI}} &= \frac{1}{2}\sqrt{3} (\mp c)(-a^2) V_{pd\sigma} \pm c(-a^2) V_{pd\pi} \\
V_{z,3z^2-r^2}^{\mathrm{V/VI}} &= \mp c (c^2 - \frac{1}{2} a^2) V_{pd\sigma} + \sqrt{3} (\mp c) a^2 V_{pd\pi}
\end{aligned}
$$

We now continue with the first and second atom, i.e. $(l, m, n) = (-\frac{1}{2}\sqrt{3}a, \pm\frac{1}{2}a, \mp c)$, respectively, and therefore

$$V^{\mathrm{I,II}}_{x,xy} = \sqrt{3}(\frac{3}{4}a^2)(\pm\frac{1}{2}a)V_{pd\sigma} + (\pm\frac{1}{2}a)[1-2(\frac{3}{4}a^2)]V_{pd\pi}$$

$$V^{\mathrm{I,II}}_{x,yz} = \sqrt{3}(-\frac{\sqrt{3}}{2}a)(\pm\frac{1}{2}a)(\mp c)V_{pd\sigma} - 2(-\frac{\sqrt{3}}{2}a)(\pm\frac{1}{2}a)(\mp c)V_{pd\pi}$$

$$V^{\mathrm{I,II}}_{x,zx} = \sqrt{3}(\frac{3}{4}a^2)(\mp c)V_{pd\sigma} \mp c[1-2(\frac{3}{4}a^2)]V_{pd\pi}$$

$$V^{\mathrm{I,II}}_{x,x^2-y^2} = \frac{1}{2}\sqrt{3}(-\frac{\sqrt{3}}{2}a)(\frac{3}{4}a^2-\frac{1}{4}a^2)V_{pd\sigma} + (-\frac{\sqrt{3}}{2}a)(1-\frac{3}{4}a^2+\frac{1}{4}a^2)V_{pd\pi}$$

$$V^{\mathrm{I,II}}_{x,3z^2-r^2} = (-\frac{\sqrt{3}}{2}a)[c^2-\frac{1}{2}(\frac{3}{4}a^2-\frac{1}{4}a^2)]V_{pd\sigma} - \sqrt{3}(-\frac{\sqrt{3}}{2}a)c^2V_{pd\pi}$$

$$V^{\mathrm{I,II}}_{y,xy} = \sqrt{3}(\frac{1}{4}a^2)(-\frac{\sqrt{3}}{2}a)V_{pd\sigma} + (-\frac{\sqrt{3}}{2}a)[1-2(\frac{1}{4})a^2]V_{pd\pi}$$

$$V^{\mathrm{I,II}}_{x,yz} = \sqrt{3}(\frac{1}{4}a^2)(\mp c)V_{pd\sigma} \mp c[1-2(\frac{1}{4}a^2)]V_{pd\pi}$$

$$V^{\mathrm{I,II}}_{y,zx} = \sqrt{3}(\pm\frac{1}{2}a)(-\frac{\sqrt{3}}{2}a)(\mp c)V_{pd\sigma} - 2(-\frac{\sqrt{3}}{2}a)(\mp\frac{1}{2}a)(\mp c)V_{pd\pi}$$

$$V^{\mathrm{I,II}}_{y,x^2-y^2} = \frac{1}{2}\sqrt{3}(\mp\frac{1}{2}a)(\frac{3}{4}a^2-\frac{1}{4}a^2)V_{pd\sigma} \pm \frac{1}{2}a(1+\frac{3}{4}a^2-\frac{1}{4}a^2)V_{pd\pi}$$

$$V^{\mathrm{I,II}}_{y,3z^2-r^2} = \mp\frac{1}{2}a[c^2-\frac{1}{2}(\frac{3}{4}a^2+\frac{1}{2}a^2)]V_{pd\sigma} + \sqrt{3}(\mp\frac{1}{2}a)c^2V_{pd\pi}$$

$$V^{\mathrm{I,II}}_{z,xy} = \sqrt{3}(-\frac{\sqrt{3}}{2}a)(\mp\frac{1}{2}a)(\mp c)V_{pd\sigma} - 2(-\frac{\sqrt{3}}{2}a)(\mp\frac{1}{2}a)(\mp c)V_{pd\pi}$$

$$V^{\mathrm{I,II}}_{z,yz} = \sqrt{3}c^2(\mp\frac{1}{2}a)V_{pd\sigma} \mp \frac{1}{2}a(1-2c^2)V_{pd\pi}$$

$$V^{\mathrm{I,II}}_{z,zx} = \sqrt{3}c^2(-\frac{\sqrt{3}}{2}a)V_{pd\sigma} - \frac{\sqrt{3}}{2}a(1-2c^2)V_{pd\pi}$$

$$V^{\mathrm{I,II}}_{z,x^2-y^2} = \frac{1}{2}\sqrt{3}(\mp c)(\frac{3}{4}a^2-\frac{1}{4}a^2)V_{pd\sigma} \pm c(\frac{3}{4}a^2-\frac{1}{4}a^2)V_{pd\pi}$$

$$V^{\mathrm{I,II}}_{z,3z^2-r^2} = \mp c[c^2-\frac{1}{2}(\frac{3}{4}a^2-\frac{1}{4}a^2)]V_{pd\sigma} + \sqrt{3}(\mp c)(\frac{3}{4}a^2-\frac{1}{4}a^2)V_{pd\pi}$$

The same procedure has to be done for the third and fourth atom. Unfortunately, the resulting matrix was to complex to be solved analytically. Please use the HYBRID program to calculate the hybridization

and make sure that the resulting Hamiltonian is compatible with your ionic Hamiltonian (compare the used matrix elements and their sign).

B.4 Hexagonal symmetry

For hexagonal (D_{3h}, $\overline{6}m2$) symmetry the procedure is alike; this symmetry is equation wise very similar to trigonal symmetry, except tat we have here a horizontal mirror plane whereas D_{3d} had a diagonal/dihedral reflection plane. Please use also for this symmetry the HYBRID program.

B.5 In a spherical harmonic basis

The Hamiltonian can be expanded in spherical harmonics (see Refs. 6 and 7, and Chapter 3); the crystalline electric field (CEF) is given by $V_{\mathrm{CEF}} = \sum_i Z_i e^2/|\boldsymbol{R}_i - \boldsymbol{r}|$, where Z_i is the valence state and $\boldsymbol{R}_i$ the coordinate of the i-th anion, and $\boldsymbol{r}$ denotes the position of the d electrons of the transition-metal ion of interest. The CEF coefficients are then given by

$$A_l^m = \langle\psi|V_{\mathrm{CEF}}|\psi\rangle \tag{B.7}$$

with $\Psi_{n,l,m} = R_{n,l}(r)Y_l^m(\theta,\phi)$. We can now expanded the potential in spherical harmonics,

$$V_{\mathrm{CEF}} = \sum_i \frac{Ze^2}{R_i} \sum_{l=0}^{\infty} \sum_{m=-l}^{l} \frac{4\pi}{2l+1} \left(\frac{r}{R_i}\right)^l Y_l^m(\theta_i,\phi_i) Y_l^m * (\theta_i,\phi_i). \tag{B.8}$$

Using $\langle r^l\rangle = \int_0^\infty r^k |R_{3d}|^2\, r^2\, \mathrm{d}r$, $C_l^m = 4\pi/(2l+1)Y_l^m$, and $B_l^m = (2l+1)/4\pi\, A_l^m \langle r\rangle$ (cf. Section 3.2), the potentialfor d orbitals is given by

$$V(\boldsymbol{r}) = B_0^0\, C_0^0 + \sum_{\mu=-2}^{2} B_2^\mu\, C_2^\mu + \sum_{\mu=-4}^{4} B_4^\mu\, C_4^m. \tag{B.9}$$

The coefficients B_l^m can be obtained from a Hamiltonian in a basis of real d obitals ($\{d_{xy}, d_{zx}, \ldots\}$) using the following equations [8].

$$B_0^0 = \frac{1}{5}(V_{x^2-y^2} + V_{xy} + V_{zx} + V_{yz} + V_{3z^2-r^2})$$

$$B_2^0 = \frac{1}{2}(-2V_{x^2-y^2} - 2V_{xy} + V_{zx} + V_{yz} + 2V_{3z^2-r^2})$$

$$B_2^1 = \frac{1}{2}[\sqrt{6}(\mathrm{i}V_{xy,zx} - V_{xy,yz} - V_{zx,x^2-y^2} - \mathrm{i}V_{yz,x^2-y12} + \mathrm{i}V_{yz,3z^2-r^2}) - \sqrt{2}V_{zx,z^2-r^2}]$$

$$B_2^2 = \frac{1}{4}[4\sqrt{2}(\mathrm{i}V_{xy,3z^2-r^2} - V_{x^2-y^2,3z^2-r^2}) + \sqrt{6}[V_{zx} - V_{yz} - 2\mathrm{i}V_{yz,zx}]]$$

$$B_4^0 = \frac{3}{10}(V_{x^2-y^2} + V_{xy} - 4V_{zx} - 4_{yz} + 6V_{3z^2-r^2})$$

$$B_4^1 = \frac{3}{10}\sqrt{5}(-\mathrm{i}V_{xy,zx} + V_{xy,yz} + V_{zx,x^2-y^2} - 2\sqrt{3}V_{zx,3z^2-r^2} + \mathrm{i}V_{yz,x^2-y^2} + 2\mathrm{i}\sqrt{3}V_{yz,3z^2-r^2})$$

$$B_4^2 = \frac{3}{10}\sqrt{10}(\sqrt{3}V_{x^2-y^2,3z^2-r^2} - \mathrm{i}\sqrt{3}V_{xy,z^2} + V_{zx} - V_{yz} - 2\mathrm{i}V_{yz,zx})$$

$$B_4^3 = \frac{3}{10}\sqrt{35}(\mathrm{i}V_{xy,zx} + V_{xy,yz} - V_{zx,x^2-y^2} + \mathrm{i}V_{yz,x^2-y^2})$$

$$B_4^4 = \frac{3}{20}\sqrt{70}(V_{x^2-y^2} - V_{xy} - 2\mathrm{i}V_{xy,x^2-y^2}),$$

where the not shown coefficients can be obtained via the relation $B_l^{-m} = (-1)^m (B_l^m)^*$.

These expansion applies to both the ionic crystal field and to the transtion metal–ligand hybridization. For the latter, the author's HYBRID program can be used, which numerically obtains these parameters for any symmetry. The expansion parameters are then used as input for the configuration-interaction cluster calculation (e.g. Tanaka's XTLS program).

B.6 Two-center integrals by Slater and Koster

In this small section we only list the Slater-Koster integrals two-center approximation as published by Slater and Koster [2], which can also be found in Harrison's book [3]; a general formula and a table for f and

g orbitals can be found in Sharma's article [4]. The vector between two ions is $(l\hat{\boldsymbol{x}}, m\hat{\boldsymbol{y}}, n\hat{\boldsymbol{z}})$, where $\hat{\boldsymbol{x}}$, $\hat{\boldsymbol{y}}$ and $\hat{\boldsymbol{z}}$ are unit vectors; note that equations assume that $l^2 + m^2 + n^2 = 1$. Using cyclic permutations, $(x, l) \to (y, m) \to (z, n)$, the missing integrals can be created.

$E_{s,s} =$	$V_{ss\sigma}$
$E_{s,x} =$	$lV_{sp\sigma}$
$E_{x,x} =$	$l^2V_{pp\sigma} + (1 - l^2)V_{pp\pi}$
$E_{x,y} =$	$lmV_{pp\sigma} - lmV_{pp\pi}$
$E_{x,z} =$	$lnV_{pp\sigma} - lnV_{pp\pi}$
$E_{s,xy} =$	$\sqrt{3}lmV_{sd\sigma}$
$E_{s,x^2-y^2} =$	$\frac{1}{2}\sqrt{3}(l^2 - m^2)V_{sd\sigma}$
$E_{s,3z^2-r^2} =$	$[n^2 - \frac{1}{2}(l^2 + m^2)]v_{sd\sigma}$
$E_{x,xy} =$	$\sqrt{3}l^2mV_{pd\sigma} + m(1 - 2l^2)V_{pd\pi}$
$E_{x,yz} =$	$\sqrt{3}lmnV_{pd\sigma} - 2lmnV_{pd\pi}$
$E_{x,zx} =$	$\sqrt{3}l^2nV_{pd\sigma} + n(1 - 2l^2)V_{pd\pi}$
$E_{x,x^2-y^2} =$	$\frac{1}{2}\sqrt{3}l(l^2 - m^2)V_{pd\sigma} + l(1 - l^2 + m^2)V_{pd\pi}$
$E_{y,x^2-y^2} =$	$\frac{1}{2}\sqrt{3}m(l^2 - m^2)V_{pd\sigma} - m(1 + l^2 - m^2)V_{pd\pi}$
$E_{z,x^2-y^2} =$	$\frac{1}{2}\sqrt{3}n(l^2 - m^2)V_{pd\sigma} - n(l^2 - m^2)V_{pd\pi}$
$E_{x,3z^2-r^2} =$	$l[n^2 - \frac{1}{2}(l^2 + m^2)]V_{pd\sigma} - \sqrt{3}ln^2V_{pd\pi}$
$E_{y,3z^2-r^2} =$	$m[n^2 - \frac{1}{2}(l^2 + m^2)]V_{pd\sigma} - \sqrt{3}mn^2V_{pd\pi}$
$E_{z,3z^2-r^2} =$	$n[n^2 - \frac{1}{2}(l^2 + m^2)]V_{pd\sigma} + \sqrt{3}n(l^2 + m^2)V_{pd\pi}$
$E_{xy,xy} =$	$3l^2m^2V_{dd\sigma} + (l^2 + m^2 - 4l^2m^2)V_{dd\pi}$ $+(n^2 + l^2m^2)V_{dd\delta}$
$E_{xy,yz} =$	$3lm^2nV_{dd\sigma} + ln(1 - 4m^2)V_{dd\pi}$ $+ln(m^2 - 1)V_{dd\delta}$
$E_{xy,zx} =$	$3l^2mnV_{dd\sigma} + mn(1 - 4l^2)V_{dd\pi}$ $+mn(l^2 - 1)V_{dd\delta}$
$E_{xy,x^2-y^2} =$	$\frac{3}{2}lm(l^2 - m^2)V_{dd\sigma} + 2lm(m^2 - l^2)V_{dd\pi}$ $+\frac{1}{2}lm(l^2 - m^2)V_{dd\delta}$
$E_{yz,x^2-y^2} =$	$\frac{3}{2}mn(l^2 - m^2)V_{dd\sigma} - mn[1 + 2(l^2 - m^2)]V_{dd\pi}$ $+mn[1 + \frac{1}{2}(l^2 - m^2)]V_{dd\delta}$
$E_{zx,x^2-y^2} =$	$\frac{3}{2}nl(l^2 - m^2)V_{dd\sigma} + nl[1 - 2(l^2 - m^2)]V_{dd\pi}$ $-nl[1 - \frac{1}{2}(l^2 - m^2)]V_{dd\delta}$
$E_{xy,3z^2-r^2} =$	$\sqrt{3}lm[n^2 - \frac{1}{2}(l^2 + m^2)]V_{dd\sigma} - 2\sqrt{3}lmn^2V_{dd\pi}$

$$
\begin{aligned}
& & & +\tfrac{1}{2}\sqrt{3}lm(1+n^2)V_{dd\delta} \\
E_{yz,3z^2-r^2} = & & & \sqrt{3}mn[n^2-\tfrac{1}{2}(l^2+m^2)]V_{dd\sigma} \\
& & & +\sqrt{3}mn(l^2+m^2-n^2)V_{dd\pi} \\
& & & -\tfrac{1}{2}\sqrt{3}mn(l^2+m^2)V_{dd\delta} \\
E_{zx,3z^2-r^2} = & & & \sqrt{3}ln[n^2-\tfrac{1}{2}(l^2+m^2)]V_{dd\sigma} \\
& & & +\sqrt{3}ln(l^2+m^2-n^2)V_{dd\pi} \\
& & & -\tfrac{1}{2}\sqrt{3}ln(l^2+m^2)V_{dd\delta} \\
E_{x^2-y^2,x^2-y^2} = & & & \tfrac{3}{4}(l^2-m^2)^2V_{dd\sigma}+[l^2+m^2-(l^2-m^2)^2]V_{dd\pi} \\
& & & +[n^2+\tfrac{1}{4}(l^2-m^2)^2]V_{dd\delta} \\
E_{x^2-y^2,3z^2-r^2} = & & & \tfrac{1}{2}\sqrt{3}(l^2-m^2)[n^2-\tfrac{1}{2}(l^2+m^2)]V_{dd\sigma} \\
& & & +\sqrt{3}n^2(m^2-l^2)V_{dd\pi} \\
& & & +\tfrac{1}{4}\sqrt{3}(1+n^2)(l^2-m^2)V_{dd\delta} \\
E_{3z^2-r^2,3z^2-r^2} = & & & [n^2-\tfrac{1}{2}(l^2+m^2)]^2V_{dd\sigma}+3n^2(l^2+m^2)V_{dd\pi} \\
& & & +\tfrac{3}{4}(l^2+m^2)^2V_{dd\delta}
\end{aligned}
$$

B.7 References

[1] A. Tanaka and T. Jo, *Resonant 3d, 3p and 3s photoemission in transition metal oxides predicted at 2p threshold*, Journal of the Physical Society of Japan **63**, 2788 (1994). DOI: 10.1143/JPSJ.63.2788.

[2] J. C. Slater and G. F. Koster, *Simplified lcao method for the periodic potential problem*, Physical Review **94**, 1498 (1954). DOI: 10.1103/PhysRev.94.1498.

[3] W. A. Harrison, *Electronic Structure and the Properties of Solids: The Physics of the Chemical Bond*. (Dover, New York, 1989). ISBN: 0486660214.

[4] R. R. Sharma, *General expressions for reducing the slater-koster linear combination of atomic orbitals integrals to the two-center approximation*, Physical Review B **19**, 2813 (1979). DOI: 10.1103/PhysRevB.19.2813. Erratum: Physical Review B **22**, 5015 (1980).

[5] G. H. Golub and C. F. V. Loan, *Matrix-computations*. (North Oxford Academic, Oxford, 1983). ISBN: 0946536007. HYBRID uses the LAPACK routines dgeqrf, dorgqr, and dgesvd; http://www.netlib.org/lapack/.

[6] J. C. Slater, *Quantum Theory of Atomic Structure*. (McGraw-Hill, New York, 1960).
[7] T. Hotta, *Orbital ordering phenomena in d- and f-electron systems*, Reports on Progress in Physics **69**, 2061 (2006). DOI: 10.1088/0034-4885/69/7/R02.
[8] M. W. Haverkort, Ph.D. thesis, Universität zu Köln, (2005). arXiv:cond-mat/0505214

If your experiment needs statistics, you ought to have done a better experiment.

— Ernest Rutherford, 1871–1937

C Energy conversion

SEVERAL units exists in which energy can be expressed. The SI unit is Joule (J), but for our purpose the SI accepted energy unit electron volt (eV) gives better manageable numbers. They are related by $E[\mathrm{J}] = eE[\mathrm{eV}]$, where the elementary charge is given by $e = 1.602\,176\,53(14) \times 10^{-19}\mathrm{J}$. (Constants taken from Ref. 1.) In atomic units, many equations loose their constants and thus atomic units are often preferred; their energy unit is Hartree (E_h, htr, Htr), $1E_h = 2\mathrm{Ryd} = 27.211\,3845(23)\mathrm{eV} = 1\,e^2/4\pi\varepsilon_0 a_0$, where Ryd denotes the unit Rydberg ($1\mathrm{Ryd} = R_\infty hc$).

Analogously, the following units can be regarded as energy after multiplication by a constant. For the temperature T this is done via the Boltzmann constant $E = k_B T$, $k_B = 8.617\,343(15) \times 10^{-5}\mathrm{eV\,K^{-1}}$, whereas the Bohr magneton $\mu_B = 5.788\,381\,804(39) \times 10^{-5}\mathrm{eV\,T^{-1}}$ is used for the magnetic field B. The frequency ν (in Hz), wavelength λ (in m) and wavenumber λ^{-1} (in inverse m) are related to the energy via the Planck constant $h = 4.135\,667\,43(35) \times 10^{-15}\mathrm{eV\,s}$ as $E = h\nu = hc/\lambda = hc\lambda^{-1}$.

Thus $1\mathrm{eV} = 11\,604\mathrm{K} = 17275\mathrm{T} = 8065.54\mathrm{cm}^{-1} = 1.23\mu\mathrm{m} = 241.79\mathrm{THz} = 36.749\mathrm{mHtr} = 73.498\mathrm{mRyd}$.

C.1 References

[1] B. N. Taylor and P. J. Mohr, *NIST Reference on Constants, Units, and Uncertainty* (2003), http://physics.nist.gov/cuu/index.html Based on '2002 CODATA recommended values'.

Whatever Nature has in store for mankind, unpleasant as it may be, men must accept, for ignorance is never better than knowledge. — Enrico Fermi, 1901–1954

D Magnetization and susceptibility

The magnetization $\boldsymbol{M}$ of a material in response to an applied magnetic field $\boldsymbol{H}$ is given by $\boldsymbol{M} = \chi \boldsymbol{H}$, where the proportionality factor χ is the magnetic volume susceptibility (also written as χ_m or χ_v). Both $\boldsymbol{M}$ and $\boldsymbol{H}$ are measured in units of amperes per metre and thus χ is unitless. The magnetization is also often given in units of Bohr magneton ($\mu_B = e\hbar/2m_e$) per volume. The magnetic induction or magnetic flux density $\boldsymbol{B}$, measured in Tesla, is given by $\boldsymbol{B} = \mu_0(\boldsymbol{H} + \boldsymbol{M}) = \mu_0(1+\chi)\boldsymbol{H} = \mu_0\mu_r\boldsymbol{H} = \mu\boldsymbol{H}$, where μ is the magnetic permeability; the magnetic constant $\mu_0 = 4\pi \times 10^{-7}\mathrm{N}\cdot\mathrm{A}^{-2}$ is the permeability of the vacuum. Materials are classified by their susceptibility as paramagnetic if $\chi > 0$ (field is strengthened by the material) and as diamagnetic if $-1 \leq \chi < 0$ (field is weakened); in the superconducting state $\chi = -1$ (perfect diamagnet).

The susceptibility is given by the tensor

$$\chi_{ij} = \frac{M_i}{H_j} \tag{D.1}$$

and is frequency dependent; throughout the whole thesis only the diagonal in a non-oscillating (DC) field is considered. For a paramagnetic material the magnetization is given in a simplified model (Curie's law) as $\boldsymbol{M} = C\boldsymbol{B}/T$ where T is the absolute temperature in kelvins and C is the material specific Curie constant. This can be enhanced to describe the behaviour of a ferro- or antiferromagnet above the, respectively, Curie or Néel temperature by replacing T by $T - \Theta$ where Θ is the Curie–Weiss temperature; Θ is vanishing for a paramagnet, negative for an antiferromagnet and positive for a ferromagnet.

The starting point for Curie's Law is a set of identical ions with angular moment J (see, e.g., Ashcroft/Mermin [1]) which gives for the magnetization of N ions in volume V

$$M = -\frac{N}{V}\frac{\mathrm{d}F}{\mathrm{d}H} = \frac{N}{V} g(J,L,S)\mu_B J B_J\left(\frac{JH}{k_B T} g(HLS)\mu_B\right), \tag{D.2}$$

where F is the free energy, g the Landé g factor

$$g = \frac{3}{2} + \frac{1}{2}\frac{S(S+1) - L(L+1)}{J(J+1)} \tag{D.3}$$

and the Brillouin function B_J is given by

$$\begin{aligned} B_J(x) &= \frac{2J+1}{2J}\coth\left(\frac{2J+1}{2J}x\right) - \frac{1}{2J}\coth\left(\frac{1}{2J}x\right) \\ &= \frac{J+1}{3J}x + O(x^3); \end{aligned} \tag{D.4}$$

in the last step, $B_J(x)$ has been expanded for small x. In the low-field, high-temperature limit, i.e. $g(J,L,S)\mu_B H \ll k_B T$, the small-$x$ limit of Brillouin function can be used and the susceptibility simplifies to the following form of Curie's Law

$$\chi = \frac{N}{V}\frac{(g\mu_B)^2}{3}\frac{J(J+1)}{k_B T} = \frac{N}{V}\frac{p^2\mu_B^2}{3k_B T} = \frac{N}{V}\frac{\mu_{\text{eff}}^2}{3k_B T}, \tag{D.5}$$

where we have defined in the last two terms the effective Bohr magneton number p and the effective moment μ_{eff}. Replacing – as above – the T by $T - \Theta$ extends this equation to ferro- and antiferromagnets. Note, however, that there are several cases where using Eq. (D.5) gives misleading ('wrong') results as can be seen in FIG. 5.9 of Chapter 5.

If one has calculated, e.g. using configuration-interaction cluster calculation, the expectation values $\langle \hat{S}_z \rangle = \hbar S_z$ and $\langle \hat{L}_z \rangle = \hbar L_z$ (or alternatively $\hat{L}_x/\hat{S}_y$ or ...), the magnetization is given by

$$M_z(T) = -\sum_i f_i(T)(L_z^{(i)} + 2S_z^{(i)})\mu_B/V \tag{D.6}$$

where the sum runs over the all states and f_i is the Boltzmann distribution

$$f_i(T) = \frac{1}{Z}\mathrm{e}^{-E_i/k_B T}, \quad Z = \sum_i \mathrm{e}^{-E_i/k_B T} \tag{D.7}$$

and Z is called partition sum. To compare this number with literature, we convert it to emu per mole (EMU = electromagnetic unit), where throughout this thesis emu $\equiv$ cm^{-3} is used. In the cgs system (centimetre-gauss-second), the field H has the unit Oersted

(Oe = $\mathrm{s}\sqrt{\mathrm{g/cm}}$), the magnetic induction B the unit Gauss (G = $\mathrm{s}\sqrt{\mathrm{g/cm}}$) with 1T = 10^4G, $\mu_0 = 1$; thus the magnetization has the unit emu $\cdot$ G/cm^3. Consequently, the susceptibility χ_v is given in units emu $\cdot$ G/cm^{3}Oe = 1. Often the magnetization is given per mass: the magnetization is then given in m^3/kg (SI) or emu/g (cgs); or it is given per molar mass as m^3/mol (SI) respectively emu/mol (cgs). Therefore, in order to obtain the magnetization in emu per mole (or emu Gauss per mole and Oersted) one has to calculate

$$\chi = \frac{M}{H} = \frac{-\sum_i f_i(T)(L_z^{(i)} + 2S_z^{(i)})\mu_B}{H_{\mathrm{Tesla}}} \frac{N_A}{10}, \tag{D.8}$$

with the Avogadro number $N_A = 6.022\,141\,79(30) \times 10^{23}\mathrm{mol}^{-1}$ and Bohr magneton $\mu_B = 927.400\,915(23) \times 10^{-26}\mathrm{J\,T}^{-1}$; the $\frac{1}{10}$ comes from the Tesla to Gauss conversion. If you happen to have a magnetic field in electronvolt, you need to divide it by Bohr magneton $\mu_B = 5.788\,381\,7555(79) \times 10^{-5}\mathrm{eV\,T}^{-1}$ ($1/\mu_B \approx 17.276\mathrm{T/meV}$) to obtain Tesla.

D.1 References

[1] N. W. Ashcroft and N. D. Mermin, *Solid State Physics*. (Holt, Rinehart and Winston, New York, 1976). ISBN: 0030839939.

Nature, and Nature's laws lay hid in night.
God said, Let Newton be! *and all was light.*
— Alexander Pope, 1688–1744

E Units and fundamental constants

E.1 Units

The International System of Units, universally abbreviated SI (from the French *Le Système International d'Unités*) covers all areas of physics, it widely used and standardized (ISO 1000, DIN 1301) and is the only legal unit in the EU (ECC directives 80/181 and 89/617). But SI units have two disadvantages: The numbers for typical observables of atoms are usually tiny and one has to carry a lot of constants through the calculation. Therefore other unit systems have been devised.

There exist several primers about SI units, for instance at the Bureau International des Poids et Mesures (http://www.bipm.org/) or at the physics page of the NIST [1].

E.1.1 Atomic Units

When using atomic units (a. u.), the Planck constant is 2π ($\hbar = 1$) and those constants are one: electron mass ($m_\mathrm{e} = 1$; atomic unit of mass), elementary charge ($e = 1$; atomic unit of charge) and the Bohr radius ($1 = a_0 = 4\pi\varepsilon_0\hbar^2/m_\mathrm{e}e^2$; atomic unit of length). Therefore the electric constant has to be $\varepsilon_0 = 1/4\pi$ and since $\alpha = e^2/4\pi\varepsilon_0\hbar c \approx 1/137$, the vacuum speed of light is $c = 1/\alpha$. The energy is measured in hartree ($E_\mathrm{H} = e^2/4\pi\varepsilon_0 a_0 = \alpha^2 m_\mathrm{e}c^2 = 1$) and the atomic unit of time is $\hbar/E_\mathrm{H} = 1$.

E.2 'Convenient units'

This is not a official system of units since the problem defines what is convenient. The advantage is that one can use all SI units and replace only a few by a different frame of reference; typically these are length and energy. The length is then measured in Ångströms ($1\text{Å} = 10^{-10}\text{m}$) and the energy in electron volts ($1\text{eV} = 1e\,\text{J/C}$). One

may also choose to measure the mass in electron volts using this relation: $E = mc^2 \Rightarrow m = E/c^2$. See Appendix C for the relation of electron volts to temperature, magnetic field, wavelength and frequency.

E.3 Fundamental constants

Taken from the 'NIST Reference on Constants, Units, and Uncertainty' [1].

Table E.1 Fundamental constants

Quantity	**Symbol**	**Value**	**Unit**
speed of light in vacuum	c, c_0	299 792 458	$\mathrm{m\,s^{-1}}$
magnetic constant	μ_0	$4\pi \times 10^{-7}\,\mathrm{N\,A^{-2}}$	
		$= 12.566\,370\,614\ldots \times 10^{-7}$	$\mathrm{F\,m^{-1}}$
electric constant $1/\mu_0 c^2$	ε_0	$8.854\,187\,817\ldots \times 10^{-12}$	$\mathrm{F\,m^{-1}}$
Newtonian constant of gravitation	G	$6.674\,28(67) \times 10^{-11}$	$\mathrm{m^3\,kg^{-1}\,s^{-2}}$
Planck constant	h	$6.626\,068\,96(33) \cdot 10^{-34}$	J s
$h/2\pi$	$\hbar$	$1.054\,571\,628(53) \times 10^{-34}$	J s
elementary charge	e	$1.602\,176\,487(40) \times 10^{-19}$	C
magnetic flux quantum $h/2e$	Φ_0	$2.067\,833\,667(52) \times 10^{-15}$	Wb
conductance quantum $2e2/h$	G_0	$7.748\,091\,7004(53) \times 10^{-5}$	S
electron mass	m_e	$9.109\,382\,15(45) \times 10^{-31}$	kg
proton mass	m_p	$1.672\,621\,637(83) \times 10^{-27}$	kg
proton-electron mass ratio	$m_\mathrm{p}/m_\mathrm{e}$	1 836.152 672 47(80)	
fine-structure constant $e^2/4\pi\varepsilon_\hbar\hbar c$	α	$7.297\,352\,5376(50) \times 10^{-3}$	
inverse fine-structure constant	α^{-1}	137.035 999 679(94)	
Rydberg constant $\alpha m_\mathrm{e} c/2h$	R_∞	10 973 731.568 527(73)	$\mathrm{m^{-1}}$
Avogadro constant	N_A, L	$6.022\,141\,79(30) \times 10^{23}$	$\mathrm{mol^{-1}}$
Faraday constant $N_\mathrm{A} e$	F	96 485.3399(24)	$\mathrm{C\,mol^{-1}}$
molar gas constant	R	8.314 472(15)	$\mathrm{J\,mol^{-1}K^{-1}}$
Boltzmann constant R/N_A	k	$1.380\,6504(24) \times 10^{-23}$	$\mathrm{J\,K^{-1}}$
Stefan-Boltzmann constant $(\pi^2/60)k^4/\hbar^3 c^2$	σ	$5.670\,400(40) \times 10^{-8}$	$\mathrm{W\,m^{-2}\,K^{-4}}$

Table E.2 Non-SI units excepted for use with the SI

Quantity	Symbol	Value	Unit
electron volt: (e/C) J	eV	$1.602\,176\,487(40) \times 10^{-19}$	J
(unified) atomic mass unit $1\mathrm{u} = m_\mathrm{u} = \frac{1}{12}m(^{12}\mathrm{C})$ $= 10^{-3}\mathrm{kg\,mol^{-1}}/N_A$	u	$1.660\,538\,782(83) \times 10^{-27}$	kg

Atomic units

- a. u. of charge: elementary charge: $e = 1.602\,176\,462(63) \times 10^{-19}\mathrm{C}$
- a. u. of mass: electron mass: $m_\mathrm{e} = 9.109\,381\,88(72) \times 10^{-31}\mathrm{kg}$
- a. u. of action: reduced Planck constant: $\hbar = h/2\pi = 1.054\,571\,596(82) \times 10^{-34}$
- a. u. unit of length: Bohr radius (bohr): $a_0 = 0.529\,177\,2083(19) \times 10^{-10}\,m$
- a. u. of energy, Hartree energy (hartree, Ha): $E_\mathrm{h} = e^2/4\pi\varepsilon_0 a_0 = 2R_\infty = \alpha^2 m_e c^2 = 4.359\,743\,81(34) \times 10^{-18}\mathrm{J}$
- a. u. of time: $\hbar/E_\mathrm{h} = 2.418\,884\,326\,500(18) \times 10^{-17}\mathrm{s}$
- a. u. of force: $E_\mathrm{h}/a_0 = 8.238\,721\,81(64) \times 10^{-8}\mathrm{N}$
- a. u. of velocity: $a_0 E_\mathrm{h}/\hbar = \alpha c = 2.187\,691\,2529(80) \times 10^{6}\mathrm{m\,s^{-1}}$
- a. u. of momentum: $\hbar/a_0 = 1.992\,851\,51.16) \times 10^{24}\mathrm{kg\,m\,s^{-1}}$
- a. u. of current: $eE_\mathrm{h}/\hbar = 6.623\,617\,53(26) \times 10^{-3}\mathrm{A}$
- a. u. of charge density: $e/a_0^3 = 1.081\,202\,285(43) \times 10^{12}\mathrm{C\,m^{-3}}$
- a. u. of electric potential: $E_\mathrm{h}/e = 27.211\,3834(11)\mathrm{V}$
- a. u. of electric field: $E_\mathrm{h}/ea_0 = 5.142\,206\,24(20) \times 10^{11}\mathrm{V\,m^{-1}}$
- a. u. of electric field gradient: $E_\mathrm{h}/ea_0^2 = 9.717\,361\,53(39) \times 10^{21}\mathrm{V\,m^{-2}}$
- a. u. of electric dipole moment: $ea_0 = 8.478\,352\,67(33) \times 10^{-30}\mathrm{C\,m}$
- a. u. of electric quadrupole moment: $ea_0^2 = 4.486\,551\,00(18) \times 10^{-40}\mathrm{C\,m^2}$
- a. u. of electric polarizability: $e^2 a_0^2/E_\mathrm{h} = 1.648\,777\,251(18) \times 10^{-41}\mathrm{C^2\,m^2\,J^{-1}}$

E.4 References

[1] B. N. Taylor and P. J. Mohr, *NIST Reference on Constants, Units, and Uncertainty* (2003), http://physics.nist.gov/cuu/index.html Based on '2002 CODATA recommended values'.

It was beautiful and simple as all truly great swindles are.
— O. Henry, 1862–1910

Erklärung

Ich versichere, daß ich die von mir vorgelegte Dissertation selbständig angefertigt, die benutzten Quellen und Hilfsmittel vollständig angegeben und die Stellen der Arbeit – einschließlich Tabellen, Karten und Abbildungen –, die anderen Werken im Wortlaut oder dem Sinn nach entnommen sind, in jedem Einzelfall als Entlehnung kenntlich gemacht habe; daß diese Dissertation noch keiner anderen Fakultät oder Universität zur Prüfung vorgelegen hat; daß sie – abgesehen von unten angegebenen Teilpublikationen – noch nicht veröffentlicht worden ist sowie, daß ich eine solche Veröffentlichung vor Abschluß des Promotionsverfahrens nicht vornehmen werde. Die Bestimmungen der Promotionsordnung sind mir bekannt. Die von mir vorgelegte Dissertation ist von Prof. Dr. L. Hao Tjeng betreut worden.

Tobias Burnus

Je haïs comme la mort l'état de plagiaire; Mon verre n'est pas grand mais je bois dans mon verre.
I hate like death the situation of the plagiarist; the glass I drink from is not large, but at least it is my own.
— Alfred de Musset, 1810–1857

Publications

Publication by the author which are related to this thesis.

1. Hua Wu, Tobias Burnus, Zhiwei Hu, Christine Martin, Antoine Maignan, Júlio C. Cezar, Nicholas B. Brookes, Arata Tanaka, and Hao Tjeng, *Ising magnetism and ferroelectricity in* Ca_3CoMnO_6, submitted (2008). OAI: arXiv:0806.1607

2. Tobias Burnus, Zhiwei Hu, Hua Wu, Júlio C. Cezar, Seiji Niitaka, Hidenori Takagi, Chun Fu Chang, Nicholas B. Brookes, Hong-Ji Lin, Ling-Yun Jang, Arata Tanaka, Keng S. Liang, Chien-Te Chen, L. Hao Tjeng, *X-ray absorption and x-ray magnetic dichroism study on* Ca_3CoRhO_6 *and* Ca_3FeRhO_6. Physical Review B **77**, 205111 (2008). DOI: 10.1103/PhysRevB.77.205111 OAI: arXiv:0803.0293

3. Muhammed A. Hossain, Zhiwei Hu, Maurits W. Haverkort, Tobias Burnus, Chun Fu Chang, Stefan Klein, Jonathan D. Denlinger, Hong-Ji Lin, Chien-Te Chen, Roland Mathieu, Y. Kaneko, Yoshinori Tokura, S. Satow, Y. Yoshida, H. Takagi, Arata Tanaka, Ilya S. Elfimov, George A. Sawatzky, L. Hao Tjeng and Andrea Damascelli, *Crystal-field level inversion in lightly Mn-doped* $Sr_3Ru_2O_7$, Physical Review Letters, **101**, 016404 (2008). DOI: 10.1103/PhysRevLett .101.016404 OAI: arXiv:0801.2995

4. Tobias Burnus, Zhiwei Hu, Hui-Huang Hsieh, V. L. Joseph Joly, P. A. Joy, Maurits W. Haverkort, Hua Wu, Arata Tanaka, Hong-Ji Lin, Chien-Te Chen and L. Hao Tjeng, *Local electronic structure and magnetic properties of* $LaMn_0.5Co_0.5O_3$ *studied by x-ray absorption and magnetic circular dichroism spectroscopy*, Physical Review B 77, 125124 (2008). DOI: 10.1103/PhysRevB.77.125124 OAI: arXiv:0709.3243

5. Tobias Burnus, Zhiwei Hu, Maurits W. Haverkort, Júlio C. Cezar, Delphine Flahaut, Vincent Hardy, Antoine Maignan, Nicholas B. Brookes, Arata Tanaka, Hui-Huang Hsieh, Hong-Ji Lin, Chien-Te Chen and L. Hao Tjeng, *Valence, spin, and orbital state of Co ions in one-dimensional $Ca_3Co_2O_6$: An x-ray absorption and magnetic circular dichroism study*, Physical Review B **74**, 245111 (2006). DOI: 10.1103/PhysRevB.74.245111 OAI: arXiv:cond-mat/0611545

6. Hua Wu, Zhiwei Hu, Tobias Burnus, Jonathan D. Denlinger, Peter G. Khalifah, David G. Mandrus, Ling-Yun Jang, Hui-Huang Hsieh, Arata Tanaka, Keng S. Liang, Jim W. Allen, Robert J. Cava, Daniel I. Khomskii and L. Hao Tjeng, *Orbitally driven spin-singlet dimerization in $S = 1$ $La_4Ru_2O_10$*, Physical Review Letters **96**, 256402 (2006). DOI: 10.1103/PhysRevLett.96.256402 OAI: arXiv :org:cond-mat/0606445

7. Maurits W. Haverkort, Zhiwei Hu, Júlio C. Cezar, Tobias Burnus, Helena Hartmann, Marco Reuther, C. Zobel, Thomas Lorenz, Arata Tanaka, Nicholas B. Brookes, Hui-Huang Hsieh, Hong-Ji Lin, Chien-Te Chen and L. Hao Tjeng, *Spin State Transition in $LaCoO_3$ Studied Using Soft X-ray Absorption Spectroscopy and Magnetic Circular Dichroism*, Physical Review Letters **97**, 176405 (2006). DOI: 10.1103/PhysRevLett.97.176405 OAI: arXiv:cond-mat/0610457

8. Szilárd I. Csiszar, Maurits W. Haverkort, Tobias Burnus, Zhiwei Hu, Arata Tanaka, Hui-Huang Hsieh, Hong-Ji Lin, Chien-Te Chen, Tjipke Hibma and Liu Hao Tjeng, *Aligning spins in antiferromagnetic films using antiferromagnets* (unpublished, 2005). Submitted. OAI: arXiv:cond-mat/0504520

Study as if you were to live for ever; live as if you were to die tomorrow.

— St Edmund of Abingdon, c.1175–1240

Curriculum Vitæ

11 August 1978	Born in Freiburg im Breisgau, Germany
1984–1989	Elementary School "Weiherhof-Grundschule" in Freiburg
1989–1992	Secondary School "Friedrich-Gymnasium" in Freiburg
1992–1998	Secondary School "Lilienthal-Oberschule" in Berlin, Germany
1996	Half-year intermezzo at the "Burn Coat Senior High-school" in Worcester, Massachusetts, USA
1998	Final exam "Abitur" (school-leaving examination)
1998–2004	Study of Physics at the Physics Department of Freie Universität Berlin
2001	Half-year intermezzo as Erasmus student at the Dipartimento di Fisica of Università degli Studi di Bologna, Italy
2003–2004	Diploma (∼Master) thesis "Time-Dependent Electron Localization Function" in the Research Group of Eberhard K. U. Gross at the Institute of Theoretical Physics, Freie Universität Berlin
2004–2008	Ph. D. study in the group of L. Hao Tjeng at the Second Physical Institute, Universität zu Köln in Cologne, Germany

Periodic Table

$1^2S_{1/2}$ H Hydrogen *Wasserstoff* 1.00794 $1s$ **1**, 1																	2^1S_0 He Helium *Helium* 4.002602 $1s^2$
$3^1S_{1/2}$ Li Lithium *Lithium* 6.941 $1s^2 2s$ **1**	4^1S_0 Be Beryllium *Beryllium* 9.3227 $1s^2 2s^2$ **2**											$5^1P^o_{1/2}$ B Boron *Bor* 10.811 $1s^2 2s^2 2p$ **3**	6^3P_0 C Carbon *Kohlenstoff* 12.0107 $1s^2 2s^2 2p^2$ **4**,2,-**4**	$7^4S^o_{3/2}$ N Nitrogen *Stickstoff* 14.0067 $1s^2 2s^2 2p^3$ 5,4,3,2,-**3**	8^3P_2 O Oxygen *Sauerstoff* 15.9994 $1s^2 2s^2 2p^4$ -**2**,-1	$9^2P^o_{3/2}$ F Fluorine *Fluor* 18.9984032 $1s^2 2s^2 2p^5$ -**1**	10^1S_0 Ne Neon *Neon* 20.1797 $1s^2 2s^2 2p^6$
$11^2S_{1/2}$ Na Sodium *Natrium* 22.989770 $[Ne]3s$ **1**	12^1S_0 Mg Magnesium *Magnesium* 24.3050 $[Ne]3s^2$ **2**											$13^1P^o_{1/2}$ Al Aluminium *Aluminium* 26.981538 $[Ne]3s^2 3p$ **3**	14^3P_0 Si Silicon *Silizium* 28.0855 $[Ne]3s^2 3p^2$ **4**,-4	$15^4S^o_{3/2}$ P Phosphorus *Phosphor* 30.973761 $[Ne]3s^2 3p^3$ **5**,3,-3	16^3P_2 S Sulfur *Schwefel* 32.065 $[Ne]3s^2 3p^4$ **6**,4,2,-2	$17^2P^o_{3/2}$ Cl Chlorine *Chlor* 35.453 $[Ne]3s^2 3p^5$ 7,5,3,1,-**1**	18^1S_0 Ar Argon *Argon* 39.948 $[Ne]3s^2 3p^6$
$19^2S_{1/2}$ K Potassium *Kalium* 39.0983 $[Ar]4s$ **1**	20^1S_0 Ca Calcium *Calcium* 40.078 $[Ar]4s^2$ **2**	$21^2D_{3/2}$ Sc Scandium *Scandium* 44.955910 $[Ar]3d4s^2$ **3**	22^3F_2 Ti Titanium *Titan* 47.867 $[Ar]3d^2 4s^2$ **4**,3	$23^4F_{3/2}$ V Vanadium *Vanadium* 50.9415 $[Ar]3d^3 4s^2$ **5**,4,3,2,0	24^7S_3 Cr Chromium *Chrom* 51.9961 $[Ar]3d^5 4s$ 6,**3**,2,0	$25^6S_{5/2}$ Mn Manganese *Mangan* 54.938049 $[Ar]3d^5 4s^2$ 6,**3**,2,0,-2	26^5D_4 Fe Iron *Eisen* 55.845 $[Ar]3d^6 4s^2$ **3**,2,0,-1	$27^4F_{9/2}$ Co Cobalt *Kobalt* 58.933200 $[Ar]3d^7 4s^2$ **3**,2,0	28^3F_4 Ni Nickel *Nickel* 58.6934 $[Ar]3d^8 4s^2$ **2**,1	$29^2S_{1/2}$ Cu Copper *Kupfer* 63.546 $[Ar]3d^{10} 4s$ **2**	30^1S_0 Zn Zinc *Zink* 65.409 $[Ar]3d^{10} 4s^2$ **2**	$31^2P^o_{1/2}$ Ga Gallium *Gallium* 69.723 $[Ar]3d^{10} 4s^2 4p$ **3**	32^3P_0 Ge Germanium *Germanium* 72.64 $[Ar]3d^{10} 4s^2 4p^2$ **4**	$33^4S^o_{3/2}$ As Arsenic *Arsen* 74.92160 $[Ar]3d^{10} 4s^2 4p^3$ 5,3,-3	34^3P_2 Se Selenium *Selen* 78.96 $[Ar]3d^{10} 4s^2 4p^4$ 6,4,-2	$35^2P^o_{3/2}$ Br Bromine *Brom* 79.909 $[Ar]3d^{10} 4s^2 4p^5$ 7,5,3,1,-**1**	36^1S_0 Kr Krypton *Krypton* 83.798 $[Ar]3d^{10} 4s^2 4p^6$ **2**
$37^2S_{1/2}$ Rb Rubidium *Rubidium* 85.4678 $[Kr]5s$ **1**	38^1S_0 Sr Strontium *Strontium* 87.62 $[Kr]5s^2$ **2**	$39^2D_{3/2}$ Y Yttrium *Yttrium* 88.90585 $[Kr]4d5s^2$ **3**	40^3F_2 Zr Zirconium *Zirkonium* 91.224 $[Kr]4d^2 5s^2$ **4**,3	$41^6D_{1/2}$ Nb Niobium *Niob* 92.90638 $[Kr]4d^4 5s$ **5**,3	42^7S_3 Mo Molybenum *Molybdän* 95.94 $[Kr]4d^5 5s$ **6**,5,4,3,2,0	$43^6S_{5/2}$ Tc Technetium *Technetium* (98) $[Kr]4d^5 5s^2$ **7**	44^5F_5 Ru Ruthenium *Ruthenium* 101.07 $[Kr]4d^7 5s$ 8,6,**4**,**3**,2,0,-2	$45^4F_{9/2}$ Rh Rhodium *Rhodium* 102.90550 $[Kr]4d^8 5s$ 5,**4**,**3**,2,**1**,0	46^1S_0 Pd Palladium *Palladium* 106.42 $[Kr]4d^{10}$ 4,**2**,0	$47^2S_{1/2}$ Ag Silver *Silber* 107.8682 $[Kr]4d^{10} 5s$ 2,**1**	48^1S_0 Cd Cadmium *Cadmium* 112.411 $[Kr]4d^{10} 5s^2$ **2**	$49^1P^o_{1/2}$ In Indium *Indium* 114.818 $[Kr]4d^{10} 5s^2 5p$ **3**	50^3P_0 Sn Tin *Zinn* 118.710 $[Kr]4d^{10} 5s^2 5p^2$ **4**,2	$51^4S^o_{3/2}$ Sb Antimony *Antimon* 121.760 $[Kr]4d^{10} 5s^2 5p^3$ 5,**3**,-3	52^3P_2 Te Tellurium *Tellur* 127.60 $[Kr]4d^{10} 5s^2 5p^4$ 6,4,-2	$53^2P^o_{3/2}$ I Iodine *Iod* 126.90447 $[Kr]4d^{10} 5s^2 5p^5$ 7,5,3,1,-**1**	54^1S_0 Xe Xenon *Xenon* 131.293 $[Kr]4d^{10} 5s^2 5p^6$ 2,4,6
$55^2S_{1/2}$ Cs Cesium *Cesium* 132.90545 $[Xe]6s$ **1**	56^1S_0 Ba Barium *Barium* 137.327 $[Xe]6s^2$ **2**		72^3F_2 Hf Hafnium *Hafnium* 178.49 $[Xe]4f^{14} 5d^2 6s^2$ **4**	$73^4F_{3/2}$ Ta Tantalum *Tantal* 180.9479 $[Xe]4f^{14} 5d^3 6s^2$ **4**	74^5D_0 W Tungsten *Wolfram* 183.84 $[Xe]4f^{14} 5d^4 6s^2$ **6**,5,4,3,2,0	$75^6S_{5/2}$ Re Rhenium *Rhenium* 186.207 $[Xe]4f^{14} 5d^5 6s^2$ **7**,6,4,2,-1	76^5D_4 Os Osmium *Osmium* 190.23 $[Xe]4f^{14} 5d^6 6s^2$ 8,6,**4**,3,2,0,-2	$77^4F_{9/2}$ Ir Iridium *Iridium* 192.217 $[Xe]4f^{14} 5d^7 6s^2$ 6,**4**,3,2,**1**,0,-1	78^3D_3 Pt Platinum *Platin* 195.078 $[Xe]4f^{14} 5d^9 6s$ **4**,2,0	$79^2S_{1/2}$ Au Gold *Gold* 196.96655 $[Xe]4f^{14} 5d^{10} 6s$ **3**,1	80^1S_0 Hg Mercury *Quecksilber* 200.59 $Xe]4f^{14} 5d^{10} 6s^2$ **2**,1	$81^1P^o_{1/2}$ Tl Thallium *Thallium* 204.3833 $[Hg]6p$ 3,**1**	82^3P_0 Pb Lead *Blei* 207.2 $[Hg]6p^2$ 4,**2**	$83^4S^o_{3/2}$ Bi Bismuth *Bismut* 208.98038 $[Hg]6p^3$ 5,**3**	84^3P_2 Po Polonium *Polonium* (209) $[Hg]6p^4$ 6,**4**,2	$85^2P^o_{3/2}$ At Astatine *Astat* (210) $[Hg]6p^5$ 7,5,3,1,-**1**	86^1S_0 Rn Radon *Radon* (222) $[Hg]6p^6$ **2**
$87^2S_{1/2}$ Fr Francium *Francium* (223) $[Rn]7s$ **1**	87^1S_0 Ra Radium *Radium* (226) $[Rn]6p^2$ **2**		$104^3F_2?$ Rf Rutherfordium *Rutherfordium* (261) $Rn]5f^{14} 6d^2 7s^2$	105 Db Dubnium *Dubnium* (262)	106 Sg Seaborgium *Seaborgium* (266)	107 Bh Bohrium *Bohrium* (264)	108 Hs Hassium *Hassium* (277)	109 Mt Meitnerium *Meitnerium* (268)	110 Uun Ununnilium *Ununnilium* (281)	111 Uuu Unununium *Unununium* (272)	112 Uub Ununbium *Ununbium* (285)		114 Uuq Ununquadium *Ununquadium* (289)		116 Uuh Ununhexium *Ununhexium* (292)		

$57^2D_{3/2}$ La Lanthanum *Lanthan* 138.9055 $[Xe]5d6s^2$ **3**	$58^1G^o_4$ Ce Cerium *Cer* 140.116 $[Xe]4f5d6s^2$ 4,**3**	$59^4I^o_{9/2}$ Pr Praseodymium *Praseodym* 140.90765 $[Xe]4f^3 6s^2$ 4,**3**	60^5I_4 Nd Neodymium *Neodym* 144.24 $[Xe]4f^4 6s^2$ **3**	$61^6H^o_{5/2}$ Pm Promethium *Promethium* (145) $[Xe]4f^5 6s^2$ **3**	62^7F_0 Sm Samarium *Samarium* 150.36 $[Xe]4f^6 6s^2$ **3**,2	$63^8S^o_{7/2}$ Eu Europium *Europium* 151.964 $[Xe]4f^7 6s^2$ **3**,2	$64^9D^o_2$ Gd Gadolinium *Gadolinium* 157.25 $[Xe]4f^7 5d6s^2$ **3**	$65^6H^o_{15/2}$ Tb Terbium *Terbium* 158.92534 $[Xe]4f^9 6s^2$ **4**,3	66^5I_8 Dy Dysprosium *Dysprosium* 162.500 $[Xe]4f^{10} 6s^2$ **3**	$67^4I^o_{15/2}$ Ho Holmium *Holmium* 164.93032 $[Xe]4f^{11} 6s^2$ **3**	68^3H_6 Er Erbium *Erbium* 167.259 $[Xe]4f^{12} 6s^2$ **3**	$69^2F^o_{7/2}$ Tm Thulium *Thulium* 168.93421 $[Xe]4f^{13} 6s^2$ **3**,2	70^1S_0 Yb Ytterbium *Ytterbium* 173.04 $[Xe]4f^{14} 6s^2$ **3**,2	$71^2D_{3/2}$ Lu Lutetium *Lutetium* 174.967 $[Xe]4f^{14} 5d6s^2$ **3**
$89^1D_{3/2}$ Ac Actinium *Actinium* (227) $[Rn]6s7s^2$ **3**	90^3F_2 Th Thorium *Thorium* 232.0391 $[Rn]6d^2 7s^2$ **4**	$91^4K_{11/2}$ Pa Proactinium *Proactinium* 231.03588 $[Rn]5f^2 6d7s^2$ **5**,4	$92^5L^o_6$ U Uranium *Uranium* 238.02891 $[Rn]5f^3 6d7s^2$ **6**,5,4,3	$93^6L_{11/2}$ Np Neptunium *Neptunium* (237) $[Rn]5f^4 6d7s^2$ 6,5,**4**,3	94^7F_0 Pu Plutonium *Plutonium* (244) $[Rn]5f^6 7s^2$ 6,5,**4**,3	$95^8S^o_{7/2}$ Am Americium *Americium* (243) $[Rn]5f^7 7s^2$ 6,5,4,**3**	$96^9D^o_2$ Cm Curium *Curium* (247) $[Rn]5f^7 6d7s^2$ **4**,3	$97^6H^o_{15/2}$ Bk Berkelium *Berkelium* (247) $[Rn]5f^9 7s^2$ **4**,3	98^5I_8 Cf Californium *Californium* (251) $[Rn]5f^{10} 7s^2$ **4**,3	$99^4I^o_{15/2}$ Es Einsteinium *Einsteinium* (252) $[Rn]5f^{11} 7s^2$ **3**	100^3H_6 Fm Fermium *Fermium* (257) $[Rn]5f^{12} 7s^2$ **3**	$101^2F^o_{7/2}$ Md Mendelevium *Mendelevium* (258) $[Rn]5f^{13} 7s^2$ **3**	102^1S_0 No Nobelium *Nobelium* (259) $[Rn]5f^{14} 7s^2$ 3,**2**	$103^2P^o_{1/2}$ Lr Lawrencium *Lawrencium* (262) $[Rn]5f^{14} 7s^2 7p?$ **3**